THE UNIVERSITY *of* EDINBURGH

Ammonia Water Mixtures at Extreme Pressures and Temperatures

Victor Naden Robinson

Doctor of Philosophy
The University of Edinburgh
August 2019

Abstract

The ice giants Uranus and Neptune, and exoplanets like them, contain large amounts of water, ammonia, and methane ices, as well as hydrogen in various forms. Yet it is unknown how these compounds organize themselves under the extreme conditions of pressure and temperature in the planetary interiors - for instance, would they occur as a mixture, or instead as well-separated layers within the planets. While individual ices at high pressures and temperatures have been studied in great detail, the properties of their mixtures are much less explored. Experiments have previously investigated ammonia water mixtures to moderate pressures of 10-40 GPa finding rich phase diagrams. Here the binary phase diagram of ammonia-water mixtures is explored computationally as a function of composition, pressure and temperature close to planetary conditions.

Crystal structure prediction methods utilizing the particle swarm optimization approach were employed to find stable solid phases at different densities reflecting the pressure ranges found in ice giants. Accurate energetics of different solid structures was ensured by utilizing electronic structure methods within the framework of density functional theory. Ammonia and water were investigated individually in the ground state to gauge the computational methodology and allow comparisons with the ground state mixtures. Benchmark crystal structure prediction results for the individual ices confirmed results of previous experimental and computational studies.

For the ammonia hydrates at low pressures the canonical mixing ratios previously seen in experiments (1:2, 1:1, and 2:1) are found to be stable. These mixtures form molecular compounds and, with increasing pressure, ionic phases due to proton transfer from water to ammonia. For all hydrates, new high-pressure structures are presented that supersede existing literature results. The phase evolution of the different hydrates is discussed in terms of energetics, vibrational and electronic properties.

An overarching study of all hydrates reveals that at pressures above 1 Mbar ammonia-rich hydrates dominate, stabilized by a remarkable structural evolution involving fully ionic phases with $O^{2-}(NH_4^+)_2$ units in the 2:1 hydrate, and $O^{2-}(N_2H_7^+)_2$ in a newly predicted 4:1 hydrate. In those compounds, all water molecules are completely deprotonated, an unexpected bonding phenomenon not seen before. Beyond 500-550 GPa, close to the core-mantle boundary of Neptune, all mixtures are predicted to become unstable towards decomposition into the constituents ammonia and water.

Ammonia-water mixtures that were found stable in the static ground state binary phase diagram were studied at elevated temperatures using ab initio molecular dynamics simulations. Heating these mixtures resulted in the emergence of plastic and superionic phases in all mixtures. The former is characterized by excited molecules and ionic species rotating and are also able to exhibit symmetry breaking due to temporary proton transfer depending on the mixture and the specific crystal structure. The latter exhibit fast diffusing protons in three dimensions that travel through the solid O-N sub-lattice. Further heating results in full melting, with melt lines established for all mixtures and found to be close to the Uranus and Neptune isentropes. The dynamical properties of these heated mixtures were then analyzed in terms of local structure, diffusivity, chemical abundances, and bond life-times. Covalent N-H bonds were found to be more persistent than O-H bonds, suggesting the high temperature convex hull of these mixtures may still favour ammonia-rich hydrates. Although ionicity stabilized the cold ammonia-rich hydrates, the relative abundance of ionic vs charge-neutral species decreased with temperature, leading to a more charge-balanced system. A pressure-temperature phase diagram of the ammonia-water system is presented for four different mixing ratios and up to 600 GPa and 7000 K, indicating regions of molecular, ionic, plastic, superionic, and fluid character.

Declaration

I declare that this thesis was composed by myself, that the work contained herein is my own except where explicitly stated otherwise in the text, and that this work has not been submitted for any other degree or processional qualification except as specified.

Parts of this work have been published: New phases of de-protonated ammonia hemihydrate described in chapter 4 were published in [1]. Investigating the binary phase diagram of ground-state ammonia water mixtures at high pressure covered in chapters 4 and 5 was published in [2]. Molecular dynamics studies revealing the plastic and superionic nature of high-pressure ammonia-water mixtures detailed in chapter 6 was published in [3]. During this PhD time was also spent studying the alkali metals under pressure which is not contained in this thesis: a theoretical study on the stability and electride nature of host-guest incommensurate structures was published in [4], and a study understanding the thermodynamics of the chain-melted phase of matter was published in [5].

Victor Naden Robinson, August 2019

Acknowledgements

I would like to thank supervisor Andreas Hermann for both his sound advice and the wealth of patience he has offered over the years. My second supervisor Miguel Martinez-Canalonez frequently challenged me on many ideas and offered alternative perspectives on theoretical physics. Professor Graeme Ackland has been a scientific and at many times a life guide, to whom I am grateful to have had the company of. Pete Cooke, Lewis Conway, James Aston, Harry Keen, Gavin Woolman, Pattanasak Teeratchanan, Ioan Magdau, and Miriam Marquez have all provided friendly discussion without hesitation in times of scrutiny. Ana Fialho and Miriam Pena Alvarez for always showing up with support. I thank my parents for having supported me in pursuing my interests. Zachery Sherlock and Ross Fletcher for boosting my creativity. Alex Hamilakis for always being fair. Ken Reid for keeping me going. I would like to thank Giulio De Magistris, Alexander Slowman, Matthew Neat, and Scott Taylor for the food and being a family.

Contents

Abstract i

Acknowledgements iv

Contents v

List of Figures ix

List of Tables xxi

1 Introduction 1

2 Theoretical Methods 6

2.1 Electronic Structure Methods 8

2.1.1 The Many Electron Hamiltonian 8

2.1.2 Hartree-Fock 9

2.1.3 The Hohenberg-Kohn Theorems 10

2.1.4 The Kohn-Sham Equations 11

2.1.5 The Variational Principle 15

2.1.6 Exchange-Correlation Functionals 15

2.1.7 Periodic systems and k-points 19

2.1.8 Plane-wave basis 20

2.1.9 Pseudopotentials 21
2.1.10 Wavefunction Based Methods 23
2.2 Crystal Structure Searching 27
2.2.1 General Features of the PES 32
2.2.2 Random Methods 33
2.2.3 Particle Swarm Optimization 35
2.3 Further Electronic Structure Methods 37
2.3.1 Hellman-Feynman Theorem 37
2.3.2 The Stress Tensor 37
2.3.3 Electron Localization Function 38
2.3.4 Mulliken Charges 40
2.3.5 Bader Analysis 41
2.3.6 Lattice Dynamics: Calculating Phonons 41
2.3.7 Optical Spectroscopy 43
2.3.8 Free Energy 44
2.4 Molecular Dynamics 45
2.4.1 Newtonian Dynamics 45
2.4.2 Radial Distribution Function 46
2.4.3 Mean Squared Displacement 48
2.4.4 Bond Life-times 49
2.4.5 Calculation Details 51

3 Individual Ices: Water and Ammonia 53

3.1 Phase Diagram of Water 53

3.2 Phase Diagram of Ammonia 58
3.3 Summary of Ground State Structures 60
3.4 Energetics for Water and Ammonia 63
3.4.1 Water 63
3.4.2 Ammonia 65
3.4.3 Finite Temperature Stability 67
3.5 Simulated Vibrational Spectroscopy for Water and Ammonia 71
3.6 Ammonia and Water Mulliken Charges 75
3.7 Concluding Remarks 76

4 Results for known hydrates 77

4.1 Introduction 77
4.2 Ammonia Hemihydrate 79
4.3 Ammonia Monohydrate 98
4.4 Ammonia Dihydrate 106
4.5 Concluding Remarks 113

5 Comparative study of Ammonia Water Mixtures 115

5.1 New Ammonia-rich Hydrate Under Pressure: AQH 118
5.2 Comparative Energetics of Ammonia Hydrates 122
5.3 Equations of State 126
5.4 Ionic Motifs Under Pressure 128
5.5 Conclusions 136

6 Ab Initio Molecular Dynamics 138

6.1 Previous Work 139

6.2 Phase Diagrams 142
6.2.1 Superionic Regions 146
6.2.2 Melting Lines 148
6.3 Excited Region: Plastic and Warm Phases 150
6.4 Radial and Pair Distribution Functions 154
6.5 Neutral vs Charged Species 157
6.6 Chemical Composition 159
6.7 Covalently Bonded Protons 161
6.8 Bond Life-times 163
6.9 Diffusion Regimes 166
6.10 Concluding Remarks 167

7 Conclusion 168

Bibliography 171

The First Appendix - Crystallographic Information 194

The Second Appendix - Phonon Dispersions 213

The Third Appendix - Molecular Dynamics 219

The Fourth Appendix - ADH AIMD Analysis 226

The Fifth Appendix - AMH AIMD Analysis 231

The Sixth Appendix - AQH AIMD Analysis 236

The Seventh Appendix - AHH AIMD Analysis 241

List of Figures

(2.1) Relationship between electron density and the solutions to the Hamiltonian with an external potential leading to the ground state wave-function established by first HK theorem. 11

(2.2) Diagrammatic picture of solving the KS equations using KS orbitals and how this relates to the HK theorem for the many body problem. 13

(2.3) Flow chart for solving the KS equations self-consistently while ignoring spin. 14

(2.4) Example description of a pseudopotential in red comparing the all electron (AE) in blue (dashed) potential and wavefunction. The wavefunctions correspond respectively to the potential, both of which are equal for $r > r_c$. 22

(2.5) ICSD statistics taken for the number of crystal structures consisting of a certain number of elements starting from unary, binary, ternary and so forth. 29

(2.6) ICSD statistics taken for the number of crystal structures with an integer number of formula units and any chemical composition. 30

(2.7) ICSD statistics taken for the number of crystal structures stored over a given pressure. Note that the value for zero pressure is 182,757 crystal structures and pressures are not always given in the metadata. 30

(2.8) ICSD statistics showing the number of crystal structures for the 50 most common space groups labeled with their space group number. Inset shows the number of structures with a certain integer number of symmetry operations. 31

(2.9) (a) Example PES and (b) 2D PES showing how basins can be defined [120] in a similar way to partitioning in the Bader scheme introduced later in this chapter. 32

(2.10) Crystal structure of Ammonia Monohydrate phase II, nitrogen atoms are in blue and oxygen atoms are in red. [125] 34

(2.11) Particles traversing a PES on the left. On the right are minima finding methods: (a) and (b) random sampling schemes, (c) a genetic algorithm, and (d) the CALYPSO method [132]. 36

(2.12) Example of the measurement performed by the RDF showing the coordination shell between $r + dr$. 46

(2.13) Example RDF of AIMD simulations of 128 Molten Lithium atoms under PBC at 15 GPa as a function of temperature. The distribution is broadened with increasing temperature and for a liquid $g(r)$ should tend to 1 at long separation. The shaded blue section represents the area integrated out for the first coordination shell. 47

(2.14) Example MSD for Solid BCC (blue) and Molten (red) Lithium at 15 GPa upon heating. 49

(3.1) Phase diagrams for H_2O from recent experimental and theoretical works. From top left: shock experiments showing evidence of superionicity taken from [165], calculated phase diagram of the high pressure superionic phases from taken [166], and a low pressure phase diagram taken from [167]. 54

(3.2) High PT phase diagram of ice (left) and the proton probability distribution for BCC superionic ice (right) are shown, both taken from [175]. Phase $I4_2$-d was found unstable to $P3_12_1$ in later work [176]. 55

(3.3) Oxygen (red) and proton(grey) distributions along the OHO plane in BCC ice taken from [191]. In (a) atom trajectories are plotted showing the proton localization in the BCC lattice and in (b) the trajectories are projected along the $OH\cdots O$ bond showing whether this is unimodal, bimodal, or delocalized. . . . 56

(3.4) Calculated phase diagram for H_2O is shown in (a). The green region refers to the plastic regime, light blue is superionic from a bonding analysis, and dark blue is superionic from diffusion analysis. In (a) the solid lines refer to phase boundaries that were previously known, the dashed lines represent new phase boundaries found. and dots represent different AIMD simulations. A summary of experimental melting lines for H_2O is shown in (b) taken from [192]. 57

(3.5) Phase diagrams of NH_3. Top left Shows the combined experimental and computational findings [197]. Top right shows the higher pressure solid ionic phases of ammonia predicted in [26]. Bottom shows a calculated phase diagram including experimental transition data by Bethkenhagen et al, [198]. 58

(3.6) High pressure phases of H_2O ice including X (100 GPa), $Pbcm$ (400 GPa), and $P3_121$ (1000 GPa). 59

(3.7) Original search results for NH_3 at 500 GPa with 8 f.u. (red) and tight relaxation results with a harder choice of pseudopotential, energy cut-off, and k-point mesh. The literature ground state result of Pnma at 500 GPa (4 f.u.) was recovered. Structures are ordered by their enthalpy from the original search results. Tightly refined structures may not maintain the same energy ranking as the original set as seen for structures 14-18. 62

(3.8) Relative ground state Enthalpy for proton ordered H_2O ice phases as a function of pressure where the inset shows the low pressure phase transitions. 64

(3.9) Top: Relative enthalpies for proton ordered NH_3 phases as a function of pressure calculated with the PBE functional. Below: Including ZPE and the Gibbs free energy at T = 300 K for the low pressure regime shows the $Pa\bar{3}$ phase becoming destabilized. 65

(3.10) Crystal structures of the two competing cubic structures of NH_3 at 2 GPa. Phase $P2_13$ is FCC in its heavy atom atom positions, though the face sites remain off centre and phase $Pa\bar{3}$ has a distorted hexagonal arrangement. 66

(3.11) Calculated phase diagram of H_2O. Phase boundaries (black dashed thin-line), the melting line (black dashed thick-line), and the plastic region (light green), were taken from AIMD [192] including the ice X transition line from interpolation. Coloured regions are shown for stability given by phonon calculations for ordered phases. Experimental phase boundaries (block dotted lines) for the lower pressures were taken from [220]. 67

(3.12) Low pressure phase diagram for the NH_3 system up to 50 GPa with melting and plastic experimental phase boundaries taken from [26]. 69

(3.13) Full phase diagram for the NH_3 system up to 460 GPa. Superionic, melting, and plastic phase boundaries were taken from [26]. 70

(3.14) Zone-centered phonons for high pressure H_2O ice phases as a function of pressure. Comparative data from the literature is also shown [221–223]. 71

(3.15) Zone-centered phonons for low pressure H_2O ice phases as a function of pressure. Comparative data from the literature is also shown [221–223]. 72

(3.16) High frequency zone-centered phonons for NH_3 ice phases found to be energetically stable at T = 300 K as a function of pressure. 73

(3.17) Zone-centered phonons for low pressure NH_3 ice phases (top left), low pressure vibrons only (top right), and calculated unstable phases of $P2_1/c$ and $P2_1/m$ (below) over their relevant pressure range. 74

(3.18) Calculated Mulliken Charges for NH_3 (blue) and H_2O (red) systems as a function of pressure. 75

(4.1) (left) The DMA structure with a BCC ($Im\bar{3}m$) arrangement of substitutionally disordered oxygen or nitrogen atoms (black) and partially occupied proton sites (white) taken from Wilson et al [48] on AHH. (right) The DMA structure shown for AMH by Liu et al [49]. 78

(4.2) The proposed phase diagram of ammonia hemihydrate (AHH) taken from Wilson et al [48]. Here the dash-dotted line refers to the region where water-rich (AMH and ADH for example) samples would dehydrate and form AHH-II and ice VII or VIII. The triangle symbol is the observed freezing point into AHH-I and the solid line is the melting line. The open symbols are points where both AHH-II and AHH-DMA were observed. Grey and black circles and squares refer to different heating runs detailed by Wilson et al [48]. The arrow on the right refers to a phase transition around 19 GPa from AHH-II to AHH-DMA. 80

(4.3) Calculated enthalpies for 5 unique variations of AHH-I. 81

(4.4) Enthalpy Volume plot for a structure search with AHH at 300 GPa, note that the gradient of enthalpy with volume gives pressure. 83

(4.5) Convex hull data for mixing ratios from 6:1 to 1:5 for the binary (H_2O:NH_3) system. The lowest enthalpy structures from structure searching with CALYPSO are plotted. Up to 4000 structures were optimized at a given mixing ratio. The ice phases forming the convex hull are taken to be $Pbca$ for H_2O and $Pca2_1$ for NH_3. 84

(4.6) Enthalpies of formation of AHH phases as a function of pressure, relative to decomposition into ice and ammonia (or $\frac{2}{5}$ NH_4 + 1/5 N_3H_7 above 450 GPa, see arrow), shown in the range 0-100 GPa (left) and 50-800 GPa (right). The shaded region in the left panel denotes an approximate enthalpy range of quasi-BCC structures, with a lower bound by the most stable approximant we found (see text). Dashed and dotted lines indicate decomposition reactions into other ammonia hydrates. 85

(4.7) Fully deprotonated ammonia hemihydrate structures. From top left: *Amma* phase at 80 GPa; $P\bar{3}m1$ phase at 100 GPa; *Pnna* phase at 300 GPa; and *Pnma* phase at 600 GPa. Red (blue, white) spheres denote O (N, H) atoms. All phases are drawn to the same scale, and hydrogen bonds from NH_4^+ to O are shown as dashed lines. 86

(4.8) XRD patterns of representative quasi-BCC phases found in our structure searches, all simulated with λ=1.54056Å at 40 GPa, and labeled by space group. Right-hand side shows some of the near-cubic local arrangements of each structure (black lines are to guide the eye and not unit cells). Red (blue, white) spheres denote O (N, H) atoms. The "bcc-DMA" pattern is for an idealized disordered bcc lattice with 2:1 N:O site occupancy and a=3.05Å. 87

(4.9) P-T phase diagram of AHH phases, computed within the quasi-harmonic approximation. The dashed region labeled "elements" at highest pressures represents predicted decomposition into the constituent ices of NH and OH. The dashed black line indicates the computed melting line of AMH [229], while solid black (grey) lines indicate calculated planetary isentropes of Uranus (Neptune) [232]. 89

(4.10) Phase diagram for ammonia hemihydrate based on H+ZPE calculations, and plotted on a logarithmic pressure scale. 90

(4.11) (left) Monoclinic Phase $P2_1/m$ at 400 GPa. (right) Monoclinic Phase $P2_1/c$ at 650 GPa. $P2_1/m$ is monoclinic distortion of the highly symmetric $P\bar{3}m1$ structure, whereas $P2_1/c$ is a symmetry-broken variant of the $P2_1/m$ structure. 90

(4.12) Zone-centered vibrational frequencies of AHH phases in their respective room-temperature range of stability, focusing on the molecular vibron region of 2400-3800 cm^{-1}. Phases are indicated along the top and are colored as in Figure 4.6. Solid (dashed) lines represent Raman (IR) active modes. Open triangles refer to OH stretch modes (seen until 40 GPa), and filled circles refer to NH stretches. Inset shows electron localisation function (ELF) plot for the $P\bar{3}m1$ phase at 300 GPa. The isosurface value is 0.75, and 2D cut colors range from blue (ELF=0) to red (ELF=1). 92

(4.13) Electronic band gaps for various phases at different pressures, as obtained from DFT calculations. Shaded line follows the respective most stable AHH phase at every pressure. 94

(4.14) The evolution of the average H-coordination of the oxygen atoms in AHH as a function of pressure. Above 65 GPa, there are no more donated hydrogen bonds, as all water/hydroxyl molecules are completely deprotonated. 95

(4.15) The phase diagram of ammonia monohydrate (AMH) taken from Liu et al [49]. 98

(4.16) Relative enthalpies of formation of AMH phases, on a logarithmic pressure scale and relative to decomposition into NH_3 and H_2O. Black circles show the P4/nmm phase reported by Griffiths et al [240], and gray open symbols are phases suggested by Bethkenhagen et al.[206]. 99

(4.17) The P-T phase diagram of AMH constructed using the harmonic approximation. The dashed line indicates the experimental melting line,[230] the gray diamond indicates the superionicity triple point from DFT,[206] and an approximate liquid region is indicated. 100

(4.18) Crystal structures of the AMH $P4nmm$ [240] and $P4_3$ phases at 10 and 50 GPa, respectively. Red (blue, white) spheres denote O (N, H) atoms, and covalent bonds are indicated. Hydrogen bonds are shown by bashed black lines. The $P4_3$ phase has a quasi-BCC arrangement highlighted by black lines. 102

(4.19) Snapshots from BCC AIMD simulations of AMH created by Liu et al simulating the DIMA phase taken from [49]. 102

(4.20) Crystal structures of the AMH $P2_1/m$, and $P2_12_12_1$ phases at 200 and 500 GPa, respectively. 103

(4.21) AMH phase diagram with ZPE included. 103

(4.22) Raman and Infrared spectroscopy for phases of AMH. 105

(4.23) The phase diagram of ammonia dihydrate (ADH) taken from Wilson et al [48]. The dotted dehydration line is where ADH structures break down into ice and AHH. The dash-dotted line is the liquidus line for ADH, within this region solid crystals and coexist with an ammonia-rich fluid in thermodynamics equilibrium. Dashed arrows refer to experimental pathways taken into the DMA phase. 106

(4.24) Relative enthalpy of formation of ADH phases, on a logarithmic pressure scale and relative to decomposition into NH_3 and H_2O. 107

(4.25) P-T phase diagram obtained from harmonic approximation, also including the experimental melting line,[44] the computationally predicted $I4_1cd$ phase and onset of superionicity,[207] and a tentative sketch of the liquid region. 108

(4.26) Ionic structures ADH-I* at 3 GPa (left) and ADH-II* at 12 GPa (right), derived by proton transfer from molecular ADH-I and ADH-II, respectively. 108

(4.27) Left: crystal structure of the half-ionic ADH $I4_1cd$ phase at 10 GPa. Top right: newly predicted $Ama2$ phase at 20 GPa. Bottom right: the high-pressure $P2_1/m$ phase at 60 GPa. In all phases, local body-centered features are highlighted. 109

(4.28) ADH phase diagram with ZPE included. 111

(4.29) Raman and Infrared spectroscopy for phases of ADH. 112

(5.1) Ammonia-water phases found in crystal structure searches, with up to 50 structures shown for each composition. From top: structure search results for $\Delta H_f(x)$ at 50, 100, and 300 GPa. The Solar ratio of 7:1 water:ammonia is indicated by the blue cross. 116

(5.2) Left: the $I4/m$ structure of AQH at 100 GPa. Right: relative formation enthalpies of AQH phases as a function of pressure against the constituent ices; inset shows covalent and hydrogen-bonded N-H separations in $N_2H_7^+$. 118

(5.3) $P-T$ phase diagram obtained using the harmonic approximation. The transition $P2_1/m \rightarrow I4/m$ is shaded. 119

(5.4) Proton transfer energy landscape for linearly interpolating the $P2_1/m \rightarrow I4/m \rightarrow P2_1/m$ structures, and barrier heights as a function of pressure to estimate the energy barrier of hydrogen bond symmetrization in the H_3N–H–NH_3 units. 120

(5.5) Infrared and Raman active modes calculated for AQH phases as a function of pressure. 121

(5.6) Phase stability ranges for binary ammonia-water mixtures as a function of pressure, for the ground state (left) and at T = 300 K (right). Stable compounds are labelled by commonly used numerals or space groups, black lines signify phase transitions. For pure ammonia, the gray region denotes decomposition into NH_4 and N_3H_7. Thin lines denote pressure regions where a phase is metastable (here defined as 5 meV/molecule above the convex hull). 122

(5.7) Phase stability ranges for binary ammonia-water mixtures as a function of pressure, for the different exchange-correlation functionals indicated along the y-axis. Stable compounds are labeled by commonly used numerals or space groups, black lines signify phase transitions. 124

(5.8) Equations of state for the ammonia - water ice system, including all mixtures discussed in this work. Top are the equations of state on a linear (top left) and logarithmic scale (top right), as well as the linear mixing ratio volume for each mixture. Below we show the deviations from the linear mixing ratio on linear (bottom left) and logarithmic (bottom right) scales. 126

(5.9) Nearest-neighbor O–H (top) and N–H (bottom) separations across all ammonia hydrates and ices, in their respective most stable ground state phase as a function of pressure. 128

(5.10) Binding energies of water-ammonia dimers and trimers from PBE calculations, relative to neutral gas phase molecules, and normalized per hydrogen bond. Blue solid line: $HOH\cdots NH_3$; green dashed line: $H_3NH\cdots OH$; purple dotted line: $H_3NH\cdots O\cdots HNH_3$. Geometries are shown as insets. 129

(5.11) Interaction potential energy surfaces for dimer and trimer setups taken from ammonia water crystals or the lowest energy representation calculated at different levels of theory. 130

(5.12) Isosurfaces of the electron localisation function (ELF=0.7) in ammonia hydrates, together with cross sections from ELF=0.7 (blue) to ELF=1.0 (red). (a) AMH-$P4/nmm$ at 10 GPa, (b) AMH-$P4_3$ at 100 GPa, (c) AHH-$P\bar{3}m1$ at 200 GPa, (d) AQH-$I4/m$ at 100 GPa. All structures drawn to the same scale. Hydrogen bonds are indicated by dashed lines. 131

(6.1) Phase diagram for AMH calculated from AIMD, taken from [229]. Yellow and red shaded regions refer to the superionic phase space for ammonia and water respectively [198, 275]. Symbols are along isochores in T-P space including the thermal pressure. Different symbols indicate solid (blue squares), superionic (purple diamonds), and fluid (orange circles) states. Solid-Solid (black lines) phase boundaries are based on phonon free energy calculations. Adiabats for Uranus and Neptune indicate the T-P path expected inside these icy planets. 140

(6.2) Superionic transition phase diagram for ADH calculated from AIMD, taken from [207]. The ionic region refers to the solid $I4_1cd$ ADH phase. 141

(6.3) Phase diagrams for the four mixtures in their region of stability. Dark blue and cyan shaded regions refer to excited (rotations and or ionised) systems and the superionic phase respectively. Orange shaded region is the liquid while solid phases are labeled and colored individually. Grey shaded region is the calculated decomposition the constituent ices of NH and OH. Experimental melt lines for ADH and AMH are from [48]. For AMH the grey cross notes the AMH triple point from [241] and the dash line represents the melt line from the same study. For ADH the dashed line with white diamonds represents the superionic transition line found in [207]. 143

(6.4) AIMD data for AMH-P4/nmm at 30 GPa, left: proton trajectories for 10 ps run at 1000 K. Right: Diffusion constants for different atomic species as a function of temperature. Long dash / short dashed / dotted lines denote onsets of excited / superionic / fluid regimes. 144

(6.5) Superionic regions for all four mixtures, and data for the individual ices is taken from [198, 275]. The highest shown pressure for each mixture corresponds to the AIMD PT grid used and roughly corresponds to their limit of stability. 146

(6.6) Combined melt lines for all four mixtures and the melting line for AMH* from [229]. 148

(6.7) Example movements of the excited phases at temperatures lower than the superionic regime. Left shows rotational modes for various unit types; Right shows temporary proton transfer. . . . 150

(6.8) Snapshot of AHH at 500 GPa and 1000 K with the proton trajectory for 5 ps shown as points. During the simulation some NH_4^+ units undergo rotations as well as temporarily donating a proton. Bonds are drawn between N,O and protons with a cutoff distance of 1.1 Å for the final trajectory step. 151

(6.9) Proton mean squared displacement for rotating units in warm AHH at 500 GPa. 152

(6.10) RDF's and PDF's for AHH at 100 GPA where dashed lines indicate the superionic phase. 154

(6.11) PDF's for AHH at 100 GPa where dashed lines indicate the superionic phase. Labels indicate the likely chemistry where and a peak is observed around a typical covalent bond length at 100 GPa. 155

(6.12) Analysis of the units making up ADH as a function of P and T. Note that the starting configuration in the ground state always contained 2/3 ionic species. Dashed lines indicate the temperature at which a superionic phase was observed and dotted indicate the melting temperature. 157

(6.13) Fraction of molecular units found in mixtures, black dashed lines are the respective melt lines. Dark blue (ionic) is a fraction of 0.0 and yellow (molecular) is 1.0. 158

(6.14) Relative abundance of most relevant species in ADH simulations. 159

(6.15) Relative abundance of most relevant species in AHH simulations. 160

(6.16) Number of X-H (X = N,O) bonds and their type in ADH as a function of temperature for various pressures. 161

(6.17) Number of X-H (X = N,O) bonds and their type in AQH as a function of temperature for various pressures. 162

(6.18) Bond life-times of X-H bonds in ADH. 163

(6.19) Bond auto correlation functions for NH and OH bonds in ADH. Dash lines refer to the superionic phase and dotted lines refer to the excited states. 164

(6.20) Estimated bond life-times τ_α from the BAC in ADH. 165

(6.21) Diffusion constants as a function of pressure in AMH. 166

(1) Left: AHH-I at 1 GPa; right: AHH-II at 10 GPa. 213

(2) From left: Cm, $P\bar{1}$, and $A2/m$ phases, all at 30 GPa. 214

(3) Left: *Amma* at 100 GPa; right: $P\bar{3}m1$ at 150 GPa. 214

(4) Left: $P2_1/m$ at 400 GPa; right: $P2_1/c$ at 650 GPa. 214

(5) Left: *Pnna* at 300 GPa; right: *Pnma* at 700 GPa. 215

(6) Left: AMH-I at 1 GPa; right: AMH-II at 3 GPa. 216

(7) Left: $P4/nmm$ at 10 GPa; right: $P4_3$ at 50 GPa. 216

(8) AMH-I at 500 GPa. 216

(9) Left: ADH-I at 1 GPa; right: ADH-II at 5 GPa. 217

(10) Left: ADH-I* at 4 GPa; right: ADH-II** at 5 GPa. 217

(11) From Left: $I4_1cd$ at 8 GPa, $Ama2$ at 30 GPa, and $P2_1/m$ at 80 GPa. 217

(12) Left: $P2_1$ at 5 GPa; right: $P2_1/m$ at 30 GPa. 218

(13) I4/m at 100 GPa. 218

(14) ADH analysis of ionicity (top left), unit types (top right, bottom left), and covalent hydrogen bonds (bottom right). 226

(15) ADH analysis of estimated bond life times (top left), ion diffusion (top right). 227

(16) ADH analysis of bond auto correlation function. 227

(17) ADH analysis of MSD. 228

(18) ADH analysis of RDF and PDF (NH,OH,HH). 229

(19) ADH analysis of PDF (NN,OO,NO). 230

(20) AMH analysis of ionicity (top left), unit types (top right, bottom left), and covalent hydrogen bonds (bottom right). 231

(21) AMH analysis of estimated bond life times (top left), ion diffusion (top right). 232

(22) AMH analysis of MSD. 232

(23) AMH analysis of bond auto correlation function. 233

(24) AMH analysis of RDF and PDF (NH,OH,HH). 234

(25) AMH analysis of PDF (NN,OO,NO). 235

(26) AQH analysis of ionicity (top left), unit types (top right, bottom left), and covalent hydrogen bonds (bottom right). 236

(27) AQH analysis of estimated bond life times (top left), ion diffusion (top right). 237

(28) AQH analysis of MSD. 237

(29) AQH analysis of bond auto correlation function. 238

(30) AQH analysis of RDF and PDF (NH,OH,HH). 239

(31) AQH analysis of PDF (NN,OO,NO). 240

(32) AHH analysis of ionicity (top left), unit types (top right, bottom left), and covalent hydrogen bonds (bottom right). 241

(33) AHH analysis of estimated bond life times (top left), ion diffusion (top right). 242

(34) AHH analysis of MSD. 242

(35) AHH analysis of bond auto correlation function. 243

(36) AHH analysis of RDF and PDF (NH,OH,HH). 244

(37) AHH analysis of PDF (NN,OO,NO). 245

List of Tables

(2.1) Summary of Jacob's Ladder starting from the bottom entry. . . . 19

(2.2) DFT parameters for different structural relaxations during ammonia water searches with CALYPSO (above) and the distance matrix used to accept generated structures (below). 52

(3.1) Table 1. Ground state structural phase evolution of water at high pressure, from DFT-PBE calculations performed in this work. . . 60

(3.2) Table 2. Ground state structural phase evolution of ammonia at high pressure, from DFT-PBE calculations. Note that the isostructural transition between phases IV and V is from experiments and are energetically equal in stability in DFT-PBE. . . . 60

(3.3) Summary of structure searches performed for ices H_2O and NH_3. The space group for the lowest energy structure found in each search is given. 61

(4.1) Summary for AHH structure searches. 82

(4.2) Summary of structure searches with 2-8 f.u. performed for AMH. 104

(4.3) Summary of structure searches with 2-8 f.u. performed for ADH. 110

(5.1) Summary of structure searches with 2-8 f.u. performed for AQH. 118

(5.2) Valence charge density analysis of ammonia hydrates based on the ELF partitioning of space. n_{basin} is total valence charge in each ELF basin; b.i.p.'s as sketched are characterised by their distances d to nearest atoms, and their ELF value; and partial charges q are summed up for the subunits discussed in the text. 132

(5.3) Bader QTAIM analysis for ammonia hydrates. n_{basin} denotes valence charge density integrated in each basin. Bond critical points (b.c.p.'s) are sketched out and characterised by their charge density ρ, Laplacian $\nabla^2\rho$, and separation from nearest atoms. Partial charges q for the different subunits come from sums of n_{basin} as appropriate. 135

(6.1) Summary of visual analysis of the dominant events in AHH-AIMD at temperatures below and across the superionic regime. 152

(1) Crystallographic information $AHHA2/m$ 194

(2) Crystallographic information $AHHP-1$ 195

(3) Crystallographic information $AHHCm$ 195

(4) Crystallographic information $AHHAmma$ 196

(5) Crystallographic information $AHHP\bar{3}m1$ 196

(6) Crystallographic information $AHHPnna$ 196

(7) Crystallographic information $AHHPnma$ 197

(8) Crystallographic information $AHHP2_1/m$ 197

(9) Crystallographic information $AHHP2_1/c$ 198

(10) Crystallographic information $AHHI$ 199

(11) Crystallographic information $AHHII$ 199

(12) Crystallographic information $AHHmolecularP1$ 200

(13) ADH simulation time (ps) summary and details for low T. 220

(14) ADH simulation time (ps) summary and details for high T. . . . 220

(15) ADH finite temperature pressure (GPa) 221

(16) AMH simulation times (ps) 222

(17) AMH Finite temperature pressure (GPa) 222

(18) AHH simulation times (ps) 223

(19) AHH finite temperature stress (GPa) 224

(20) AQH simulation times (ps) and details 225

(21) AQH finite temperature stress (GPa) 225

Chapter 1

Introduction

Mixtures of molecular ices of water, ammonia and methane (together with impurities and volatiles such as hydrogen or helium) make up a large proportion of the mantle regions of the "ice giants" Uranus and Neptune as well as large icy moons in our solar system, and are presumed to feature prominently in the large number of Neptune-like exoplanets discovered by recent and current astronomical observation campaigns [6–12]. It is not clear how molecular ices organize themselves inside these planetary bodies – whether they form segregated layers with distinct chemical and density profiles, or homogeneous mixtures corresponding roughly to the global composition ratio throughout. The low luminosity of Uranus could be explained by the presence of a thermal boundary layer in its mantle region [13, 14], which would suggest quite drastic composition gradients in its interior. High pressure conditions (which reach hundreds of GPa inside ice giants) can in general favor unexpected chemical motifs, and thus stabilize unusual compounds and stoichiometries, as found among prototypical mineral compounds [15–19] as well as individual ices [20–26]. The *mixtures* of the molecular ices might equally feature surprising pathways to stability under compression; for instance, methane's solubility in water increases significantly at pressures as low as a few GPa [27].

The properties of solids are defined by their electronic structure [28] and so electronic structure methods can be employed to study, to begin with, their energetic stability. More simple models such as pair potentials can also be used and are also cheaper to compute, though often suffer from a lack of accuracy due to their functional form and are typically fitted to known data-sets for a given

system. For a given thermodynamic point in temperature and pressure space, there may be several competing solid structures (or any material) for a given chemical makeup with similar free energy. In order to distinguish which the most stable, that which nature thus wants to form for example in the deep mantle of Neptune, a method which can accurately rank the energies of these competing structures is required to assess the correct thermodynamically stable phase. This is important when trying to predict the stable crystal structure for a material [29, 30], and increasingly useful at high pressure which has been less explored by experiment, as a tool to map the chemical space.

Electronic structure methods benefit from computing properties such as the band gap, metalization, and ab initio molecular dynamics can be computed. Employing these methods to high pressure and temperature water [21] had direct applications to understanding planetary interiors. At extreme conditions water was predicted to exhibit both solid and liquid behaviour in the "superionic" regime [21]. Other interesting phenomena occur under pressure, such single alkali metals forming host-guest structures [4] as well as having similar both solid and liquid like behaviour on heating and before melting in a "chain-melted" phase of matter [5]. Closer to home, here on Earth, electronic structure methods have been to investigate the thermal and electronic conductivity of iron by Pozzo et al [31], the melting [32], and predicted the chemistry of geophysically relevant reactions of iron with crystal structure prediction combined with electronic structure in a binary-study by Zhu et al [16]. Recently crystal structure searching combined with electronic structure methods have been used to predict the many high pressure superconductor with especially high critical temperatures (T_c). Binary hydrides have found great success as high temperature superconductors at high pressure, further motivating structure searching for binary systems, for example, Yttrium hydride was predicted to have a T_c of 251-264 K at 120 GPa [33]. High pressure is full of interesting phenomenon where electronic structure, structure searching and other methods can help discover, predict, and understand.

High pressure experiments are designed to compress a material and look for changes in physical observables. In a diamond anvil cell (DAC) [34], materials are compressed by carefully constructed diamonds which are transparent to many probes, such as X-rays which allow the sample's structure to be determined. Materials are often contained in a carefully chosen pressure medium, avoiding chemical reactions, to try and achieve hydrostatic pressure for example in a study with a Paris-Edinburgh cell by Marshall et al [35]. For pressures slightly higher

than ambient pistons-cylinders can be used to squeeze materials, but to achieve the high pressures in the cores of planets (360 GPa in Earth) DAC's are readily used but with sample sizes on the micrometer scale. These anvil experiments are typically termed static, as the material is held in a state for a long time and measured in thermodynamic equilibrium. Alternatively, there is dynamic-compression [36], which sends a shock-wave through a material to achieve a high density of atoms (but also temperature). Measurements can be performed during the short compression and are they are able to reach much higher pressures than their static counterpart. This can be performed by gas guns [37] or laser-driven ramp compression [36], where shocks can be designed to follow special pressure temperature paths, and even combined with a DAC for precompression.

Mixtures of ammonia and water are of interest due to their ability to form nearly or complete hydrogen-bonded networks, and three stoichiometric mixtures exist in nature and have been explored around ambient and low-pressure conditions: ammonia monohydrate (AMH, NH_3:H_2O=1:1), ammonia dihydrate (ADH, 1:2) and ammonia hemiydrate (AHH, 2:1) [38, 39]. These HNO hydrogen-bonded networks form integral parts of ingredients for life in DNA and RNA and so their interactions are important to understand both ambiently and when compressed. For comparison, the ammonia:water solar abundance ratio is 1:7 [40]. The individual ices pursue quite different routes under pressure: water ice follows a sequence of atomic networks above 65 GPa, where water molecules readily give up their protons to sit at the mid-points of nearest-neighbor O–O separations [22, 23, 41, 42]; whereas ammonia holds onto its protons much better, and instead self-ionizes above 120 GPa into ammonium amide over a large pressure range before (in calculations) returning to packings of neutral molecules [25, 26, 43]. First-principles calculations have proven very useful in establishing or confirming individually the different ice and hydrate phases and their properties. What is missing, however, is an overarching study of the ammonia hydrates that considers all mutual formation and decomposition reactions at various pressures and temperatures, and also explores whether *other* hydrate stoichiometries could be stabilized under specific conditions. In this thesis, we present such a study.

The three known hydrates' phase diagrams show appreciable complexity (shown in further detail in chapter 4): at various $P-T$ conditions, five solid AMH and ADH phases, as well as three solid AHH phases have been identified in experiment, even though some of their structures have not been resolved. There is some interplay between the three mixtures: both ADH and AMH decompose into AHH

and ice-VII, around 3 GPa and at 280 K and 250 K, respectively, while ADH also decomposes into AMH and ice-VII around 0.55 GPa and 190 K [44, 45]. Moreover, around 5–20 GPa and room temperature, *all* ammonia hydrates are found to form disordered molecular alloy (DMA) phases, with substitutional disorder of ammonia and water on a body-centered cubic (bcc) lattice and calculations predict partial ionization into OH^- and NH_4^+ in all hydrates [44, 46–49]. The AHH-DMA phase has been observed in two independent experiments [48, 50] that found, at low temperatures, transitions from AHH phase II at 19–30 GPa. AHH-DMA was found to remain stable up to the highest experimental pressure studied, 41 GPa [48]. The molecular and DMA phases in the three hydrates have been studied extensively through experiment and first-principles calculations, often in combined studies.

This work is organized as follows. In the next chapters, we describe the details of our calculations and methods. Then we introduce the individual ices of H_2O and NH_3 and present high pressure results for these. Following this we explore individually the high-pressure and -temperature phase diagrams of the three known ammonia hydrates; for each hydrate, we provide new insights into their high-pressure phase evolution and discuss the chemical motifs found in the most relevant phases. Subsequently, we present a comparative stability analysis of all hydrates, which enables us to predict stabilities and formation/decomposition for each individual compound on enthalpic grounds.

We show that it is important to consider all hydrates together, as their stability is mostly limited by reactions with each other, and not the simple formation from or decomposition into the constituent ices of water and ammonia. During this analysis, we also show that a new ammonia-rich 4:1-hydrate, we term ammonia quarterhydrate (AQH), emerges as an unexpectedly stable compound at relatively modest pressures. Throughout, we find that the formation of exotic ionic compounds, based on proton transfer from water to ammonia, is important to ensure stability, and that ammonia-rich phases (which provide sufficient proton acceptors) are stable to much higher pressures than water-rich phases. Eventually at pressures beyond 500 GPa we find no stable mixtures of water and ammonia, instead there is a decomposition into the separate OH and NH systems.

Investigating these materials inside the P-T conditions predicted to occur in icy bodies throughout the universe we simulated the realistic dynamics of the system. We performed molecular dynamics simulations to look at the nature of the matter, addressing whether it is solid or liquid in different regions of a planetary body.

Going from the solid to the liquid there exist intermediate stages of matter as the materials are heated into excited states, and once in the liquid form how does it comprise? Are these materials still stable to full atomic decomposition in the P-T space relevant to icy bodies? Finally, we make predictions for the stability of these mixed ices in their regions of stability both in temperature and pressure.

In chapter 2 the theoretical methods used in this work are introduced and demonstrated. In chapter 3 the individual ices of ammonia and water are introduced drawing knowledge from literature and new data is presented. In chapter 4 results on the three known hydrates (AMH, ADH, and AHH) part of which have been published in [1, 2] in collaboration with Miriam Marques, Yanming Ma and Yanchao Wang. In chapter 5 a comparative analysis of the ammonia water system is performed, comparing different mixtures and searching for new stable options published in [2]. Chapter 6 presents the results of ab initio molecular dynamics simulations (AIMD) for the ammonia water system concluding with the resulting pressure and temperature phase diagram published in [3]. Some of the AIMD trajectories have been acquired by an undergraduate summer student, Jacob Christiansen, who I co-supervised.

Chapter 2

Theoretical Methods

In this chapter theoretical methods for simulations and analysis used in this work are outlined. The main workhorse for condensed matter computation is density functional theory (DFT) [51] and is the dominant method used in this work. Here a discussion of how DFT works and its implementation in modern computer codes is presented. Other electronic structure methods commonly applied in the field of computational chemistry, such as Hartree Fock [52], Coupled Cluster [53], and Møller-Plesset Perturbation Theory [54] are also introduced as they are utilized to investigate specific questions in later chapters. Common and less common extensions of total energy calculations that gain an understanding of the ground state properties of a system are also discussed, such as the Electron Localization Function (ELF) [55], Bader Charge Analysis [56], and lattice dynamics [57].

While DFT and wave-function methods are the main methods for computing total energies, other general methods are also used. The first being Crystal Structure Searching reviewed in [58], a stochastic method used to predict the crystal structure for a given system. Such a method was used to investigate and predict stable mixtures of ammonia and water beyond the current experimental pressure range. While at its core being a problem of global optimization which is tackled stochastically, we will see that there are various methods for accelerating this process with added functionality.

The second method being molecular dynamics (MD) often referred to as ab-initio molecular dynamics (AIMD) when combined with DFT [59]. This is the main

method for simulating systems at finite temperature including temperature-driven phase transitions. The range of analysis for MD is broad in the modern-day and the methods used later in chapter 6 shall be discussed. For molecular ices in particular proton transfer, diffusion rates, and melting lines are of interest with increasing relevancy to ice giants.

2.1 Electronic Structure Methods

2.1.1 The Many Electron Hamiltonian

To calculate the total energy, E, of an interacting many-body system in condensed matter one can start by accurately solving the Time Independent Schrödinger Equation (TISE),

$$\hat{H}\Psi = E\Psi, \tag{2.1}$$

where $\hat{H}$ is the Hamiltonian operator and ψ is the many-body wavefunction, which, as well as $\hat{H}$, is a function of the coordinates of M nuclei $\{\boldsymbol{R}_i\}$ and N electrons $\{\boldsymbol{r}_i\}$ defined explicitly as,

$$\Psi = \Psi(\boldsymbol{R}_1, \boldsymbol{R}_2, \ldots, \boldsymbol{R}_M; \boldsymbol{r}_1, \boldsymbol{r}_2, \ldots, \boldsymbol{r}_N). \tag{2.2}$$

For a system of electrons and nuclei the Hamiltonian is,

$$\hat{H} = \hat{T}_e + \hat{T}_n + \hat{V}_{ee} + \hat{V}_{ne} + \hat{V}_{nn}, \tag{2.3}$$

where $\hat{T}$ are the kinetic energy operators of the electrons (e) and nuclei (n), and $\hat{V}$ are the interactions between electrons and nuclei. For the non-relativistic case of a system of positively charged ions and electrons with Coulombic interactions this can be written as,

$$\begin{aligned}\hat{H} = &-\sum_{i=1}^{N}\frac{\hbar^2}{2m_e}\nabla_i^2 - \sum_{j=1}^{M}\frac{\hbar^2}{2M_j}\nabla_j^2 + \\ &\frac{1}{2}\sum_{i\neq j}^{N}\frac{e^2}{|\boldsymbol{r}_i - \boldsymbol{r}_j|} - \frac{1}{2}\sum_{i=1}^{M}\sum_{j=1}^{N}\frac{Z_i e^2}{|\boldsymbol{R}_i - \boldsymbol{r}_j|} + \frac{1}{2}\sum_{i\neq j}^{M}\frac{Z_i Z_j e^2}{|\boldsymbol{R}_i - \boldsymbol{R}_j|},\end{aligned} \tag{2.4}$$

where $\hbar$ is Planck's constant, e is the electron charge, m_e and M_i are the electron and ionic masses respectively, and Z_i is charge of the nucleus, with $4\pi\epsilon_0$ set to unity. Equation 2.4 can be solved analytically for the hydrogen atom (1-body with a classical nucleus) but requires the use of computers entering the two-body problem and greater. This can be aided by taking certain approximations and by exploiting certain properties of the system such as later in DFT.

The first approximation made for solving this Hamiltonian is the Born-Oppenheimer approximation (BOA) also known as the adiabatic approximation [60], which

decouples the electronic and nuclear degrees of freedom,

$$\Psi_{total} = \Psi_{electronic} \cdot \Psi_{nuclei}, \tag{2.5}$$

justified by $M_i \gg m_e$ by a ratio upwards of 2000:1 meaning the electrons move significantly faster than the nuclei or that the nuclei follow the electrons. This means solving the Schrödinger equation with static nuclei, discarding their kinetic energy from the electronic Hamiltonian, while losing little accuracy. Electrons are treated quantum mechanically and nuclei classically, rewriting TISE as,

$$\hat{H}(\boldsymbol{r}_1, \boldsymbol{r}_2, \ldots, \boldsymbol{r}_N; \boldsymbol{R}_i)\Psi(\boldsymbol{r}_1, \boldsymbol{r}_2, \ldots, \boldsymbol{r}_N; \boldsymbol{R}_i) = E(\boldsymbol{R}_i)\Psi(\boldsymbol{r}_1, \boldsymbol{r}_2, \ldots, \boldsymbol{r}_N; \boldsymbol{R}_i), \tag{2.6}$$

now simplifying the system's Hamiltonian to,

$$\hat{H} = \hat{T}_e + \hat{V}_{ee} + \hat{V}_{ne} + \hat{V}_{nn}. \tag{2.7}$$

Note that the last term is a number unique to a system's nuclear geometry which can be calculated by a summation of Coulomb interactions for the nuclear charges.

2.1.2 Hartree-Fock

The simplest method for approximately solving the above Hamiltonian is the Hartree method with ansatz for the many-particle wavefunction [61],

$$\Psi(\boldsymbol{r}_1, \boldsymbol{r}_2, \ldots, \boldsymbol{r}_N) = \psi_1(\boldsymbol{r}_1)\psi_2(\boldsymbol{r}_2)\ldots\psi_N(\boldsymbol{r}_N), \tag{2.8}$$

such that the electrons are not interacting other than by the mean-field Coulomb force, leading to one-electron Schrödinger equations of the form,

$$-\frac{\hbar^2}{2m}\nabla^2\psi_i(\boldsymbol{r}) + \left(V_{en}(\boldsymbol{r}) + V_H(\boldsymbol{r})\right)\psi_i(\boldsymbol{r}) = \epsilon_i\psi_i(\boldsymbol{r}), \tag{2.9}$$

yet fails to capture the essential physics and chemistry of atoms and molecules such as atomic shell structure or chemical bonding. The electron-electron interaction is described by a classical Coulomb repulsion also known as the Hartree potential V_H [62],

$$V_H = \int \frac{n(\boldsymbol{r})}{|\boldsymbol{r} - \boldsymbol{r}'|} d\boldsymbol{r}'. \tag{2.10}$$

The Hartree-Fock (HF) method [63] includes electron-electron interactions from the Pauli exclusion principle. The HF method works well for systems such as single atoms and molecules, although fails to describe cases in which electron correlation is the dominant bonding mechanism such as dispersion forces in noble gas dimers. This is because it purely solves the Hamiltonian satisfying electron exchange included in the anti-symmetry of the wave-function. This is achieved by a use of a single Slater Determinant introduced in 1929 [64] which is a sum of products of one-electron wavefunctions χ_N ensuring the fermionic many particle wavefunction is anti-symmetric $\Psi(\boldsymbol{r}_1, \boldsymbol{r}_2) = -\Psi(\boldsymbol{r}_2, \boldsymbol{r}_1)$, given in its general form by,

$$\Psi(\boldsymbol{r}_1, \boldsymbol{r}_2, ..., \boldsymbol{r}_N) = \frac{1}{\sqrt{N}} \begin{vmatrix} \chi_1(\boldsymbol{r}_1) & \chi_2(\boldsymbol{r}_1) & \cdots & \chi_N(\boldsymbol{r}_1) \\ \chi_1(\boldsymbol{r}_2) & \chi_2(\boldsymbol{r}_2) & \cdots & \chi_N(\boldsymbol{r}_2) \\ \vdots & \vdots & \ddots & \vdots \\ \chi_1(\boldsymbol{r}_N) & \chi_2(\boldsymbol{r}_N) & \cdots & \chi_N(\boldsymbol{r}_N) \end{vmatrix}, \tag{2.11}$$

decoupling electrons allowing the single-particle Hartree-Fock equations to be written as,

$$-\frac{\hbar^2}{2m}\nabla^2\chi_i(\boldsymbol{r}) + V_{en}(\boldsymbol{r})\chi_i(\boldsymbol{r}) + V_H(\boldsymbol{r})\chi_i(\boldsymbol{r}) - \sum_j \int d\boldsymbol{r'} \frac{\chi_j^*(\boldsymbol{r'})\chi_i^*(\boldsymbol{r'})\chi_i(\boldsymbol{r})\chi_j(\boldsymbol{r})}{|\boldsymbol{r} - \boldsymbol{r'}|} = \epsilon_i\chi_i(\boldsymbol{r}). \tag{2.12}$$

The Hartree-Fock energy is always an upper bound value of the actual ground state energy. The Hartree-Fock method is used to solve the TISE normally with the Born-Oppenheimer approximation requiring a self-consistent solution starting from an initial field, i.e. converging the total energy and charge distribution. Quantum chemistry methods based on correlation expand the multi-electron wavefunction in a linear combination of Slater determinants to include the missing electron correlation (see section 2.1.10) which remains the greatest drawback of HF.

2.1.3 The Hohenberg-Kohn Theorems

So far the Schrödinger equation has been simplified and solved in HF which also includes the exact exchange interaction. Here the method of Density Functional Theory approximates exchange and correlation effects. In 1964 DFT was introduced by Hohenberg and Kohn [65]. Hohenberg and Kohn (HK) start from the Schrödinger equation using the electron density $n(\boldsymbol{r}) = \langle\Psi|\hat{n}(\boldsymbol{r})|\Psi\rangle$ which is a scalar field. Now the system can be characterized by 3 coordinates

rather than $3N$ coordinates considered in a wave-function approach.

The HK theorems are:
(1) A system of interacting particles in an external potential, $V_{ext}(\boldsymbol{r})$, has this potential uniquely determined by the ground state electron or particle density, $n(\boldsymbol{r})$. This is equivalent to the ground state electron particle density determining fully the Hamiltonian and therefore also all ground state properties of the system.

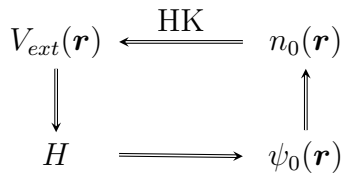

Figure 2.1 *Relationship between electron density and the solutions to the Hamiltonian with an external potential leading to the ground state wave-function established by first HK theorem.*

(2) A density functional $F[n(\boldsymbol{r})]$ exists for the energy $E[n(\boldsymbol{r})]$, in an external potential $V_{ext}(\boldsymbol{r})$, which is minimized to the global minimum of $E[n(\boldsymbol{r})]$ by the exact ground state particle density $n_0(\boldsymbol{r})$. So the exact ground state energy can be determined by,

$$E[n] = F[n] + \int n(\boldsymbol{r}) V_{ext}(\boldsymbol{r}) d^3\boldsymbol{r}. \tag{2.13}$$

Now in principle, the energy can be computed by a suitable trial guess for $n(\boldsymbol{r})$ then solved iteratively for the ground state, however the calculation remains impractical and an efficient alternative is introduced in 2.1.4. The form or construction for $F[n]$ is not known nor discussed in the original proof found in [65], and assumes non-degenerate ground states but this was extended for degenerate systems in [66–69] by Levy and Liev using the constrained search approach.

2.1.4 The Kohn-Sham Equations

One year later in a second ground breaking paper [70] Kohn and Sham (KS) offered an approach to approximating $F[n]$. Here the system of interacting electrons is mapped to a fictitious system of non-interacting electrons experiencing an effective external potential. The key ingredient for this is that the ground state electron density for the fictitious system is equal to that of the real system. This allows the system to be described by a set of one-electron Schrödinger like

equations which are known as the Kohn-Sham equations:

$$\left(-\frac{\hbar^2}{2m}\nabla_i^2 + V_{KS}(\boldsymbol{r})\right)\Psi_i(\boldsymbol{r}) = E_i\Psi_i(\boldsymbol{r}), \tag{2.14}$$

where the Kohn Sham Potential $V_{KS}(\boldsymbol{r})$ is given by,

$$V_{KS}(\boldsymbol{r}) = V_{ext}(\boldsymbol{r}) + \int \frac{n(\boldsymbol{r}')}{|\boldsymbol{r}-\boldsymbol{r}'|}d^3(\boldsymbol{r}') + V_{xc}[n(\boldsymbol{r})], \tag{2.15}$$

where ψ_i are the KS pseudo orbitals describing the electrons and give the density,

$$n(\boldsymbol{r}) = \sum_{i=1}^{N}|\psi_i(\boldsymbol{r})|^2. \tag{2.16}$$

The first two terms in equation 2.15 are simple, and the 3rd term is the exchange-correlation potential which contains the many-body interactions of the system beyond mean-field Hartree interactions. The exchange correlation potential is the functional derivative of,

$$V_{xc}(\boldsymbol{r}) = \frac{\delta E_{xc}[n]}{\delta n(\boldsymbol{r})}. \tag{2.17}$$

The ground state energy in functional form is,

$$E[n(\boldsymbol{r})] = T_e[n(\boldsymbol{r})] + V_{ee}[n(\boldsymbol{r})] + V_{ne}[n(\boldsymbol{r})], \tag{2.18}$$

and for the KS system,

$$E = T_{KS} + E_H + E_{XC} + E_{ne}, \tag{2.19}$$

and inspecting these terms we have the non-exact KS electron kinetic energy,

$$T_e[n(\boldsymbol{r})] = T_{KS} = -\sum_{i=1}^{N}\frac{\hbar^2}{2m_e}\int \psi_i^*(\boldsymbol{r})\nabla_i^2\psi_i(\boldsymbol{r})d^3\boldsymbol{r}. \tag{2.20}$$

The T_{KS} is not exact as it is for independent particles and lacks the exact corrections due to many-body effects. Orbital free DFT [71] is an alternative method with a similar approach but does not use orbitals and the exchange-correlation (XC) functional focuses on correcting the kinetic energy error in the Hamiltonian rather than the error in $V_{ee}(\boldsymbol{r})$. Finally the exchange-correlation

potential V_{xc} has no known functional form but approximations exist, some based on exact constraints. We will start with the simplest which is the local density approximation (LDA) [70] in the next section.

Once again the KS equations can be solved in an iterative manner through the procedure shown in figure 2.3.

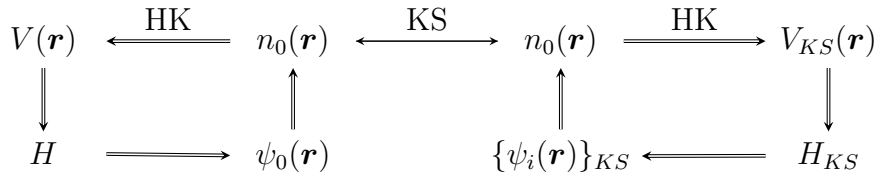

Figure 2.2 *Diagrammatic picture of solving the KS equations using KS orbitals and how this relates to the HK theorem for the many body problem.*

The self-consistent calculation work flow to find the converged ground state can be summarized in an illustration:

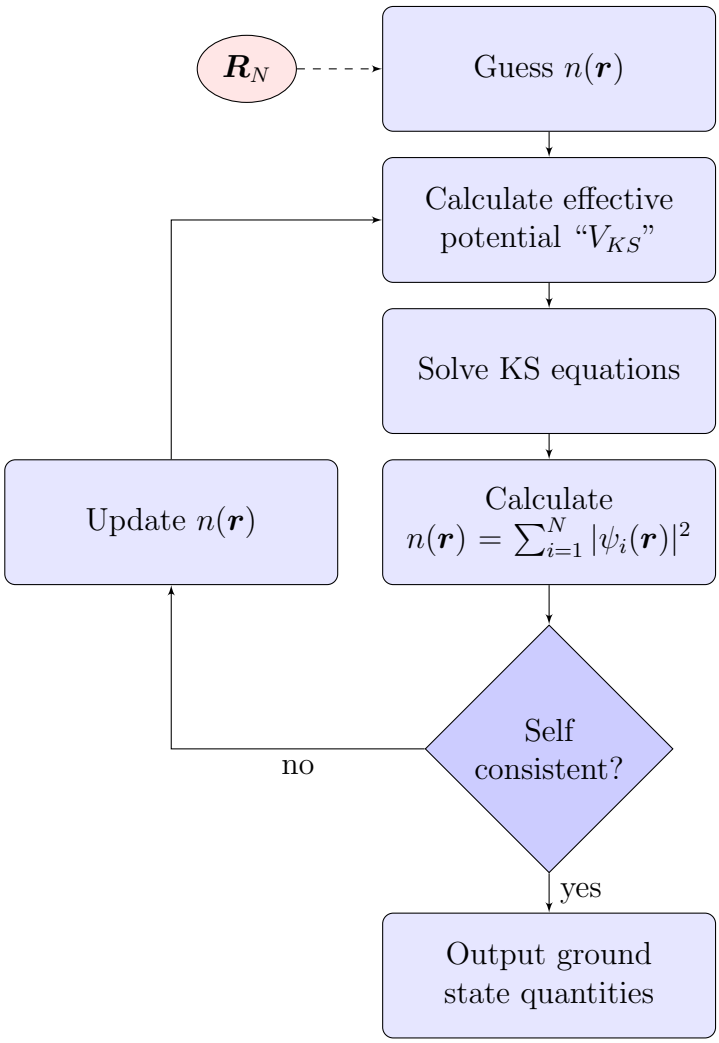

Figure 2.3 *Flow chart for solving the KS equations self-consistently while ignoring spin.*

2.1.5 The Variational Principle

The KS equations and any trial wave-function Ψ_i which is an eigenfunction of the Schrödinger equation with corresponding eigenvalues E_i, iteratively converge due to the variational principle [72]: any arbitrary trial wave-function Ψ_{trial} has a total energy always greater or equal to the ground state energy E_0. In KS DFT this minimisation is being achieved by optimising the electron density which acts as optimising the trial wave-function. From this, we can arrive at an upper-bound to the ground-state energy by,

$$E_{trial}[\Psi_{trial}] = \langle \Psi_{Trial} | \hat{H} | \Psi_{Trial} \rangle \geq E_0, \tag{2.21}$$

after which a steepest descent search for Ψ_0 can be performed. The number of iterated trial wave-functions can be great, and methods starting point such as from the atomic orbitals were not found to significantly speed up this process.

2.1.6 Exchange-Correlation Functionals

The success of DFT is due to the fact that there is a map for $n(\boldsymbol{r})$ and E between a system of interacting electrons experiencing a nuclear potential, and non-interacting electrons experiencing a nuclear potential plus an additional potential to correct for the interactions. The unknown part of KS potential was named $V_{xc}(\boldsymbol{r})$ mimicking the effects of exchange interaction and correlations between the electrons. The exact function for $V_{xc}(\boldsymbol{r})$ is not known and so this has to be approximated. The homogeneous electron gas (HEG), also known as Jellium, can be a simple tool to model systems, shown by Drude and Summerfeld [73], offering quantitatively correct conductivity results for many metals. This provides motivation to use the exchange correlation energy for the HEG as a starting point in approximating E_{xc} as,

$$E_{xc}[n] = \int n(\boldsymbol{r}) \epsilon_{xc}^{HEG}(n(\boldsymbol{r})) d\boldsymbol{r}, \tag{2.22}$$

where ϵ_{xc} is the exchange-correlation energy density for the HEG. The anti-symmetry in the electronic wave-function leads to an exchange interaction energy for swapping the coordinates of two fermions $\Psi(\boldsymbol{r}_1, \boldsymbol{r}_2) = -\Psi(\boldsymbol{r}_2, \boldsymbol{r}_1)$. In 1930 Dirac [74] showed that exchange effects in a homogeneous system can be written

as,

$$\epsilon_x = -\frac{3}{4}\left(\frac{3}{\pi}\right)^{1/3} n^{1/3} \approx -\frac{0.458}{r_s}, \tag{2.23}$$

where r_s, the Wigner-Seitz radius (which for free electrons is $r_s = (3/(4\pi n))^{\frac{1}{3}}$), is based on the average inter-electron distance for a given density, confirmed by Slater for the HEG [52]. The remaining electron correlation relies on parameterization from accurate calculations for the wave-function of the HEG using Quantum Monte Carlo methods. Ceperley and Alder [75] obtained results and Perdew and Zunger parameterized [76] these as,

$$\epsilon_c = \begin{cases} a + b \cdot \ln(r) + c \cdot r_s \ln(r_s) d \cdot r_s, & \text{if } r_s < 1. \\ \frac{\gamma}{1+\beta_1\sqrt{r_s}\beta_2 r_s}, & \text{if } r_s \geq 1. \end{cases} \tag{2.24}$$

The combination of these to form $\epsilon_{xc}^{HEG} = \epsilon_x + \epsilon_c$ is known as the Local Density Approximation (LDA) [51]. This is local as the approximation depends only on the spatial coordinate $\boldsymbol{r}$ for the electron density. When including electron spin this is written as the Local Spin Density Approximation (LDSA). The LDA performed better expected for example LDA calculations for the equilibrium lattice constant for Silicon [77] compared well with experimental results. Systems which deviate from the HEG often have the greatest error with DFT and thus the LDA performs well for metals. Other functionals exist and provide a range of choice depending on the system and what is trying to be calculated. The LDA remains subject to the fundamental error in DFT for optical properties such as underestimated band gaps due to the self-interaction [78] of the electron density.

The next improvement that was made to this was to also take into account the gradients of $n(\boldsymbol{r})$ in the General Gradient approximations (GGA's). These take the general form,

$$E_{xc}^{GGA}[n] = \int \epsilon_{xc}(n(\boldsymbol{r}), |\nabla n(\boldsymbol{r})|) d\boldsymbol{r} \dot{n}(\boldsymbol{r}). \tag{2.25}$$

Many GGA's exist, with the most popular formulation by Perdew-Burke-Ernzerhof [79] known as PBE. A similar GGA known as PBE-Sol was created to perform better in solids [80], highlighting that there is a choice of XC functional depending on the system calculated. The PBE functional gained its popularity for achieving generally good results in most situations [81] on average but by no means all. For molecules and small systems, DFT methods can be directly compared with highly accurate wave-function based methods giving an indication

of error [82] however extrapolating this into periodic systems where wave-function methods are not readily tractable and remains a challenge. Quantum Monte Carlo approaches come with their own approximations [83] but provide a useful comparison to DFT based results. Exploring a system as a function of XC functional appears important to check for consistency, with the ambition that it is possible to physically realize why certain functionals fail to produce accurate results.

Hybrid Functionals

To further improve upon local functionals a step was taken into non-local XC functionals to correct for charge transfer and the self-interaction error, where explanations for the rationale are found in [84]. These are commonly used to calculate band gaps more accurately as they can correct for the self-interaction error. Hybrid functionals use a mixture of density-based XC functional and HF referred to as exact-exchange. In this work, we make use of the HSE functional which is a range separated hybrid functional [85]. This is similar to the hybrid proposed by Perdew, Ernzerhof, and Burke known as PBE0 [86] which takes the form,

$$E_{xc}^{PBE0} = E_c^{PBE} + \alpha \left(E_x^{HF} - E_x^{PBE} \right), \tag{2.26}$$

where $\alpha = 0.25$ for PBE0 though this value can be varied, and different values are favored depending on the type of the system.

The range separated HSE has a similar form but only uses exact-exchange from HF for the short-range (SR) part and uses density based exchange for the long-range (LR) part. HSE takes the form,

$$E_{xc}^{HSE} = E_c^{PBE} + \left[\frac{1}{4} E_x^{HF}(\mu) + \frac{3}{4} E_x^{PBE}(\mu) \right] + \left[E_x^{PBE}(\mu) \right]_{LR}, \tag{2.27}$$

where μ is used to control the range-separation (usually valued 0.2, as in the HSE06 functional), and the fractions of mixing can once again be varied. When using hybrids care must be taken if one wants to remain ab-initio rather than choosing parameters that fit to the experiment.

Van Der Waals Interactions

A problem of various common V_{XC} expressions is that they do not contain the physics of instantaneous excited dipole-dipole interactions, also known as Van Der Waals forces. This is important for systems where Dispersion effects are strong, mainly in:

1. Layered Systems
2. Molecular systems with hydrogen bonding
3. Van der Waals systems such as Noble Gases

This leads to another set of corrections to capture the correct physics for a system. Van Der Waals corrections have led to set methods which generally either add additional functions in the electronic Hamiltonian (e.g. the empirical Grimme method [87]), or incorporate the correction into the XC functional itself (e.g. VdW DF2 [88]). There are many corrective schemes in practice, in this work the Tkatchenko-Scheffler (TS) [89], Grimme, and Many-Body Dispersion [90] schemes are used. The TS method adopts a parameter free summation of interatomic C_6 coefficients using the systems electron density and accurate reference data calculations for the free atoms. The Grimme dispersion scheme similarly uses damped atom-pairwise dispersion C_6 corrections parameterised on a large set of reference molecules. In the MBD scheme long-range interactions are separated and calculated by mapping the complex all-electron problem onto a set of atomic response functions which are turned on adiabatically.

Jacob's Ladder

The hierarchy of electronic structure methods is often ranked by Jacob's ladder [91], based upon the level of theory and computational cost. The general rule is that high-level theories are more computationally expensive and so climbing the ladder may achieve more accuracy for a given property but at a price summarised in table 2.1. Pointed out in [92] modern XC functionals may achieve greater accuracy in total energy but may suffer in electron density.

Table 2.1 *Summary of Jacob's Ladder starting from the bottom entry.*

Method	Dependence	Form	Example
Fully Non-Local	Unoccupied Orbitals	unocc. ψ_i	GW[93], RPA [94]
Hybrid GGA	Occupied orbitals	occ. ψ_i	PBE0
Meta-GGA	Kinetic Energy Density	$\nabla^2 r$	TPSS [95]
GGA	Gradient of density	∇r	PBE
LDA	Local density	r	LDA

2.1.7 Periodic systems and k-points

So far we have not discussed the type of system that we are trying to solve. For small systems of atoms and molecules calculations appear simple. For periodic systems such as a crystal of Avogadro's number (N_A) atoms and likely even more electrons solving the Schrödinger equation appears intractable. The use of periodic boundary conditions can be employed to reduce the system size for example in a liquid, and exploiting the periodicity of a crystal helps reduced this even further depending on the crystal symmetry. For example, a crystal of NA atoms of BCC lithium could be reduced to a 2 atom periodic conventional unit cell (or a 1 atom primitive unit cell) with periodic boundary conditions. Note some crystals have unit cells with over 100 atoms still [96]. This approximation is valid assuming that all periodic images should behave like the unit cell for the material property being investigated. Supercells can be used for when these symmetries are broken, for example when calculating phonons or lattice defect energies.

To solve the Schrödinger equation for a periodic system Bloch's theorem can be applied. For a periodic system of nuclei, there is also a potential for that system with the same periodicity,

$$V(\boldsymbol{r} + \boldsymbol{L}) = V(\boldsymbol{r}), \tag{2.28}$$

where $\boldsymbol{L}$ is a lattice vector. This will also extend to the density,

$$n(\boldsymbol{r} + \boldsymbol{L}) = n(\boldsymbol{r}). \tag{2.29}$$

However the wave-function, which is complex, will have periodic magnitude as

this is controlled by,

$$n(\boldsymbol{r}) = |\psi(\boldsymbol{r})|^2, \tag{2.30}$$

but the phase is not necessarily taking the same periodicity of the unit cell. This means the wave-function is quasi-periodic with the lattice,

$$\psi_k(\boldsymbol{r}) = e^{i\boldsymbol{k}\cdot\boldsymbol{r}} u_{\boldsymbol{k}}(\boldsymbol{r}), \tag{2.31}$$

where $u_k(\boldsymbol{r} + \boldsymbol{L}) = u_k(\boldsymbol{r})$ and $e^{i\boldsymbol{k}\cdot\boldsymbol{r}}$ is an arbitrary phase factor. As such there are solutions for any $\boldsymbol{k}$ and so the general solution for the crystal is an integral over the uniquely defined primitive cell in reciprocal space, the Brillouin zone. As this is done numerically, the Brillouin zone is broken down into a discrete grid of k-points used for Brillouin zone sampling. The number of k-points needed to converge the approximation to this integral is necessary for accurate calculations.

2.1.8 Plane-wave basis

Approaches to DFT can be categorized by their choice of basis set with which to represent the KS wavefunctions. Both CASTEP [28] and VASP [97] are plane-wave codes and as such use plane-waves as their wave-function basis set. Other codes use schemes such as a basis set of localized atomic orbitals [98], or Gaussians, or a mixture. As $\psi(\boldsymbol{r})$ is periodic a sensible choice can be to express it as a Fourier series,

$$\psi(\boldsymbol{r}) = \sum_G c_G e^{i\boldsymbol{G}\cdot\boldsymbol{r}}, \tag{2.32}$$

where c_G are complex Fourier coefficients, and $e^{i\boldsymbol{G}\cdot\boldsymbol{r}}$ is a plane-wave. The summation is performed over all reciprocal lattice vectors, typically truncated at some value. As this is a convergent series ($|\boldsymbol{G}| \to \infty : |c_G| \to 0$) the series can be truncated at some cut off, for example the energy of the highest frequency plane-wave. Now $\psi(\boldsymbol{r})$ is a vector of plane-wave coefficients c_G reducing,

$$\left\{ -\frac{\hbar^2}{2m}\nabla^2 + V[n(\boldsymbol{r})] \right\} \psi_i(\boldsymbol{r}) = E_i \psi_i, \tag{2.33}$$

to a matrix diagonalisation. A trial wave-function is guessed ψ_{trial} with c_G which is used to compute,

$$E = \psi^\dagger \hat{H} \psi, \tag{2.34}$$

followed by self-consistently optimizing the c_G coefficients to find the ground-state ψ_0. The basis set can be chosen based on both accuracy and computational efficiency.

2.1.9 Pseudopotentials

A further approximation to improving computational efficiency is to replace the core electrons with an effective potential that the valence electrons are interacting with. So much has this succeeded that it was described as the "most powerful ab initio quantum mechanical modeling method presently available" when reviewed in [99] 25 years ago and still remains relevant today. This approximation, the frozen core approximation, is valid when the core electrons play no part in the chemistry, which is not always true [100] at high density due to core overlap as atoms near one another. Freezing the core electrons means fewer one-electron wave-functions (not for hydrogen) to solve for and so can greatly reduce the computational cost for calculations. For plane-wave codes especially, the core electrons are highly localized with strong wave-function fluctuations and contain nodes, and thus require undesirably high energy cut-offs to converge.

Pseudopotentials smooth the wave-function in the core radius r_c and smoothly equal that of the original wave-function beyond r_c. This removes the core states and the valence electrons are described by un-physical wavefunctions with fewer nodes. The choice of r_c or alternatively the number of valence electrons to consider changes with density (g/cm^3) as core electrons start becoming involved in interactions as orbitals get closer and can begin to overlap.

Norm-conserving

The generation of a pseudopotential should be to maintain as many properties of the all-electron calculation, by perfectly replacing the core electrons in the eyes of the valence electrons. The criterion for norm-conservation is to preserve the total charge of the all-electron wave-function within the pseudo-wave-function [101] so that no core augmentation charges are required. The potential the valence electrons feel changes if the core charge distribution is replaced by a smoother distribution for $r < r_c$.

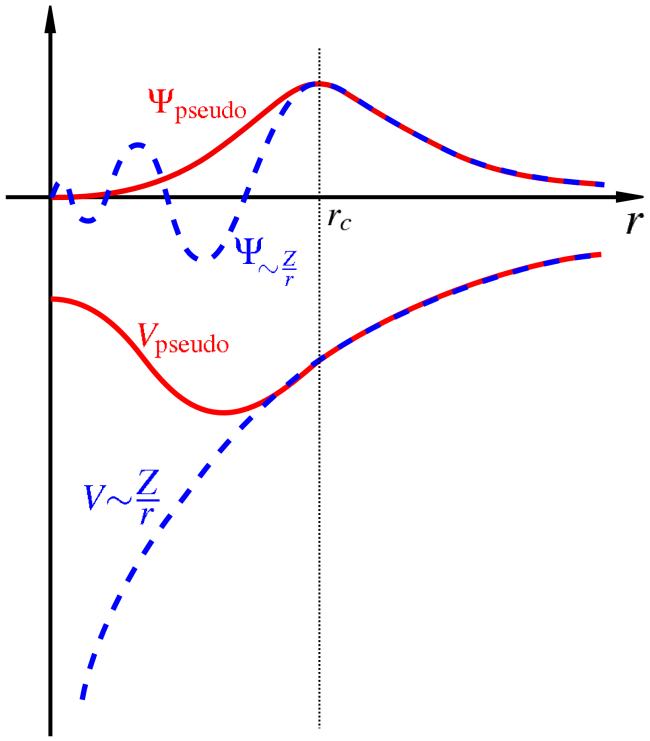

Figure 2.4 *Example description of a pseudopotential in red comparing the all electron (AE) in blue (dashed) potential and wavefunction. The wavefunctions correspond respectively to the potential, both of which are equal for $r > r_c$.*

Ultrasoft

The norm-conservation criterion is relaxed in ultrasoft pseudopotentials [102] to generate even smoother wave-functions with even lower cut off energies. The pseudo wave-function is split into two parts 1. An ultrasoft wave-function that breaks norm-conservation $\phi^{US}(\boldsymbol{r})$ and 2. a core augmentation charge which is a charge deficit for the core region to correct for this,

$$Q_{aug}(\boldsymbol{r}) = \psi^*_{AE}(\boldsymbol{r})\psi_{AE}(\boldsymbol{r}) - \phi^*_{US}(\boldsymbol{r})\phi_{US}(\boldsymbol{r}). \tag{2.35}$$

Projector Augmented Wave

An alternative method is to use projector augmented waves (PAW) [103] which in principle creates an all electron wave-function pseudopotential. The PAW potential reconstructs the original all-electron wave-function from pseudo wave-functions. All electron partial waves are added to the wave-function, and so the

corresponding pseudo partial waves have to be taken away,

$$\psi_{PAW}^{AE} = \psi^{PS} + \psi_{PAW}^{AE} - \psi_{core}^{PS}. \tag{2.36}$$

This achieves transforming the rapid oscillations in the wave-function near ionic cores to smoothly varying wave-functions, similar to US pseudopotentials.

2.1.10 Wavefunction Based Methods

Going beyond Hartree-Fock much more accurate wave-function methods exist. These are useful for comparing DFT results with accurate quantum-chemistry results. Such calculations are restricted to what is computationally tractable as these methods scale in cost more greatly than DFT. In this work, they are used for modeling the interactions between molecular dimers and trimers.

Perturbation Theory

Møller–Plesset perturbation theory (MP) is a post-HF method popular in quantum chemistry [54] and the simplest wavefunction based approximation to the correlation energy. The main idea is to improve upon the HF method by including electron correlation via Rayleigh-Schrödinger perturbation theory, where MP2 refers to a second-order perturbation. By assuming that the Hartree-Fock wavefunction is close to the true ground state wavefunction the exact Hamiltonian (operator) can be written as,

$$H = H_0 + \lambda V, \tag{2.37}$$

where V is the external perturbation (the difference between $\mathrm{V}_e e$ and V_x), λ is a dimensionless parameter that controls the magnitude of the perturbation, and H_0 is the Hartree-Fock Hamiltonian.

The HF energy can be expanded as ,

$$E = E^{(0)} + \lambda E^{(1)} + \lambda^2 E^{(2)} + \cdots , \tag{2.38}$$

and wavefunction as,

$$\Psi = \Psi_0 + \lambda \Psi_1 + \lambda^2 \Psi_2 + \cdots . \tag{2.39}$$

The expressions for the perturbed energy and wavefunction can be substituted into the Schrödinger equation and powers of λ can be collected leading to partitioned expressions for the energy,

$$E^{(0)} = \langle \Psi_0 | H_0 | \Psi_0 \rangle, \tag{2.40}$$

$$E^{(1)} = \langle \Psi_0 | V | \Psi_0 \rangle, \tag{2.41}$$

$$E^{(2)} = \langle \Psi_0 | V | \Psi^{(1)} \rangle, \tag{2.42}$$

and so forth, where $|\Psi_0\rangle$ is the Slater-determinant. From this the HF energy is $E_{HF} = \langle \Psi_0 | H_0 + V | \Psi_0 \rangle$ the sum of the zeroth and first order perturbations $E_0 = E^{(0)} + E^{(1)}$ including only exchange. Further terms include electron correlation and so the correlation energy can be approximated in MP theory as,

$$E_{correlation} = E^{(2)} + E^{(3)} + E^{(4)} + \cdots , \tag{2.43}$$

with $E^{(2)}$ being the MP2 energy and so forth. As perturbation theory is not variational this does not given an upper bound for the true ground state energy. The success of the MP methods is explored in the paper "Why does MP2 work?" [104] and explained through advantageous error cancellation.

Computationally MPn theory scales as $O(N^{n+3})$ and requires the calculation of doubly excited states from the HF ground state. MP2 generally provides high- quality results close to that of more exact methods [105], and increasing n does not always improve results where instead they may display oscillatory or slow convergence around the true ground state [106]. As well as the additional computational cost of $n > 2$ MPn calculations this is why MP2 is a popular choice to achieve results with similar accuracy to more exact levels of theory such as coupled cluster theory. MP and HF methods use a single determinant

wavefunction for the unperturbed system and newer methods are being developed with multi-determinant wave-functions.

Coupled Cluster Theory

Coupled cluster (CC) theory again starts from the HF method and constructs a many-electron wavefunction by use of an exponential cluster operator to include electron correlation, and was originally used for studying nuclear physics [107]. CC methods build from a single reference Slater determinant by incorporating a linear combination of excited state determinants. At some point the cluster expansion can be truncated such as singles (CCS), doubles (CCSD), and so forth. The CC wavefunction is written with an exponential ansatz:

$$|\Psi\rangle = e^{\hat{T}}|\psi_0\rangle, \tag{2.44}$$

where $|\psi_0\rangle$ is the reference wavefunction, which does not have to be but generally is a HF Slater determinant, and $\hat{T}$ is the cluster operator. The operation of $\hat{T}$ on the reference wavefunction produces a linear combination of excited determinants and takes the form,

$$\hat{T} = \hat{T}_1 + \hat{T}_2 + \cdots . \tag{2.45}$$

Here $\hat{T}_1$ is the operator for single excitations, expressed in second quantization as,

$$\hat{T}_1 = \sum_i \sum_a t_a^i \hat{a}_a^\dagger \hat{a}_i, \tag{2.46}$$

where $\hat{a}^\dagger$ and $\hat{a}_i$ denote the creation and annihilation operators respectively, and i, j are the occupied (particle) and a, b the unoccupied (hole) orbitals.

The CC wavefunction takes the form,

$$|\Psi_{CC}\rangle = \exp(\hat{T}_1 + \hat{T}_2 + \cdots)|\psi_0\rangle, \tag{2.47}$$

$$|\Psi_{CC}\rangle = \left[\prod_{a,i}(1 + t_a^i a_a^\dagger a_i)\right]\left[\prod_{ab,ij}(1 + t_{ab}^{ij} a_b^\dagger a_a^\dagger a_j a_i)\right]\cdots|\psi_0\rangle. \tag{2.48}$$

The configuration interaction wavefunction (closely related in form to CC) uses a linear combination of excitation operators ansatz,

$$|\Psi_{CI}\rangle = (\hat{T}_1 + \hat{T}_2 + \cdots)|\psi_0\rangle, \tag{2.49}$$

and generally requires a longer expansion to achieve convergence. The exponential form of the CC wavefunction expansion appears convergence faster with more dominant leading terms in the expansion.

In practice CC methods are usually truncated after triple excitations at $\hat{T}_3$ termed CCSDT. For large molecules CCSD(T) is used in practice and known as the "gold standard" in quantum chemistry where the (T) indicates the triple term is calculated non-iteratively using many-body perturbation theory generally for computational reasons. At times more accurate methods such as full configuration interaction (FCI, which is exact) and quantum Monte Carlo methods exist but generally comes with greater computational cost. Interestingly, using only single and double excitations (CCSD) is often outperformed by the cheaper MP2 method. However, with perturbative triple corrections (CCSD(T)) the performance is much better and is regarded as the gold standard in computational chemistry.

2.2 Crystal Structure Searching

How does matter condense? For a system of atoms at a given thermodynamic state such as a fixed temperature and pressure, there exists a structure which is the most stable, the ground state structure with the lowest free energy. All atoms making up a system exist on a potential energy surface (PES) in structure space where the stable and metastable structures form local minima. The number of minima scales exponentially with the number of atoms [108], and further complexity arises combinatorically from including different atom types. Searching for the global minima requires exploration of the minima that lie on this PES and so the search for stable crystal structures is a global optimization problem.

Scanning every one of these minima exhaustively is computationally unfeasible for large and complex systems, though some simple systems can be well mapped out. The generation of candidate structures to evaluate provides a general problem by itself. Candidates are generally generated with symmetric structures though some codes go through each space group individually including structures without symmetry (P1). It is tempting to bias searching the most likely space groups found in the Inorganic Crystal Structure Database (ICSD) [109], a data-driven approach, though avoiding parts of structure space could end up missing the correct structure. Methods which generate structures based on the current search history look for energetically favorable structural motifs and attempt to blend these together or perturb structures creating offspring which should also be favorable. The details of this procedure for the USPEX code are explored in [108]. Extensive searching with simple potentials such as Leonard-Jones has been performed to study the nature of structure space [110, 111]. To reproduce nature both accurate and efficient methods of evaluating a system's energy are required to explore the potential energy surface. It has often been found that methods with too much coarse-graining, such as classical models and those with too many energy minima, which are fast and scale well with system size N do not order the energy of different structures correctly. For systems where the electronic structure is important to accurately enough rank the energetics of different structures, DFT is often chosen. Other methods for evaluating energy have had some success especially in alloy systems with simple interactions such as the Cluster Expansion [112] and various Machine Learning [113] methods that generally rely on a DFT database to start from.

Historically the problem of how matter condenses was unsolvable from theory

but in the last 15 years or so this has changed. This has often been related to the statement of John Maddox in 1988 "One of the continuing scandals in the physical sciences is that it remains impossible to predict the structure of even the simplest crystalline solids from a knowledge of their composition" [114]. A volume of structures have since been successfully predicted, by calculation and then confirmed by experiment, and visa versa [29, 30].

Data was taken from the ICSD [109] which stores inorganic crystal structures reported in the literature to perform analysis on known crystal structures in this section. The ICSD is increasing at a rate of roughly 6000 structures per year and currently nearing 200,000 structures with 9,013 distinct structure types to date. From this, we can learn about the structure space that scientists have currently investigated and hope that this is similar to the structure space of nature in general. The data was mined without filtering it is likely that there duplicate structures, especially for popular materials. In figure 2.5 the number of ICSD structures as a function of the number of composing elements is shown. Increasing the number of elements combinatorially increases the number of possible structures in a simple non-interacting picture, though nature may act very differently from this. There exist around 1,800 different structures in the ICSD with a single element which is around 15 per element. The increase for binary and ternary structures is expected as there is a richer phase space that can be explored as well as different compositional combinations. The drop off for $N = 4$ can be seen that science has so far not studied systems (and solved structures) for $N > 3$ nearly as much or equally that nature does not favor the formation of crystal structures with $N > 3$ different elements. This is subject to confirmation bias as the simpler systems with less unique elements are more straightforward to study and solve in diffraction studies. This does provide scope on what systems have been studied so far in both theory and experiment, and structure searching reports will be heavily biased to low N.

In figure 2.6 the number of formula units for ICSD structures is shown. There appears to be a pattern with magic numbers of formula units that structures tend to prefer. This is worth noting when performing a crystal structure search. Most notable are the dips to 5 and 7 formula units and the most frequent numbers are multiples of 2 and 4. Smaller peaks appear at 12, 16, and 24 formula units which likely relate to the larger peaks at 2, 3, 4, and 8. Arguments to explain this pattern could be made based on balancing the dipole or quadrupole moments for the species, however, this is presented only to show that there

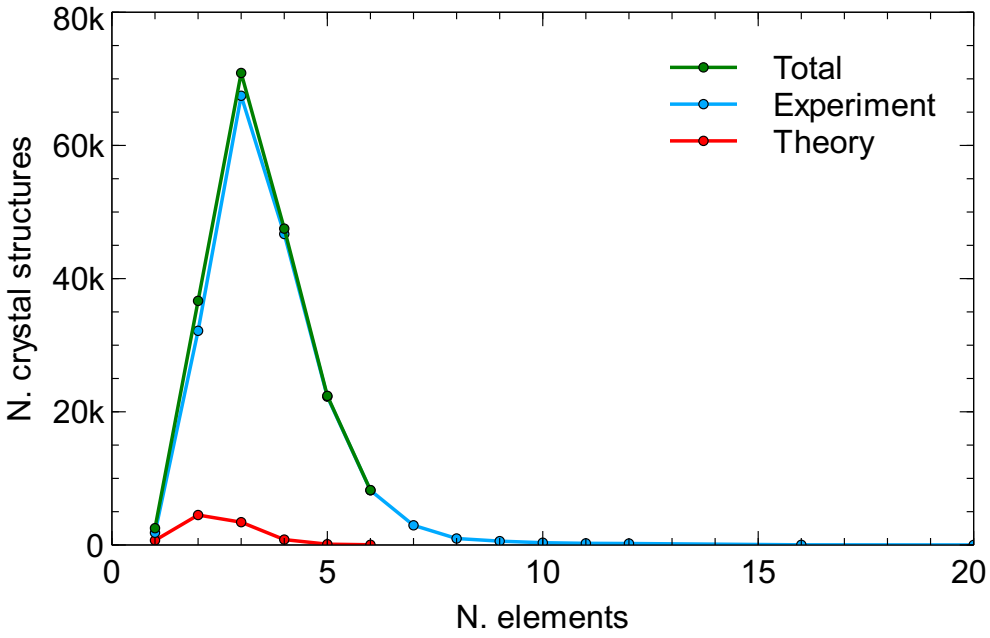

Figure 2.5 *ICSD statistics taken for the number of crystal structures consisting of a certain number of elements starting from unary, binary, ternary and so forth.*

are observable differences and patterns to the chemical space. Although data is limited theoretical studies appear to follow the same trend as the experimental reported structures.

In figure 2.7 the number of total structures reported *above* a given pressure for experiments is plotted. However, this is sensitive to the quality of meta-data the ICSD finds and so does not always list the reported pressure. There is difficulty achieving pressures greater than 300 GPa with diamond anvil cell (DAC) experiments, as well as the challenges of resolving structures at these high levels of compression.

In figure 2.8 the number of crystal structures with the top 50 most common space group is shown, as well as the number of structures with a total of N symmetry operations. This data shows a clear bias for certain space groups, and this is likely to have different statistics for different material types such as metals compared with molecular crystals. Both the material type being searched and the distribution of space groups can be taken into account to bias a search in a way that one thinks appropriate for efficiency.

Crystal structures underpin all material properties, therefore, scientific fields with interest in where atoms want to exist has a natural connection with

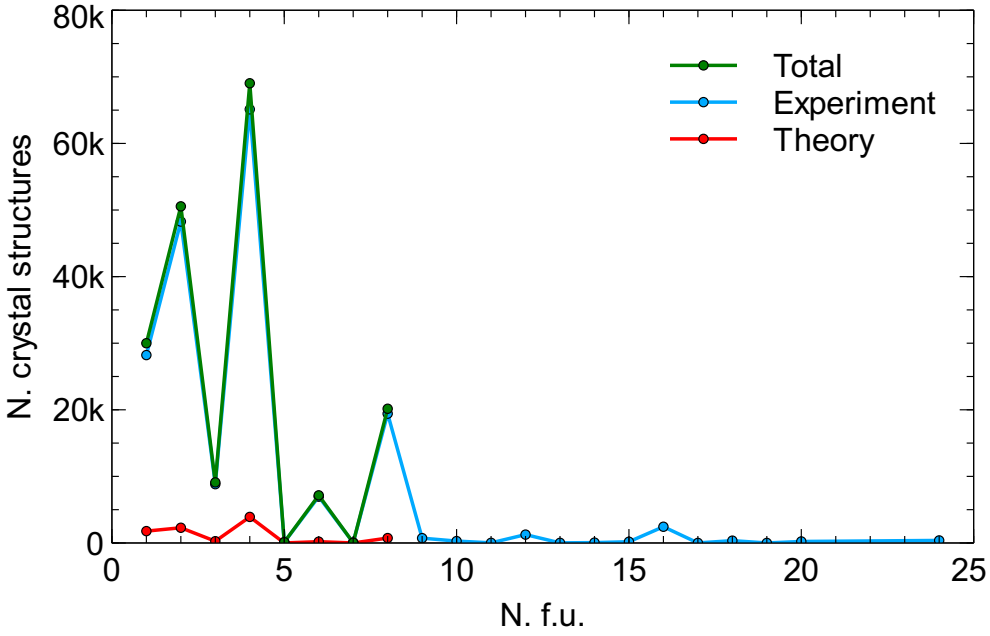

Figure 2.6 *ICSD statistics taken for the number of crystal structures with an integer number of formula units and any chemical composition.*

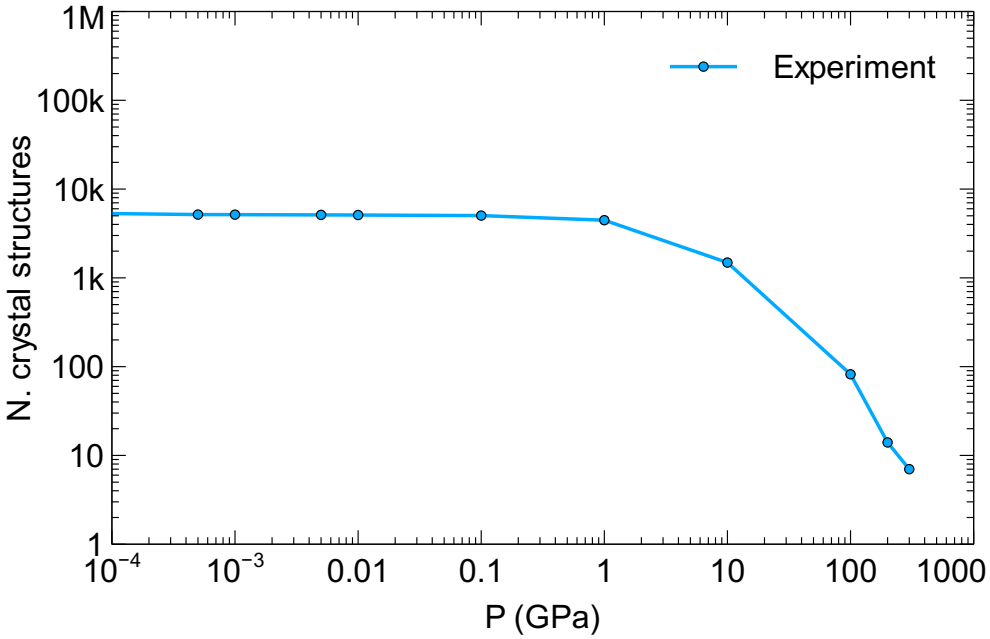

Figure 2.7 *ICSD statistics taken for the number of crystal structures stored over a given pressure. Note that the value for zero pressure is 182,757 crystal structures and pressures are not always given in the metadata.*

structure prediction. Discovering new materials can be done more affordably and rapidly with computation and work together with the still necessary experimental

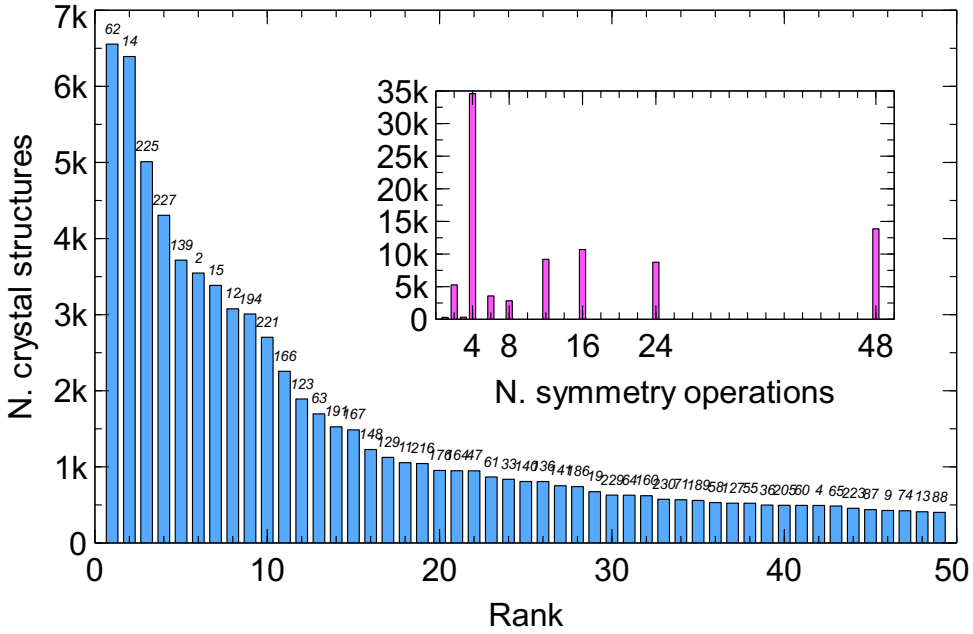

Figure 2.8 *ICSD statistics showing the number of crystal structures for the 50 most common space groups labeled with their space group number. Inset shows the number of structures with a certain integer number of symmetry operations.*

methods to confirm the reliability of these methods [29, 30]. Structure searching complements experimental data greatly e.g. x-ray diffraction (XRD) patterns may reveal a crystal unit cell but are unable to refine the atom positions. Hydrogen atoms have poor x-ray scattering so for the example of water XRD can be used to locate the oxygen atoms combined with searching to predict the hydrogen locations. Searching with experimental constraints also massively reduces the size of the PES that has to be explored, such as in [115].

Crystal structure prediction (CSP) finds solid periodic systems. Other systems such as amorphous solids [116] and glasses [117] can be studied in similar ways but with a greatly increased computational cost. Prediction of non-periodic collections of atoms is referred to as cluster prediction, for example, gold nano-particles and nano-clusters [118]. Meta-stable structures with energies close to the ground state are also a useful output from searching which may become stable with finite temperature or varying pressure or give hints towards transition states.

In essence, CSP is a stochastic method and one can never truly know when to stop searching. When the low temperature experimental structure has been found independently it is likely the ground-state structure but when searching in phase space where there are no experiments the choice of when to stop is unknown

even if a search appears to be converged. Finding the same repeated structure independently with methods such as AIRSS provides confidence of a converged result. Nonetheless, CSP is helped by generic features of the PES and by self-learning throughout the search, as described in the following sections.

2.2.1 General Features of the PES

We define a basin of attraction as a list of points that when relaxed end up in the same energy minima, of which the PES can be divided up. Here we describe some general features of the PES which are considered in crystal structure prediction [119].

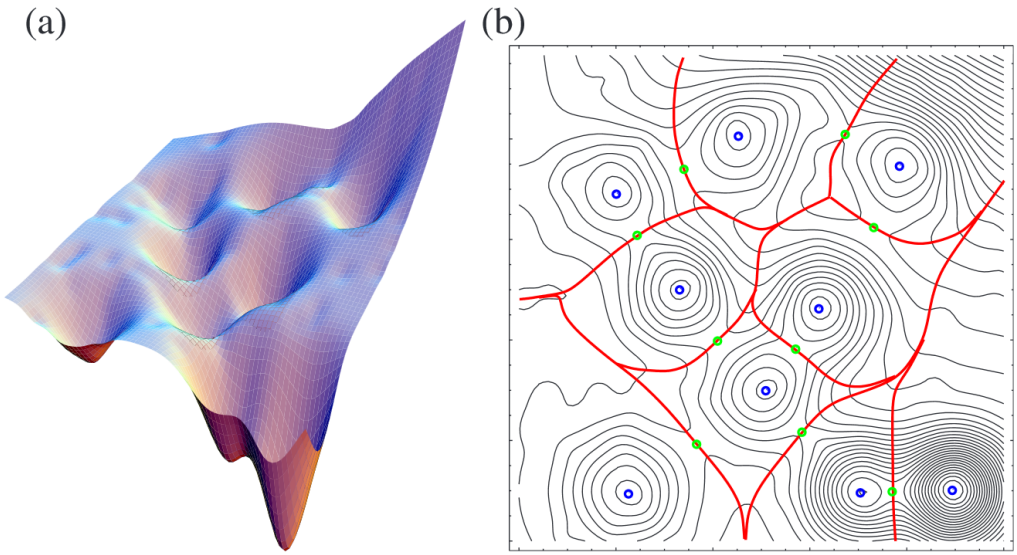

Figure 2.9 *(a) Example PES and (b) 2D PES showing how basins can be defined [120] in a similar way to partitioning in the Bader scheme introduced later in this chapter.*

(1) The majority of the PES describes structures where atoms are extremely close to one another and contain almost no minima.
(2) There is a relative smoothness of the PES at low energies as a consequence of the Bell-Evans-Polanyi principle [121]. This means that if the barrier between a basin and its neighbor is small then the neighboring basin will often have a low energy minimum.
(3) Following from (2) low energy basins typically occur near other low energy basins.
(4) A Gaussian probability distribution describes the energies of the local minima

for the PES of large systems [122].
(5) It has been shown that structures with lower energy minima are likely to have larger basin sites in parameter space [123].
(6) The probability distribution of the sizes of the basins appears to follow a power law against the minimum energy of a basin. This implies some ordering such that smaller basins fill the gaps between larger ones, see figure 2.9, similar to the Apollonian packing [120].
(7) Low and high energy minima typically correspond to symmetrical structures, consistent with the ubiquity of crystals. Pauling's "rule of parsimony" states "The number of essentially different kinds of constituents in a crystal tends to be small" [124] so the structure space is likely simple.
(8) For crystals made from organic molecules, some space groups symmetries occur much more often than others, compared with inorganic systems which have different symmetry preferences.
(9) Features of the PES are a result of the chemistry of the system, such as which atoms bond to which and typical bond lengths.

2.2.2 Random Methods

The simplest way to start searching for crystal structures is to assign random unit cells with random atomic positions scaled to some density which can then be relaxed to the nearest energy minima on the PES. This can be done repeatedly and in parallel to scan the PES and identify the most stable structures. A method adopting this strategy fully is Ab Initio Random Structure Searching (AIRSS) developed by Pickard et. al [119]. Truly random structure generation would not be useful as atoms could be generated with core overlap and so sensible or practical structures should be considered.

Structures are arranged in random configurations and then optimized to the local minimum they are located near. This method is likened to throwing darts randomly onto the PES in the hope of finding the global minimum through brute force, as implemented by the AIRSS method. AIRSS initially implemented the CASTEP code [28] for ab initio DFT relaxations via geometry optimization and now supports VASP, GULP, LAMMPS, and others. The PES increases exponentially with system size, and so the computational cost will depend upon the size of the unit cell assumed for a crystal structure. While computational

resources are ever-increasing this limitation may well rule out the prediction of structures with extremely large unit cells.

A recent triumph of AIRSS, relevant to this work, was the virtually accurate prediction of ammonia monohydrate phase II with 16 formula units in the unit cell, see figure 2.10 [125]. This search was aided by experimental information on the unit cell parameters and likely space group and hence symmetry operations helped provide sensible starting structures. Building blocks of water and ammonia molecules were also used for the structures as opposed to atoms. Such constraints bias the search, cut down the size of the PES and speed up the search drastically, and demonstrate the synergy between experiment and theory. In this area of research, it is becoming more and more common to combine Raman spectroscopy, X-ray diffraction, CSP, and neutron diffraction techniques to determine the atomic structure.

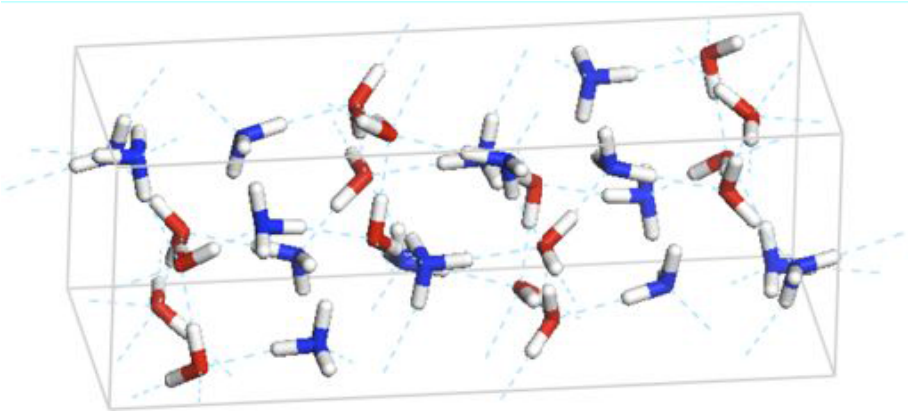

Figure 2.10 *Crystal structure of Ammonia Monohydrate phase II, nitrogen atoms are in blue and oxygen atoms are in red. [125]*

A different sampling strategy prescribes to biasing the searches from the point of cell generation, following the principles of an evolutionary algorithm [108]. There exists a fitness criterion, minimising enthalpy, which drives structure generation into certain areas of the PES based on for example bond lengths and certain symmetries that favour low energy structures. New structures are then generated in the hope of accelerating the search to find the global minimum through a self-improving method. Structure searching methods adopting a genetic algorithm (GA) include USPEX [126], and the open-source XtalOpt [127] which supports various codes for performing geometry optimizations on structures.

2.2.3 Particle Swarm Optimization

The CALYPSO code (Crystal Structure AnaLYsis by Particle Swarm Optimization [128]) follows a similar self-improving methodology to a genetic algorithm. The idea of particle swarm optimization (PSO) was first proposed by Kennedy and Eberhart [129, 130] constructing a population-based optimization method. This is a stochastic method inspired by the formation of a flock of birds, with each bird as a particle as they search for favourable air streams. Each particle is performing a multidimensional search for the best local minima to help it fly through hyperspace or PES, which is affected by the surrounding local or global minima. These individual particles can learn from past experiences of the swarm and adjust parameters to quickly arrive at the nearest best minima. Communication between these particles can lead to all particles finding the best local minima or global minima quickly. CALYPSO can perform either a local PSO or global PSO, each aimed to find either local minima or global minima. The local PSO communicates with particles nearby on the PES only whereas the global PSO communicates with all particles on the PES.

CALYPSO biases the search to create structures that fly through the PES relatively quickly, see figure 2.11, allowing for a swift exploration but also shuts off the search from certain areas which might hide the global minimum. The search is mixed with introducing a number of random samples for each generation of structure to enable exploration of the full PES. This works by measuring the velocity of certain structure parameters, such as lattice parameter or interatomic distances, across the PES shown in figure 2.11(d). With each generation structures new are generated by the PSO based on the best previous structures and the velocities of their structure parameters through the PES. The number of random structures and size of the generations that populate the structures are just some of the parameters in these searching methods [131]. In section 3.4 of this report, we have used CALYPSO to predict all currently known high pressure ground state structures for ammonia.

One can never really know when to stop searching as the process is not exhaustive. When an experimental phase is found multiple times, typically with the lowest enthalpy of the stable structures it is likely the search has converged. Searching with different codes and methods which also find the same lowest energy structure also add to the confidence of a converged result. When searching blindly a number of choices have to be made, such as the number of formula units to include in the

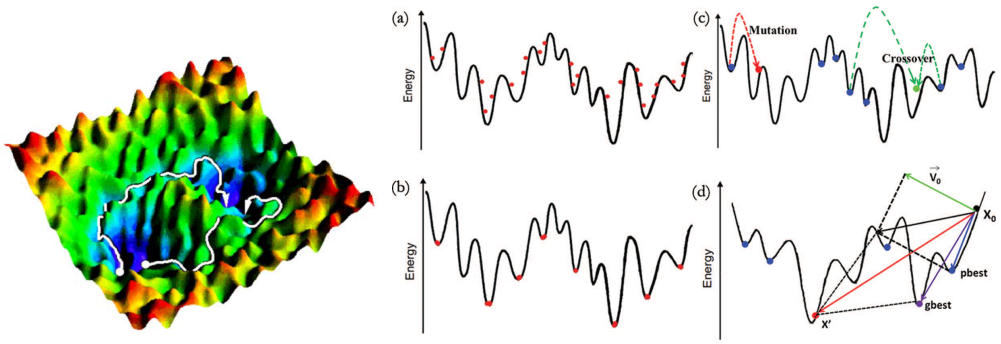

Figure 2.11 *Particles traversing a PES on the left. On the right are minima finding methods: (a) and (b) random sampling schemes, (c) a genetic algorithm, and (d) the CALYPSO method [132].*

unit cell. If the converged structure does not have all real phonons and imaginary modes are found away from the Γ point, then this is a good indicator of a larger unit cell. Other methods include simulated annealing [133], minima hopping [134], basin hopping [135], and metadynamics [136]. Recommended review articles on crystal structure prediction are [29, 30, 58, 126].

2.3 Further Electronic Structure Methods

2.3.1 Hellman-Feynman Theorem

Forces can be calculated from the Kohn-Sham wavefunctions via the Hellman-Feynman theorem [137]. This relates the first-order derivative of the total energy to the expectation value of the Hamiltonian's first-order derivative. When the derivative is with respect to spatial dimensions this gives the force. In general, the theorem gives,

$$\frac{d}{d\lambda}E_\lambda = \left\langle \Psi_\lambda \left| \frac{d}{d\lambda}\hat{H}_\lambda \right| \Psi_\lambda \right\rangle, \tag{2.50}$$

where λ is a continuous variable. For a system of 3D geometry such as a crystal the derivative of the energy with respect to $\boldsymbol{R(x, y, z)}$ gives the forces can be computed by applying the Hellman Feynman Theorem to the calculated ground state wavefunction,

$$\boldsymbol{F}_i = -\frac{\partial E}{\partial \boldsymbol{R}_i} = -\int d^3r n(\boldsymbol{r}) \frac{\partial V_{ext}(\boldsymbol{r})}{\partial \boldsymbol{R}_i}. \tag{2.51}$$

For plane wave basis functions these are independent of the ionic positions and use the same expansion coefficients used for the variational energy minimization, c_i, so the force on the atoms can be calculated by,

$$\frac{\partial \langle E \rangle}{\partial R} = \frac{\partial}{\partial R}\left\langle \sum_i c_i^* \psi_i^*(r) \left| H \right| \sum_j c_j \psi_j(r) \right\rangle = \sum_i c_i^* c_j \left\langle \psi_i^*(r) \left| \frac{\partial H}{\partial R} \right| \psi_j(r) \right\rangle. \tag{2.52}$$

2.3.2 The Stress Tensor

The stress tensor is related to the strain by the derivative of energy with respect to strain $\epsilon_{\alpha\beta}$ given by,

$$\boldsymbol{\sigma}_{\alpha\beta} = \frac{1}{\boldsymbol{\Omega}} \frac{\partial E}{\partial \boldsymbol{\epsilon}_{\alpha\beta}}. \tag{2.53}$$

where α and β are Cartesian indices and $\boldsymbol{\Omega} = \boldsymbol{a} \cdot (\boldsymbol{b} \times \boldsymbol{c})$ is the volume.

Studying systems under pressure we generally consider the stresses on each face of the unit cell, positive pressure for compression and negative pressure for expansion. Hydrostatic pressure occurs when $\boldsymbol{\sigma}_{xx} = \boldsymbol{\sigma}_{yy} = \boldsymbol{\sigma}_{zz} = -P$ which we will use for systems in this work and is generally what experiments aim to achieve in diamond anvil cells whereas shock experiments are likely to experience uniaxial stress [138].

Pulay stress [139] is an error in the stress that occurs due to an incomplete basis set or position-independent basis functions such as plane waves. Changes to unit cell shape and volume can discontinuously change the number of plane waves and fast Fourier transform (FFT) grid points. This means the basis set size varies with cell dimensions and so comparing properties of different cells develops an error without a fully converged basis set. Codes such as CASTEP implement a Finite Basis Set Correction by calculating the total energy change due to different basis set sizes and uses this to approximate corrections to the total energy and stress for different unit cell shapes.

At finite temperature, such as for molecular dynamics simulations, the pressure is calculated by including the ideal gas pressure,

$$P_{total} = P_{T=0K} + P_{IG} = -\frac{1}{3}\sum_{\alpha}\sigma_{\alpha\alpha} + \frac{Nk_BT}{V}. \tag{2.54}$$

2.3.3 Electron Localization Function

The electron localization function (ELF) was introduced by Becke and Edgecombe in the paper [55]. ELF has become a powerful tool in analyzing bonding situations such as between metallic or covalent bonds and at high pressure it is useful for identifying localized electron density in electride structures. Originally the ELF was defined as the Taylor expansion of the spherically averaged pair probability density of finding a same-spin electron to a reference electron, based on the HF description of the electron gas. The leading order quadratic term (zeroth and first terms vanish) is given by,

$$P(\boldsymbol{r}, s) = \frac{1}{3}\left(\sum_{i}^{\sigma}|\nabla\Psi_i(\boldsymbol{r})|^2 - \frac{1}{4}\frac{|\nabla\rho(\boldsymbol{r})|^2}{\rho(\boldsymbol{r})}\right)s^2 + \cdots, \tag{2.55}$$

giving $D(\boldsymbol{r})$ as,

$$D(\boldsymbol{r}) = \sum_{i}^{\sigma} |\nabla \Psi_i(\boldsymbol{r})|^2 - \frac{1}{4}\frac{|\nabla \rho(\boldsymbol{r})|^2}{\rho(\boldsymbol{r})}. \tag{2.56}$$

When the probability density is small, $D(\boldsymbol{r})$ is small and the electron is more localized. For the HEG there is a corresponding factor $D_{HEG}(\boldsymbol{r}) = \frac{3}{5}(6\pi^2)^{\frac{2}{3}}\rho(\boldsymbol{r})^{\frac{5}{3}}$ and from this Becke and Edgecombe defined the ELF as,

$$\eta(\boldsymbol{r}) = \frac{1}{[1 + \chi_{BE}^2(\boldsymbol{r})]}, \tag{2.57}$$

where,

$$\chi_{BE}(\boldsymbol{r}) = \frac{D(\boldsymbol{r})}{D_{HEG}(\boldsymbol{r})}. \tag{2.58}$$

ELF is a measure of localization *relative* to the HEG. The ratio was chosen such that high ELF values mean the electron positions are more localized (relatively) and when $\eta = 1/2$ the Pauli repulsion is the same as in the HEG for the given density.

As this was developed for the HF picture a further formulation was developed by Savin et al. [140] based on the Pauli kinetic energy density. Electrons are spatially redistributed by the Pauli principle leading to the Pauli kinetic energy $t_P(\boldsymbol{r})$ given by,

$$t_P(\boldsymbol{r}) = t(\boldsymbol{r}) - \frac{1}{8}\frac{|\nabla \rho(\boldsymbol{r})|^2}{\rho(\boldsymbol{r})}, \tag{2.59}$$

which again can be compared to the value for the HEG at the same density:

$$t_{HEG}(\boldsymbol{r}) = c_F \rho(\boldsymbol{r})^{\frac{5}{3}}, \tag{2.60}$$

where c_F is the Fermi constant

$$c_F = \frac{3}{10}(3\pi^2)^{\frac{2}{3}}. \tag{2.61}$$

For a closed shell system (no unpaired electrons) the DFT-ELF is given by,

$$ELF = \frac{1}{1 + \chi_S^2(\boldsymbol{r})}, \tag{2.62}$$

where,

$$\chi_S(\boldsymbol{r}) = \frac{t_p(\boldsymbol{r})}{t_{HEG}(\boldsymbol{r})}. \tag{2.63}$$

ELF can be used in topological analysis methods such as identifying bonding

phenomenon via finding critical points (such as the code CRITIC [141]) and provide intriguing visuals of molecular-orbitals or π-bonds. The DFT-ELF is interpreted as the influence of the Pauli principle on electron kinetic energy relative to the HEG. CALYPSO has recently developed a method for using the PSO to search for structures with high amounts of electron localization often labeled as electrides using the ELF as a fitness function [142].

2.3.4 Mulliken Charges

Electronic structure methods with a plane wave basis set lose the information of localized electron density in a system. The projection of electron density on to a Linear Combination of Atomic Orbitals (LCAO) basis set can shed light on the missing information such as atomic charge. Within CASTEP this projection to an LCAO basis set is carried out as described in [143], and the population analysis of these states is then calculated with the Mulliken formalism [144]. The plane wave calculation has eigenstates $|\psi_\alpha(\boldsymbol{k})\rangle$ along a given wave vector ($\boldsymbol{k}$) that are projected onto a likely incomplete and non-orthonormal basis set of Bloch functions formed from a LCAO basis set $|\psi_\mu(\boldsymbol{k})\rangle$. The overlap matrix of the new localised basis set is given by,

$$S_{\mu\nu}(\boldsymbol{k}) = \langle\psi_\mu(\boldsymbol{k})|\psi_\nu(\boldsymbol{k})\rangle, \tag{2.64}$$

where the quality of this projection can be assessed by a spilling parameter which is required to be low for meaningful results. The atomic charge $Q(A)$, and other populations, require the density matrix $P_{\mu\nu}(\boldsymbol{k})$ and the overlap matrix $S_{\mu\nu}(\boldsymbol{k})$, and so $Q(A)$ can be calculated from,

$$Q(A) = \sum_{\boldsymbol{k}} w_{\boldsymbol{k}} \sum_{\mu} \sum_{\nu} P_{\mu\nu}(\boldsymbol{k}) S_{\mu\nu}(\boldsymbol{k}). \tag{2.65}$$

The absolute values for atomic charge are known to have little historical meaning as they depend greatly on the initial atomic basis set. Though their relative values, for example when comparing two different phases or as a function of density, with a consistent basis set offer a useful comparison. Mulliken charges provide a cheap qualitative analysis of what the charges are doing.

2.3.5 Bader Analysis

For a condensed system, it can be difficult to define which regions of space belong to which atom, or even no atom at all. The Bader method uses the concept of partitioning continuous charge density to identify where one atom begins and another ends. From Richard Bader's "Quantum Theory of Atoms in molecules" [56] a method of dividing molecules into atoms was founded. Normally in molecules, the region in space between two atoms reach a minimum in charge density which naturally separates atoms apart. Similarly, the atom centers have a maximum in charge density. Bader uses zero flux surfaces, a 2D surface with a minima in charge density i.e. $\nabla\rho(\boldsymbol{r})\cdot\hat{n}=0$, to divide atoms. From this approach, much of the work of Bader analysis has been finding efficient ways to find these critical points, such as searching in a 3D grid, and partition atoms within the electron density [145], following gradients of charge density for a point in space to find maximums from atom centers which define basins of attraction for the charge density. This has great benefits as it only requires the electron density. The density within the Bader volume for the atom contains a charge that the atom has. The Bader scheme offers meaningful values for atomic charge, unlike more qualitative Mulliken charges.

2.3.6 Lattice Dynamics: Calculating Phonons

Lattice dynamics in harmonic form takes a Taylor expansion of the energy about the equilibrium atom co-ordinates. For a crystal of N atoms in equilibrium geometry, with co-ordinates $\boldsymbol{R}_{N,\alpha}$ (α is x, y or z), the displacement of the N^{th} atom from its equilibrium position is measured by $\boldsymbol{u}_{N,\alpha}=\boldsymbol{x}_{N,\alpha}-\boldsymbol{R}_{N,\alpha}$ where $\boldsymbol{x}_{N,\alpha}$ is the displaced coordinate. The total energy can be written as [146],

$$E=E_0+\sum_{N,\alpha}\frac{\partial E}{\partial \boldsymbol{u}_{N,\alpha}}\boldsymbol{u}_{N,\alpha}+\frac{1}{2}\sum_{N,\alpha,N',\alpha'}\boldsymbol{u}_{N,\alpha}\frac{\partial^2 E}{\partial \boldsymbol{u}_{N,\alpha}\partial \boldsymbol{u}_{N',\alpha'}}\boldsymbol{u}_{N',\alpha'}+\cdots, \quad (2.66)$$

where the second order term contains the matrix of force constants $\Phi^{N,N'}_{\alpha,\alpha'}$,

$$\Phi^{N,N'}_{\alpha,\alpha'}=\frac{\partial^2 E}{\partial \boldsymbol{u}_{N,\alpha}\partial \boldsymbol{u}_{N',\alpha'}}. \quad (2.67)$$

For equilibrium geometry the forces are all zero and so $F_{N,\alpha}=\frac{\partial E}{\partial \boldsymbol{u}_{N,\alpha}}=0$ and the

first-order term vanishes. In the Harmonic approximation [147] third order and higher terms are neglected. This can lead to significant errors when computing systems which are significantly anharmonic i.e. with asymmetric potentials. Phonon-phonon interactions are also ignored. Assuming the wavefunction is periodic under a certain Bravais lattice as in Born-von Karman periodic boundary conditions a monochromatic plane-wave displacement field can be defined as,

$$\boldsymbol{u}_{\kappa,\alpha} = \boldsymbol{\epsilon}_{mN,\alpha\boldsymbol{q}} \exp(i\boldsymbol{q} \cdot \boldsymbol{R}_{N,\alpha} - \omega(\boldsymbol{q})_m t), \tag{2.68}$$

where $\boldsymbol{q}$ is the phonon wave vector and $\boldsymbol{\epsilon}_{mN,\alpha\boldsymbol{q}}$ is the polarization vector due to these perturbations. From this we arrive at an eigenvalue equation,

$$D^{N,N'}_{\alpha,\alpha'}(\boldsymbol{q})\boldsymbol{\epsilon}_{mN,\alpha\boldsymbol{q}} = \omega^2_{m,\boldsymbol{q}}\boldsymbol{\epsilon}_{mN,\alpha\boldsymbol{q}}, \tag{2.69}$$

where $D^{N,N'}_{\alpha,\alpha'}(\boldsymbol{q})$ is the dynamical matrix, which is the mass-reduced Fourier transform of the force constant matrix,

$$D^{N,N'}_{\alpha,\alpha'}(\boldsymbol{q}) = \left(\frac{1}{M_N M_{N'}}\right)^{\frac{1}{2}} C^{N,N'}_{\alpha,\alpha'}(\boldsymbol{q}) = \left(\frac{1}{M_N M_{N'}}\right)^{\frac{1}{2}} \sum_a \Phi^{N,N'}_{\alpha,\alpha'} \exp(-i\boldsymbol{q} \cdot \boldsymbol{r}_a). \tag{2.70}$$

The eigenvalue equation setup in 2.68 can be solved numerically, the square roots of the eigenvalues are the frequencies of each mode, and the eigenvectors express the atomic displacements for the mode. In order to do this the force constant matrix $\Phi^{N,N'}_{\alpha,\alpha'}$ has be calculated which is the second derivative of the total energy with respect to two atomic displacements N, N'. First order derivatives of the total energy, i.e. forces, are computed via the Hellman-Feynman theorem eased by vanishing terms in the final expression as previously discussed. Second derivatives are more arduous:

$$\begin{aligned} E &= \langle \hat{H} \rangle \\ F &= -\frac{dE}{d\lambda} = \left\langle \psi \left| \frac{dV}{d\lambda} \right| \psi \right\rangle \\ \frac{d^2E}{d\lambda^2} &= \left\langle \frac{d\psi}{d\lambda} \left| \frac{dV}{d\lambda} \right| \psi \right\rangle + \left\langle \psi \left| \frac{dV}{d\lambda} \right| \frac{d\psi}{d\lambda} \right\rangle - \left\langle \psi \left| \frac{d^2V}{d\lambda^2} \right| \psi \right\rangle. \end{aligned} \tag{2.71}$$

Here the derivatives of the wavefunction do not vanish as the first order derivatives of the total energy did. So in order to perform ab initio lattice dynamics the electronic response to the displacement of an atom N must be computed. Typically this is done via a method of finite-displacement or via perturbation

theory. In the former calculations are performed with small and different displacements of atom N in order to numerically evaluate the derivative. In the latter perturbation theory calculations the response wavefunction $\frac{d\psi}{d\lambda}$. Methods for calculating anharmonic phonons exist at great computational expense by calculating higher order terms in the truncated Taylor expansion.

So far the energy has been calculated for an arbitrary wave-vector $\boldsymbol{q}$ but this can be done on a grid of q-points over the Brillouin zone or along a special path of high symmetry directions. The former produces phonon or vibrational density of states $F(\omega)$ plots by plotting, for example, Gaussian functions over the frequency eigenvalues, and the latter can be used to produce phonon dispersions.

2.3.7 Optical Spectroscopy

Spectroscopic techniques are commonly used in high pressure diamond anvil cell experiments as the diamonds are transparent and provide direct access to the sample. Infrared and Raman spectroscopy methods typically probe vibrational modes at the Γ point of the Brillouin zone. The frequencies of phonon modes are given by the square roots of the eigenvalues when solving the dynamical matrix as previously discussed. Assuming a completely harmonic crystal where DFT gives the correct picture then this frequency should be an almost exact match to an experiment probing this. Whether or not the mode is Raman or IR active is defined by the spectroscopic selection rules rooted in their symmetry and group theory.

Infrared mode activity is only observed for transitions or vibrational modes which cause a change in dipole moment. The OH stretch in water is an example and the C-O bond stretch which causes a large change in dipole moment.

Raman mode activity is observed for transitions which involve a change in polarisability. The H_2 vibron is an example of a Raman active mode that is often tracked during diamond anvil cell experiments as a measure of compression and should disappear coinciding with a molecular to atomic transition in hydrogen [148].

The two techniques are complementary and tend to probe different vibrational modes. For centrosymmetric molecules, IR active modes are Raman inactive and vice versa. The Raman shift observed depends on the energy spacing between the

system's modes. For gas phase (vibrons) and solid crystalline systems (phonons), the selection rules are the same, though phonons tend to have lower frequencies due to interactions (if attractive) with their neighbors. From a computational perspective, we want to predict IR and Raman activity to help experiments observe phase transitions by calculating the energy derivatives at wave-vector $\boldsymbol{q} = (0, 0, 0)$ (zone-centered frequencies). The activity of modes (IR or Raman) can be determined by the symmetry of the crystals, and codes such as CASTEP can perform this analysis. The matching of theoretical spectra to observed experimental spectra implies consistency between the real chemistry and material properties and corresponding calculations .

2.3.8 Free Energy

The Gibbs free energy as a function of pressure (P) and temperature (T) for a solid is given by,

$$G(P,T) = E + PV + E_{ZPE} + \int \frac{\hbar\omega}{exp(\frac{\hbar\omega}{k_B T} - 1)} F(\omega)\, d\omega, \tag{2.72}$$

where E_{ZPE} is the zero point energy given by,

$$E_{ZPE} = \frac{1}{2} \int F(\omega)\hbar\omega\, d\omega, \tag{2.73}$$

and $F(\omega)$ is the phonon density of states. From this, the free energies of different crystal phases can be compared at the same P and T. Here this was done within the harmonic approximation. The harmonic and quasi-harmonic approximation can be used to include the vibrational (thermal+ZPE) contributions to the free energy. Meaningful free energies require no imaginary modes, whereby there are no negative eigenvalues which indicate a soft mode in a $\boldsymbol{q}$ along the Brillouin zone. These can also appear due to a lack of q-point sampling but are a physical problem arising for systems with an energy gradient in a certain direction. These systems are not dynamically stable and typically want to break symmetry and increase the size of the unit cell. Later in this work, we see examples of new phases that were arrived at by following these soft modes into a new symmetry.

2.4 Molecular Dynamics

2.4.1 Newtonian Dynamics

To evolve an atomic system at finite temperature through time for non-relativistic velocity scales, Newtonian dynamics can be employed and here the ions are treated with the BOA. This can be used for example to simulate the dynamical properties of solid phases and investigate their melting temperature [149]. An MD simulation requires forces and corresponding particle velocities to evolve the particles after discretized time-steps Δt. For ab-initio MD a method such as DFT can be used to calculate the forces on the atoms at each time-step by relaxing the electronic structure to the ground-state with fixed nuclei and then applying the Hellman-Feynman Theorem previously discussed. Car-Parrinello MD (CPMD) [59] is an alternative method, popular when speed was more necessary, that does not self-consistently relax the electronic structure to the ground-state.

The choice of Δt should reflect the physics the simulation wants to capture and is generally a fraction less than 1/10 of the smallest period for a solid. This can be the characteristic vibrational frequency in the liquid as well, assuming no change in chemistry, but at very high temperatures the dynamics require even smaller time steps to avoid atoms getting too close between steps.

For a long enough simulation, the system should reach Ergodic conditions and be in equilibrium. The Ergodic Hypothesis states that over long periods of time the system will reach thermodynamic equilibrium. It is thought that after a long enough period of time the system forgets its initial state, and probing this system should give the same as ensemble-averaged results.

Here we use the Canonical ensemble, NVT, (fixing the number of particles, volume and temperature) under the Born-Oppenheimer approximation, conserves this pseudo Hamiltonian:

$$\hat{H} = \left\langle \Psi \left| \hat{H}_e \right| \Psi \right\rangle + \frac{1}{2} \sum_{i=1}^{N} \sum_{j=1}^{N} \frac{Z_i Z_j}{|\boldsymbol{R}_i - \boldsymbol{R}_j|} + \sum_{i=1}^{N} \frac{P_i^2}{2M_i} + \sum_{i=1}^{M} \frac{p_{\xi_i}^2}{2Q_i} + N_f k_B T \xi_1 + k_B T \sum_{i=2}^{M} \xi_i, \tag{2.74}$$

with a Nose-Hoover [150] chain of M thermostats with N_f ionic degrees of freedom to act as a heat bath. Q_i are the thermostat fictitious masses, ξ_i are the degrees of freedom for the thermostat, $\hat{H}_e$ is the electron Hamiltonian. Newtonian MD

treats the nuclei classically, which in some cases is not appropriate such as for light nuclei, and certain methods such as path-integral MD have been developed to overcome this [151]. A fundamental drawback from non-quantum corrected molecular dynamics is that zero point motion is not included. Coloured noise addresses this drawback by using a quantum thermal bath [152].

The temperature is kept on average constant by the thermostat which can be calculated by equipartition. In reality, the simulation will oscillate around the specified temperature. For the i^{th} time-step the temperature is,

$$T_i = \frac{1}{3Nk_B} \sum_{j=1}^{N} M_j v_j^2, \tag{2.75}$$

where N is the number of nuclei and j is the index of the nuclei. As the temperature is increased and constrained by a fixed volume the thermal pressure should increase so long as the thermal expansion of the system is positive, as for an ideal gas. This means heating a given fixed cell will follow isochores rather than isobars offered by NPT simulations. The thermal pressure is a combination of the ideal gas pressure and the ab initio stress tensor discussed previously and was sampled every 10 time-steps in simulations.

2.4.2 Radial Distribution Function

The Radial Distribution Function (RDF) is a pair correlation function describing the radial packing of a system. It gives the probability of finding a particle at a distance r from another particle. It equal to the Fourier transform structure factor, $s(q)$, and so is directly measurable by diffraction experiment for liquids and solids.

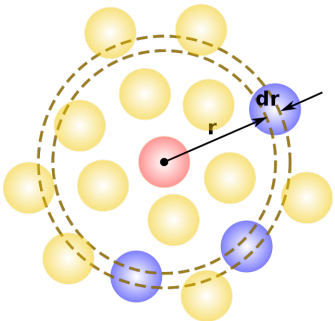

Figure 2.12 *Example of the measurement performed by the RDF showing the coordination shell between $r + dr$.*

The RDF, $g(r)$, can be calculated from the ensemble average of the inter-particle distances given by,

$$g(r) = \frac{1}{\rho} \langle \sum_{i,j=1}^{N} \delta(\boldsymbol{r}_{ij} - \boldsymbol{r}) \rangle \,, \tag{2.76}$$

where $\rho = N/V$ is the particle density, $\boldsymbol{r}_{ij}$ is the radial distance between particles i and j. In 3D the coordination shell has the volume of a spherical shell and so this can be written as,

$$V_{shell} = 4\pi r^2 \rho dr. \tag{2.77}$$

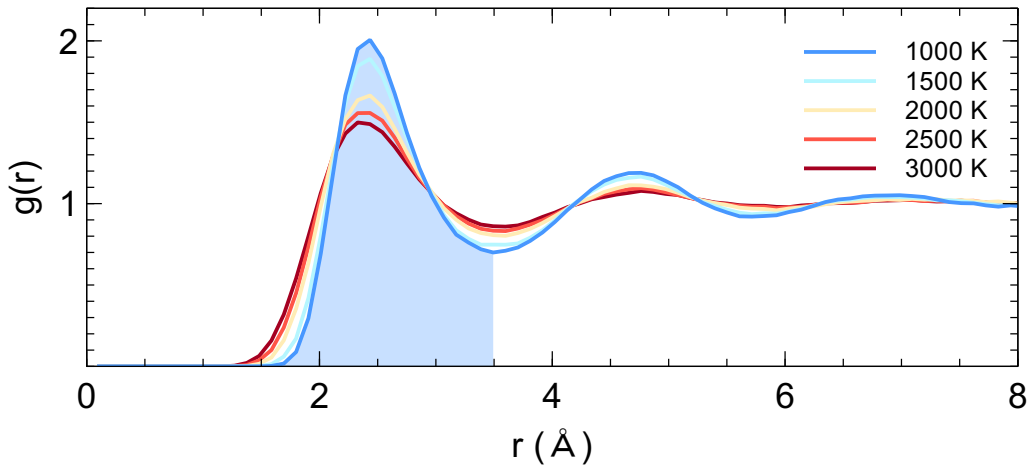

Figure 2.13 *Example RDF of AIMD simulations of 128 Molten Lithium atoms under PBC at 15 GPa as a function of temperature. The distribution is broadened with increasing temperature and for a liquid $g(r)$ should tend to 1 at long separation. The shaded blue section represents the area integrated out for the first coordination shell.*

The RDF is built stochastically as a function of simulation time and so requires trajectories to sample enough equilibrium states for the RDF to converge. The RDF is limited to a maximum radial distance r_{max} by the size of the simulation box. In 3D this is,

$$r_{max} = \frac{\sqrt{3}}{2} \cdot a, \tag{2.78}$$

where a is the lattice constant assuming a cubic simulation box. This is because

any values greater than r_{max} are sampling the same distribution as previously due to periodic boundaries conditions. When calculating the RDF numerically the bin size that is used to create a histogram at different values of r should be chosen based on the box size and system temperature to ensure a smooth $g(r)$.

The RDF can be used to calculate values such as the coordination number, c_n, representing the number of nearest-neighbors in the first coordination shell for a system. For close-packed structures such as FCC and HCP, this number should equal 12 which is the number of nearest neighbors in the static solid case. Thermal broadening between 2 near-neighbor groups can occur in systems such as BCC where the static nearest neighbor shells are 8 (first) and 6 (second) but in a molecular dynamics simulation at temperature, these shell distances are very close and the $c_n(BCC)$ has a value of 14. This is given by the function,

$$c_n = 4\pi \int_{r_0}^{r_1} r^2 g(r) \rho dr, \tag{2.79}$$

where r_1 is taken to be the radial value of the first minimum of $g(r)$ (see figure 2.13).

2.4.3 Mean Squared Displacement

For mobile particles the Mean Square Displacement (MSD) measures the diffusion of particles through the system. For a stable solid the thermal vibrations about lattice sites should be visible as the system evolves but the value of the MSD should remain constant over time. The MSD per particle can be calculated by,

$$MSD(t) = \langle (\boldsymbol{r}(t) - \boldsymbol{r}_0)^2 \rangle = \frac{1}{N} \sum_{n=1}^{N} (\boldsymbol{r}_n(t) - \boldsymbol{r}_n(0))^2, \tag{2.80}$$

where $\boldsymbol{r}_0$ is the initial coordinate, N is the number of particles is the system, and $\boldsymbol{r}$ or $\boldsymbol{r}_n(t)$ is the coordinate at a time t later. This is a useful criterion for identifying the phase for a system: solid, partially molten, and liquid states have qualitatively different MSD behavior making it easy to identify melting and look out for solid-solid phase transitions.

For a simple liquid, the MSD should scale linearly with time and the gradient linearly increasing temperature [153]. Taking the gradient of the MSD gives the

self-diffusion coefficient by the Einstein relation,

$$MSD(t) = 2dDt, \tag{2.81}$$

for d number of spatial dimensions. For $d = 3$,

$$D = \lim_{t\to\infty} \frac{MSD(t)}{6t} = \lim_{t\to\infty} \frac{1}{N} \sum_{n=1}^{N} (r_n(t) - r_n(0))^2. \tag{2.82}$$

For superionic phases of ice the proton conductivity can be characterized by the non-zero proton diffusion constant.

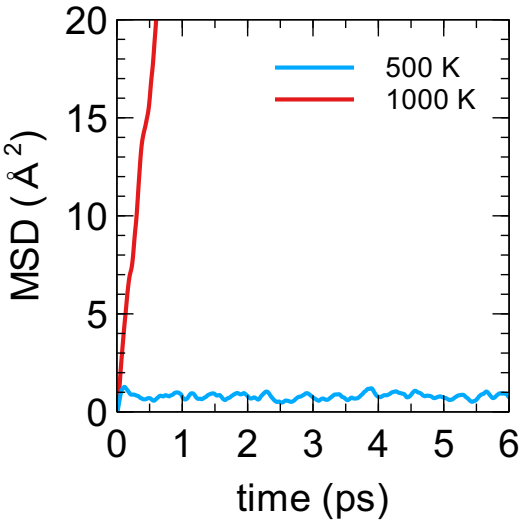

Figure 2.14 *Example MSD for Solid BCC (blue) and Molten (red) Lithium at 15 GPa upon heating.*

2.4.4 Bond Life-times

In simulated systems where bonds break and reform during the simulation time, it is possible to estimate the mean bond life-time. A simple example is water: even at ambient conditions proton transfer occurs which requires a covalent bond to break and another to form creating a set of OH^- and OH_3^+ units. The bond life-time is a function of phase, pressure, and temperature. From the solid-state and under high pressure ice can be heated into the superionic regime [154]. This requires covalent OH bonds to break and possibly reform else-where (hopping) or the H atoms travel as a fluid around the O sub-lattice possibly forming brief H_2 bonds. There are many methods for calculating the bond life-time for an atom

i to an atom j [155]. Here we took a first-order ensemble average by tracking individual bonds up to some cut-off distance, and the bond life-time τ_{BLT} was calculated by,

$$\tau_{BLT} = \frac{1}{N} \sum_{i,j;r_{ij}<r_c}^{N} (\tau_{formation} - \tau_{break}), \tag{2.83}$$

where τ is the point in time, N is the number of recorded bonds over the simulation, and r_c is a suitable radial distance cut-off corresponding to the maximum bond length for the system of interest such as 1.1 Å for for the O-H bond in ice. Note this is normalized over the number of bonds recorded and not by the number of molecules.

This approximation for the life-time of the bonds is crude, and in the superionic regimes, we expect to have many bonds changing, breaking and even reforming very quickly. A more general approach was used by calculating a bond auto-correlation (BAC) function. The BAC, $\beta(t)$, measures the probability of a chosen bond existing at a time t later, and then more usefully taking the ensemble average for the system, $\langle\beta(t)\rangle$. In summary, the BAC assigns a list of bonds every time step based on the proton nearest neighbor, then scans over all other time steps to work out the probability that this bond exists and a time t later under the criterion that the nearest neighbor remains the same. For ammonia water mixtures only covalent O-H and N-H bonds were considered so proton nearest neighbors were restricted to O and N atoms. When all bonds are stable the function should tend to a constant, and to decay when the bonds are changing. In the BAC bonds are allowed to reform (be considered the same bond) if the proton j returns to atom i:

$$\beta(t) = \left\langle \frac{b_{ij}(t_0) \cdot b_{ij}(t_0 + t)}{b_{ij}(t_0)^2} \right\rangle, \tag{2.84}$$

where $b_{ij}(t_0)$ is an initial list of bonds (such as H_1 to O_8) and if this bond still exists at a time t later then the product in the numerator is equal to unity. The characteristic decay of the BAC with changing bonds can be fitted with an appropriate function and has a relevant time constant τ associated with the bond life-times. The definition of a bond for this BAC was for a proton to have the same nearest neighbour heavy atom (oxygen for example) as the all other time steps. The BAC yield rich information on the nature of the bond decay and unexpectedly revealed profiles related to the specific crystal structure in certain cases.

2.4.5 Calculation Details

DFT

DFT calculations were performed with the CASTEP code [28]. Exchange-correlation effects were described within the generalized gradient approximation (GGA) using the Perdew-Burke-Ernzerhof (PBE) functional [156] unless otherwise stated, and ultrasoft pseudopotentials. Final structure relaxations were done with "hard" pseudopotentials with radii cutoffs no greater than 1.2 Å for oxygen and nitrogen, and 0.6 Å for hydrogen. Plane-wave cutoffs of $E_c = 1000$ eV and k-point densities of $20/\text{Å}^{-1}$ were found to give sufficiently converged energies and forces.

Structure searching with CALYPSO

Solid crystalline structures were searched for using the particle swarm optimization algorithm as implemented in CALYPSO (crystal structure analysis by particle swarm optimization)[131, 157] together with density functional theory total energy calculations. Structure predictions of ammonia-water mixtures were performed with up to 16 formula units of $(H_2O)_X(NH_3)_Y$, where X and Y are integers, and at 5, 10, 20, 30, 50, 80, and 100 – 1000 GPa in increments of 100 GPa. Ratios of molecules (X:Y) for searches were: (6:1, 5:1, 5:2, 4:1, 3:1, 3:2, 2:1, 7:3, 1:1, 3:7, 1:2, 2:3, 1:3, 1:4, 2:5). These searches were performed for the three canonical mixing ratios of ammonia dihydrate (ADH), ammonia monohydrate (AMH), and ammonia-hemihydrate (AHH). At 50, 100, and 300 GPa a binary search was performed to look for other stable mixing ratios. If a new mixing ratio was found to be stable, further searches were performed for this stoichiometry at relevant pressures. Structure predictions at pressures over 1 TPa and up to 5 TPa failed to find structures stable against decomposition into NH_3 and H_2O.

Each structure was optimized in CALYPSO 4 times with increasing accuracy with each new calculation. All searching was performed with the PBE functional, both local and global PSO, generation populations of 20 or 30 and starting volumes chosen based on the equation of state of known phases at a given pressure. The details for each calculation step are listed in table 2.2.

CALYPSO takes a distance matrix as input for creating crystal structures. Settings chosen are listed in table 2.2 which helped bias more molecular and ionic initial structures to be created and avoiding formation H_2 molecules. The

N	Basis Precision	E_c (eV)	K-points (1/Å)	Force Tol (eV/Å)
1	Medium	490	0.12	0.3
2	Medium	490	0.12	0.5
3	Medium	490	0.10	0.3
4	Fine	544	0.07	0.5

$\boldsymbol{R}_{xy}$ (Å)	H	N	O
H	0.8	1.0	1.0
N	1.0	1.5	1.0
O	1.0	1.1	1.5

Table 2.2 *DFT parameters for different structural relaxations during ammonia water searches with CALYPSO (above) and the distance matrix used to accept generated structures (below).*

minimum inter-atomic spacing between any two species can be specified as R_{xy} in Å where x and y are the atomic species. This cuts down the structure space that is explored but with sensible choices such as not allowing hydrogen atoms to have overlapping orbitals one can avoid high energy initial structures.

AIMD

Exchange-correlation was again described by PBE and with the same pseudopotentials as for ground state calculations. Plane-wave cutoffs were reduced to $E_c = 700$ eV and only the Γ-point was sampled for constructed supercells. A time-step of 0.5 fs was used with the NVT ensemble where the pressure was sampled every 10 time steps.

Chapter 3

Individual Ices: Water and Ammonia

The high pressure crystal structure of ice has been deeply explored, along with over 1000 papers detailing the properties of ice at ambient pressure.

3.1 Phase Diagram of Water

While water is a simple molecule there are at least 18 crystalline phases of H_2O ice. The crystalline phases as well as amorphous phases [158] are enumerated with Roman numerals if a diffraction pattern is collected for them, shown in figure 3.1. The low pressure phases obey the ice rules [159, 160] in which each water molecule donates two hydrogen bonds and receives two hydrogen bonds directed towards at the oxygen lone pairs summing to 4 hydrogen bonds per water. More simply there are not "empty" hydrogen bonds and the protons cannot point at one another in the ordered or disordered ices. For each ordered ice there exists a configurationally proton disordered (higher symmetry) version of the same heavy atom sub-lattice, such as ice VIII to ice VII with oxygen atoms on an ordered BCC lattice. This order-disorder transition in ice has an entropy known as Pauling entropy [161] $S_0 = Nk_Bln(3/2)$. The disordered phase can form a glass upon cooling unless doped with KOH [162] as this encourages proton transfer and creates a gap in the ice rules enabling order to propagate, althought not necessary with ice VII/VIII. Other phases of ice are suggested

in the literature by theory generally by looking at different ways of organizing ice-rules conforming networks and structure searching [163, 164].

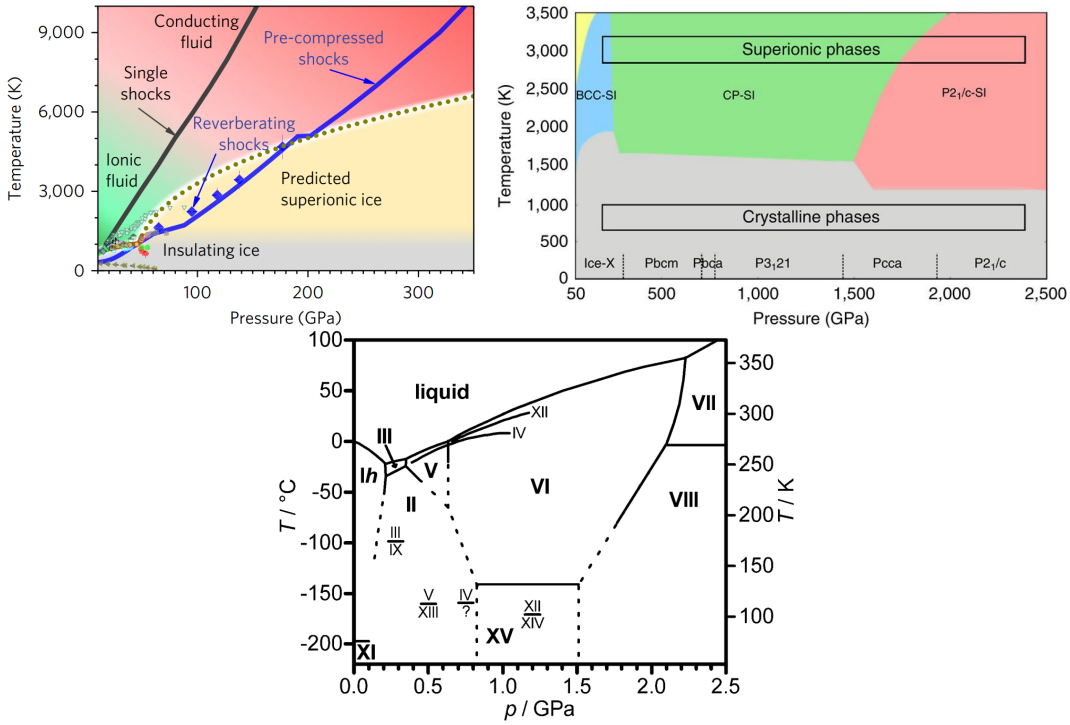

Figure 3.1 *Phase diagrams for H_2O from recent experimental and theoretical works. From top left: shock experiments showing evidence of superionicity taken from [165], calculated phase diagram of the high pressure superionic phases from taken [166], and a low pressure phase diagram taken from [167].*

At higher temperatures (above 500 K at 5 GPa) a plastic phase of ice has been proposed from simulation where the water molecules are able to rotate about their molecular sites (BCC in ice VII) [168–173] In these phases, the ice rules are generally obeyed and the molecular rotations should have a correlation that reflects this due to the high energetic cost of breaking the ice rules. At higher pressures (5–100 GPa) and higher temperature (800 K at 30 GPa) ice VII and X (with symmetric hydrogen bonds [174]) and above transition in calculations into a superionic regime.

In the superionic phase, the hydrogen sub-lattice melts, losing long-range order. This can be seen in the hydrogen RDF having a typical liquid profile [154], and the MSD rapidly increasing as a function of temperature as the protons enter this diffusive regime while the oxygen atoms retain their solid lattice. In figure 3.2 the calculated probability distribution of protons is shown in 3D for visualization. The region of PT space where superionic ice is predicted to exist is shown in

figure 3.1. For comparison, the PT conditions in the interior of icy bodies such as Neptune and Uranus are plotted in figure 3.2, suggesting the phase is relevant to the mantle of icy planets and the generation of magnetic fields.

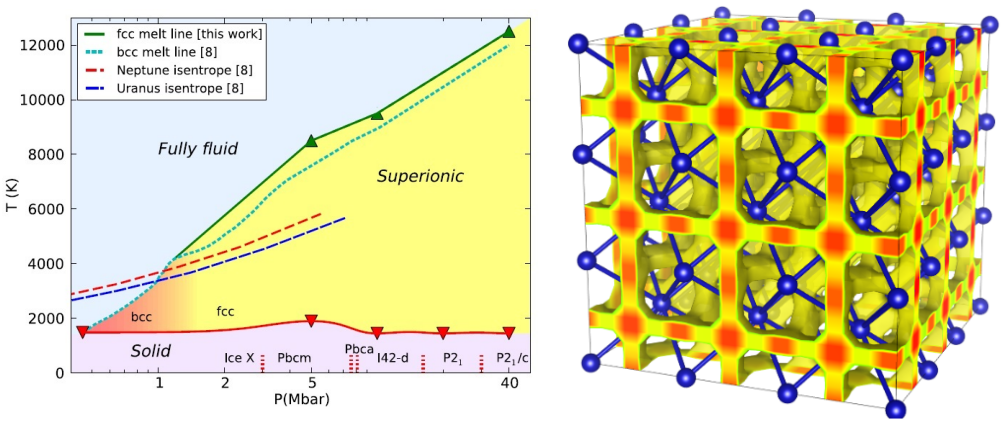

Figure 3.2 *High PT phase diagram of ice (left) and the proton probability distribution for BCC superionic ice (right) are shown, both taken from [175]. Phase $I4_2$-d was found unstable to $P3_12_1$ in later work [176].*

Superionicity in ice was first theorized by Ivan Ryzhkin [177] considering proton hopping and defects and first simulated classically by Demonts et al. [178] describing the phase as a "fast-ion proton conductor". Shocked water was also proposed to have diffusive protons in the 1985 study [179]. The first AIMD simulations of superionic ice (and ammonia) were by Cavazzoni et al. [154], and later followed a wealth of further studies [175, 180–184]. Superionicity is not just limited to ices such as sublattice melting in PbF_2 [185, 186]. Indeed superionic materials, transitions, and dynamics are discussed in a review article [187]. Classical force-fields were trained on AIMD data, which allowed the dissociation of the OH bonds and could describe the superionic transition [188].

While experiments have been carried out to investigate superionicity, the measurements remain indirect yet consistent with the expected properties such as reflectivity. Conductivity measurements, for example, cannot rule out that the conductance is due to the diffusive protons or from the water molecules themselves, though spectroscopy evidence exists [165, 179, 189]. More recently a laser-driven shock-compression experimental study [165] was carried out with further supporting evidence for the superionic phase with optical reflectivity and absorption measurements and X-ray diffraction of the oxygen crystal structure by Millot et al [190] observing a BCC to FCC transition.

Evidence for a transition of the solid O sub-lattice between different phases of superionic ice from BCC to a more dense FCC was put forward in [175] as shown in figure 3.2 with a higher melting temperature and again by Sun et al [166]. Superionic-superionic phase transitions in pure ice were further investigated in 2016 [191] and later similar work showed the first ab-initio simulations of plastic ice in 2018 [192].

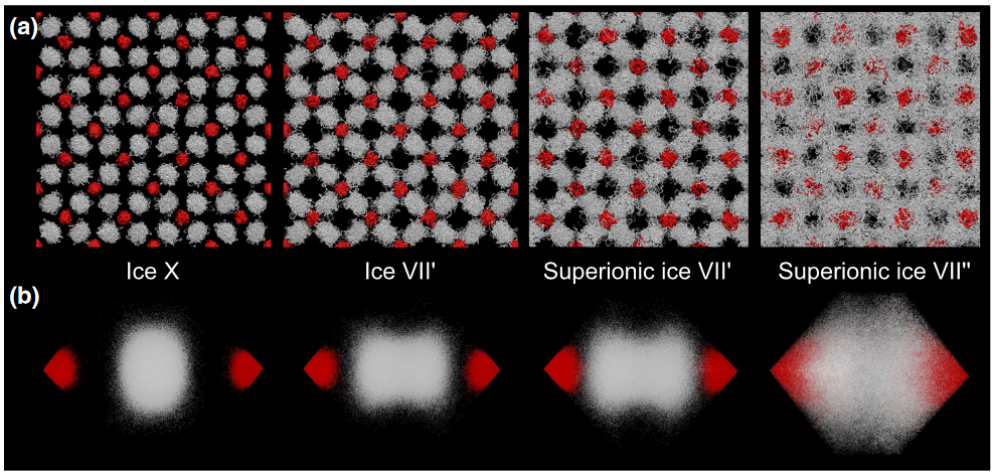

Figure 3.3 *Oxygen (red) and proton(grey) distributions along the OHO plane in BCC ice taken from [191]. In (a) atom trajectories are plotted showing the proton localization in the BCC lattice and in (b) the trajectories are projected along the $OH\cdots O$ bond showing whether this is unimodal, bimodal, or delocalized.*

Hernandez and Caracas focused primarily on the BCC sub-lattice of oxygen atoms for ices over 2 GPa and simulations extend to under 200 GPa. They investigated the transition between ice VII - ice X and the superionic regime, and in doing so found two distinct phases of superionicity within the BCC oxygen sub-lattice. These phases were termed superionic ice VII' and superionic ice VII" visualized in figure 3.3. The difference between VII' and VII" can be seen as the proton distribution leaving the containment of the ice VII configurationally disordered lattice sites along the BCC diagonals.

Using different superionic phases and identifying a molecular crystal plastic regime a phase diagram was produced [192] shown in 3.4 along with an up to date summary of experimental melting line measurements. The plastic phase was identified by counting OH rotation rates through the trajectories while the H translation rates were still zero, and when both rates were finite this was deemed superionic VII".

While the MD is purely AIMD without quantum corrections they see a transition

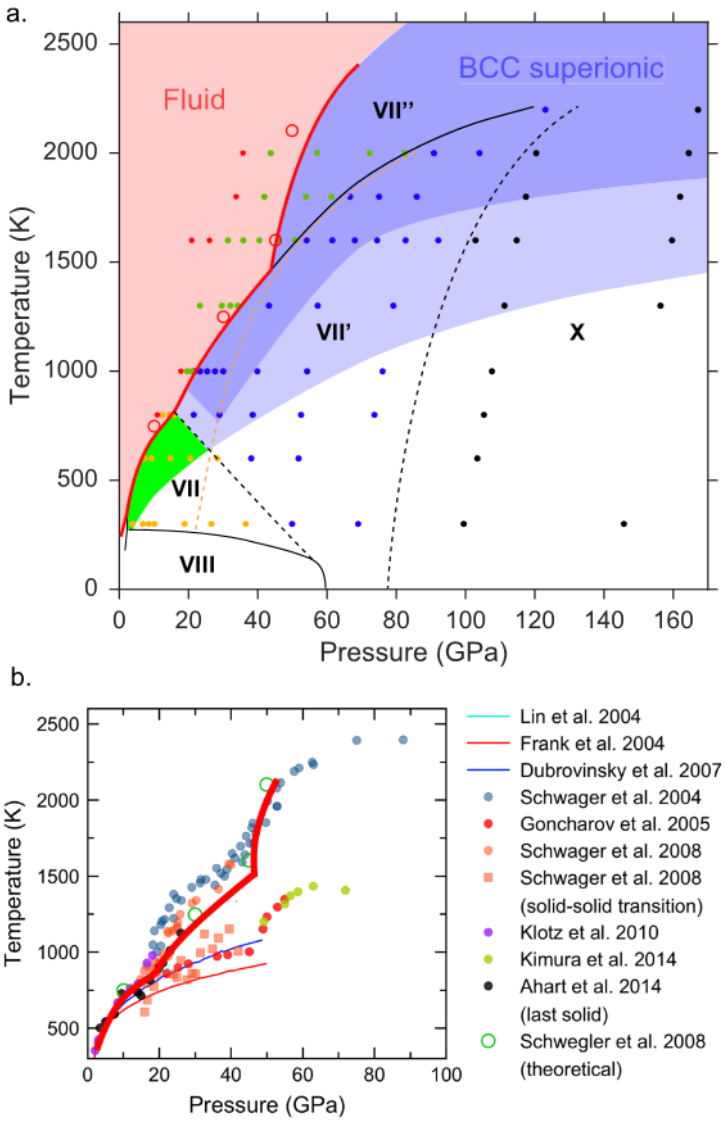

Figure 3.4 *Calculated phase diagram for H_2O is shown in (a). The green region refers to the plastic regime, light blue is superionic from a bonding analysis, and dark blue is superionic from diffusion analysis. In (a) the solid lines refer to phase boundaries that were previously known, the dashed lines represent new phase boundaries found. and dots represent different AIMD simulations. A summary of experimental melting lines for H_2O is shown in (b) taken from [192].*

from ice VII to ice X between 70 and 100 GPa depending on temperature which is similar to results found in [193] where PIMD was used to account for quantum proton distributions and to obtain a phase diagram in the lower temperature ice VII, VIII, X transition region. There are many scales on which to view the ice phase diagrams and this is likely true for mixtures of ammonia and water ices with different complexities at different T and P conditions.

3.2 Phase Diagram of Ammonia

Ammonia has been studied less than water but was recently been investigated up to 200 GPa in experiment [26] and up to 500 GPa in structure prediction [194, 195]. At low pressures, ammonia forms molecular crystals with each molecule donating and receiving three hydrogen bonds. Around 14 GPa ammonia is thought to undergo an isosymmetric phase transition to phase V [194] where the full structure is unknown and a discontinuity in compression was observed at 55 GPa [196] suggesting a possible phase VI, both of the space group $P2_12_12_1$.

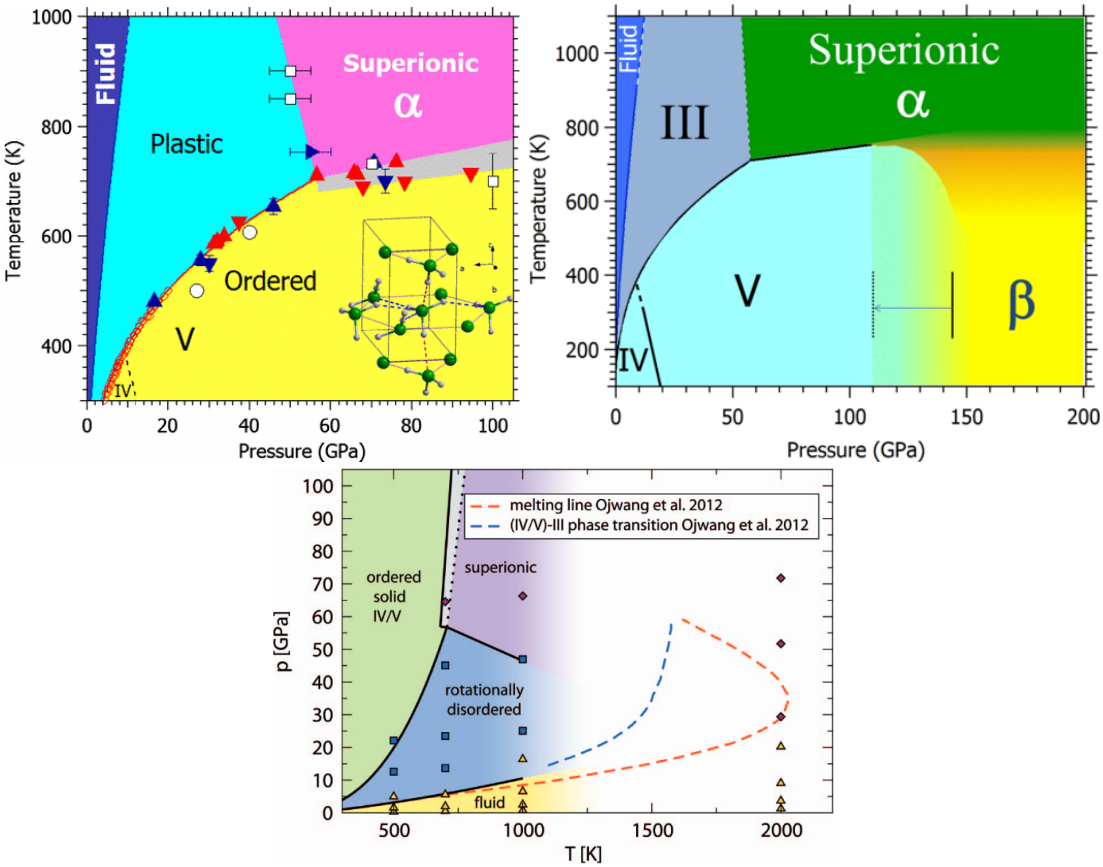

Figure 3.5 *Phase diagrams of NH_3. Top left Shows the combined experimental and computational findings [197]. Top right shows the higher pressure solid ionic phases of ammonia predicted in [26]. Bottom shows a calculated phase diagram including experimental transition data by Bethkenhagen et al, [198].*

At pressures above 100 GPa NH_3 is predicted to form ionic phases [194] further reviewed in [199] and returns to a molecular crystal at 440 GPa. This ionic transition may be important when studying ammonia mixtures and has been the subject of a joint experimental and theoretical study of ammonia monohydrate

observing ionic Raman signatures [199]. A recent study of the N-H binary system predicts that NH_3 becomes thermodynamically unstable at 460 GPa and decomposes into a more favourable stoichiometry of N_3H_7 and NH_4 [195]. Hydrogen bonding in ammonia is much weaker than in ice (2 kcal mol^{-1} vs. 5 kcal mol^{-1}) [200, 201]. The van der Waals forces are also important with a similar energy scale to that in water [202], which as previously mentioned can be a challenge for DFT. Possible Phase VI suggested by a Raman study is thought to show symmetrization of a hydrogen bond around 60 GPa [203].

Studies of ammonia also predicted superionicity as reported by Cavazzoni et al. [154] and others, including Li et al. [204] more recently. Heating the ordered phases produces two rotationally disordered (plastic) phases of ammonia, phases II (HCP) and III (FCC) [205]. The superionic phase for ammonia was reported to have been discovered at 57 GPa and 700 K by Ninet et al [197]. A difference in the nitrogen sub-lattice was reported depending on the thermodynamic pathway taken and probe technique.

Comparing phase diagrams found in the literature, most seem to agree on the temperatures required to enter the superionic state for the various materials considered yet the superionic melting line measured for ice has not been fully measured experimentally. If mixtures of water and ammonia, for example, lower the P and T conditions required to access the superionic phase to the conditions accessible to neutron experiments or other probes then this may encourage the conclusive discovery of this phase in ice mixtures.

Mixtures of both NH_3 and H_2O are likely to also exhibit superionic behavior, and have been investigated by computational studies [206, 207]. A methane water mixture is predicted to augment the properties of superionic phases [208].

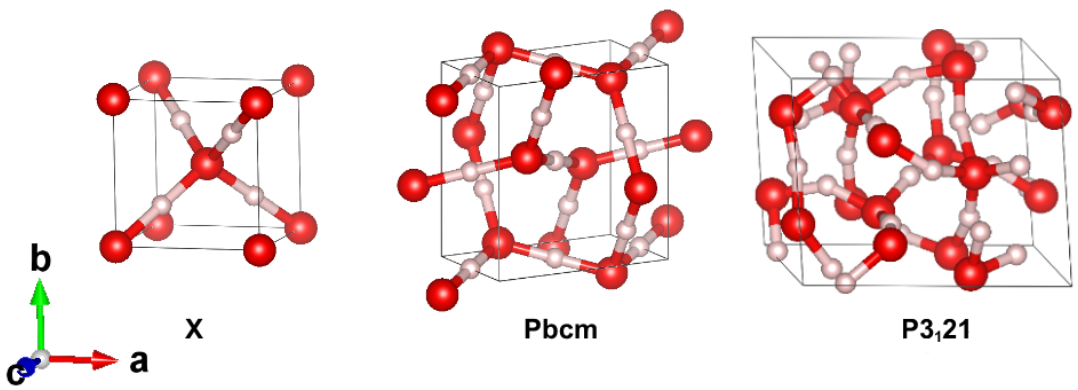

Figure 3.6 *High pressure phases of H_2O ice including X (100 GPa), Pbcm (400 GPa), and $P3_121$ (1000 GPa).*

3.3 Summary of Ground State Structures

A summary containing recent predictions on high pressure ice up to 6 TPa by Pickard et al. [176] reports H_2O decomposes into H_2O_2 and a hydrogen-rich phase slightly over 5 TPa. The low pressure phases of ice consist of proton ordered packed water molecules until phase Ice X (see figure 3.6) above 60 GPa in which the hydrogen atoms move to the midpoints between neighbouring oxygen atoms [209]. The calculated high pressure phase sequences are summarised in table 3.1 for water and table 3.2 for ammonia. These phases are taken from the literature and the stability pressure range results from calculations in this work.

Space group	Stability range (TPa)	No. f.u.	Source
Ice X	0.1–0.30	2	[174]
Pbcm	0.30-0.71	4	[210]
Pbca	0.71-0.78	8	[211]
$P3_121$	0.78-2.01	12	[176]
Pcca	2.01-2.24	12	[176]
C2	2.24-2.36	12	[176]
$P2_1$	2.36-2.75	4	[212–214]
$P2_1/c$	2.75-6.06	8	[213]
C2/m	6.06–	2	[212]

Table 3.1 *Table 1. Ground state structural phase evolution of water at high pressure, from DFT-PBE calculations performed in this work.*

Space group	Stability range (GPa)	No. f.u.	Source
$P2_13$	0–4	4	[215]
$P2_12_12_1$ (IV)	4-14	4	[205]
$P2_12_12_1$ (V)	14-100	4	[216]
Pma2	100-176	4	[194]
$Pca2_1$	176-300	8	[217]
$P2_1/m$	300-440	4	[194]
Pnma	440-460	4	[194]

Table 3.2 *Table 2. Ground state structural phase evolution of ammonia at high pressure, from DFT-PBE calculations. Note that the isostructural transition between phases IV and V is from experiments and are energetically equal in stability in DFT-PBE.*

Now that water and ammonia have been introduced, from here on results from this study are presented. To start this work structure searching was performed for ammonia to both confirm current results in the literature (from the AIRSS

method) and to look for any new structures. For ammonia, all high pressure structures previously found were again found by the PSO with Calypso. Although not every search initially found the lowest energy structure (as shown in table 3.3), the higher energy structures sometimes contained the lowest energy literature structure as was the case for $Pca2_1$ at 250 GPa. In figure 3.7 an example of search results for $Z = 8$, Z is the number of formula units, at 500 GPa is given, where the ranking refers to the energetic order of structures found. Searching was performed with coarse DFT parameters in order to scan more structures and then the best structures were optimized with tightly converged parameters. When using cheaper settings for searching it is important that the energetic ranking of structures from the coarse settings is similar to that of the tight settings, and this is achieved.

NH_3	**P (GPa)**	**Z**	**Space group**
	50	4	$P2_12_12_1$
	80	4	$P2_1$
	150	4	Amm2
	250	4	Pma2
	250	8	P1
	300	8	P1
	400	4	Pma2
	500	4	P-4_2m
	500	8	Pnma
	1000	4	Pnma
H_2O	**P (GPa)**	**Z**	**Space group**
	4000	16	P1
	4000	24	$P2_1$

Table 3.3 *Summary of structure searches performed for ices H_2O and NH_3. The space group for the lowest energy structure found in each search is given.*

The total energies between the two data sets are different as a different pseudopotential was used for each, one being more expensive. The lowest 3 structures found in the searches are shown in the inset, where *Pnma* is the lowest enthalpy structure for NH_3 at 500 GPa consistent with literature. Searching was performed with 8 f.u. of NH_3 and the structure found for *Pnma*, which has 4 f.u., contained two unit cells. In practice, but not always, the step-wise energetic ordering of structures seen in figure 3.7 for the lowest 3 energetic structures indicates that each of these structures has the same unit cell and hence the same enthalpy. However, there may be more than one structure with very similar

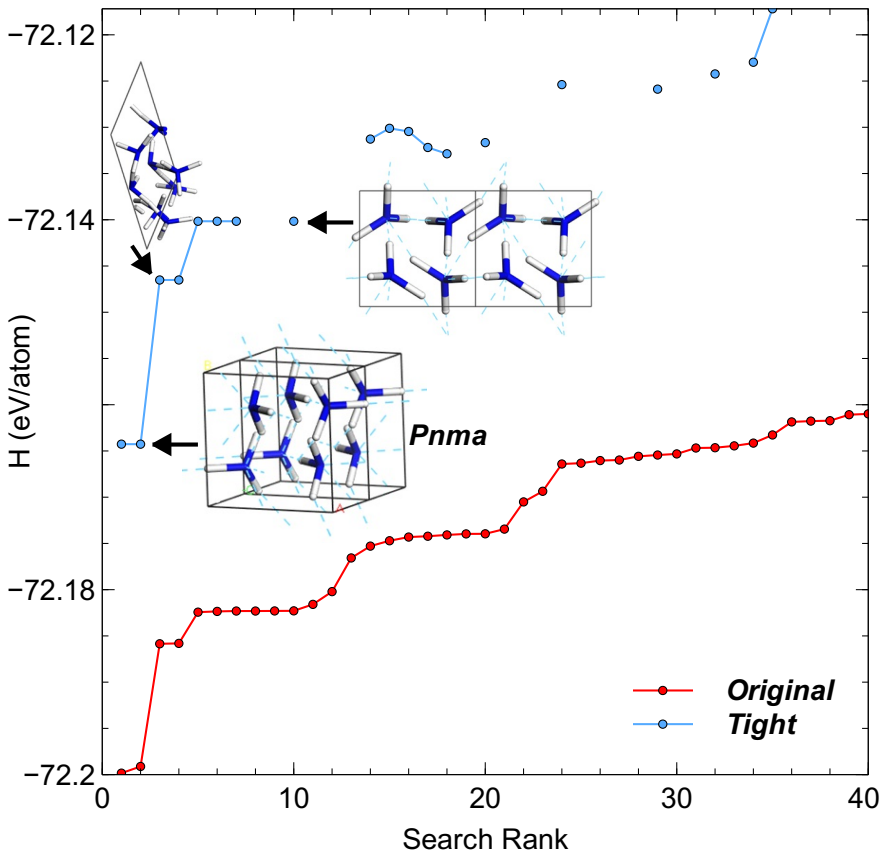

Figure 3.7 *Original search results for NH_3 at 500 GPa with 8 f.u. (red) and tight relaxation results with a harder choice of pseudopotential, energy cut-off, and k-point mesh. The literature ground state result of Pnma at 500 GPa (4 f.u.) was recovered. Structures are ordered by their enthalpy from the original search results. Tightly refined structures may not maintain the same energy ranking as the original set as seen for structures 14-18.*

energetics and so this can be misleading.

3.4 Energetics for Water and Ammonia

Here we summarize all calculations performed on pure water and ammonia. Firstly the enthalpy for the ordered ice phases up to 1 TPa was calculated and compared with each other as well as literature results. In order to aid observation of these phases experimentally we calculated their spectroscopic signatures for both infra-red and Raman techniques. Mulliken charges were also calculated to see if this offers quantitative discrimination of the different crystal phases. Later in this thesis, the effect of different functionals of on the thermodynamic stability of ice, ammonia, and mixtures is considered. Finally, we compare free energies for ice phases up to 1 TPa and 1000 K for the harmonic approximation. Disordered and plastic phases are not considered in free energy calculations, and so phase boundaries found in literature have been included to give a more complete description.

3.4.1 Water

The ground state enthalpy was calculated for the ordered phases of ice at the PBE level of theory and compared in figure 3.8. Phase transitions occur at pressures greater than those experimentally found by a factor of 10 which can be accounted to the lack of including dispersion with PBE [218]. The order of phases found by PBE is the same as experiment: XI $\rightarrow$ IX $\rightarrow$ XV $\rightarrow$ VIII $\rightarrow$ X so forth for the proton ordered ice phases. This justifies the use of PBE as a general starting functional for the ices. PBE results in higher transition pressures than experiments without van der Waals corrections. This is more noticeable at lower pressures where the phase sequence is increasing the number of near neighbors in the first radial shell, as also observed in liquid water with increasing pressure. At high pressure the different phases have more similar packings and so this is less of a problem when comparing energy differences.

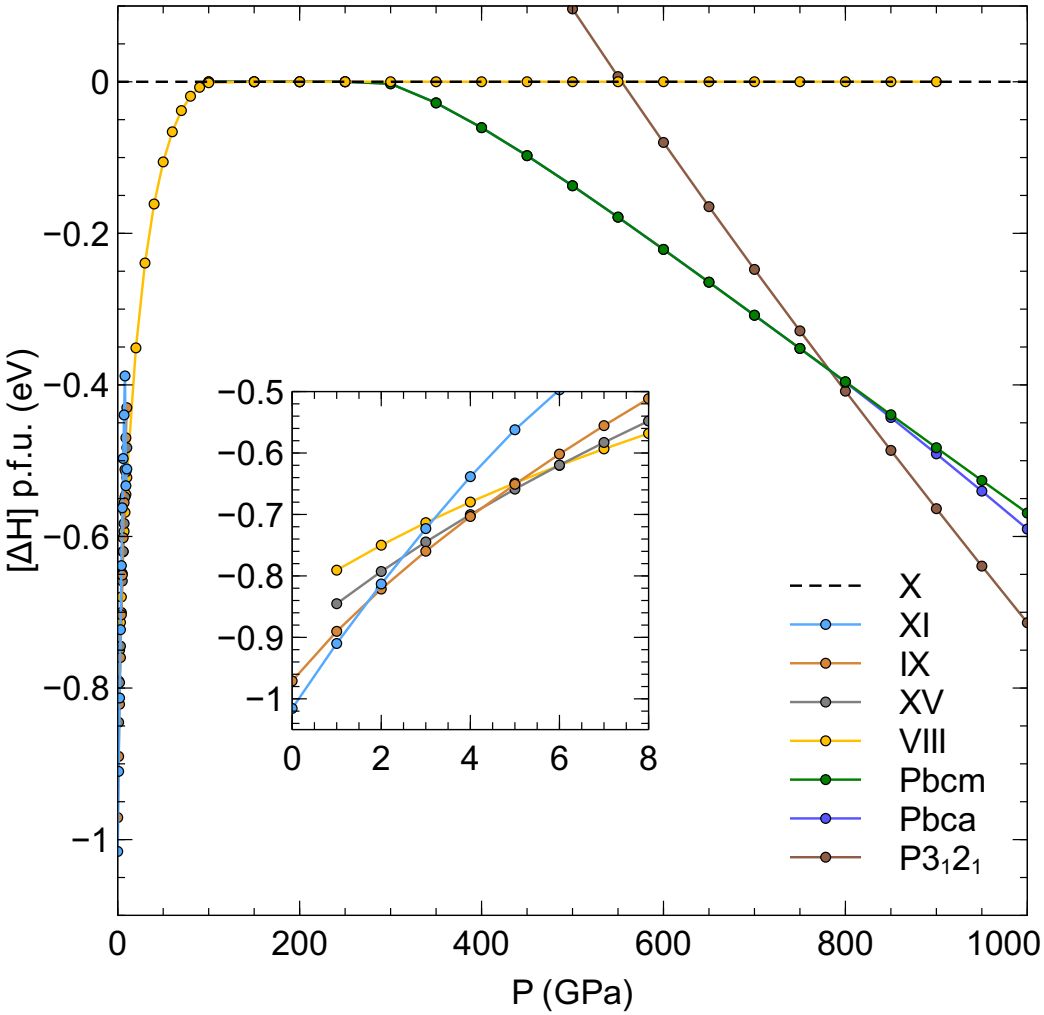

Figure 3.8 *Relative ground state Enthalpy for proton ordered H_2O ice phases as a function of pressure where the inset shows the low pressure phase transitions.*

Comparing static ground state enthalpies with DFT predicts ice-VIII transitions to ice-X at 100 GPa. In experiment however, this can be found at much earlier pressures above 60 GPa [174]. This is due to the lack of quantum effects being included in these calculations which play a role in the proton symmetrization [219].

3.4.2 Ammonia

The calculated ammonia phase diagram is shown in figure 3.9. This agrees with literature [217] including decomposition into $\frac{2}{5}NH_4 + \frac{1}{5}N_3H_7$ above 440 GPa.

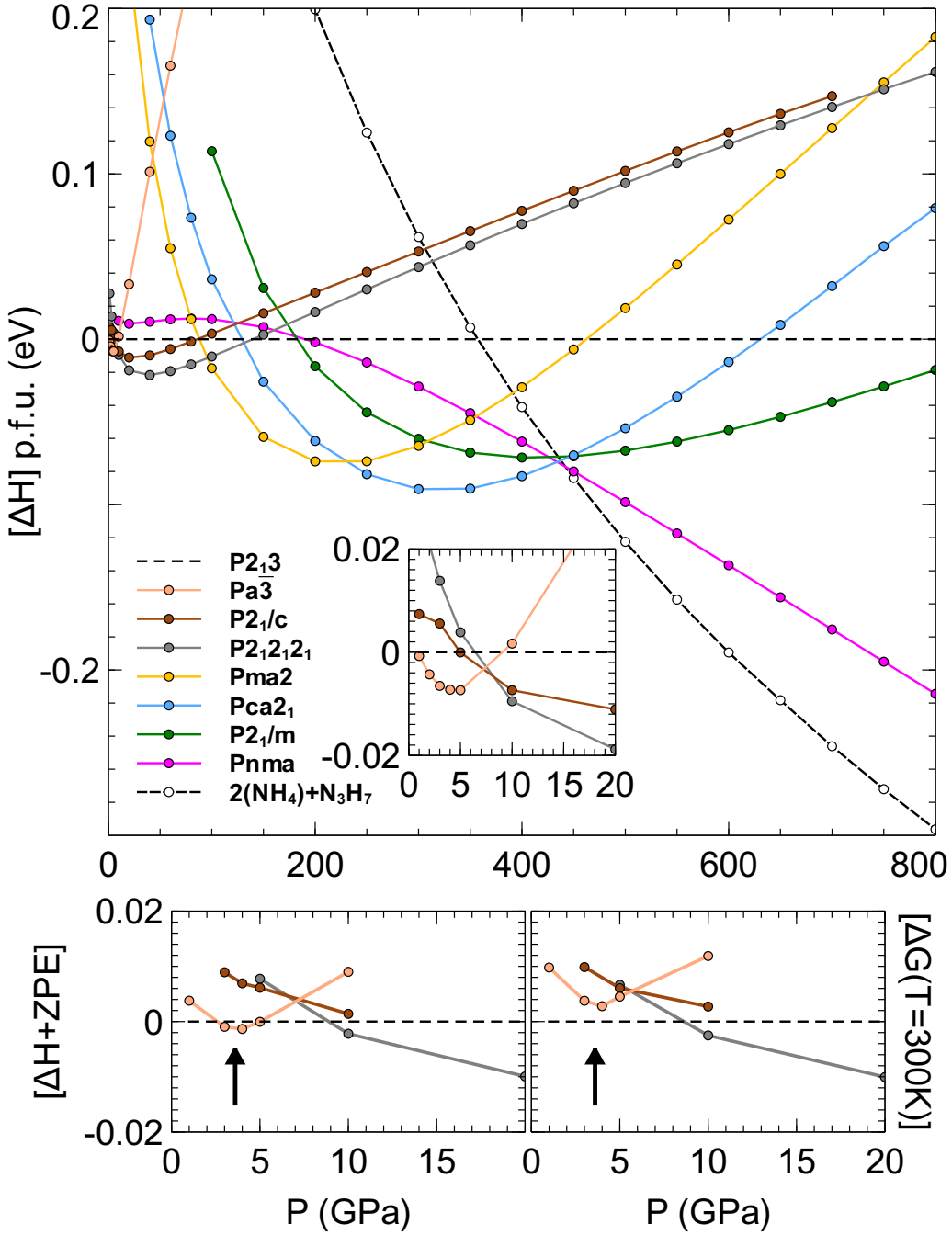

Figure 3.9 *Top: Relative enthalpies for proton ordered NH_3 phases as a function of pressure calculated with the PBE functional. Below: Including ZPE and the Gibbs free energy at $T = 300$ K for the low pressure regime shows the $Pa\bar{3}$ phase becoming destabilized.*

For NH_3 in the low pressure region (P < 20 GPa) a $Pa\bar{3}$ phase is predicted to be more stable than the experimental $P2_13$ phase from 0.5 to 7 GPa. These two phases are perhaps similar in structure and shown in figure 3.10. It is stable in PBE, PBE+TS, PBE+Grimme, and PBE+MBD calculations in this work though always by less than 10 meV/p.f.u.. Including vibrational contributions from phonon calculations appears to destabilize this phase, reducing stability to less than 2 meV/p.f.u. at T=0 K and it is metastable at T=300 K. This may explain why the $Pa\bar{3}$ phase has not been seen experimentally. Though as the energy differences are small and sensitive to the dispersion correction a thorough well-converged DFPT study moving from harmonic to the quasi-harmonic approximation would better confirm this. Otherwise, as with H_2O ice, the PBE functional gets the ammonia phases in the correct order with the molecular to ionic transition below 100 GPa.

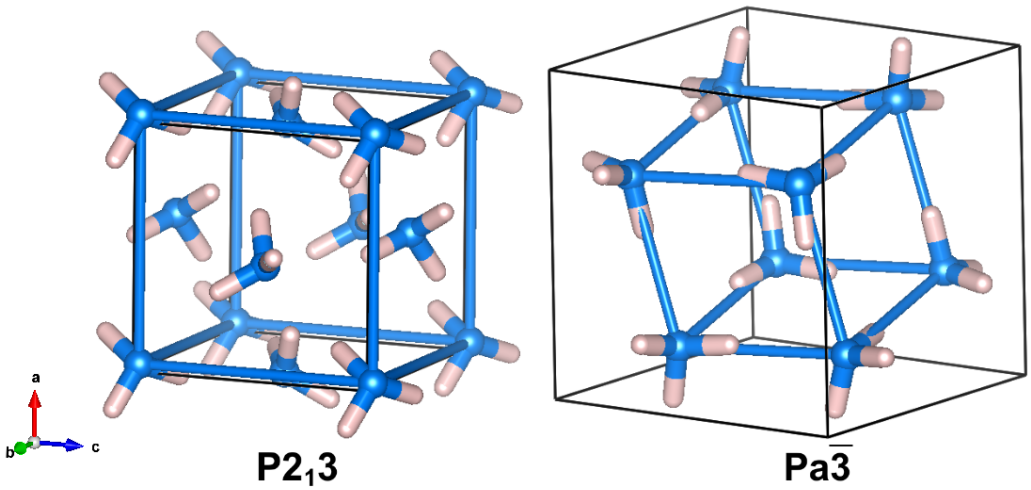

Figure 3.10 *Crystal structures of the two competing cubic structures of NH_3 at 2 GPa. Phase $P2_13$ is FCC in its heavy atom atom positions, though the face sites remain off centre and phase $Pa\bar{3}$ has a distorted hexagonal arrangement.*

3.4.3 Finite Temperature Stability

Including the vibrational effects of zero point motion (T=0 K) tends to favour transitions into denser phases. This and the effects entropy (T>0 K), populating the excited phonon modes, is captured in figure 3.11 on a logarithmic scale for the ordered crystalline H_2O phase diagram. Most phase transitions are almost

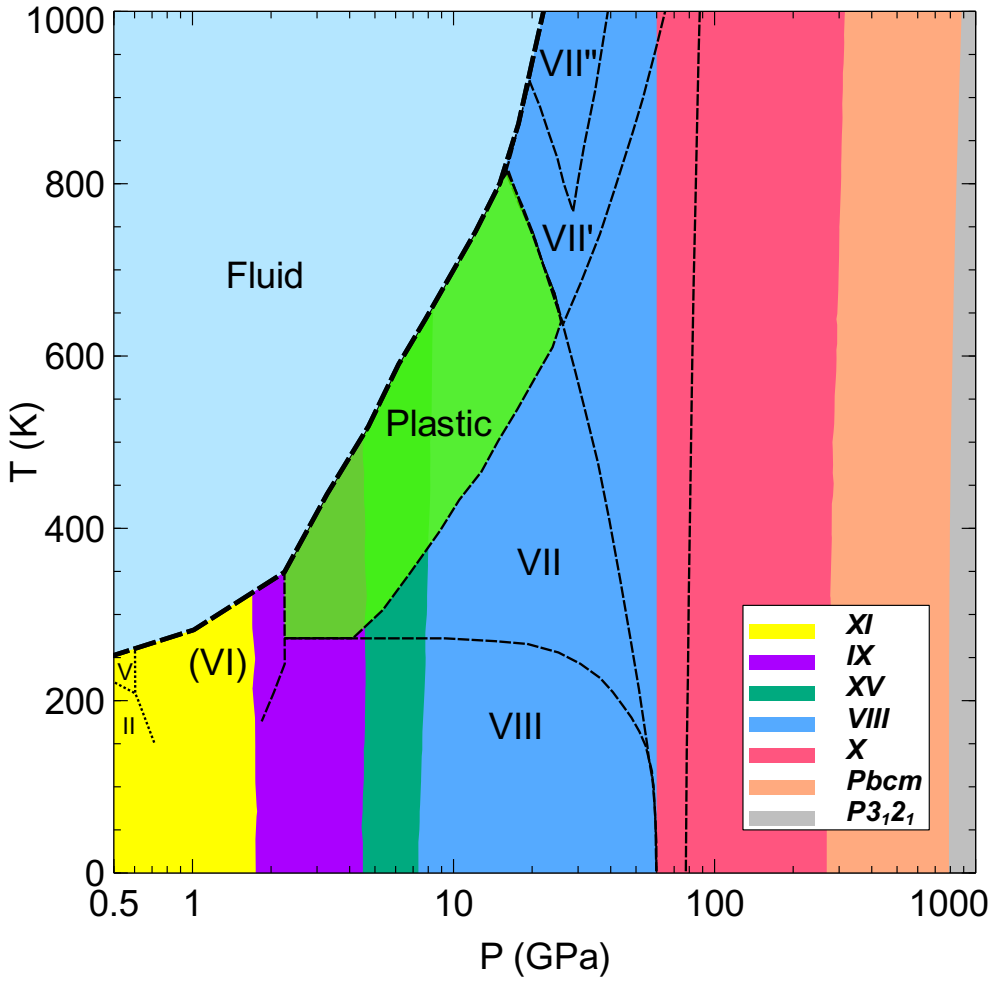

Figure 3.11 *Calculated phase diagram of H_2O. Phase boundaries (black dashed thin-line), the melting line (black dashed thick-line), and the plastic region (light green), were taken from AIMD [192] including the ice X transition line from interpolation. Coloured regions are shown for stability given by phonon calculations for ordered phases. Experimental phase boundaries (block dotted lines) for the lower pressures were taken from [220].*

vertical in their regions of stability (along the lines of experimental temperatures) up to 1000 K suggesting entropic effects are not dominant. The transition from ice VIII to ice X is incorrectly modeled due to imaginary modes arising in ice-X below 120 GPa [209] leading to inaccurate calculations of the Gibbs free

energy between 50–100 GPa. This highlights the need for quantum corrections to correctly describe the proton symmetrization - whether the proton distribution is bimodal or unimodal between oxygen sites.

Including the effect of phonons in the harmonic approximation and comparing free energies for ammonia on a grid of PT points are shown in figure 3.12 where the $Pa\bar{3}$ phase has a limited stability region which decays with increased temperature. At higher temperatures NH_3 enters a plastic phase where the molecules are free to rotate about their heavy atom sites. This would imply that there are many local minima with energetics close to the ground state which can be accessed upon heating, of which $Pa\bar{3}$ may be one.

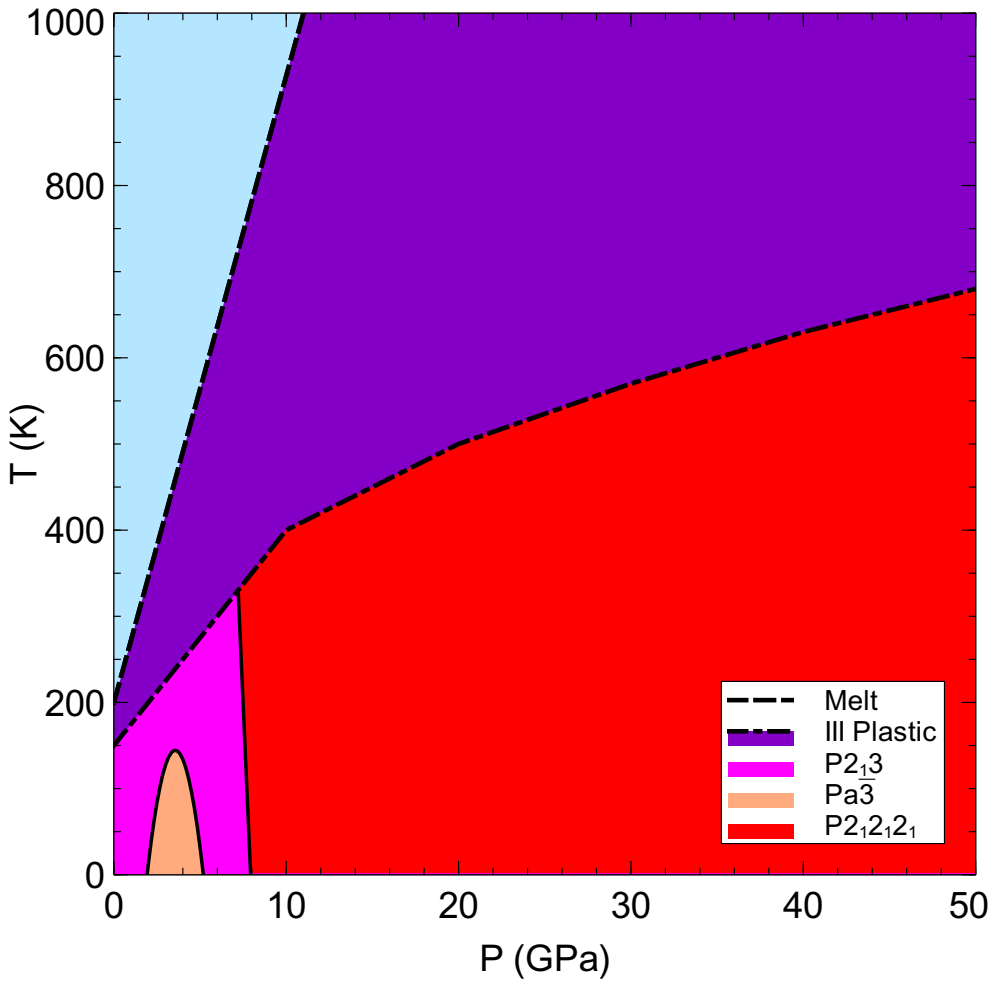

Figure 3.12 *Low pressure phase diagram for the NH_3 system up to 50 GPa with melting and plastic experimental phase boundaries taken from [26].*

Extending the ammonia phase diagram to 480 GPa not including the $Pa\bar{3}$ phase, the reentrant molecular phase of Pnma is suppressed by the decomposition into $\frac{2}{5}NH_4 + \frac{1}{5}N_3H_7$. The pressure phase evolution of ammonia goes from molecular to ionic to decomposition above 440 GPa at T= 0K. On heating, ammonia enters plastic (experimentally) and superionic (calculated and experimentally) regions as observed in pure H_2O.

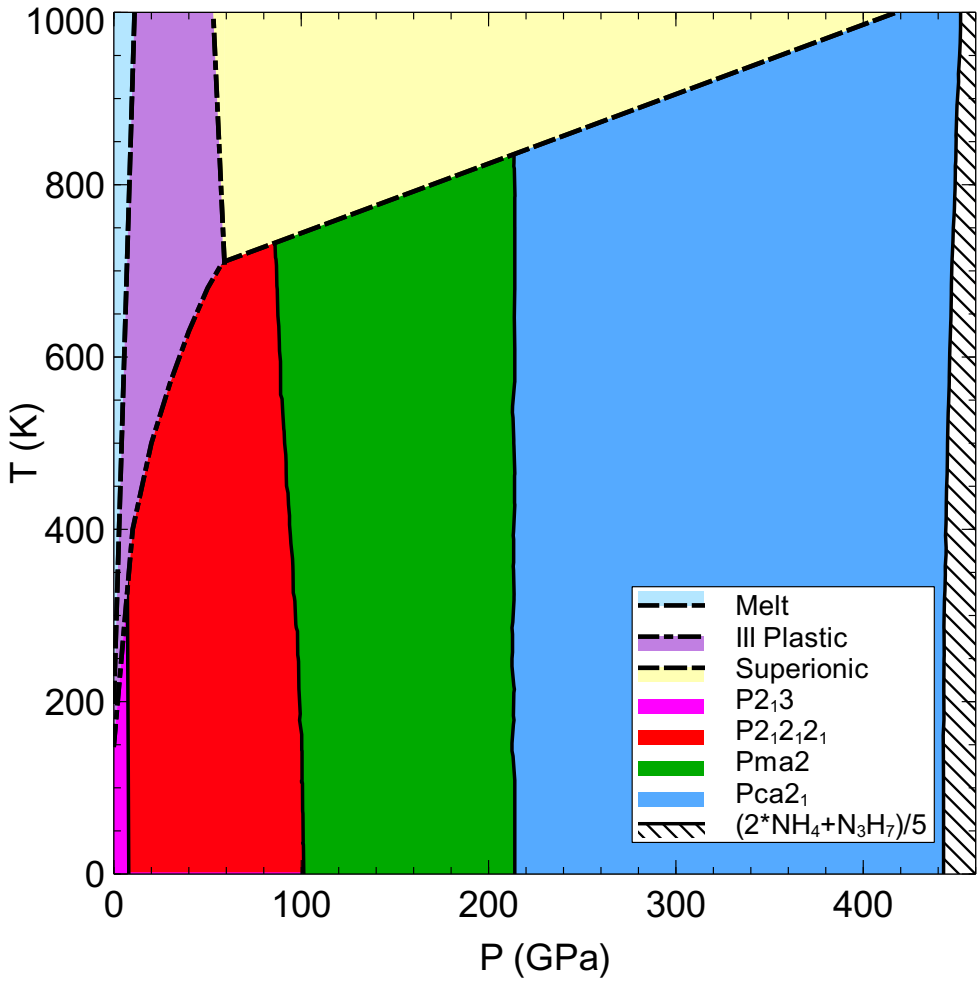

Figure 3.13 *Full phase diagram for the NH_3 system up to 460 GPa. Superionic, melting, and plastic phase boundaries were taken from [26].*

3.5 Simulated Vibrational Spectroscopy for Water and Ammonia

Raman and infra-red absorption techniques are able to detect phase transitions between phases of ice. In figure 3.14 we plot the simulated spectroscopic signature for different phases according to their stability within PBE (100 GPa was chosen for the ice VIII–X transition). At low pressures the high-frequency O–H vibron is decreasing in energy with pressure showing the covalent bond weakening as ice progresses towards proton symmetrization under compression. Once settling in ice-X the O–H stretch moves to increasingly higher frequencies with pressure signaling that the bond is strengthening.

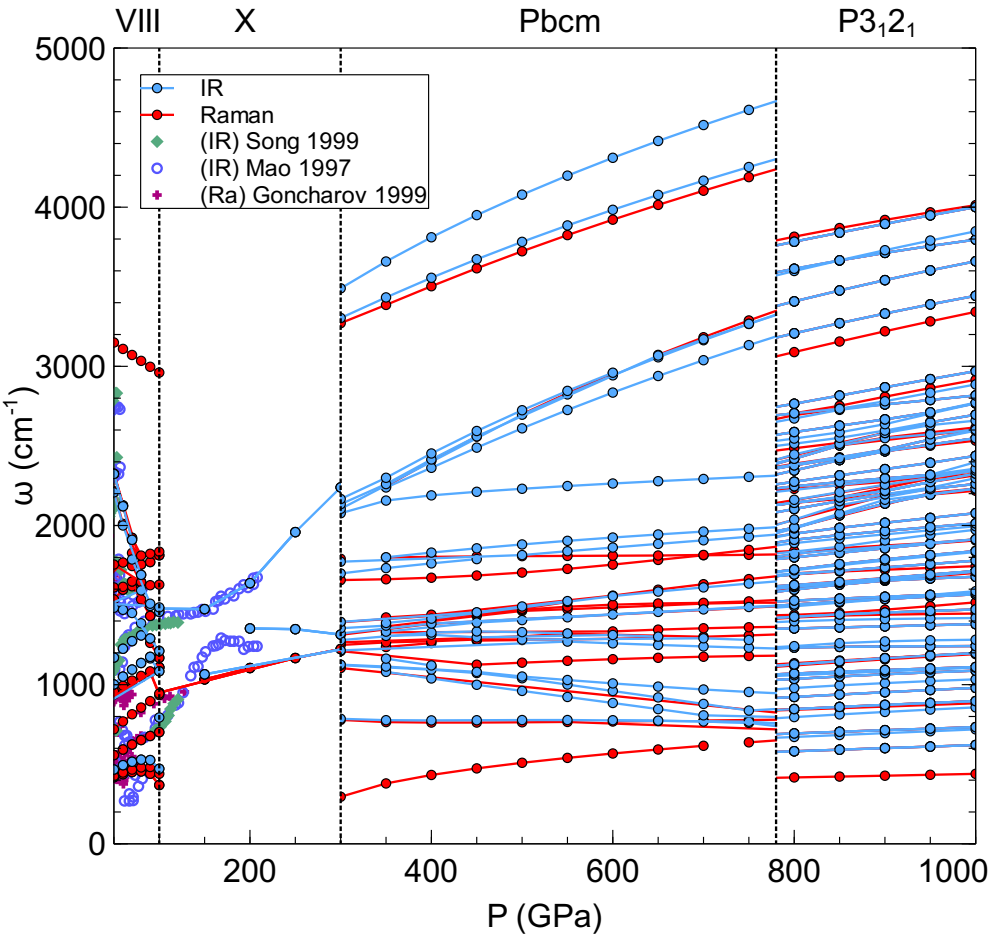

Figure 3.14 *Zone-centered phonons for high pressure H_2O ice phases as a function of pressure. Comparative data from the literature is also shown [221–223].*

For the low pressure phases, the spectroscopic signal as a sequence of pressure is shown in figure 3.15. These transitions occur at pressures roughly an order of magnitude greater than experiment though the number of modes will be correct and spectral lines could be extrapolated back to the experimental density. Though the O–H vibron weakens with pressure within each phase, at each transition the vibrons strengthen to a higher set of frequencies.

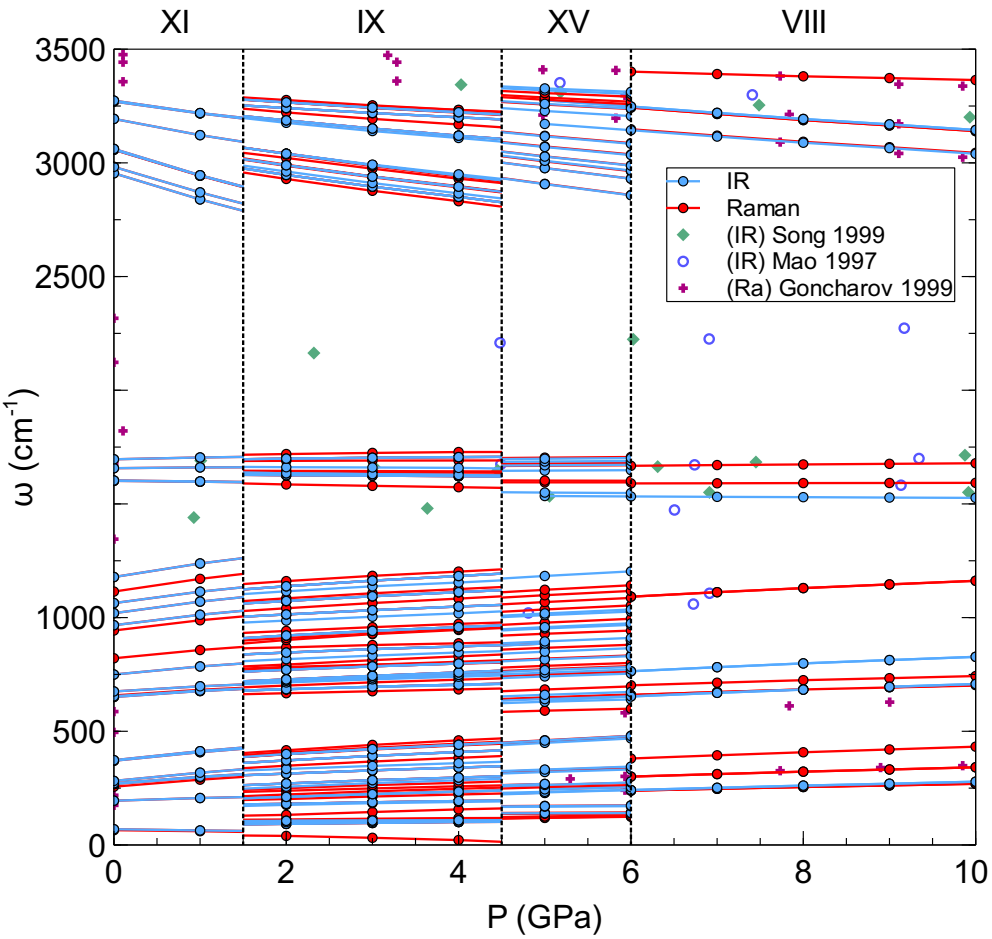

Figure 3.15 *Zone-centered phonons for low pressure H_2O ice phases as a function of pressure. Comparative data from the literature is also shown [221–223].*

In ammonia, the bonding changes are more varied. While at lower pressures (below 100 GPa) some N–H vibrons become stiffer, others become weaker. This is different from the water case where all protons are delocalizing in conjunction, whereas in ammonia only some of the protons are transferring (1/3) yet ionizing every NH_3 molecule. This can be seen in figure 3.16 for phase $P2_12_12_1$ where there are 12 vibrons counting both IR and Raman active modes. Of these modes 4 increase with pressure, another 4 increase less drastically, and the final 4 are decreasing with pressure consistent with the structure wanting to ionize into NH_4^+ and NH_2^- units.

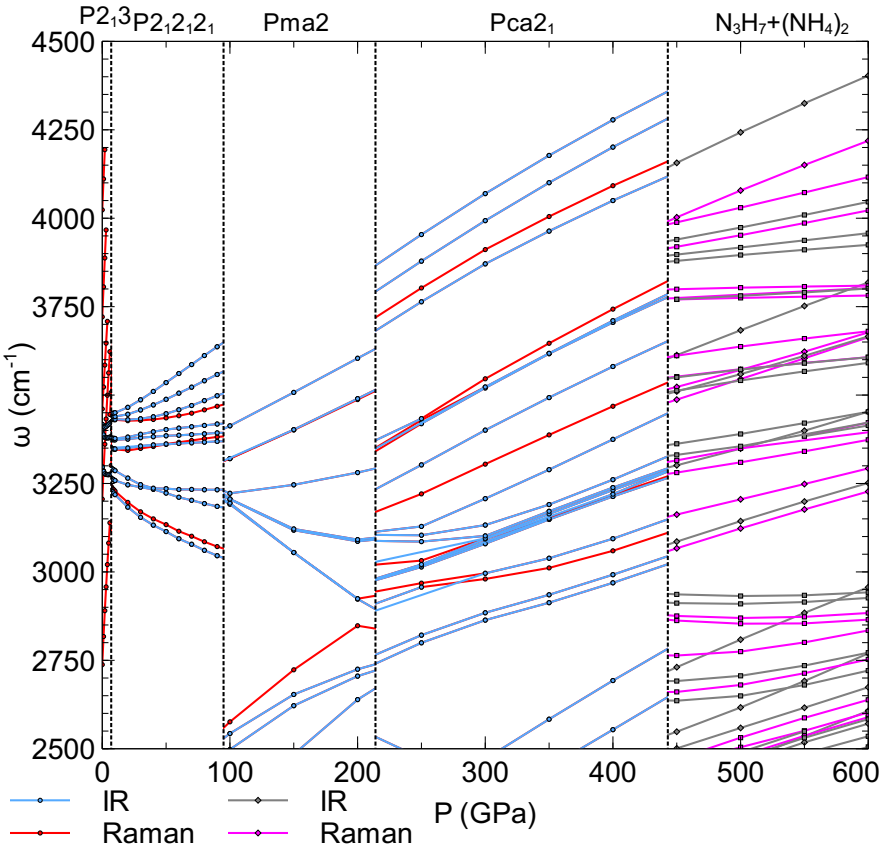

Figure 3.16 *High frequency zone-centered phonons for NH_3 ice phases found to be energetically stable at $T = 300$ K as a function of pressure.*

Above 440 GPa decomposition occurs and the spectroscopic signal for both NH_4 and N_3H_7 are included together in figure 3.16. Once ionized above 90 GPa the N–H vibrons increase in frequency with pressure and this continues above 440 GPa in the decomposed structures.

The spectroscopic signal for unstable phases from literature such as $P2_1/c$ (metastable around 7.5 GPa), formerly stable $P2_1/m$ (300–400 GPa before $Pca2_1$ was found), and the possibly stable $Pa\bar{3}$ phase were also calculated in figure 3.17. It may be possible to access these phases in experiment and so their spectroscopic signal is provided here.

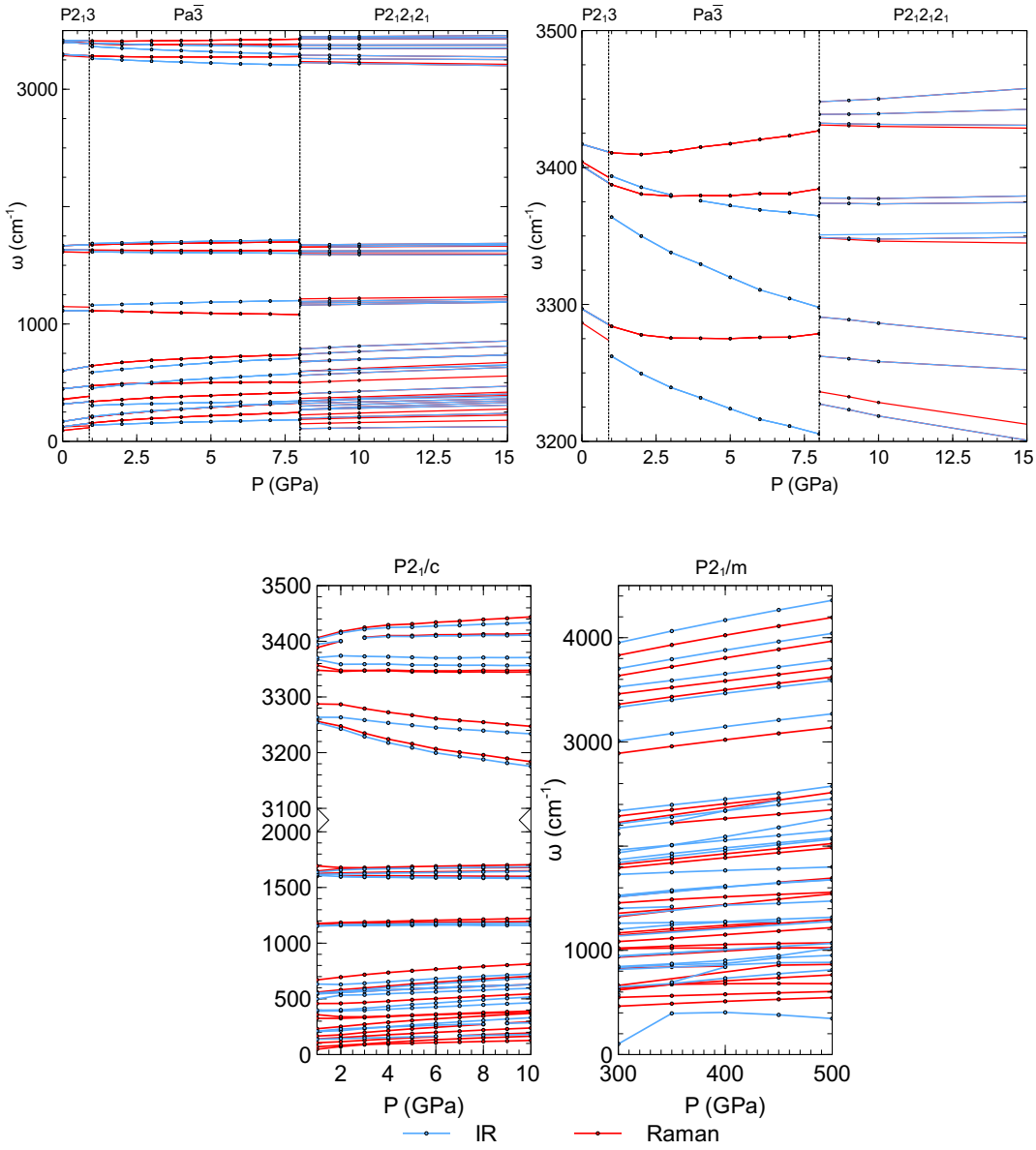

Figure 3.17 *Zone-centered phonons for low pressure NH_3 ice phases (top left), low pressure vibrons only (top right), and calculated unstable phases of $P2_1/c$ and $P2_1/m$ (below) over their relevant pressure range.*

With increasing pressure, the structures becoming more stable tend to have strengthening of their chemical bonds evident in the calculated spectroscopic

signals, which is particularly true for molecular systems unless they want to eventually dissociate their covalent bond such as in compressed hydrogen.

3.6 Ammonia and Water Mulliken Charges

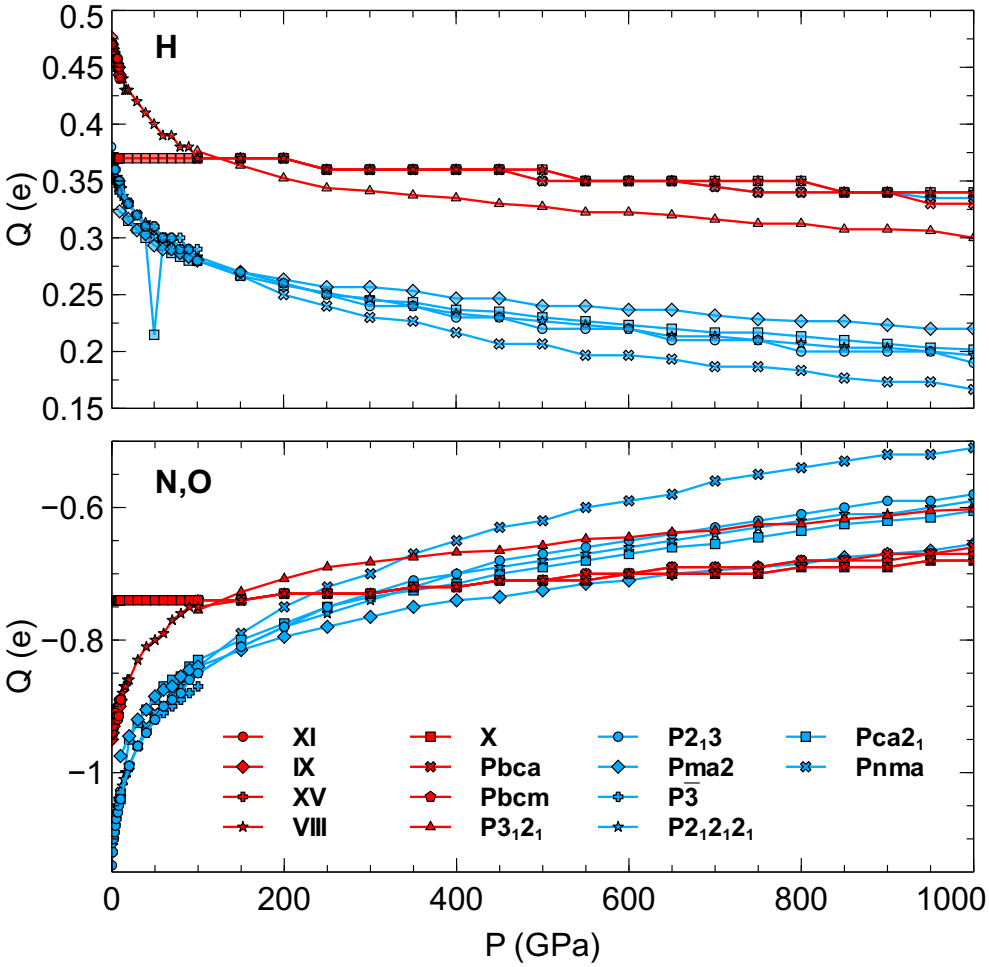

Figure 3.18 *Calculated Mulliken Charges for NH_3 (blue) and H_2O (red) systems as a function of pressure.*

We plot the Mulliken charges on the different O-H and N-H ions in figure 3.18. Individually there appears to be little information captured by this, suggesting the ice phases are all fairly similar but with different molecular or ionic packing. Ice X deviates from this at lower pressures as the symmetry maintains the proton symmetrization, while at higher pressures $P3_12_1$ further decreases the charge difference between O and H ions. No dipole moments for the crystal or molecules were calculated but are likely to vary between the different phases.

For ammonia and water, the polarization on H decreases with pressure while the N ions also become more neutral. Comparatively we can see the H ions in water ice are more polarized than in ammonia ice. This makes sense as water molecules have a stronger dipole moment than those of ammonia. This could mean ammonia plays the role of a malleable molecule that can be substituted into and dope water ice structures with little energy cost while still offering a negative N ion to accept hydrogen bonds. The less polar and less strong hydrogen bonding of ammonia can also mean that ammonia water networks can disorder with temperature more readily as these bonds are easier to escape or break.

3.7 Concluding Remarks

We have seen that high pressure changes the way crystals of both water and ammonia behave. Proton symmetrization in ice X and the molecular to ionic to molecular transition in ammonia are the most dramatic changes. Structure searching and electronic structure methods prove valuable for learning about the ices and have been combined with experimental studies to understand these individual phase diagrams. Heating this phases both allow for excitations into plastic and superionic phases before eventual melting. We will draw from this knowledge in the next chapters when investigating mixtures of both these ices together.

Chapter 4

Results for known hydrates

4.1 Introduction

All ices feature a ladder of interactions, ranging from covalent, ionic/electrostatic, hydrogen bonding (though not in methane) to weak dispersion interactions. It is the interplay of these interactions, and their relative emphasis as the molar volumes are reduced, that drive intriguing phase transitions, and the emergence of new structural features. Mixing different individual ices together allows for a new ladder of interactions to emerge, even unexpectedly so. As previously discussed ammonia has been predicted to form an ionic crystal $(NH_4)^+(NH_2)^-$ above 100 GPa [194] and confirmed in experiment [25, 26]. The energetic cost of breaking the N–H bond is outweighed by ionic bonding $NH_4^+ \cdots NH_2^-$ and more compact packing. Water leaves the molecular state via another route, forming the atomic ice-X network structure with symmetric hydrogen bonds at 60 GPa[224] while at terapascal pressures, it is predicted to take up more complex phases that can be seen as partially ionic OH^-/H_3O^+ [22, 23]. At low temperatures, nuclear quantum effects are expected to influence the phase diagram of hydrogen-bonded systems,[225] while at high temperatures, superionicity is predicted to occur in both water and ammonia. Structure prediction methods have proved a useful tool to explore the phase space of the individual ices under pressure. In this chapter, we will build from this knowledge by searching for stable phases of mixtures of ammonia and water. Here we start with the only three stoichiometric mixtures found stable in nature up to 10 GPa before searching for other mixing ratios which may be stabilized under high pressure.

The three stoichiometric mixtures that exist in nature close to ambient conditions are: ammonia monohydrate (AMH, NH_3:H_2O=1:1), ammonia dihydrate (ADH, 1:2) and ammonia hemihydrate (AHH, 2:1) [39]. Their phase diagrams are relatively complex: six AMH phases, four ADH phases, and two AHH phases are known at various $P-T$ conditions, even though some of their structures have not been resolved. AHH has arguably been studied the least among the ammonia hydrates, possibly because of its high ammonia content, far removed from the solar abundance ratio 1:7, and is therefore expected to be rare in nature. However, it is a crucial phase at high pressure and temperature, where both ADH and AMH decompose into AHH+ice-VII, around 3 GPa and at 280 K and 250 K, respectively [38, 44]. At slightly higher pressures (around 5–20 GPa) and room temperature, *all* ammonia hydrates are found to form disordered molecular alloy (DMA) phases, which feature substitutional disorder of ammonia and water (maybe partially ionized into OH^-/NH_4^+) on a body-centered cubic (bcc) lattice[44, 46, 48–50]. In fact, this phase was studied in AMH and shown to be partially molecular and ionized at the same time in by Liu et al [49]. The AHH-DMA phase has been observed in two independent experiments [48, 50] that found, at low temperatures, transitions from AHH phase II at 19–30 GPa. AHH-DMA was found to remain stable up to the highest pressure studied, 41 GPa [48].

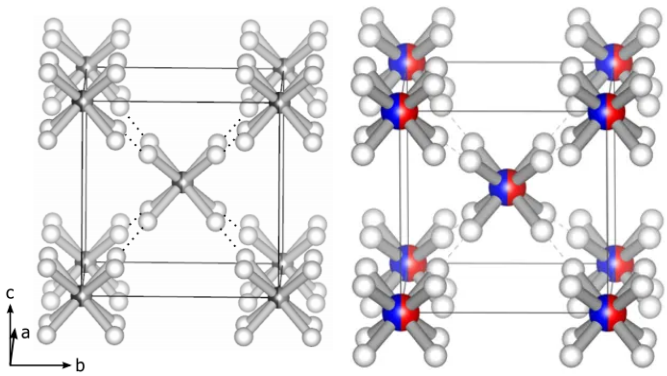

Figure 4.1 *(left) The DMA structure with a BCC ($Im\bar{3}m$) arrangement of substitutionally disordered oxygen or nitrogen atoms (black) and partially occupied proton sites (white) taken from Wilson et al [48] on AHH. (right) The DMA structure shown for AMH by Liu et al [49].*

Previous first-principles calculations have been carried out to resolve high-pressure molecular phases in the ammonia hydrates [226, 227]. In AMH, calculations predicted that an ionic phase transition should stabilize $NH_4^+ \cdot OH^-$ over $NH_3 \cdot H_2O$ around 6 GPa.[228] A more stable ionic structure was proposed

more recently [199] and subsequent crystal structure searches on AMH uncovered higher-pressure ionic phases, which were then used as starting points for ab initio molecular dynamics simulations to investigate the superionic regime of AMH.[229] These studies attempted to explore molecular mixtures at conditions present deep within icy planetary bodies using electronic structure calculations, but there is an inherent assumption that AMH is indeed a relevant stoichiometry at elevated pressures in the water-ammonia phase diagram. This assumption needs to be clarified by studies on other mixtures, first and foremost ADH and AHH, to ultimately construct a coherent picture of the inner structure of icy planets as dependent on the overall composition.

The following describes in detail structure searching and analysis in the ammonia-water system, starting with the known hydrates of 2:1 Ammonia Hemihydrate (AHH), 1:1 Ammonia Monohydrate (AMH), and 1:2 Ammonia Dihydrate (ADH).

4.2 Ammonia Hemihydrate

The three phases of AHH have all been identified from neutron diffraction studies, see figure 4.2, in part as they occur as decomposition products of AMH and ADH [38, 45, 48, 230]. However, their respective regions of stability are less well established than for the other hydrates, and there are indications for high-pressure phase transitions beyond 30–40 GPa that have yet to be identified [50]. Later in this computational study, we suggest that AHH undergoes a transition at 40 GPa and room temperature to an ionic structure with fully deprotonated water molecules, $(NH_4^+)_2O^{2-}$, which in a sequence of phase transitions remain stable up to at least 500 GPa, before eventual decomposition [1].

Here, we present results from crystal structure predictions in conjunction with electronic structure calculations of compressed ammonia hemihydrate, AHH. Above 65 GPa, beyond the stability regime of the DMA phase, we find a sequence of new high-pressure phases that ensure AHH remains a stable (and indeed dominant) composition within the water-ammonia phase diagram to very high pressures. The structures uncovered here are fully ionic and combine atomic O^{2-} anions and molecular NH_4^+ cations. Oxides are a major thermodynamic sink and found in virtually all fields of chemistry and materials science, but these ammonium oxide structures represent to our knowledge the first example where water in a hydrate compound becomes completely deprotonated by application of

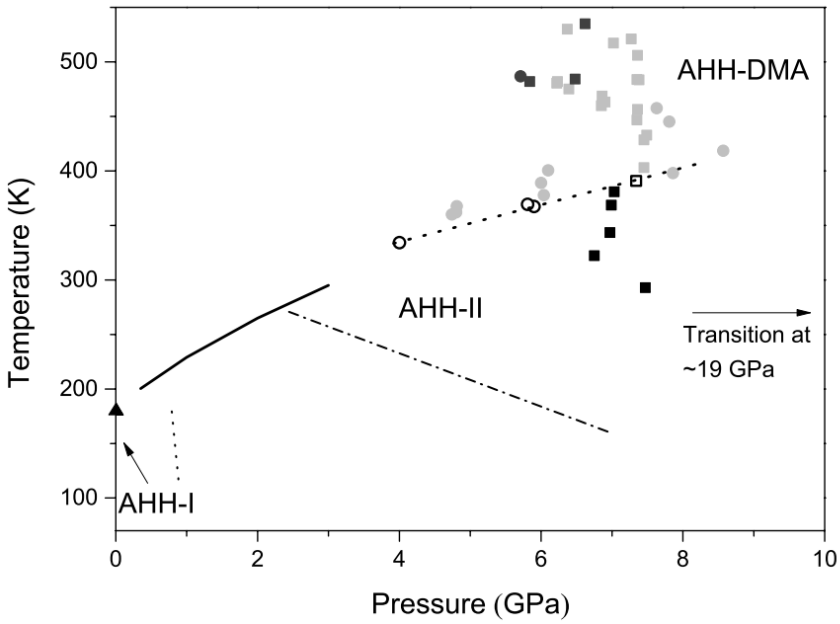

Figure 4.2 *The proposed phase diagram of ammonia hemihydrate (AHH) taken from Wilson et al [48]. Here the dash-dotted line refers to the region where water-rich (AMH and ADH for example) samples would dehydrate and form AHH-II and ice VII or VIII. The triangle symbol is the observed freezing point into AHH-I and the solid line is the melting line. The open symbols are points where both AHH-II and AHH-DMA were observed. Grey and black circles and squares refer to different heating runs detailed by Wilson et al [48]. The arrow on the right refers to a phase transition around 19 GPa from AHH-II to AHH-DMA.*

pressure. A sequence of such structures remains stable up to 550 GPa and elevated temperatures, where decomposition into the constituents water and ammonia is predicted to occur.

Two structures of AHH have been solved, phases I and II. In experiments at $T = 200$ K, the transition I→II is estimated to occur around 1 GPa [48]. In our ground state calculations, this transition occurs at 4 GPa, slightly above the experimental estimate, but in line with the negative Clapeyron slope seen in experiment. In Figure 4.6 we show the evolution of the relative ground state enthalpies,

$$\Delta H_f = H_f(\mathrm{AHH}) - [H_f(\mathrm{H_2O}) + 2H_f(\mathrm{NH_3})] \tag{4.1}$$

as a function of pressure on two different scales (0-100 and 50-800 GPa), for the known and new phases. This represents the different phases' enthalpic stability towards decomposition into the molecular constituents of H_2O and NH_3, where at each pressure we have chosen the most stable H_2O and NH_3 phases.

AHH-I is proton-disordered on one ammonia site. We used an ordered approximate of the unit cell with space group $P2_1/c$ in our calculations. Within the AHH-I unit cell, there are five distinct structures to choose the proton ordering. As Figure 4.3 shows, the relative enthalpy difference between these five structures is very small. AHH-II is proton-ordered with space group $P2_1/c$.

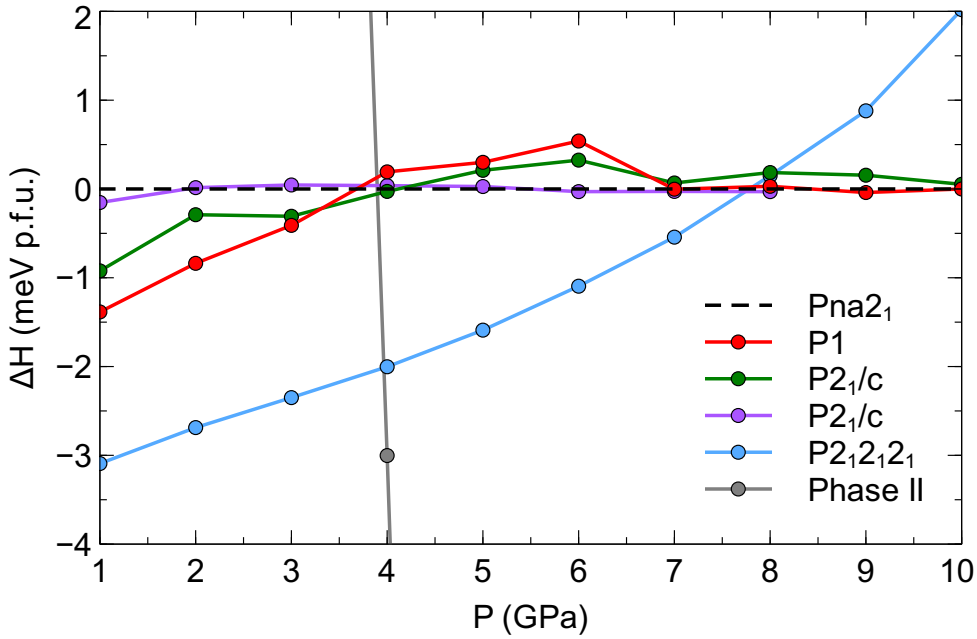

Figure 4.3 *Calculated enthalpies for 5 unique variations of AHH-I.*

Z **P (GPa)**	**4** **N**	**5** **N**	**6** **N**	**Space group**
30	1590	510	750	P1
50	2910	840	1650	P1
80	3360	2130	1890	Cmca
100	2790	1470	2370	$P\bar{3}m1$
200	4200	960	1260	P1
300	2670	1260	1320	$P\bar{3}m1$
400	3930	1830	1470	P1
600	3180	1230	1890	$P2_1$
800	3570	1950	1500	P1
1000	1470	1050	990	P1
2000	1290	690	120	Ccme
3000	1710	390	600	Pnma
4000	1200	630	630	P1
5000	1440	780	630	$P2_12_12_1$

Table 4.1 *Summary for AHH structure searches.*

In table 4.1 we show the results of structure searching at pressures ranging from 30 GPa to 5,000 GPa. The number of different structures relaxed for different numbers of formula unit of AHH is also shown, and the spacegroup of the most stable structure found by the search. There are many structures that would appear higher in ranking the lowest energy structure and may end reach stability at the same or other pressures after a tighter relaxation.

In figure 4.4 the volume is plotted against the enthalpy for all structures relaxed (over 5000) at 300 GPa. This appears to have a candle formation originating from the most stable structure and volume where the structures end up densely clustered. Other low energy structures with much lower or greater volumes may become relevant at higher pressures or lower pressures respectively. The best structures from each of the structure searches were relaxed through the entire pressure range and compared with the ground state enthalpy of the pure ices. This eventually resulted in the ground state phase diagram for AHH shown in figure 4.6. In figure 4.5 the convex hull also at 300 GPa is shown for the ammonia water system, where we see AHH is the most relevant and so was chosen as an ideal starting point for analyzing high pressure ice mixtures.

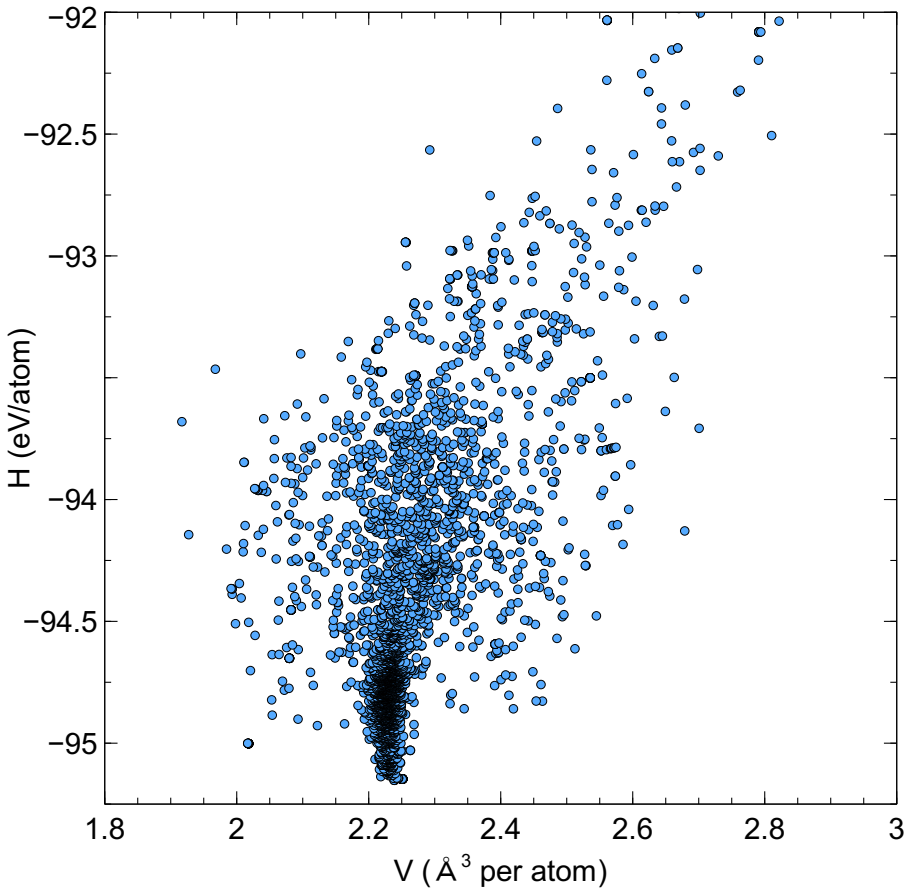

Figure 4.4 *Enthalpy Volume plot for a structure search with AHH at 300 GPa, note that the gradient of enthalpy with volume gives pressure.*

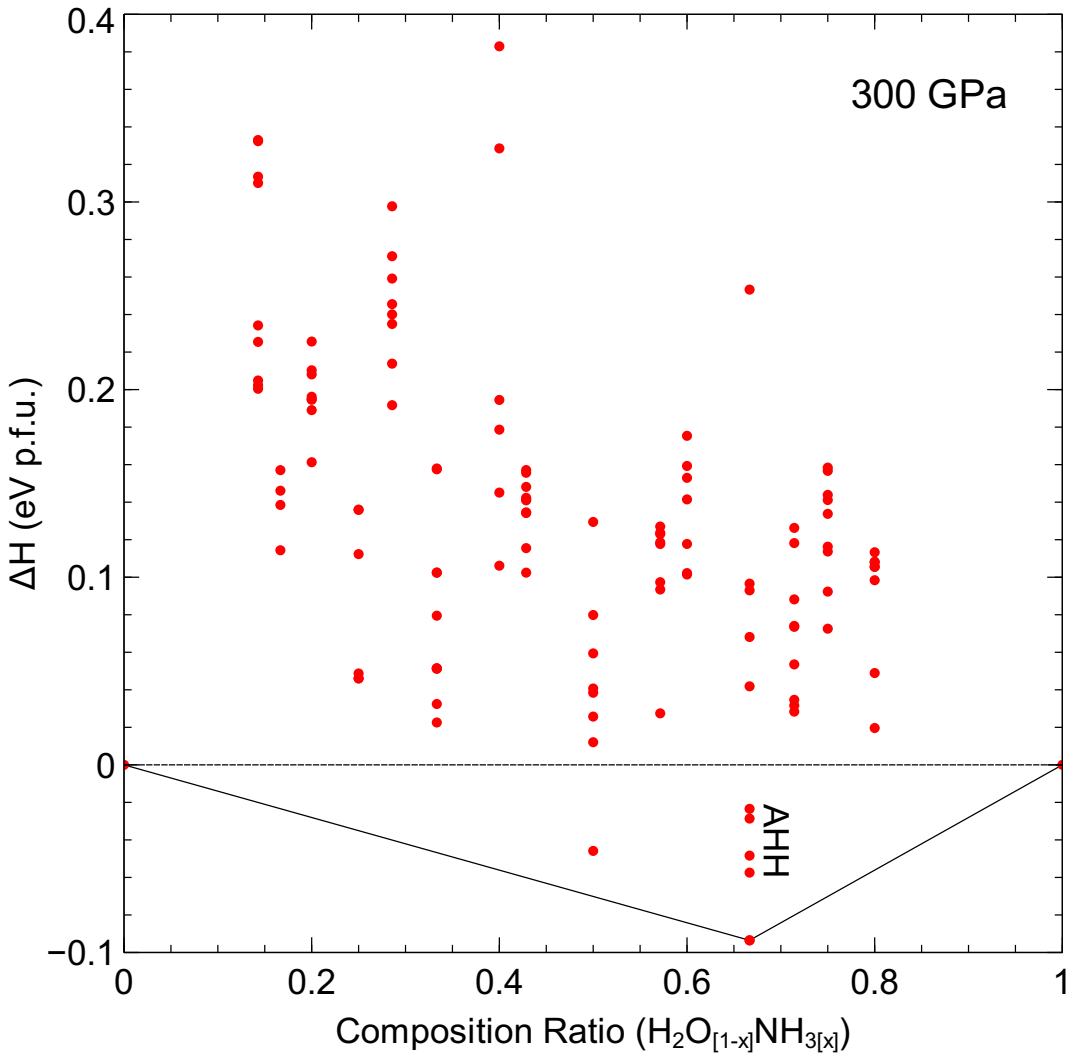

Figure 4.5 *Convex hull data for mixing ratios from 6:1 to 1:5 for the binary (H_2O:NH_3) system. The lowest enthalpy structures from structure searching with CALYPSO are plotted. Up to 4000 structures were optimized at a given mixing ratio. The ice phases forming the convex hull are taken to be Pbca for H_2O and $Pca2_1$ for NH_3.*

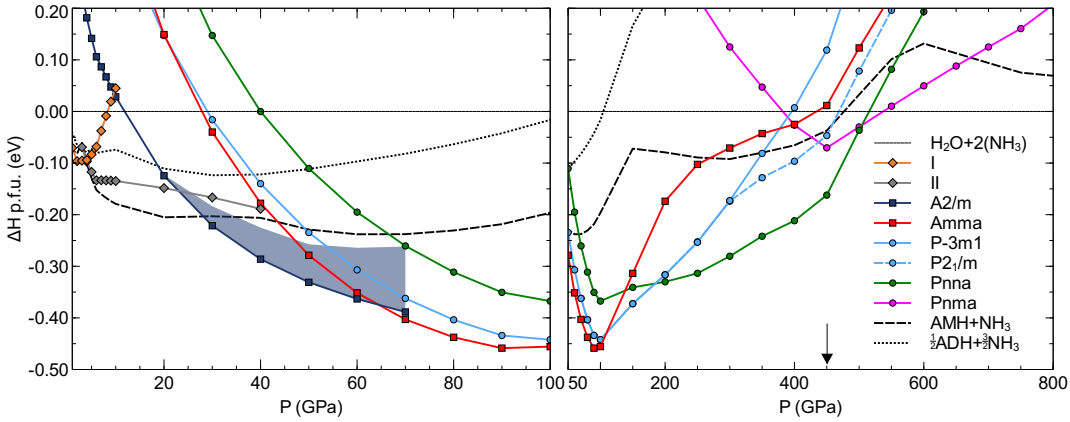

Figure 4.6 *Enthalpies of formation of AHH phases as a function of pressure, relative to decomposition into ice and ammonia (or $\frac{2}{5}$ NH_4 + 1/5 N_3H_7 above 450 GPa, see arrow), shown in the range 0-100 GPa (left) and 50-800 GPa (right). The shaded region in the left panel denotes an approximate enthalpy range of quasi-BCC structures, with a lower bound by the most stable approximant we found (see text). Dashed and dotted lines indicate decomposition reactions into other ammonia hydrates.*

We show in Figure 4.6 also the relative enthalpies of potential decomposition products of AHH, namely $H_f(\mathrm{AMH} + \mathrm{NH_3})$ and $1/2H_f(\mathrm{ADH} + 3\mathrm{NH_3})$, of which AMH and ADH will be discussed in the next sections. A decomposition of AHH into ADH and ammonia is never favorable; in fact, just below 100 GPa, we find ADH itself to become unstable towards decomposition into water and ammonia ice. For AMH, we find that at low pressures a proposed tetragonal ionic $\mathrm{NH_4^+}\cdot\mathrm{OH^-}$ phase [199] is, up to 28 GPa, more stable than AHH. This phase has not yet been seen in experiments on compressed AMH.

Amongst AHH phases, above 23 GPa in our calculations, AHH-II is followed by several quasi-bcc phases, which are indicated by the shaded region in Figure 4.6 and which are energetically competitive up to 65 GPa. As a phase transition to a substitutionally disordered bcc structure has been observed at 19 GPa in room-temperature experiments, we would expect to find many competing quasi-bcc structures in this pressure region. All relevant structures we find in this region are half-ionized, i.e. of the composition $\mathrm{NH_3}\cdot\mathrm{NH_4^+}\cdot\mathrm{OH^-}$, and feature hydrogen bonds.

These structures are not immediately obvious to be quasi-bcc – see appendix 1 for full structural details – but occupy a pressure range where experiment has observed the bcc DMA structure. Upon closer inspection, the underlying quasi-bcc structure becomes apparent, both in real and reciprocal space: representative

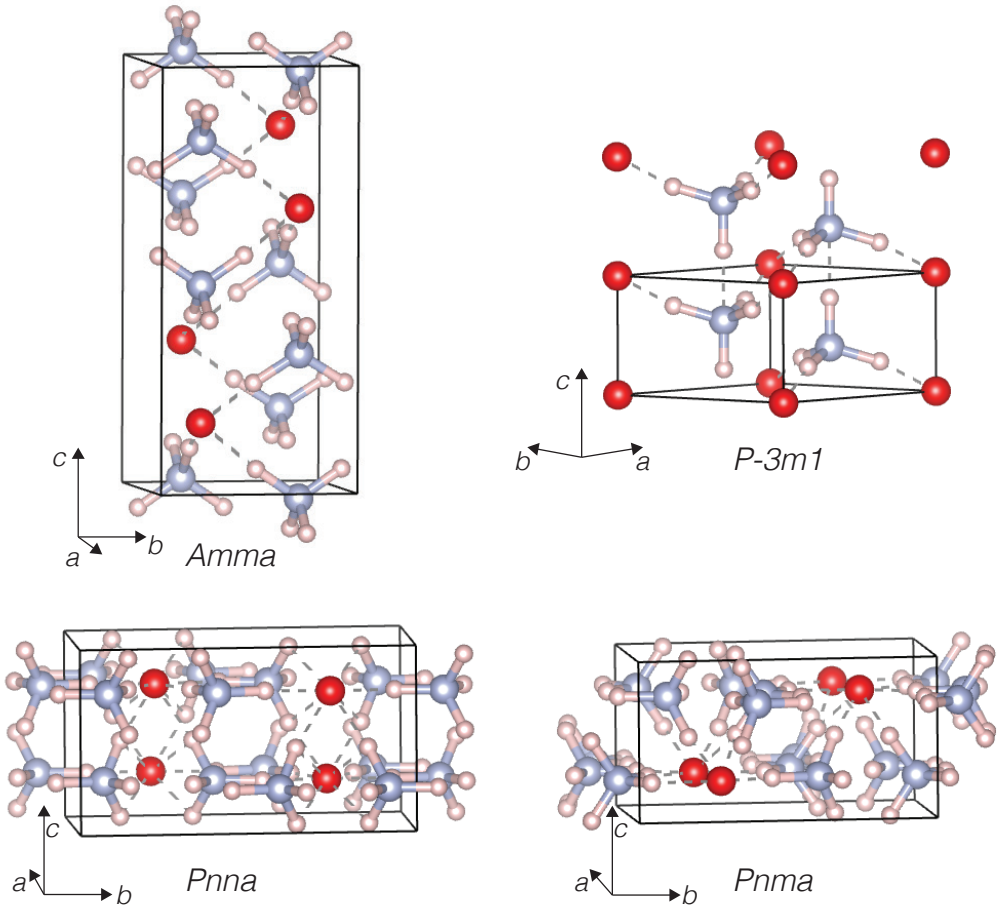

Figure 4.7 *Fully deprotonated ammonia hemihydrate structures. From top left: Amma phase at 80 GPa; $P\bar{3}m1$ phase at 100 GPa; Pnna phase at 300 GPa; and Pnma phase at 600 GPa. Red (blue, white) spheres denote O (N, H) atoms. All phases are drawn to the same scale, and hydrogen bonds from NH_4^+ to O are shown as dashed lines.*

structures feature locally quasi-cubic molecular arrangements, and their simulated powder x-ray diffraction peaks cluster around the peaks of an ideal bcc lattice seen in figure 4.8. This suggests that the structure search algorithms attempt to construct disordered phases in the pressure range around 20–60 GPa. Similar results were also seen at low pressures, where AHH-I is stable: searching the configuration space with too small unit cells to reproduce the actual phase I structure, which has 12 molecules in the unit cell, resulted in candidate structures that mimicked the molecular herringbone arrangements of AHH-I. In the gas phase with well-separated entities, the proton transfer process $NH_3{+}H_2O{\rightarrow}NH_4^+{+}OH^-$ is endothermic by about 8 eV; it is enabled here by ionic bonding and a more compact packing of the constituents ($\Delta V/V = -3.3\%$ for AHH-II$\rightarrow$ $C2/m$ at 20 GPa). It is possible that these structures could be the basis

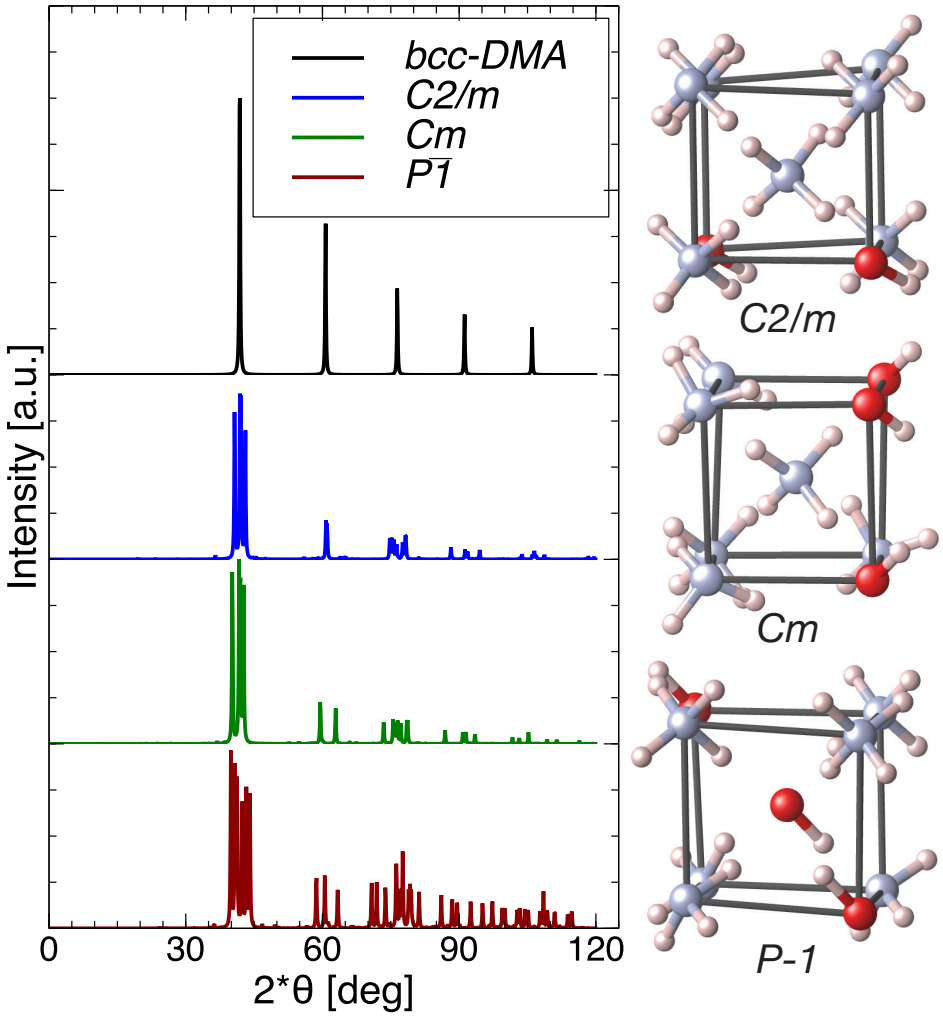

Figure 4.8 *XRD patterns of representative quasi-BCC phases found in our structure searches, all simulated with λ=1.54056Å at 40 GPa, and labeled by space group. Right-hand side shows some of the near-cubic local arrangements of each structure (black lines are to guide the eye and not unit cells). Red (blue, white) spheres denote O (N, H) atoms. The "bcc-DMA" pattern is for an idealized disordered bcc lattice with 2:1 N:O site occupancy and a=3.05Å.*

of an ordered low-temperature form of the DMA phase for AHH. Experimentally no further phase transitions have been observed in AHH up to 40 GPa.

At 63 GPa, we find in our calculations a new orthorhombic structure of *Amma* symmetry that is energetically most stable, with the intriguing attribute of doubly deprotonated water: all H_2O have donated both protons to two NH_3 molecules, which results in a fully ionic ammonium oxide compound $(NH_4^+)_2{\cdot}O^{2-}$. At 110, 180, and 505 GPa in the ground state we find three more phase transitions, first

to a trigonal $P\bar{3}m1$ structure, followed by two orthorhombic phases of *Pnna* and *Pnma* symmetry, and all with the same features of fully deprotonated water and molecular ammonium cations. These structures are shown in Figure 4.7, and details of their crystal structures are tabulated in appendix 1. The emergence of this sequence of ionic structures is responsible for the extended stability of AHH against decomposition into ice and ammonia to much larger pressures, see Figure 4.6. Eventually, at 540 GPa in the ground state, we find that AHH decomposes into ice and ammonia. For this decomposition, we took into account recent computational work that found NH_3 to decompose into N_3H_7 and NH_4, which we find above 450 GPa (see arrow in right panel of Figure 4.6 [195]). Note that water ice is not expected to decompose until multi-TPa pressures are reached [24, 231].

It has been suggested that the PBE functional overstabilizes charge transfer in the $NH_3{+}H_2O{\rightarrow}NH_4^+{+}OH^-$ reaction [227]. We therefore re-optimized all structures using the PBE+TS functional, which includes dispersion corrections [89], and found little quantitative difference of the relevant structural evolution: the transition from half- to fully ionic phases (the onset of stability of the *Amma* phase) is found at 58 GPa, while decomposition of the *Pnma* phase into the individual ices is calculated to occur at 458 GPa.

To estimate the effects of finite temperature, we calculated free energies for all phases using the harmonic approximation, which takes into account the vibrational entropy. The latter might well influence the phases' stability range, as we find quite a diverse chemistry in the progression from hydrogen-bonded molecular to fully ionic phases. Figure 4.9 shows the resulting phase diagram. This implies an earlier onset of stability for the fully ionic phases, with the *Amma* phase becoming stable at 40–50 GPa at low temperatures, but also eventual decomposition at lower pressures than in the ground state, as low as 470 GPa depending on temperature. The temperature dependence of the stability of most phases, apart from the eventual decomposition, is actually relatively weak, and changes compared to the ground state results shown in Figure 4.6 are mostly due to zero point energy (ZPE) effects (see figure 4.10 for a plot of H+ZPE as a function of pressure). This can be rationalized with the qualitative change in proton coordination at the ionization transition and its influence on the molecular vibron modes that will dominate the ZPE. We find that the stability region of the $P\bar{3}m1$ phase is much increased, at the expense of the orthorhombic *Pnna* and *Pnma* phases. In fact, two monoclinic phases of $P2_1/m$ and $P2_1/c$ symmetry

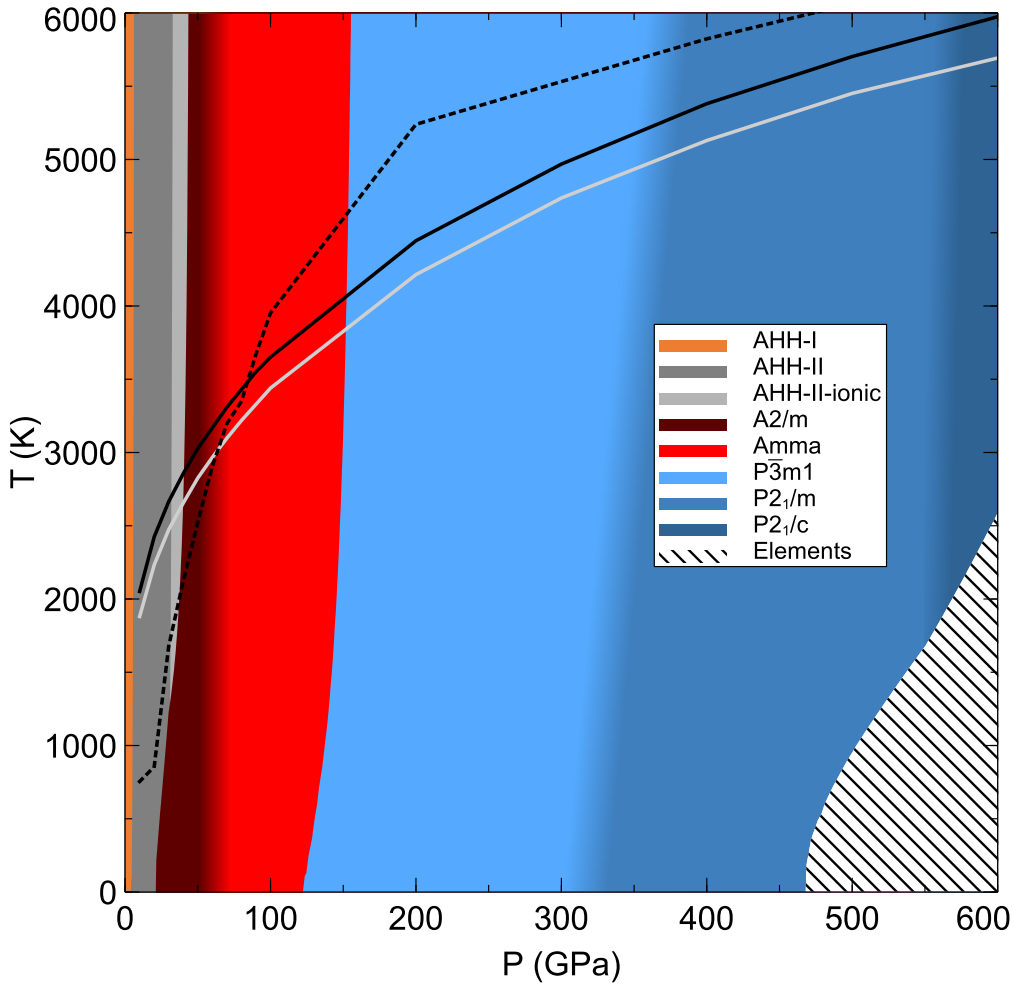

Figure 4.9 *P-T phase diagram of AHH phases, computed within the quasi-harmonic approximation. The dashed region labeled "elements" at highest pressures represents predicted decomposition into the constituent ices of NH and OH. The dashed black line indicates the computed melting line of AMH [229], while solid black (grey) lines indicate calculated planetary isentropes of Uranus (Neptune) [232].*

(see figure 4.11), which are the results of soft phonon modes in $P\bar{3}m1$ at very high pressures (see appendix 1 for structural information), become stable around 300–350 GPa and 550 GPa, respectively, and dominate the high-pressure regime of the P-T phase diagram. For perspective, we show in Figure 4.9 the mantle isentropes of Uranus and Neptune, as well as the melting line of AMH obtained from MD simulations.[229] Both the melting and onset of superionicity (which we suspect to occur significantly below the melting line) are not considered in our quasi-harmonic approach here.

We show in Figure 4.10 the enthalpies $H = U + PV$ plus contributions from vibrational zero point energies (ZPE). Note at high pressures the extended stability region of the $P\bar{3}m1$ phase and its symmetry-reduced variant $P2_1/m$, while the orthorhombic phases *Pnna* and *Pnma* are less relevant than in the ground state.

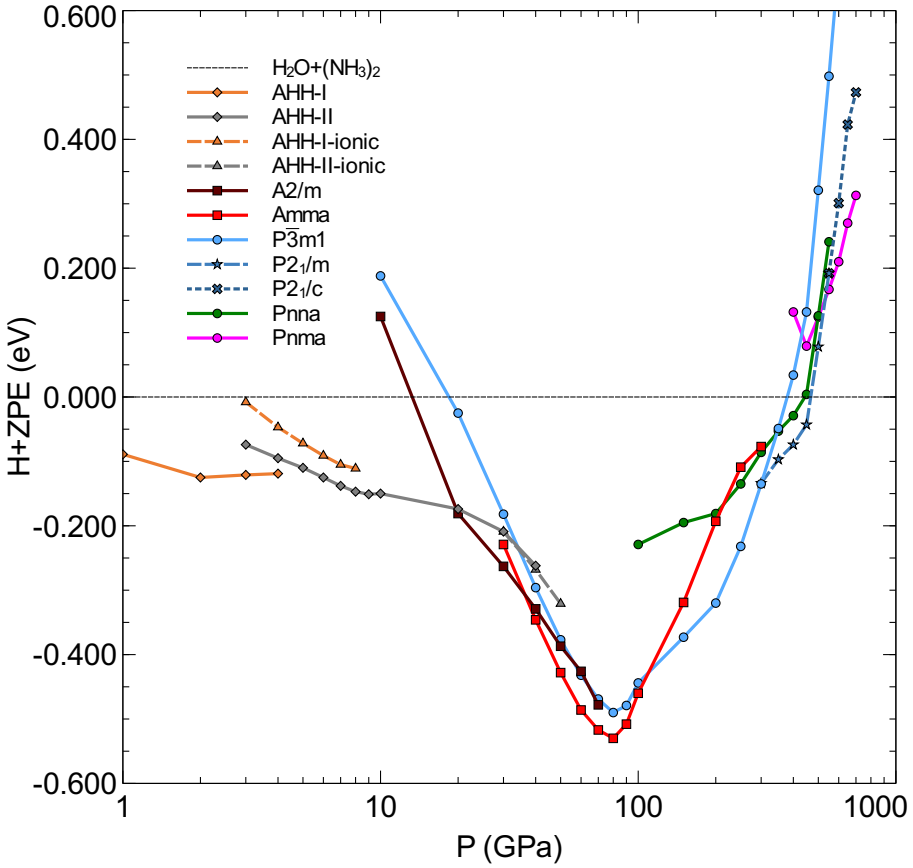

Figure 4.10 *Phase diagram for ammonia hemihydrate based on H+ZPE calculations, and plotted on a logarithmic pressure scale.*

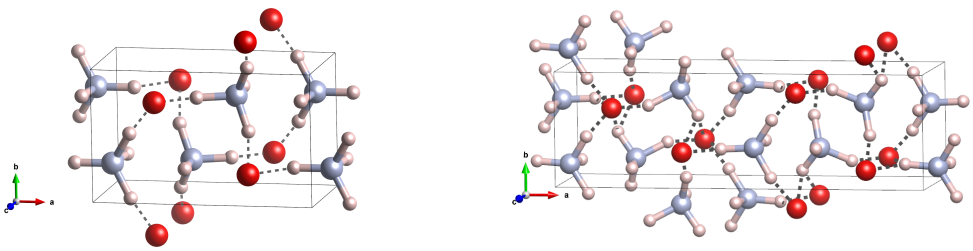

Figure 4.11 *(left) Monoclinic Phase $P2_1/m$ at 400 GPa. (right) Monoclinic Phase $P2_1/c$ at 650 GPa. $P2_1/m$ is monoclinic distortion of the highly symmetric $P\bar{3}m1$ structure, whereas $P2_1/c$ is a symmetry-broken variant of the $P2_1/m$ structure.*

The de-protonation reaction of OH^- in the gas phase, NH_3+OH^- →NH_4^++O^{2-}, is endothermic by about 16 eV, and is shown in further detail in chapter 5. This is twice the energy needed to remove the first proton off the water, yet comes as a natural follow-up to the partial deprotonation of H_2O. The process requires (i) more pV work being exerted on the system, and (ii) a proton acceptor molecule, NH_3. Highly compressed AHH provides both and, as a consequence, forms fully ionic compounds at high pressure. These are further stabilized by more compact packing, facilitated by the presence of spherical O^{2-} anions. Some of the ionic phases resemble known structure types. The $P\bar{3}m1$ structure, for instance, is (if we assume spherical NH_4^+) the CdI_2 structure type, a well-known AB_2 ionic structure [233]. The assignments of molecules in these high-pressure phases are supported by their structural properties: the *longest* nearest-neighbour N-H separations decrease from 1.10 Å in *Amma* at 60 GPa to 0.99 Å in *Pnma* at 600 GPa, while the *shortest* nearest-neighbour O$\cdots$H separations decrease from 1.35 Å to 1.17 Å for the same structures and pressures. The O-H separations at 60 GPa, for instance, are well above the separations seen in molecular water in ice-VIII at the same pressure (1.03 Å). A topological Bader charge analysis [234] also supports the ionic picture suggested above: the partial charges on O/NH_4 are -1.27/+0.64e at 100 GPa in *Amma*, and are almost constant across the entire pressure range: -1.28/+0.64e in $P\bar{3}m1$ at 100 GPa, -1.30/+0.65e in *Pnna* at 300 GPa, and -1.26/+0.63e in *Pnma* at 600 GPa.

In the inset of Figure 4.12 we show an electron localization function (ELF) isosurface and 2D cut for the $P\bar{3}m1$ phase, which confirm the presence of covalent bonds along the N-H separations, and the lack thereof around the oxygen anion – for the latter, ELF reveals its closed-shell character, but there are no local ELF maxima between the O^{2-} and NH_4^+ entities. Around the transition from the quasi-bcc phases, at 60 GPa, the *Amma* phase is more compact by 1.4 % than the lowest-energy quasi-bcc phase. Further transitions lead to ever more compact arrangements: $\Delta V/V = -0.7/-0.5\%$ at 120/300 GPa, the respective onsets of stability of the $P\bar{3}m1$ and $P2_1/m$ phases at room temperature. This is in part facilitated by higher coordination of the O^{2-} anion: because of its spherical character, in absence of covalent bonds or localized lone pairs, it is a much more flexible hydrogen-bond acceptor than H_2O, which prefers low-density tetrahedral coordination up to very high pressures [23]. In *Amma* and $P\bar{3}m1$, the oxygen anion is six-fold coordinated to N-H bonds, which increases to eight-fold coordination in *Pnna*.

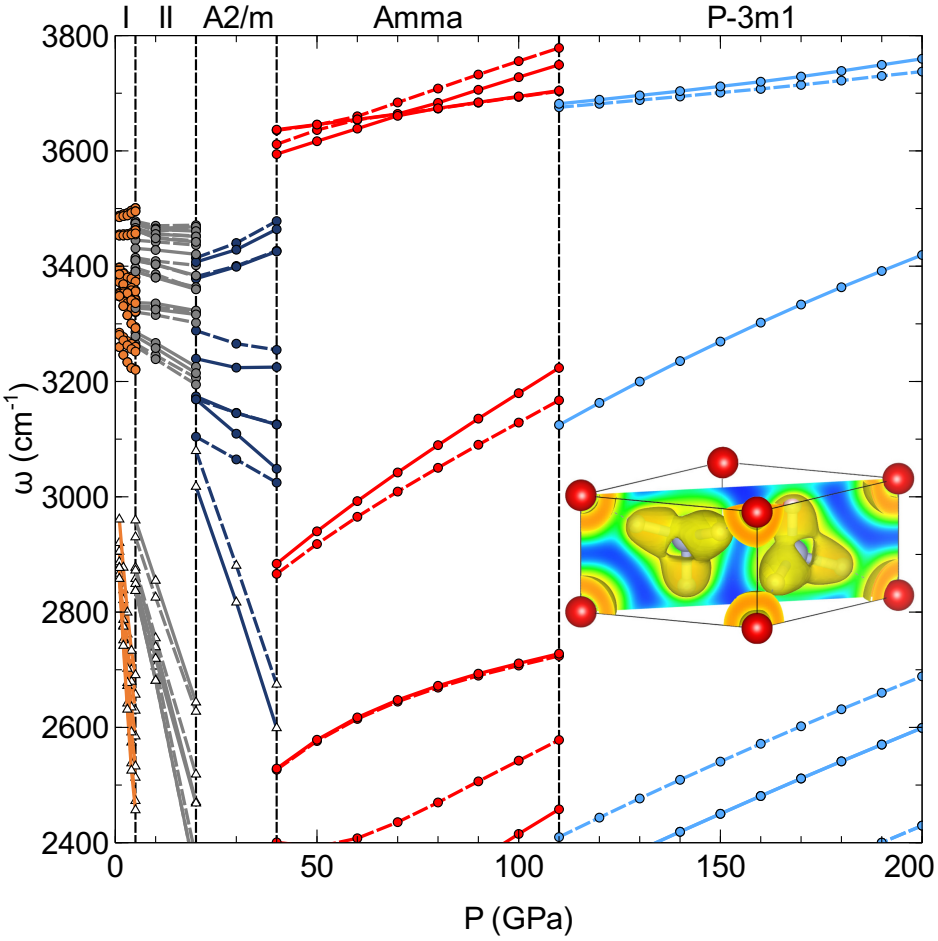

Figure 4.12 *Zone-centered vibrational frequencies of AHH phases in their respective room-temperature range of stability, focusing on the molecular vibron region of 2400-3800 cm^{-1}. Phases are indicated along the top and are colored as in Figure 4.6. Solid (dashed) lines represent Raman (IR) active modes. Open triangles refer to OH stretch modes (seen until 40 GPa), and filled circles refer to NH stretches. Inset shows electron localisation function (ELF) plot for the $P\bar{3}m1$ phase at 300 GPa. The isosurface value is 0.75, and 2D cut colors range from blue (ELF=0) to red (ELF=1).*

The complete absence of O-H stretch modes in the ionic high-pressure AHH phases should aid their spectroscopic detection. In Figure 4.12, we show the pressure evolution of the intramolecular N-H stretch modes up to 200 GPa, calculated within the harmonic approximation. Across phases I, II, and the half-ionized quasi-bcc phases, the N-H vibron bands occupy a range that broadens from 3300-3500 cm^{-1} at 1 atm to 3000-3500 cm^{-1} at 40 GPa. These frequency ranges are in reasonable agreement with experimental data, but shifted by about 100 cm^{-1}, likely due to anharmonic effects [50, 235]. A significant change should be noticeable at the transition from quasi-bcc to completely ionized phases: there

are no vibrational modes in the previously mentioned frequency range, instead N-H stretch modes in the *Amma* phase occur at much higher frequencies, around 3600 cm^{-1} in our calculations, and increase strongly with pressure. These modes involve stretches along N-H$\cdots NH_4^+$ hydrogen bonds. Another set of modes increases very strongly from 2700 cm^{-1} at 40 GPa to 3200 cm^{-1} at 110 GPa, and involves stretches along N-H$\cdots O^{2-}$ hydrogen bonds. At the transition to $P\bar{3}m1$ at 110 GPa, with a much simpler mode structure, both sets of vibrational frequencies decrease, by about 20-80 cm^{-1}, but continue to rise significantly with further increased pressure. The continuous hardening of the molecular vibrons is an indication that the intramolecular bonds in the NH_4^+ units strengthen under compression; neither phase shows signs of impending transitions to a network structure, for instance with symmetric N-H-O or N-H-N bonds.

Electronically, all high-pressure phases, due to charge and/or proton transfer, are wide-gap insulators. In figure 4.13 we show the evolution of the electronic band gap as a function of pressure for the most relevant phases. At low pressures, up to about 100 GPa in some structures, the band gaps increase with pressure; an effect previously noted in molecular crystals with polar units, where compression creates competing effects of widening electronic bands and shifts of intramolecular orbital states [236, 237].

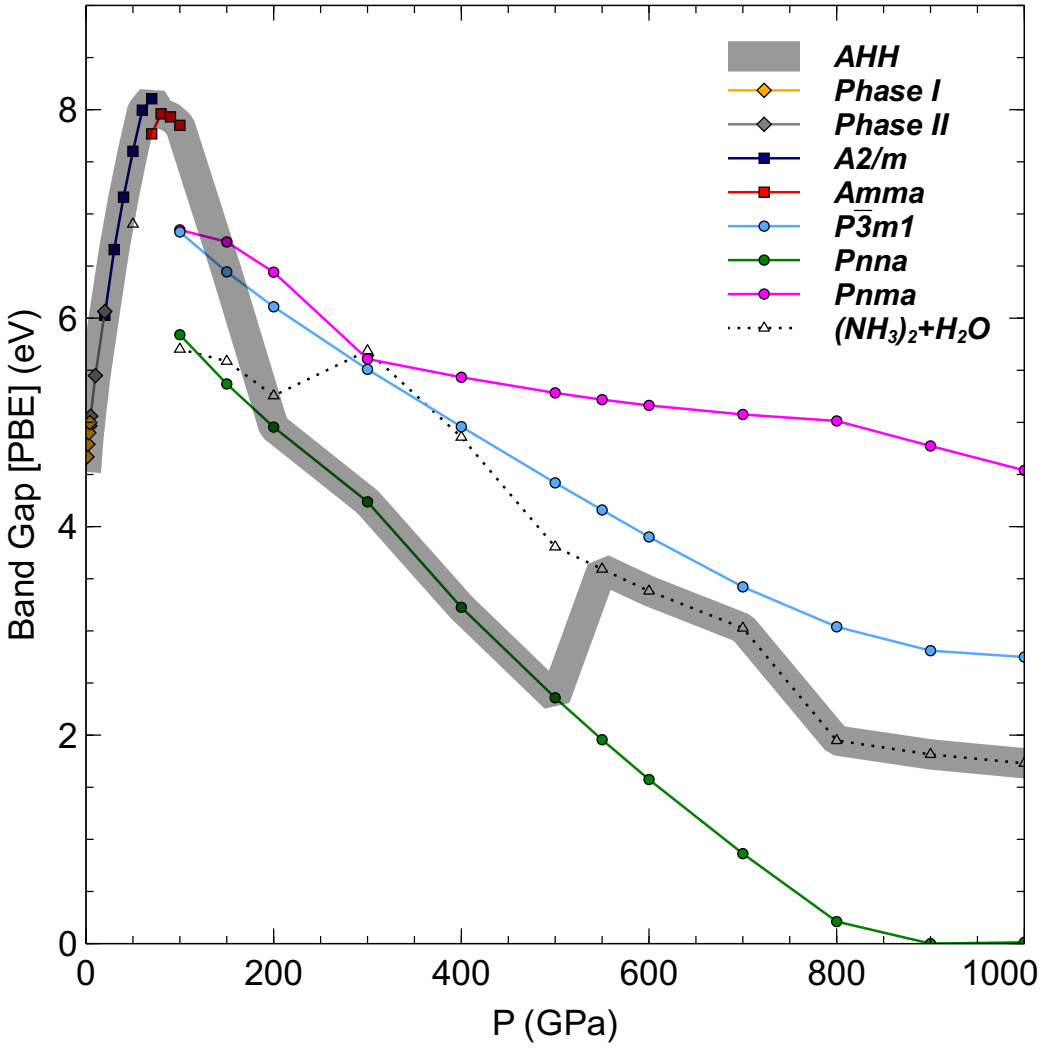

Figure 4.13 *Electronic band gaps for various phases at different pressures, as obtained from DFT calculations. Shaded line follows the respective most stable AHH phase at every pressure.*

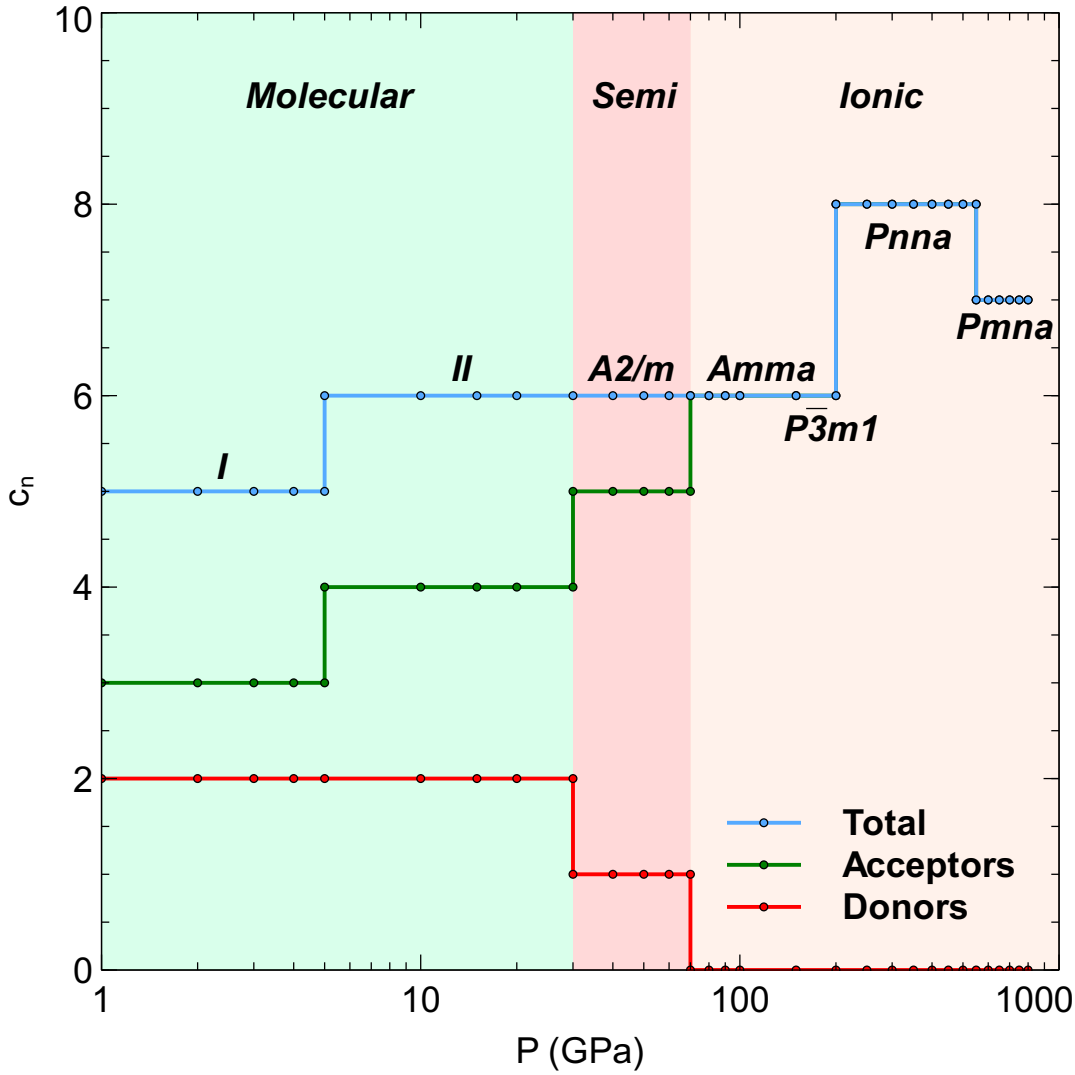

Figure 4.14 *The evolution of the average H-coordination of the oxygen atoms in AHH as a function of pressure. Above 65 GPa, there are no more donated hydrogen bonds, as all water/hydroxyl molecules are completely deprotonated.*

From these ground state calculations, we deduce that compressed AHH goes through three distinct regimes as pressures are applied beyond the stability range of the known molecular phase II. Firstly, above 10 GPa, a range of quasi-cubic, partially ionized structures are stabilized, by 100 meV/f.u. compared with phase II at 40 GPa, see Figure 4.6 . Subsequently, above 65 GPa, a sequence of fully ionic structures is stabilized, which feature the unusual motif of doubly deprotonated water (i.e., O^{2-} anions). These structures benefit from ionic bonding and high coordination of hydrogen bonds shown in figure 4.14. Finally, above 500 GPa, separation into the constituents ice and ammonia (which itself is likely to decompose into other hydronitrogens) becomes favorable. This general trend is unaffected by an increase in temperature, considered here within the harmonic approximation. However, zero point energy effects lead to slightly different stability ranges for each phase, and promote distortions of the CdI_2-like $P\bar{3}m1$ phase; the onset of fully ionic phases should occur around 40 GPa at room temperature. Close to ambient conditions, the formation of molecular ammonia-water compounds is aided by energetically favorable hydrogen bonds between the two species [238]. With increased compression, a different factor contributes: proton transfer, in particular in a 2:1-ammonia:water compound, results in large stabilization due to ionic interactions and higher packing densities.

Complete deprotonation of water molecules in a compound is an intriguing chemical motif, and we are not aware of its presence in other hydrous systems. Water ionization can be achieved through thermal activation, for instance in ice or ammonia monohydrate, in transitions to superionic phases. In those temperature-induced transitions, protons are diffusive and free to move through a quasi-static lattice of the heavy nuclei. The triple points of solid, fluid, and superionic phases in water and AMH, estimated from simulations, are at $(P, T) = (25\ \text{GPa}, 1200\ K)$ and $(20\ \text{GPa}, 800\ K)$, respectively [21, 229]. In AHH, the ionization of water is achieved through a different mechanism, purely through pV work, and the protons thus removed from the water molecules are not diffusive but bound in NH_4^+ units instead. Higher pressures ($P > 65$ GPa) are needed to induce this ionization, but the resulting molecular units are arguably stronger bound than in the lower pressure region.

To investigate the high-pressure AHH phases more closely at the conditions expected in large icy planets, molecular dynamics calculations at elevated temperatures are required. One interesting question is whether a superionic region exists in AHH, and if so, how the onset temperature of superionicity is

affected by (i) the presence of heavy cation and anion species both, and (ii) the seemingly increased N-H bond strengths in the molecular NH_4^+ units as pressure increases. For ice, ammonia, and ammonia monohydrate, the onset temperatures of superionicity are calculated to be relatively insensitive to pressure (therefore also insensitive to the underlying crystal structure) and to occur around 2000, 1000, and 1000 K, respectively.[21, 229, 239] In compressed AHH, the strongly bound ammonium cations could suggest that relatively high temperatures are needed to induce proton mobility, which in turn would lead to reduced thermal and electrical conductivity in any such layer present in planetary interiors. In chapter 6 we present results AIMD calculations on AHH and other relevant mixtures.

4.3 Ammonia Monohydrate

Two low-pressure, low-temperature phases of AMH, AMH-I, and AMH-II, have been fully resolved. A computational prediction by Griffiths et al. suggests that a tetragonal ionic phase, $(NH_4)^+(OH)^-$, becomes more stable than AMH-II above 2.8 GPa [240]. The high-pressure phase evolution of AMH has recently been studied computationally by Bethkenhagen et al., who aimed to identify relevant solid phases to be used as initial configurations for molecular dynamics (MD) simulations [206]. The latter was then used to construct a $P-T$ phase diagram that studied the onset of superionicity and eventual melting of AMH. A triple point between solid, fluid, and superionic phases was found around $P = 20$ GPa and $T = 800$ K. The ground state high-pressure phases uncovered in the crystal structure prediction process proved to be relevant to obtain accurate equations-of-state data even at high temperatures [206], but the deviation of density and internal energy from linearly mixing the pure water and ammonia equation-of-state are at the single percent level [241].

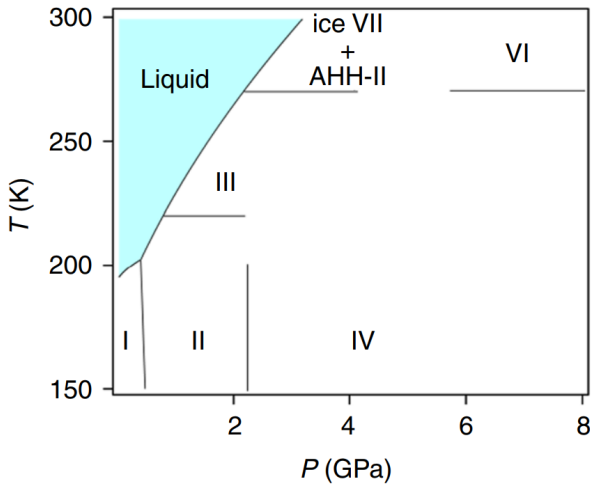

Figure 4.15 *The phase diagram of ammonia monohydrate (AMH) taken from Liu et al [49].*

In AMH, there have been full structural solutions of three solid phases [38, 46, 49, 226, 230], with AMH-III and AMH-IV still unsolved, see figure 4.15 for a phase diagram in pressure and temperature space. Several density functional theory (DFT) studies have predicted the stability of ionic ammonium hydroxide phases, $(NH_4)^+(OH)^-$, over the molecular $(NH_3)(H_2O)$ phases, above around 5 GPa [228, 240]. The P4/nmm phase, while predicted to be very stable, has been difficult to observe in experiments. Only traces of these ionic phases have been observed experimentally, possibly due to frustration of the transition kinetics from the DMA phase [49]. Furthermore, using a combination of crystal structure prediction and molecular dynamics calculations, the phase diagram of AMH has been explored computationally up to 800 GPa and 6000 K, in the process establishing a sequence of high-pressure phase transitions at low temperatures, as well as regions of superionicity (where protons are diffusive but a crystalline lattice of heavy ions remains) and eventual melting [206].

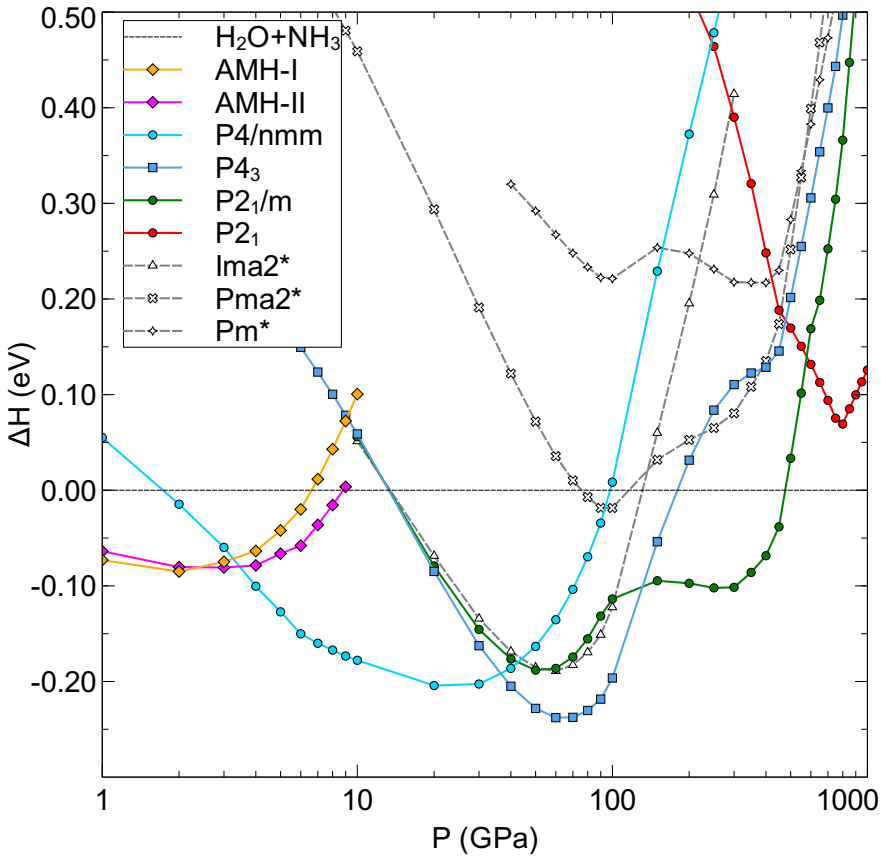

Figure 4.16 *Relative enthalpies of formation of AMH phases, on a logarithmic pressure scale and relative to decomposition into NH_3 and H_2O. Black circles show the P4/nmm phase reported by Griffiths et al [240], and gray open symbols are phases suggested by Bethkenhagen et al.[206].*

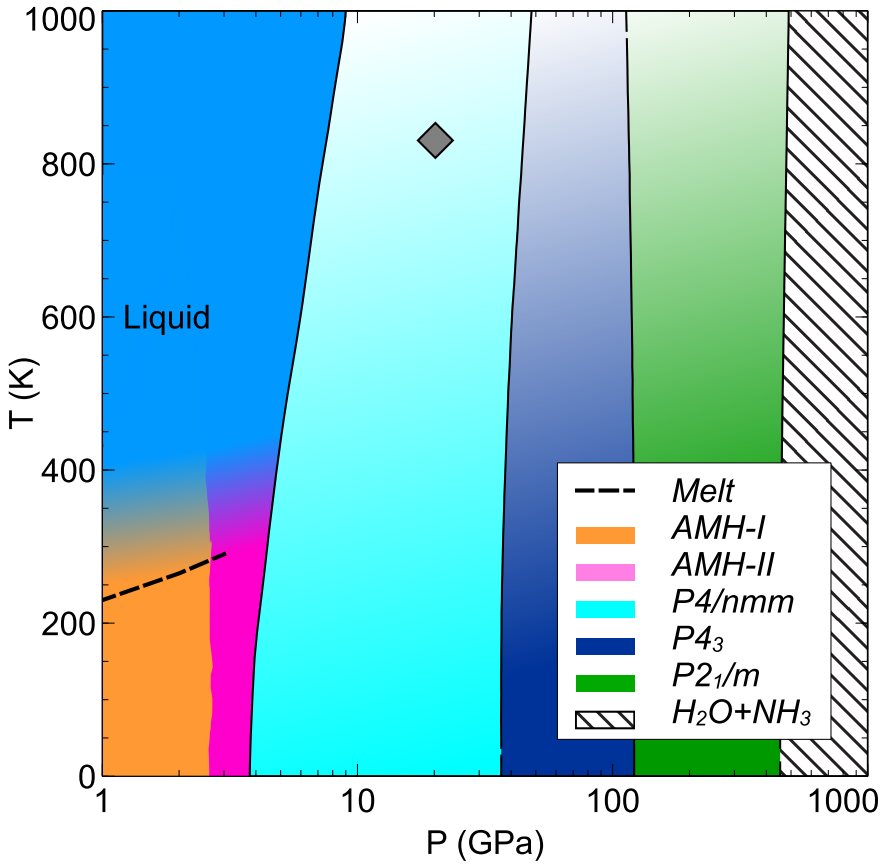

Figure 4.17 *The P-T phase diagram of AMH constructed using the harmonic approximation. The dashed line indicates the experimental melting line,[230] the gray diamond indicates the superionicity triple point from DFT,[206] and an approximate liquid region is indicated.*

In figure 4.16 we show the enthalpies of formation of the known AMH phases, those proposed by Griffiths *et al.* and (in gray symbols) by Bethkenhagen *et al.*, all drawn relative to decomposition into the constituents. Our calculations confirm the literature findings regarding phase succession and transition pressures: at 3.5 GPa the proposed structure by Griffiths *et al.* becomes more stable than AMH-II; at 45 GPa it gives way to an orthorhombic $Ima2$ phase; at 140 GPa another orthorhombic phase, $Pma2$, becomes stable; and above 570 GPa a monoclinic Pm phase is most stable. All of those phases are ionic, of the form $(NH_4^+)(OH^-)$, and represent different arrangements of the ammonium and hydroxyl groups. However, note from Figure 4.16 that these previously reported phases become unstable towards decomposition into pure water and ammonia at pressures above $\sim$ 120 GPa. This would make AMH, its appealing simple stoichiometry notwithstanding, much less important inside icy planets' mantles than hitherto thought.

In Figure 4.16 we also include results from our structure searches, listed in table 4.2. These uncovered a sequence of high-pressure phases that are, above 35 GPa, more stable than those proposed in the literature. Most importantly, these structures delay the decomposition of AMH into the pure ices to almost 500 GPa in the ground state.

We find two new phases that are relevant over this large pressure range: a tetragonal $P4_3$ structure from 35 to 140 GPa, and a monoclinic $P2_1/m$ phase between 140 and 470 GPa. The $P4_3$ phase, like the $P4/nmm$ phases it supersedes, is an ionic structure that comprises OH^- and NH_4^+ groups. The hydroxyl groups in the $P4_3$ phase form one-dimensional hydrogen-bonded spirals (see Figure 4.18); in comparison to the $P4/nmm$ structure, with linear O-H$\cdots$O-H chains, and the $Ima2$ structure, with planar zig-zag O-H$\cdots$O-H chains, this leads to a more compact overall arrangement. At 50 GPa, the $P4_3$ structure is 2.5% and 0.4% more compact than the $P4/nmmm$ and $Ima2$ structures, respectively. The molecular units of $P4_3$ are arranged overall in what can be interpreted as a quasi-BCC layout, as indicated in Figure 4.18. Liu et al simulated quasi BCC crystals for AMH in figure 4.19 snapshots they presented are shown for comparison. The $P4_3$ structure therefore seems to be an ordered (and ionic) variant of the DMA phase observed experimentally at high temperatures. A proper model of the DMA phase would require the analysis of all possible microscopic configurations in adequate supercells of the DMAs body-centered cubic heavy atom lattice, and their occupancy at given temperatures to compare free energies. A recent combined experimental and computational study of AMH-DMA reported diffractive and spectroscopic properties of low-energy candidates for this phase from (4,4,4) supercell calculations by Liu et al [49].

At 140 GPa a monoclinic ionic $P2_1/m$ structure (8 f.u./cell) becomes more stable than $P4_3$ and remains the most stable AMH phase over a large pressure range, up to 470 GPa. In this phase, protons of hydroxyl groups are positioned close to the mid-points along O–H–O bonds, and those form one-dimensional chains along the a axis, see Figure 4.20. These O-H chains are themselves arranged in a matrix of NH_4^+ cations, a structural motif for instance seen in the high-pressure phases of the alkali hydroxides (Rb,Cs)OH [242, 243]. In half of the O-H chains the O–H–O connections are symmetric and linear, while in the other half they are asymmetric and bent, and form hydrogen-bonded (H_2O)–O. With increased pressure, the $P2_1/m$ phase continuously adopts a higher symmetry $P2_12_12_1$ phase with half as many atoms in the unit cell, and where all O–H–O bonds are symmetric and

buckled; see Figure 4.20 for their relation. The symmetrization of O-H bonds in AMH happens at much higher pressures than what is seen e.g. in the transition of pure ice from molecular ice-VIII to atomic ice-X [41, 244–246].

Above 470 GPa, the $P2_1/m$ phase is no longer stable with respect to decomposition into the molecular ices, and we find no other stable AMH phases in our searches. Note that NH_3 itself has been predicted to decompose into other hydronitrogens above 460 GPa [195], which we have considered here for all baseline calculations.

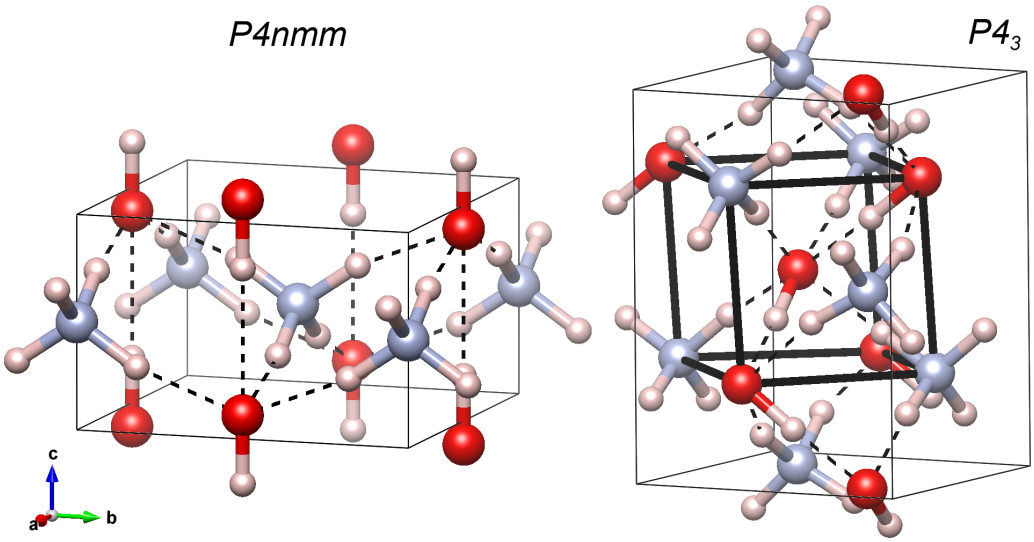

Figure 4.18 *Crystal structures of the AMH P4nmm [240] and $P4_3$ phases at 10 and 50 GPa, respectively. Red (blue, white) spheres denote O (N, H) atoms, and covalent bonds are indicated. Hydrogen bonds are shown by bashed black lines. The $P4_3$ phase has a quasi-BCC arrangement highlighted by black lines.*

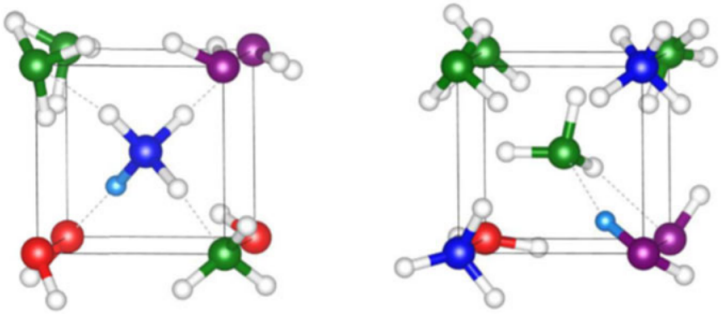

Figure 4.19 *Snapshots from BCC AIMD simulations of AMH created by Liu et al simulating the DIMA phase taken from [49].*

We applied the harmonic approximation to obtain estimates of free energies for all phases by considering vibrational entropies. The resulting $P-T$ phase diagram

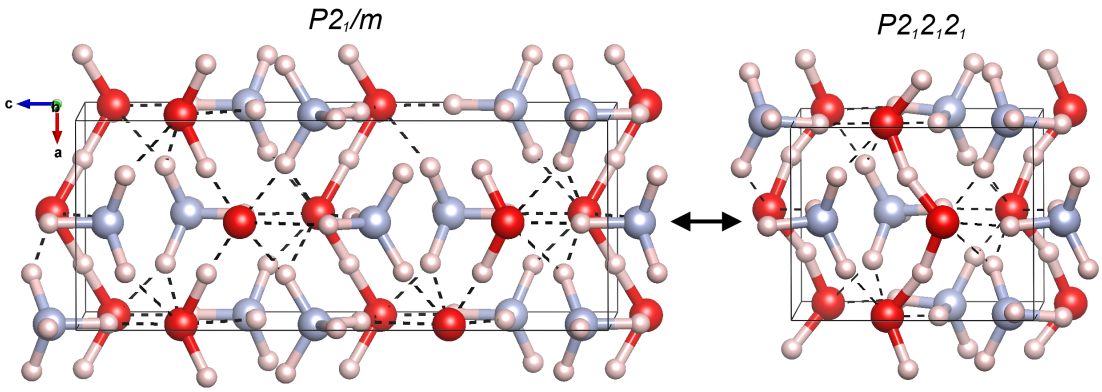

Figure 4.20 *Crystal structures of the AMH $P2_1/m$, and $P2_12_12_1$ phases at 200 and 500 GPa, respectively.*

is shown in Figure 4.17. The inclusion of ZPE does not change the stability range for the phases very much (see figure 4.21), and elevated temperatures also have a somewhat small effect, as most phase boundaries are almost vertical. For reference, we include in Figure 4.17 the experimental melting line and a triple point of the solid, liquid, and superionic phases found in previous DFT calculations, based on other solid phases [206]. Both reference points should help put the validity of the harmonic approximation into context: we do not expect it to provide accurate answers above 1000 K for most of the pressure range studied here.

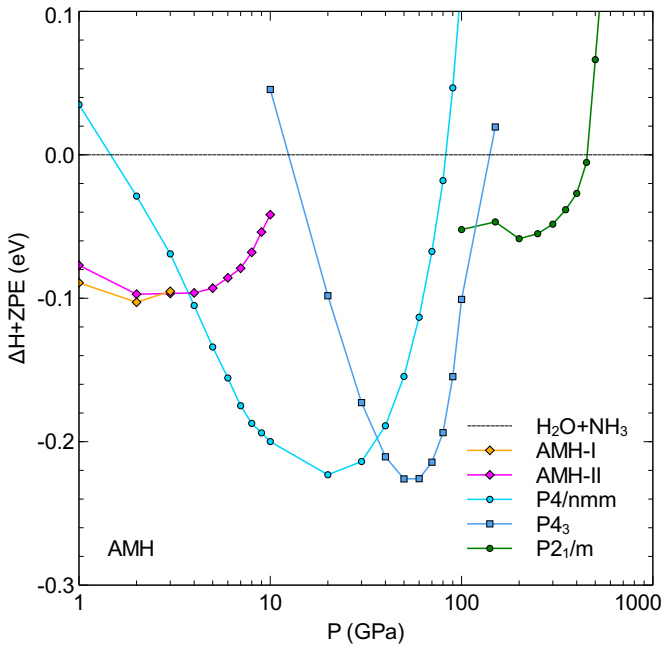

Figure 4.21 *AMH phase diagram with ZPE included.*

In summary, we find that AMH shows a richer phase diagram than previously

P (GPa)	Space group
30	P4/nmm
50	$P4_3$
80	$P4_3$
100	$P4_3$
200	$I2_12_12_1$
300	Pma2
400	Pma2
500	$P2_12_12_1$
600	Cc
700	$P2_1$
800	$Pmc2_1$
900	$Pmc2_1$
1000	$Pmc2_1$
1500	$P\bar{1}$
2000	$P\bar{1}$
3000	$P\bar{1}$
4000	$P2_1/c$
5000	$P2_1/c$

Table 4.2 *Summary of structure searches with 2-8 f.u. performed for AMH.*

assumed. A set of new phases extends the stability of AMH against decomposition into the ices from $\sim$ 120 GPa (when considering all phases known in the literature) to 470 GPa. These new phases are a sequence of ionic structures $(OH^-)\cdot(NH_4^+)$ with ever more compact arrangements and eventual formation of one-dimensional symmetric -[-O–H-]- chains in an ammonium matrix. The molecular vibrons of phases I and II can be seen to weaken in the Raman and IR spectra shown in figure 4.22 while the ionic phases come in with strong vibrons becoming stiffer with pressure. AMH is a strong candidate for ionic stability at high pressure as the 1:1 ratio naturally forms only ionic units with no molecules left over.

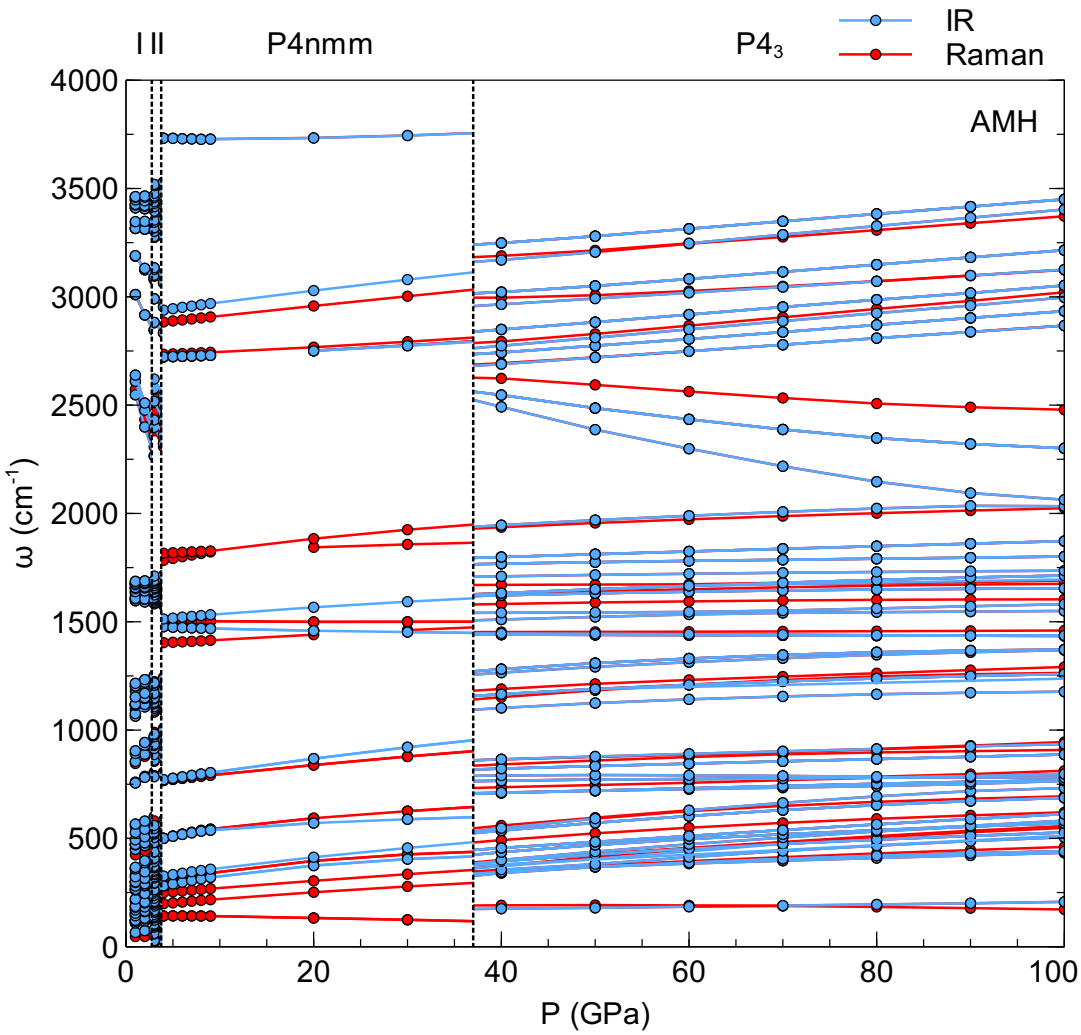

Figure 4.22 *Raman and Infrared spectroscopy for phases of AMH.*

4.4 Ammonia Dihydrate

To complete the survey of known hydrates, we also investigate the high-pressure structural evolution of ADH compounds. This is the most water-rich ammonia hydrate known at ambient conditions and closest to the solar abundance ratio of water and ammonia, and could therefore be of significance at extreme conditions. Three of its solid phases, including the DMA phase, have been solved [38, 47, 227, 230] with ADH-IV still to be clarified, although its unit cell dimensions have been reported [247]. A recent DFT study suggested the formation of an ionic phase, $(NH_4^+)(OH^-)(H_2O)$, at 12 GPa, stable up to at least 45 GPa [207] and potential superionicity at elevated temperatures has been investigated. However, we find the ADH phase diagram to be somewhat richer, see Figure 4.24.

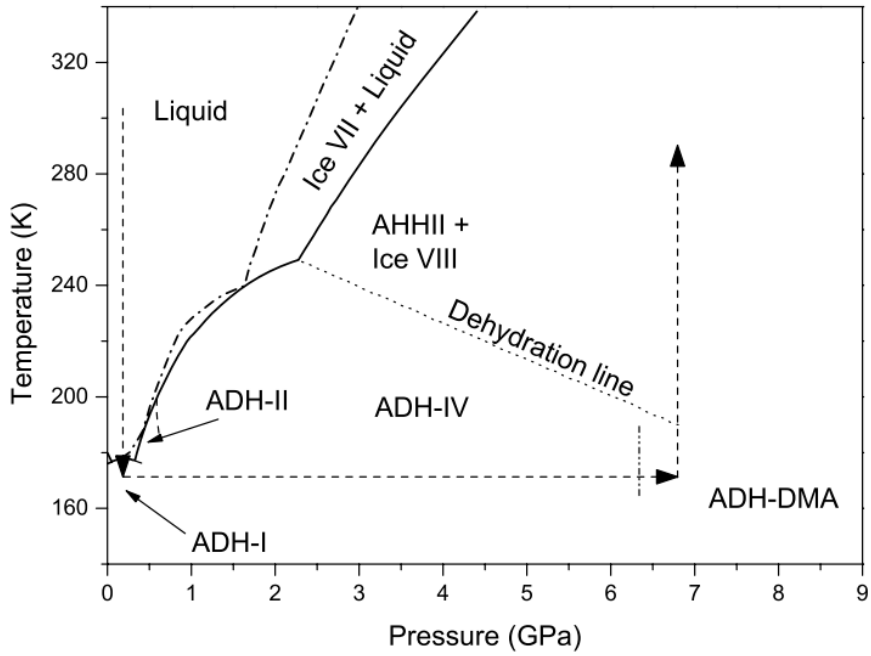

Figure 4.23 *The phase diagram of ammonia dihydrate (ADH) taken from Wilson et al [48]. The dotted dehydration line is where ADH structures break down into ice and AHH. The dash-dotted line is the liquidus line for ADH, within this region solid crystals and coexist with an ammonia-rich fluid in thermodynamics equilibrium. Dashed arrows refer to experimental pathways taken into the DMA phase.*

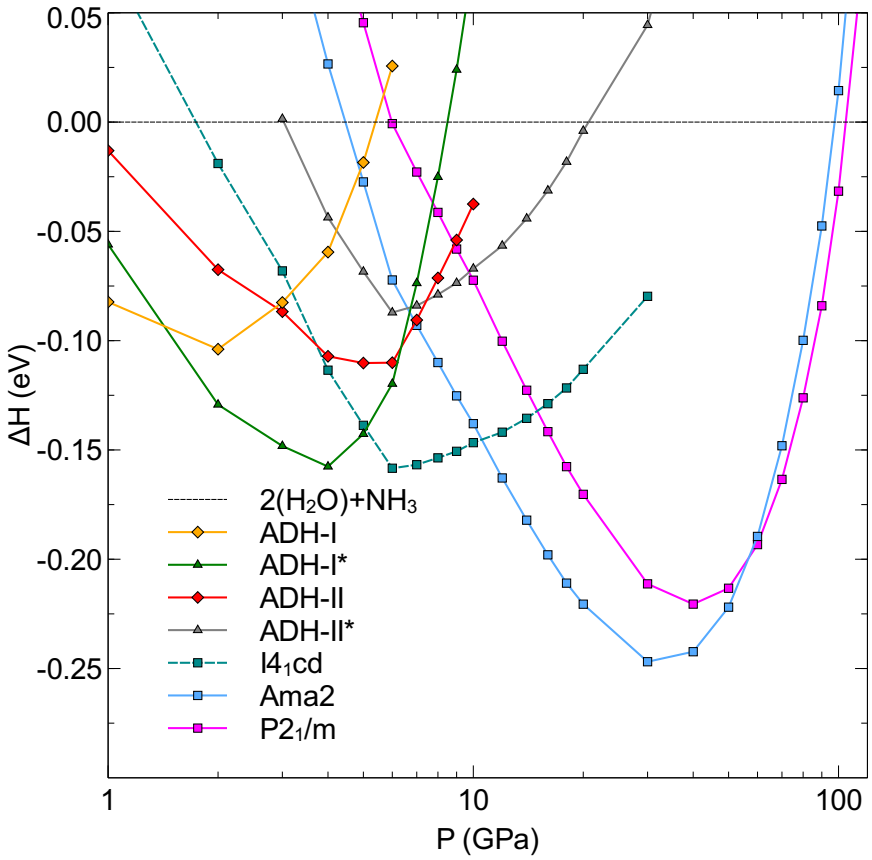

Figure 4.24 *Relative enthalpy of formation of ADH phases, on a logarithmic pressure scale and relative to decomposition into NH_3 and H_2O.*

At low pressures, we find ADH-I to be most stable; it would be superseded by ADH-II at ∼3 GPa if not for the emergence of an ionic variant of ADH-I. This phase, which we call ADH-I* here, emerges through a proton transfer along a particular hydrogen bond, HO-H$\cdots$NH$_3$ → HO$\cdots$H-NH$_3$, equivalent to that seen in early calculations on compressed AMH [228] and AHH [248]. The molecular ADH-II phase has a similar transition to an ionic variant ADH-II* above 7 GPa; see Figure 4.26 for both structures. The ADH-I* phase is stable from 1.5 to 5 GPa in our calculations and displaces the known ADH-II from stability. Above 5 GPa the recently suggested $I4_1cd$ phase becomes more stable. That phase, however, remains only stable up to 10 GPa, where we find a new orthorhombic phase of $Ama2$ symmetry to become more stable; and a monoclinic $P2_1/m$ phase stable above 60 GPa. The $Ama2$ and $P2_1/m$ phases, shown in Figure 4.27, then extend the stability region of ADH towards decomposition into the ices to over 100 GPa. However, neither the tetragonal $I4_1cd$ phase (with Z = 16 molecules per cell) nor the base-centered orthorhombic $Ama2$ phase (with Z = 4) match the suggestion for ADH-IV based on neutron diffraction data (primitive orthorhombic lattice

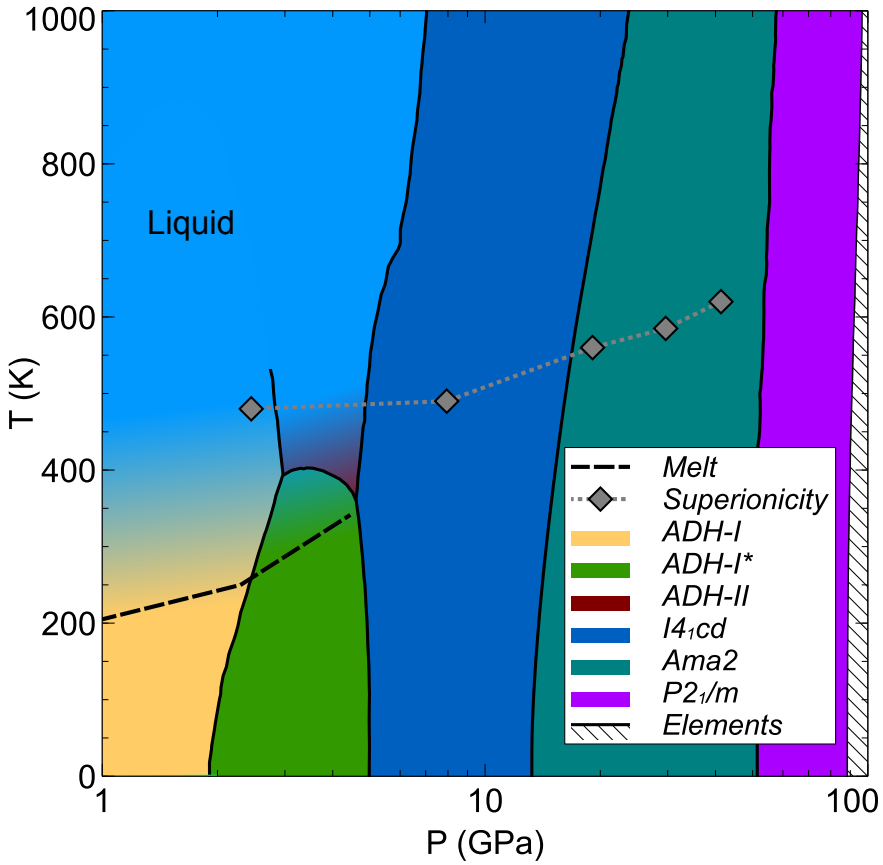

Figure 4.25 *P-T phase diagram obtained from harmonic approximation, also including the experimental melting line,[44] the computationally predicted $I4_1cd$ phase and onset of superionicity,[207] and a tentative sketch of the liquid region.*

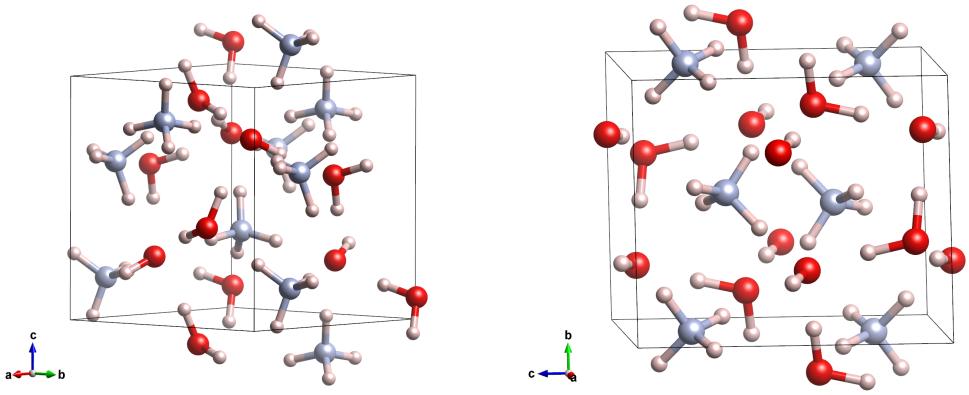

Figure 4.26 *Ionic structures ADH-I* at 3 GPa (left) and ADH-II* at 12 GPa (right), derived by proton transfer from molecular ADH-I and ADH-II, respectively.*

with Z = 8) [247]. A triple point is observed in the finite-temperature phase diagram shown in figure 4.25, however, this lies above the current experimental melting line.

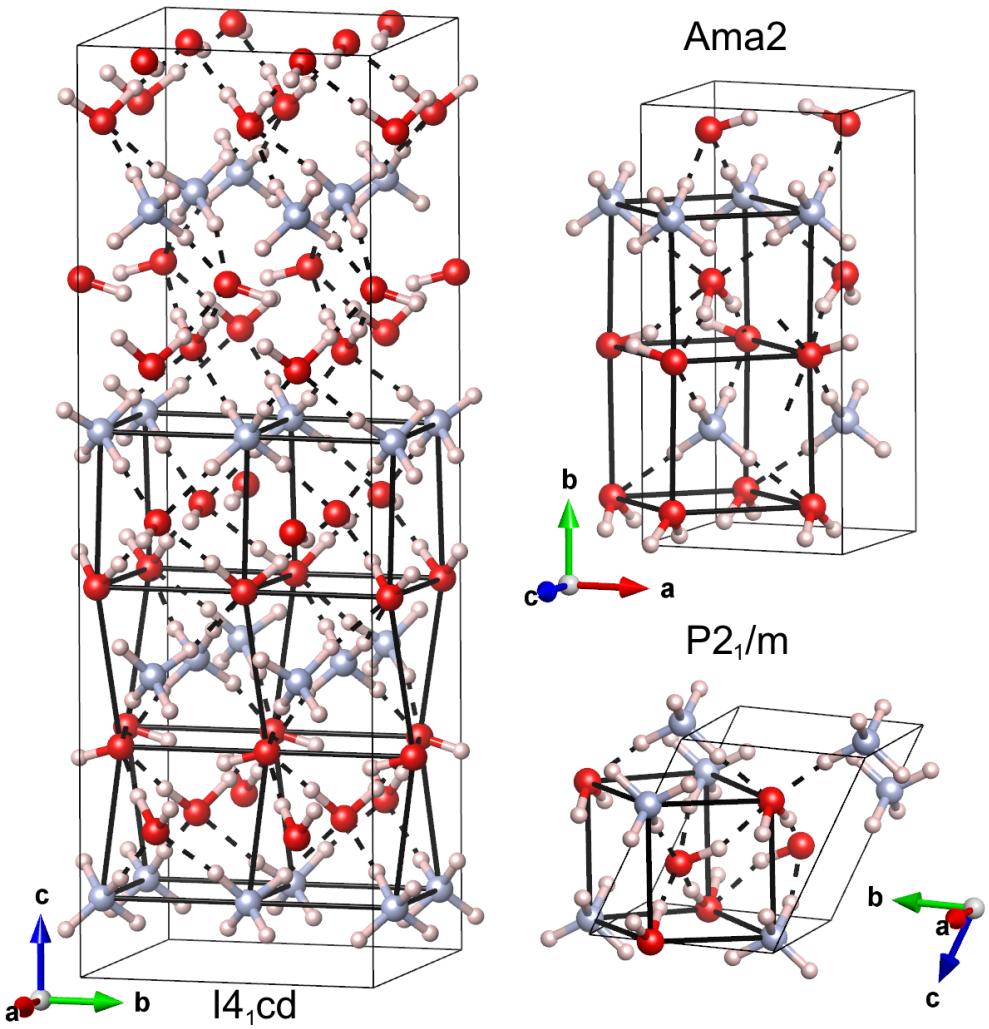

Figure 4.27 *Left: crystal structure of the half-ionic ADH $I4_1cd$ phase at 10 GPa. Top right: newly predicted $Ama2$ phase at 20 GPa. Bottom right: the high-pressure $P2_1/m$ phase at 60 GPa. In all phases, local body-centered features are highlighted.*

In line with the other hydrates discussed above, ionization of water molecules becomes preferable under pressure, and the ADH-I*, $I4_1cd$, $Ama2$, and $P2_1/m$ phases all can be seen as $(OH^-)(NH_4^+)(H_2O)$. The latter three all arrange in seemingly layered structures, see Figure 4.27: along the c axis, they feature alternate layers of NH_4^+, H_2O, and OH^-. Overall, this optimizes ionic interactions, as the ionic components NH_4^+ and OH^- are adjacent, while the water dipole moments are aligned along the local electric field established by adjacent ammonium and hydroxyl layers. In addition, all structures are fully hydrogen

P (GPa)	Space group
30	$P2_12_12_1$
50	Ama2
80	$Pna2_1$
100	P1
200	$P2_12_12_1$
300	P1
400	$P2_1/m$
600	Pc
800	Abm2
1000	Pc
2000	Cc
3000	Pc
4000	Pc
5000	$P2_12_12_1$

Table 4.3 *Summary of structure searches with 2-8 f.u. performed for ADH.*

bonded: all NH_4^+ groups donate four hydrogen bonds; all water molecules donate and accept two bonds, respectively; and all OH^- groups donate one hydrogen bond and accept four. These favorable electrostatic interactions, together with a more compact arrangement, outweigh the energetic cost of the proton transfer compared to the molecular phases ADH-I and -II, and stabilize these phases over ADH-I* as well; at 20 GPa, the relative volume collapse from ADH-I* and from $I4_1cd$ to $Ama2$ is 7.3% and 4.5%, respectively.

Eventually, however, and at much lower pressures than for the other two hydrates, ADH becomes unstable towards decomposition into the ices. The Raman and IR spectra for ADH shown in figure 4.29 shows the high pressure phases, $Ama2$ onward, have weakening or flat modes with only a few strengthening in pressure. This decomposition is predicted to happen around the pressure where (in ground state calculations) atomic ice-X becomes more stable than molecular ice-VIII. The inclusion of zero point energy, shown in figure 4.28, maintains the phase sequence as the enthalpic picture but decreases the transition pressure.

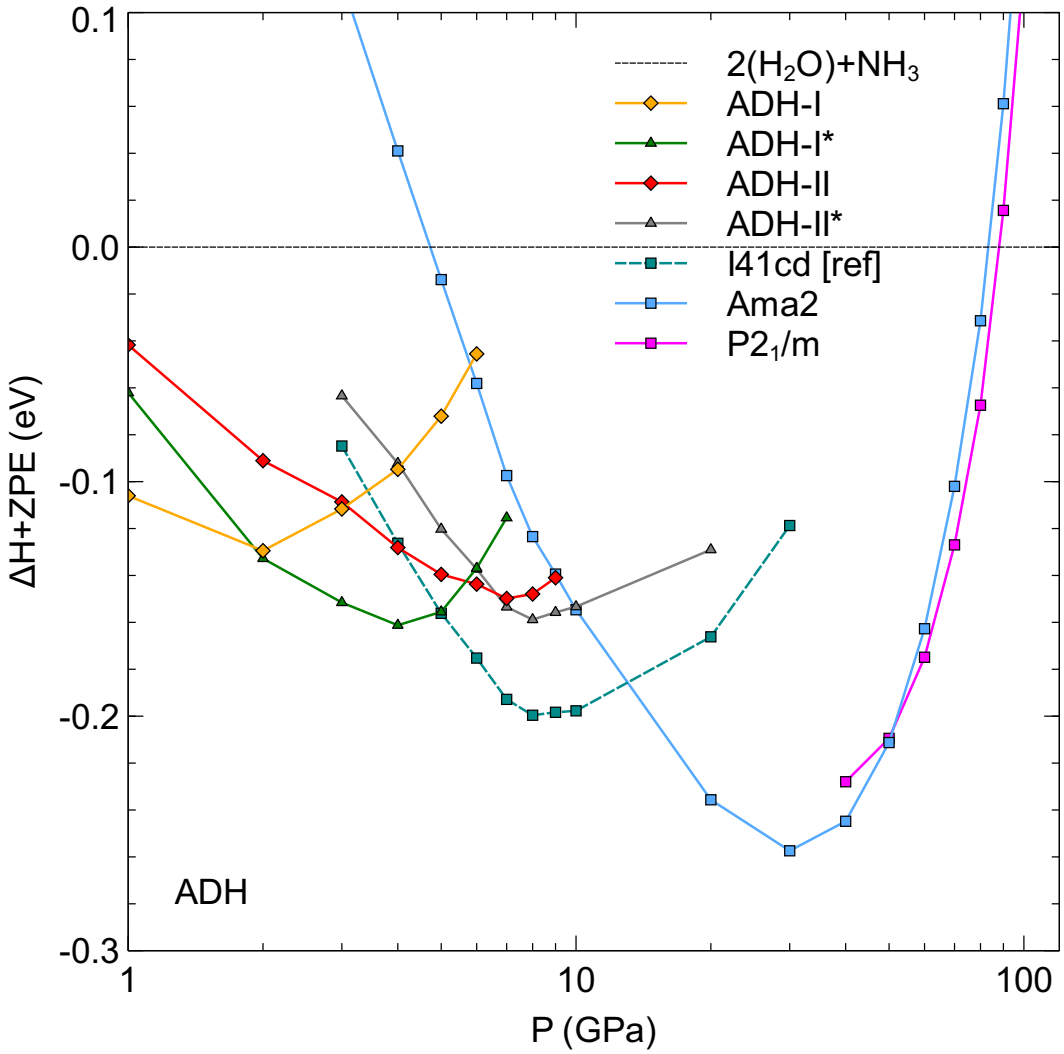

Figure 4.28 *ADH phase diagram with ZPE included.*

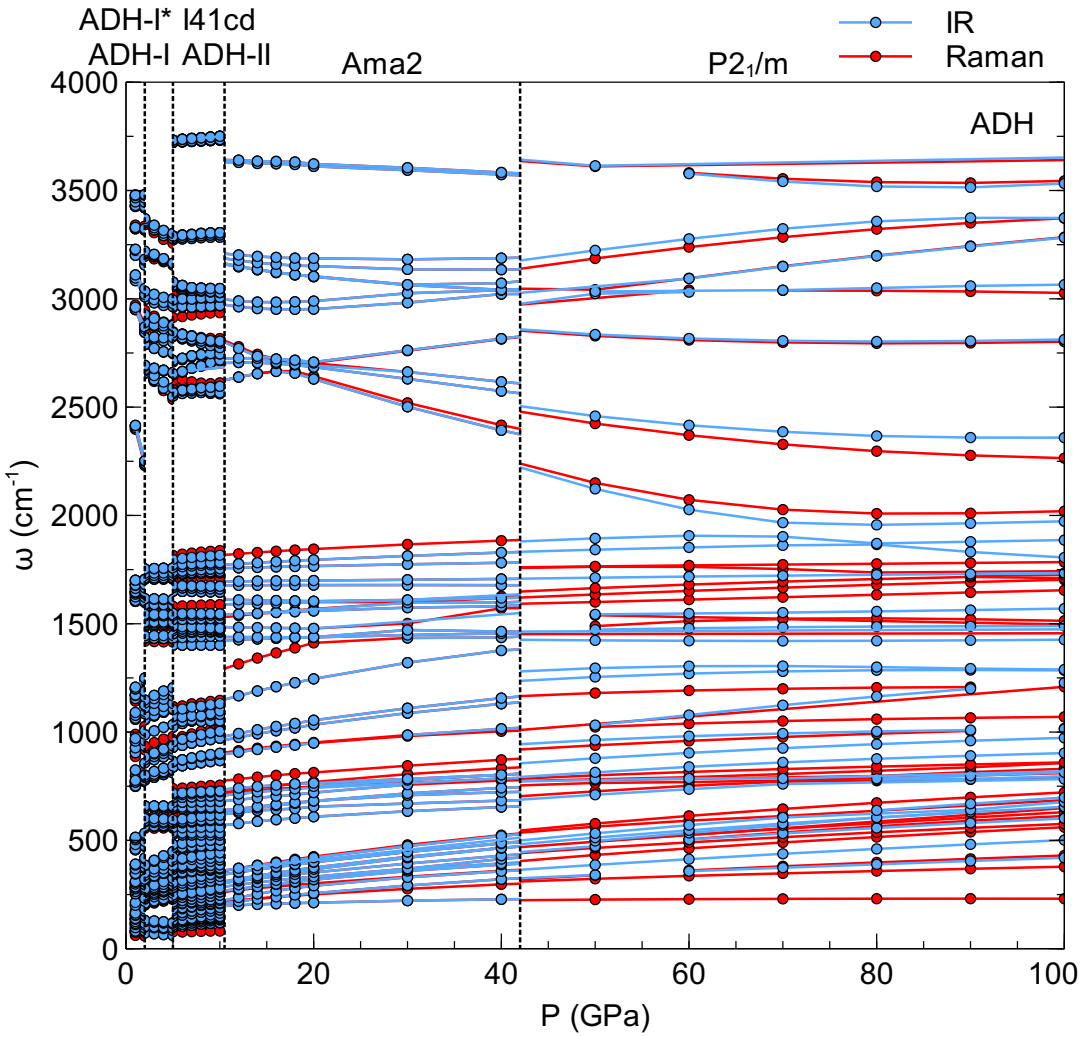

Figure 4.29 *Raman and Infrared spectroscopy for phases of ADH.*

4.5 Concluding Remarks

In this chapter, we have seen the three known hydrates go from molecular to semi-ionic to as fully-ionic as possible under compression. Many structures have been optimized in total, with some beautiful and some not so beautiful crystals as a result. Structure searching has revealed from new arrangements for water not previously known for AHH with fully deprotonated O^{2-} anion over roughly 40 GPa. In AMH we have revised the phase diagram and extended the stability due to decomposition into the constituent ices. In ADH we found some further high pressure phases, building on previous work. Surprisingly semi-ionic forms of ADH phases I and II were stable at very low pressures, and this is the hydrate closest to the cosmic abundance ratio.

In an elegant way, quasi-BCC structures have emerged in all the hydrates here, AMH, ADH, and AHH within the pressure range where the DMA/DIMA has been observed experimentally. This suggests that the searching is working well, but the potential surface may have many quasi-BCC phases with similar energies. It is possible that some of these quasi-BCC structures are the ground state for the given hydrate, but there is difficulty in experiment accessing these as suggested by Liu et al [49]. Overall at the highest pressures of 500 GPa both AMH and AHH become unstable, ADH at 100 GPa before this, and perhaps all ammonia water mixtures are unstable beyond this pressure. The convex hull at 300 GPa for different mixing ratios shows that AHH remains dominant at high pressure. At other pressures this remains unknown and we shall investigate this in the following chapter.

Cosmic abundance ratios for ammonia:water is approximately 1:7, quite far removed from the 2:1 compound considered here. However, AHH is relevant at relatively low pressures, where it appears in the phase diagrams of both of the other known stoichiometric compounds: both are more water-rich than AHH, but decompose into AHH-II and pure ice at appropriate pressure-temperature conditions. AHH is also very relevant at high pressures, and not just compared to the known AMH and ADH compositions: at 300 GPa, we find in an extensive structure search across all $(NH_3)_x(H_2O)_{1-x}$ compounds (ranging from $x = 1/6$ to $x = 5/6$) that, besides the pure ices, only AHH is stable against decomposition, see the convex hull plot in figure 4.5. It is therefore conceivable that AHH, driven by its ability to form completely ionic phases, precipitates out of *any* ammonia-water mixture under high-pressure conditions. At 300 GPa in our calculations,

AHH-$P\bar{3}m1$ has a density of 3.50 g/cm^3, which is 16% lighter than the most stable ice phase at the same pressure ($Pbcm$ symmetry, 4.17 g/cm^3). Thus, compressed water-rich ammonia-water mixtures in a planetary environment (e.g. in a 1:7 ratio or similar) could segregate into a layer of ammonia-rich ionic AHH solution above an ocean of pure water ice. The enthalpic gain achieved in this separation will need to compete with the entropy of mixing of the homogeneous mixture.

Another consequence of the prolonged stability of AHH under pressure is that ammonia reservoirs should always form compounds with water, at least until 450 GPa where it is predicted to decompose. Unless an icy planet's ammonia:water ratio is larger than 2:1, which is unlikely due to cosmic observations, ammonia will be unlikely to exist on its own up to pressures around 500 GPa, where we see demixing to become favourable.

Chapter 5

Comparative study of Ammonia Water Mixtures

So far, we have discussed the individual hydrates, and mostly probed their stability against decomposition into the constituent ices. However, other reactions can and must be considered – some are already known from experimental studies: both molecular AMH and ADH decompose into AHH-II and excess ice-VII/VIII. Other reactions are possible; for instance, AMH could decompose into a combination of a water-rich (such as ADH) and an ammonia-rich hydrate (such as AHH). Likewise, AHH could decompose into a more water-rich hydrate and an appropriate amount of pure ammonia. Cataloging all those reactions could be done by hand, but also summarized very succinctly in a convex hull diagram. There, we plot the relative enthalpy of formation for an arbitrary hydrate AXH, which shall be $(H_2O)_{1-x}(NH_3)_x$, against the relative ammonia content x:

$$\Delta H_f(x) = H_f(\mathrm{AXH}) - (1-x)H_f(H_2O) - xH_f(NH_3) \tag{5.1}$$

By construction, the compound whose enthalpies form the *convex hull* of $\Delta H_f(x)$ are stable against decomposition into any other binary mixture of ammonia and water, at the given external pressure conditions. While so far we only considered $x = 1/3$, $1/2$, and $2/3$, ammonia hydrates could in principle take up any other composition. We therefore performed crystal structure searches with Calypso across the entire binary H_2O–NH_3 phase diagram, at 50, 100, and 300 GPa. Those pressures were chosen to correspond to the emergence of (half-)ionic phases across all hydrates, the predicted destabilization of ADH, and the region of stability of

fully ionic phases in AHH, respectively.

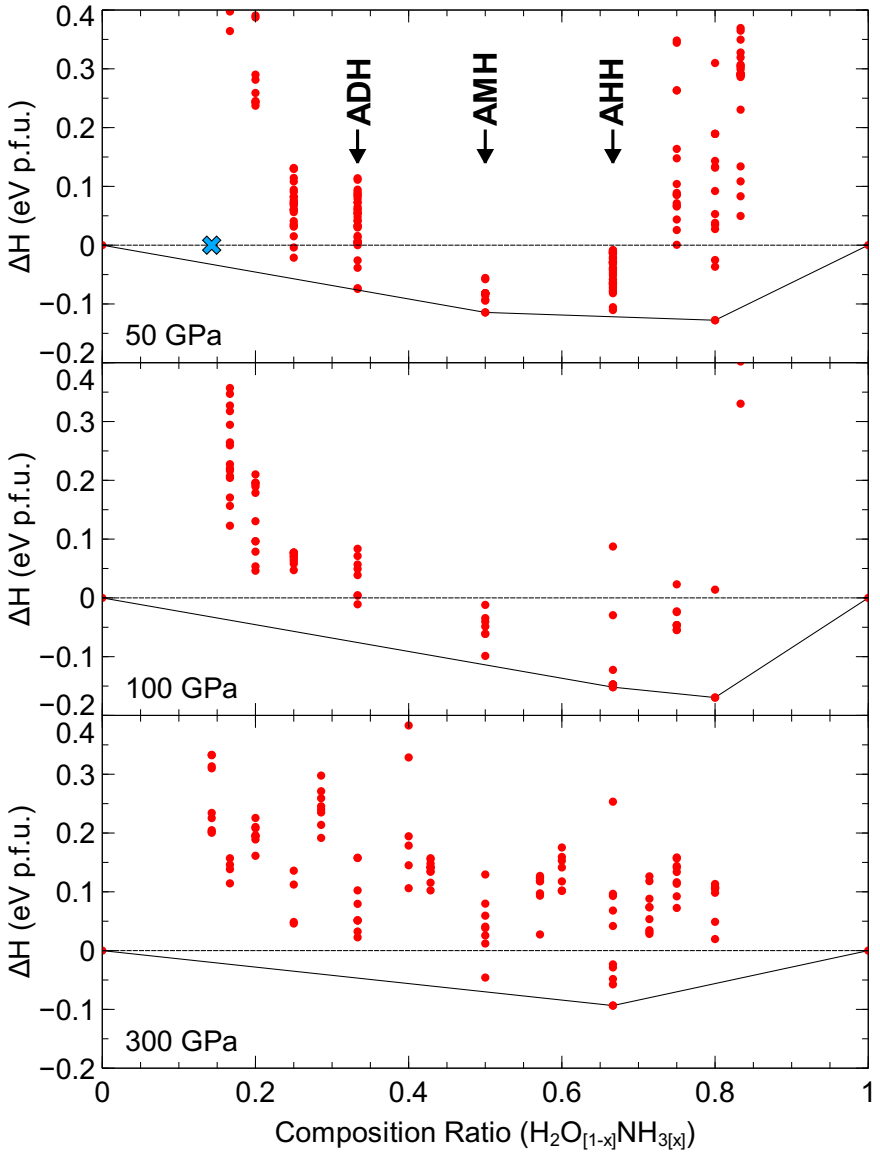

Figure 5.1 *Ammonia-water phases found in crystal structure searches, with up to 50 structures shown for each composition. From top: structure search results for $\Delta H_f(x)$ at 50, 100, and 300 GPa. The Solar ratio of 7:1 water:ammonia is indicated by the blue cross.*

In Figure 5.1, we show the primary outcomes of these structure searches. It becomes clear immediately that the discussion so far, concentrating on individual hydrates, is insufficient. For instance, at 100 GPa, all three known hydrates have negative enthalpies of formation ($\Delta H_f < 0$ for their respective best structures), but only AHH ($x = 2/3$) is part of the convex hull. At 50 GPa, AMH ($x = 1/2$) is present on the convex hull, while ADH and AHH are very close but technically metastable. Taking the most relevant phases for each composition

from these search results and optimizing them across the entire pressure range, we then constructed convex hulls on a much denser sequence of pressure points. This allows us to predict the formation and decomposition conditions for each individual compound with much higher precision, and those results will be discussed in detail in the next subsection.

A very intriguing feature of Figure 5.1 is, however, the emergence of a new ammonia-rich hydrate phase at $x = 0.8$: a 4:1 ammonia quarterhydrate $(NH_3)_4(H_2O)$ (AQH from here on), found initially at 100 GPa, is predicted to become more stable than the constituent ices above 8.5 GPa. A representative structure of this compound is shown in Figure 5.2.

5.1 New Ammonia-rich Hydrate Under Pressure: AQH

AQH is first stabilised against decomposition into the ices in a partially ionic monoclinic $P2_1$ phase, see Figure 5.2. This phase contains NH_3, NH_4^+, and OH^- units, with the heavy N and O atoms arranged in a face centered tetragonal setup. Above 25 GPa, we find another monoclinic phase, $P2_1/m$ that, like AHH phases in a similar pressure range, features fully deprotonated water molecules – effectively forming a $(NH_4^+)_2(NH_3)_2O^{2-}$ compound.

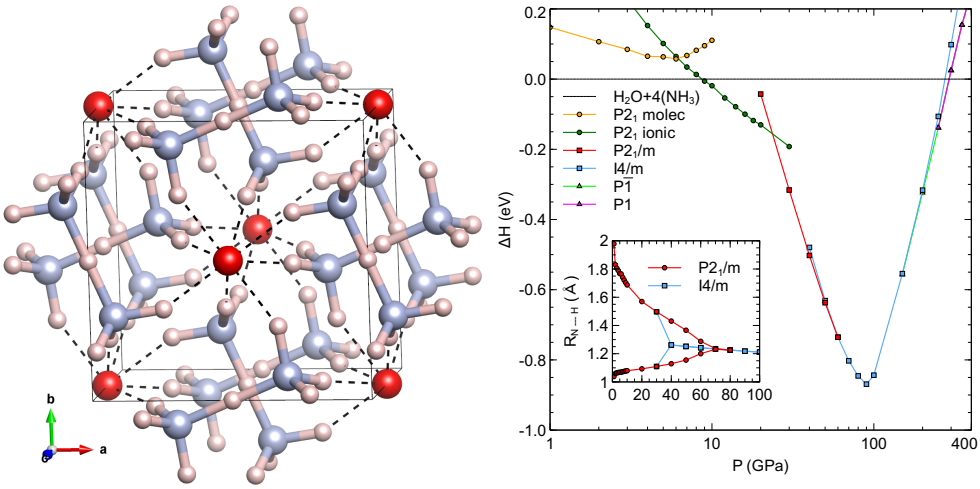

Figure 5.2 *Left: the I4/m structure of AQH at 100 GPa. Right: relative formation enthalpies of AQH phases as a function of pressure against the constituent ices; inset shows covalent and hydrogen-bonded N-H separations in* $N_2H_7^+$.

P (GPa)	Space group
10	$P2_1$
50	$P2_1/m$
100	I4/m
200	I4/m
300	I4/m
400	I4

Table 5.1 *Summary of structure searches with 2-8 f.u. performed for AQH.*

The ammonium and ammonia molecules are hydrogen-bonded as $H_3N\text{-}H^+ \cdots NH_3$. As in the fully ionic AHH phases, the spherically symmetric oxygen anion can act as a very efficient hydrogen-bond acceptor: in the $P2_1/m$ phase of AQH, each oxygen atom accepts 12 hydrogen bonds from NH_3/NH_4 units. With

increased pressure, the ammonia-ammonium hydrogen bonds symmetrize; we find this transition to occur just above 60 GPa. Above this pressure, AQH contains symmetric $N_2H_7^+$ cations with a proton at the mid-point between two NH_3 molecules, thus forming a H_3N–H–NH_3 unit. Now in a higher symmetry tetragonal $I4/m$ structure, the $N_2H_7^+$ cations are stacked above each other along the c axis, but rotated by 90° to minimize steric repulsion and maximise hydrogen bonding to the oxygen anions, see Figure 5.2. Within the ab plane, the cations are in a herringbone arrangement for the same reason. The high hydrogen-bond coordinations of the oxygen atoms remain.

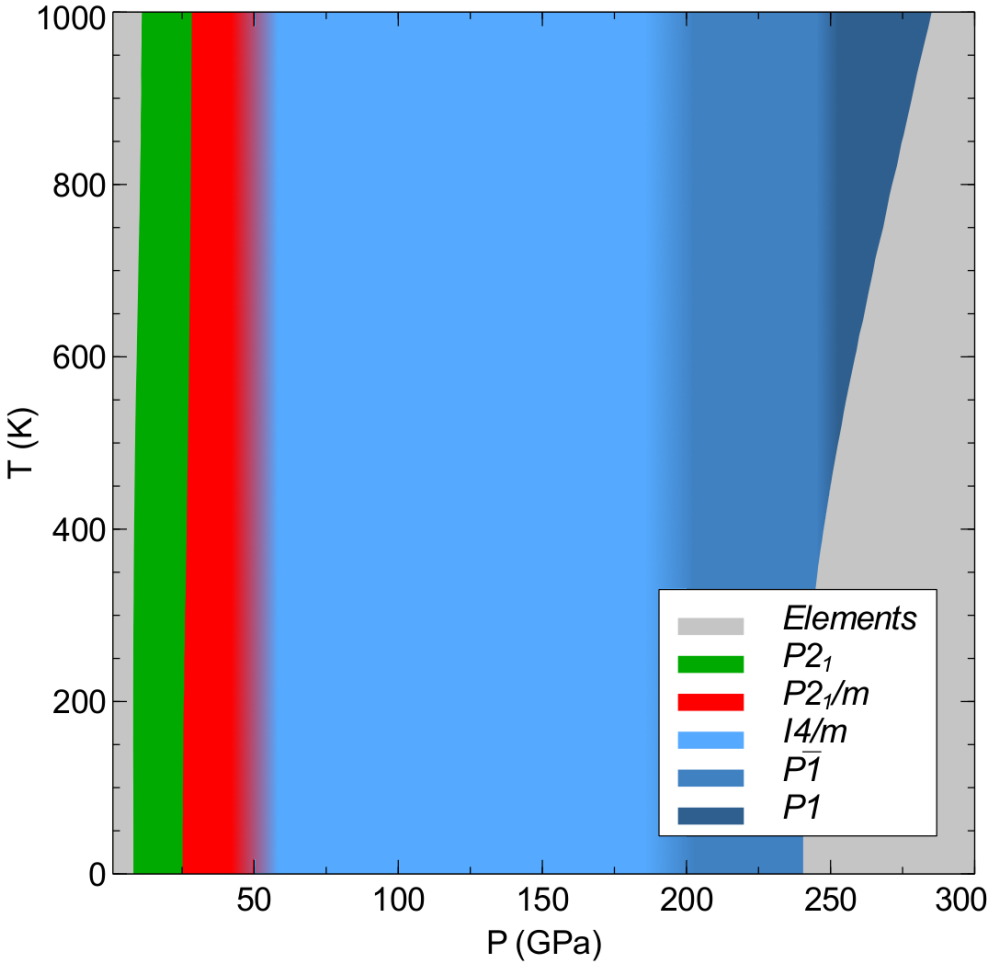

Figure 5.3 *$P-T$ phase diagram obtained using the harmonic approximation. The transition $P2_1/m \rightarrow I4/m$ is shaded.*

The $N_2H_7^+$ cation has not been seen before in any ammonia hydrates, but forms as part of the ammonia adduct of ammonium iodide, $NH_4I{\cdot}NH_3$ [249–251]. Very recently this unit has appeared in another in the study of high pressure ammonia hydrides [252]. At ambient conditions, the cation is in the symmetry-broken H_3N-

$H^+ \cdots NH_3$ state, and takes up a rotationally disordered position in a CsCl-like structure, together with the counterion I^-. In AQH, there are twice as many cations as O^{2-} anions, and the structure deviates from a simple ionic structure to optimize packing of the non-spherical $N_2H_7^+$ cations under compression.

With increased pressure, we find a sequence of symmetry-reductions to lower the enthalpy of AQH with respect to the $I4/m$ structure. Retaining the same ionic building blocks, two monoclinic $P\bar{1}$ and $P1$ phases are stable between 200 and 300 GPa. At 300 GPa, decomposition into the ices becomes favourable again, see Figure 5.2. The P-T phase diagram from harmonic free energies is shown in Figure 5.3. The structural sequence is unaffected by vibrational effects, but decomposition into the ices is predicted to occur slightly earlier than in the ground state, around 240 GPa at low temperatures.

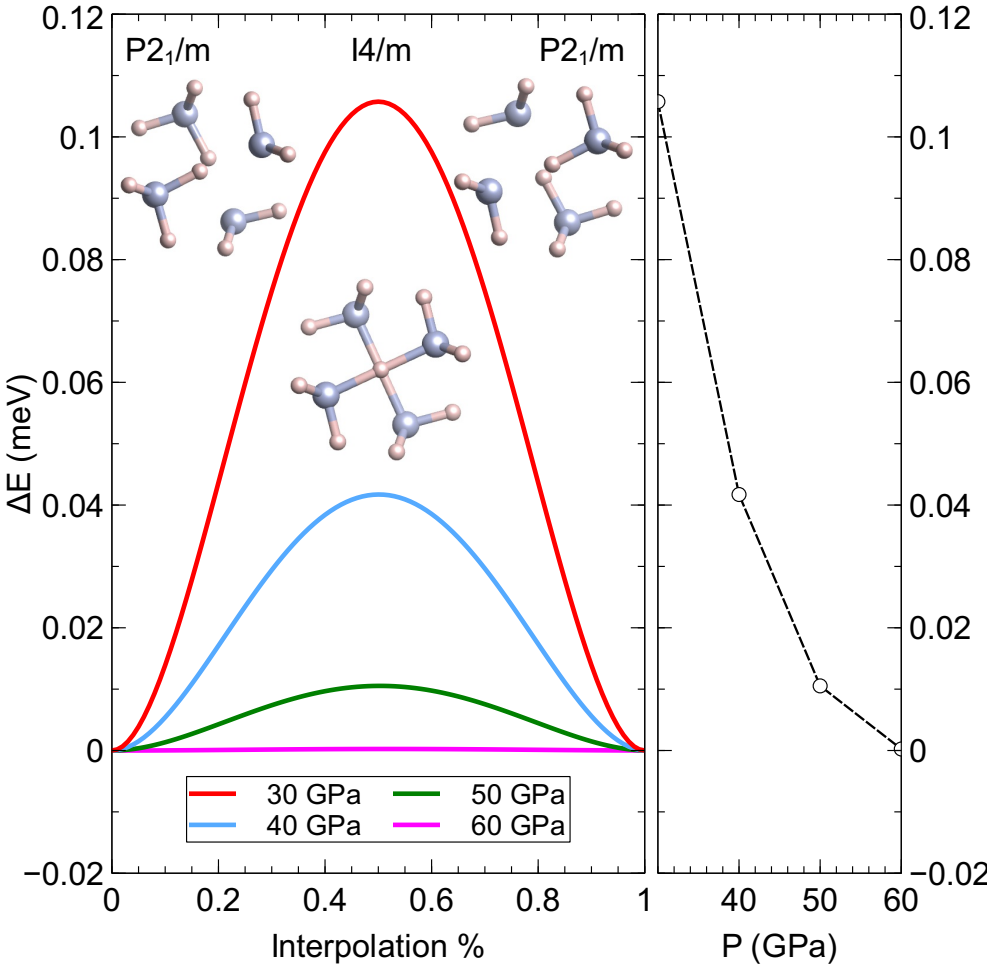

Figure 5.4 *Proton transfer energy landscape for linearly interpolating the $P2_1/m \rightarrow I4/m \rightarrow P2_1/m$ structures, and barrier heights as a function of pressure to estimate the energy barrier of hydrogen bond symmetrization in the H_3N–H–NH_3 units.*

We investigated the barriers towards the formation of the symmetric $N_2H_7^+$ cation by monitoring the covalent and hydrogen-bonded N–H separations in the low-pressure $P2_1/m$ phase (see inset in Figure 5.2) and by modelling the barrier of interconversion of H_3N–H$\cdots NH_3$ to $H_3N\cdots$H–NH_3 (see Figure 5.4). The N–H separations in the $P2_1/m$ structure equalize between 60 and 70 GPa. Likewise, the barrier of proton hopping along the hydrogen bond becomes negligibly small at 60 GPa. Nuclear quantum effects have the potential to lower such symmetrization barriers, as seen in ice and hydrous minerals [253, 254], and it is thus conceivable that AQH could be stabilised with symmetric $N_2H_7^+$ cations at 50 GPa or below. The Raman and infrared spectra is shown in figure 5.5 where modes for $P2_1/m$ can be seen softening as this symmetrization takes place, and then going to rise again once the $I4/m$ structure has been reached.

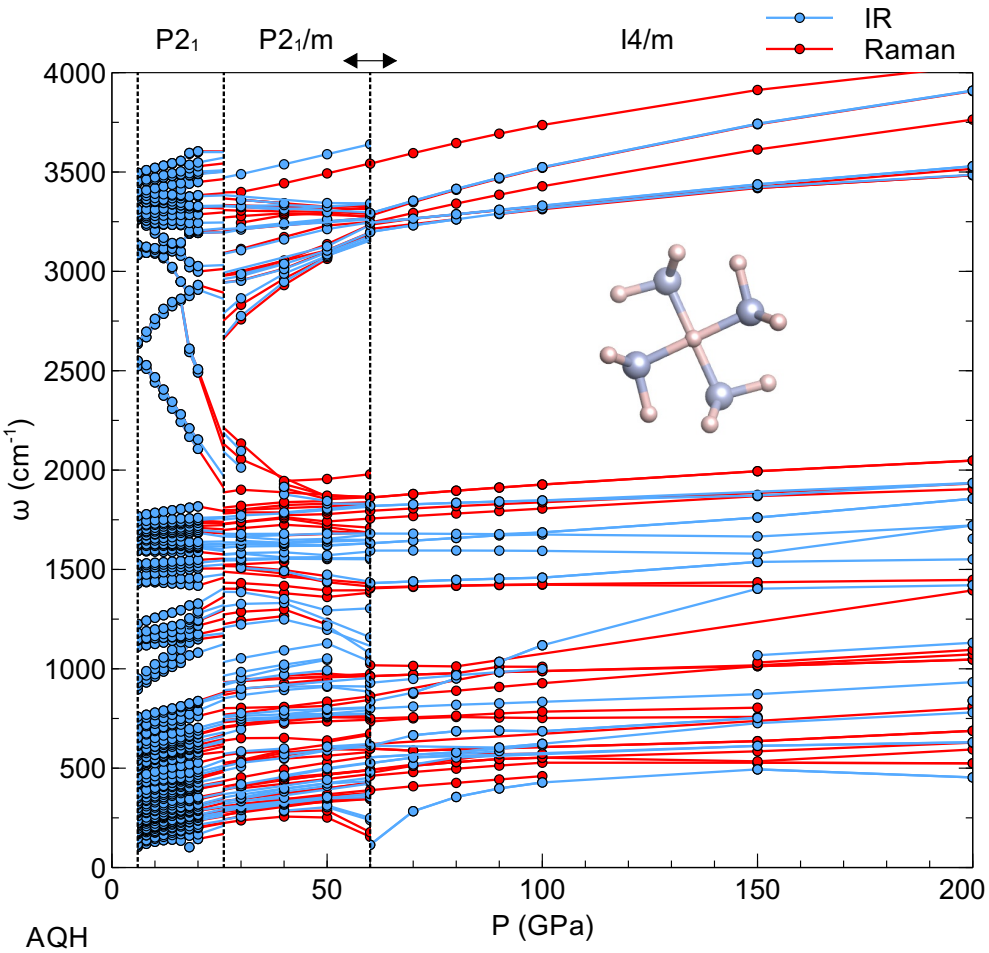

Figure 5.5 *Infrared and Raman active modes calculated for AQH phases as a function of pressure.*

5.2 Comparative Energetics of Ammonia Hydrates

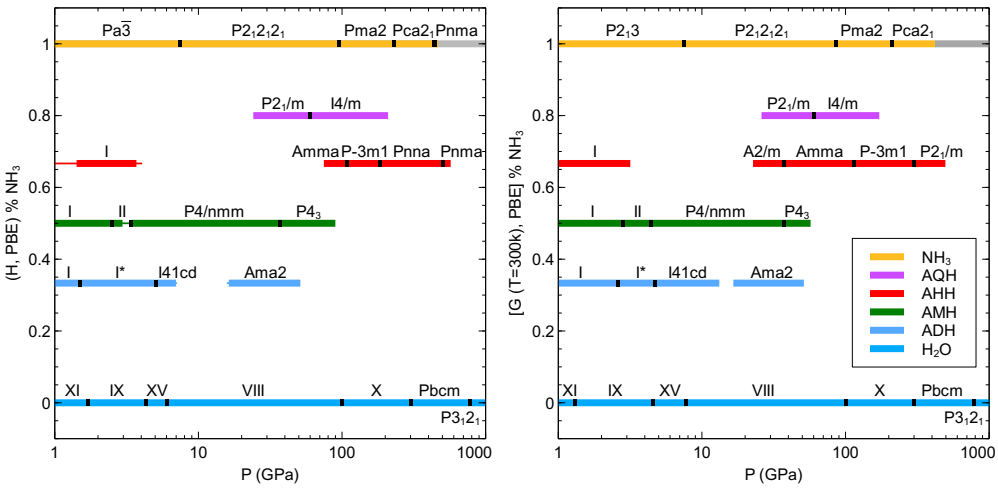

Figure 5.6 *Phase stability ranges for binary ammonia-water mixtures as a function of pressure, for the ground state (left) and at $T = 300$ K (right). Stable compounds are labelled by commonly used numerals or space groups, black lines signify phase transitions. For pure ammonia, the gray region denotes decomposition into NH_4 and N_3H_7. Thin lines denote pressure regions where a phase is metastable (here defined as 5 meV/molecule above the convex hull).*

By analyzing the information on individual compounds from the previous subsections as accumulated in the convex hull diagrams across the entire pressure regime, we can obtain individual stability ranges for all ammonia-water mixtures under pressure that consider every possible decomposition reaction. Those stability ranges are displayed in Figure 5.6, where we show both ground state and room temperature results. The latter include lattice vibrational entropic effects within the harmonic approximation, applied to all compounds. In both cases, coloured bars correspond to regions of stability of the various mixtures. Their endpoints (or intermediate gaps) signal that a specific mixture becomes unstable against one or more decomposition reactions, which we discuss below for every mixture involved.

In the ground state, we find AMH to be stable from $P = 1$ atm up to 85 GPa. The transition from AMH-I to AMH-II, in experiment seen around 0.5 GPa, happens in our calculations at 2.5 GPa. Above 85 GPa AMH decomposes into the highly stable ionic AHH phases and ice. The stability range of AMH is thus much smaller than if only the constituent ices are considered – Figure 4.16 would suggest that AMH is stable (in a sequence of new phases) up to 470 GPa; but the highly stable

ionic AHH phases make a decomposition into AHH and pure ice favorable above 85 GPa. Based on room temperature free energies, we predict that AMH should decompose at even smaller pressures, around 60 GPa. For the other hydrates, we find similar stability constraints due to non-trivial decomposition reactions.

We find ADH to be initially unstable, but stable in the region $P = 0.5 \ldots 6.6$ GPa, and $P = 17.2 \ldots 48.5$ GPa. Due to the emergence of half-ionic ADH-I*, the experimentally known phase ADH-II does not appear in our calculated phase diagrams. In the intermediate pressure region, and also above its maximum point of stability, ADH is found unstable against decomposition into AMH and ice. This agrees with experiment, which finds a strongly temperature dependent decomposition of ADH-IV into AMH and ice at pressures 2.5-6.5 GPa [255]. However, experiments find the ADH-DMA phase (which we do not model here) at pressures above 6.5 GPa [44, 47], which marks a re-entrant stability of ADH at high pressures. The newly found Ama2 phase represents such a re-entrant region of stability for ADH and is responsible in our calculations for an extension of ADH stability to almost 50 GPa.

AHH is found stable at $P = 1.5 \ldots 3.5$ GPa in the ground state and again from $P = 79 \ldots 540$ GPa, where decomposition into the ices eventually takes place. Here, the intermediate pressure instability is also due to the decomposition into AMH and ice. While AHH-I is correctly found stable, the high-pressure phase AHH-II does also not appear on the phase diagrams. In fact, we find both ADH and AHH unstable in certain regions of the phase diagram (at 6.6–17.2 GPa and 3.5–79 GPa) where neither has been found in experiment to decompose.

While these discrepancies could in part be due to our calculations not including satisfactory structural models for some of the phases relevant in these pressure regions (such as ADH-IV and ADH-DMA) we also find that calculated regions of instability are considerably smaller when considering room temperature free energies (12.5–17 GPa and 3–24 GPa). This suggests that the ionic $P4/nmm$-AMH structure is energetically very stable in the ground state (leading to spurious metastability of both ADH and AHH), but not so dominant at elevated temperatures. Note that we have not considered anharmonic corrections to the phonon frequencies in this work. Proton transfers are responsible for several of the new ammonia hydrate phases, and the vibrational properties of the different chemical species thus created might have different anharmonic correction terms. The anharmonicity of the O–H and N–H stretch modes most notably could lead to different ZPE terms and free energies that affect the relative stability of the

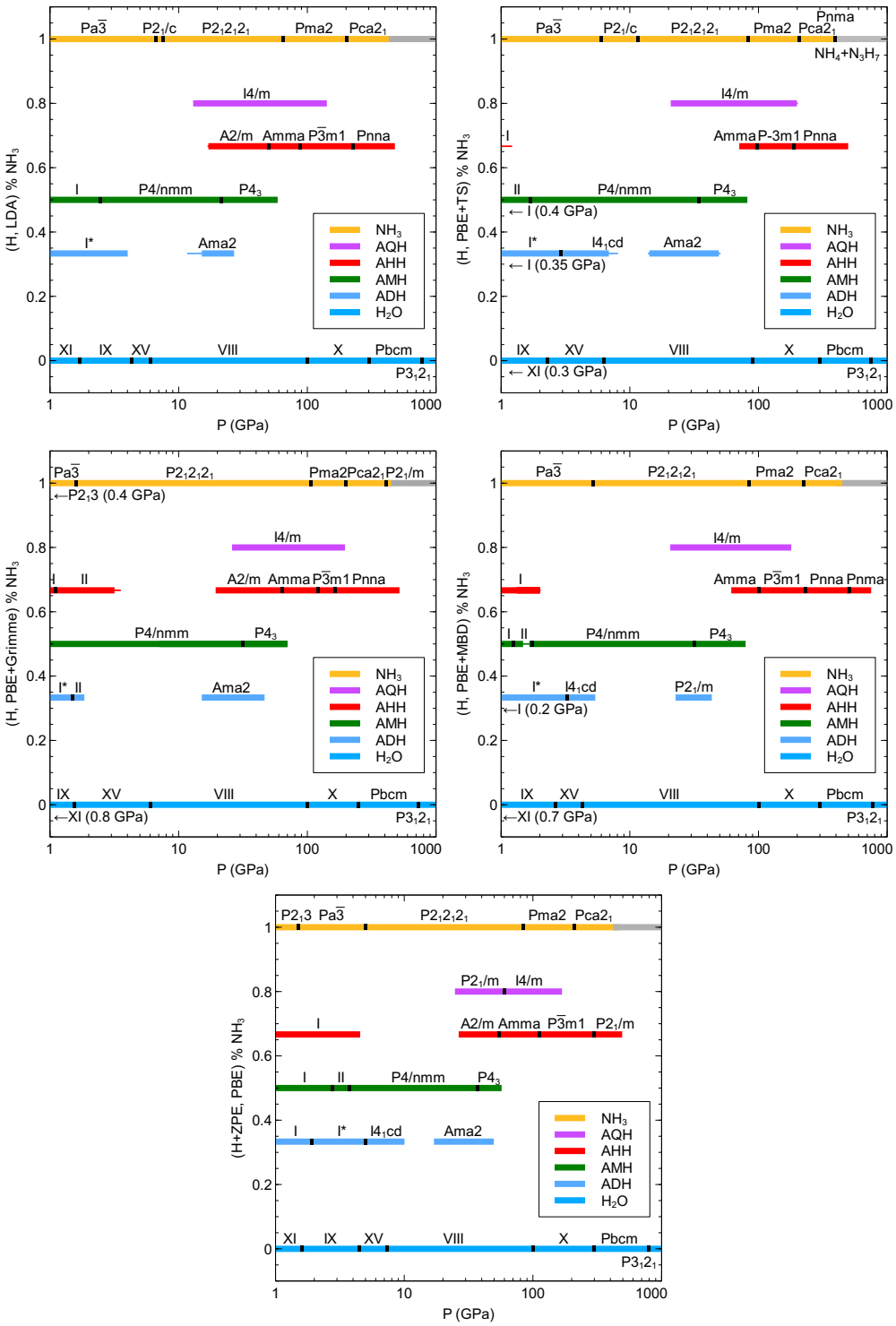

Figure 5.7 *Phase stability ranges for binary ammonia-water mixtures as a function of pressure, for the different exchange-correlation functionals indicated along the y-axis. Stable compounds are labeled by commonly used numerals or space groups, black lines signify phase transitions.*

half- or fully ionic phases [256, 257]. That said, it is also possible that low-temperature compression experiments on ADH and AHH might fail to overcome kinetic barriers towards decomposition into AMH and ice, just like compressed AMH itself might be unable to convert to the $P4/nmm$ phase [49].

The new AQH phase is stable in the ground state from 25.5 . . . 198 GPa. At either end of this pressure range, a decomposition into AHH and NH_3 is more stable than AQH. Like AHH, the AQH structures across their stability range benefit from strong ionic interactions and high coordination upon the formation of the unusual $N_2H_7^+$ cation. It seems plausible that AQH can be formed in a high-pressure synthesis reaction of a 2:1 molar mixture of pure ammonia and AHH.

The discrepancies between our calculations and the experimental phase diagrams for both ADH and AHH hydrates in the low-pressure regions might also be contributed to by the semilocal exchange-correlation functional that has been argued to overstabilize ionic structures [240]. This could lead to spurious stabilisation of ADH-I* over ADH-II, and of AMH-$P4/nmm$ over both ADH and AHH. However, the relative stabilities of the different hydrates are qualitatively unaffected for various other exchange-correlation functionals; in figure 5.7 we show phase diagrams equivalent to Figure 5.6 obtained from the LDA functional as well as from dispersion-corrections of the Grimme (D2), Tkatchenko-Scheffler (TS), and many-body dispersion (MBD) type [87, 89, 90]. While the density-based dispersion corrections of the vdW-DF2 type (e.g., in the form of revPBE-vdW2) and the meta-GGA SCAN functional have been shown to give very good results for the high-pressure phase sequence of molecular ices [258–260], it is not clear whether this also applies to other molecules and mixtures such as those studied here. For hydrogen hydrates, the PBE functional returns more accurate phase stabilities than dispersion corrections of the vdW-DF type, [261, 262], while for noble gas hydrates it shows less overbinding than any dispersion-corrected functional [263]. At pressures beyond the molecular phases (from 10's to 100's of GPa, as considered here) the semilocal description of PBE should become even more appropriate, as electron densities tend to become more uniform [264], and non-bonded interactions become very similar amongst competing quasi-close-packed structures [265].

5.3 Equations of State

The equations of state for the four mixtures that were found stable, as well their constituent components of water and ammonia are shown in figure 5.8. Dashed lines refer to the linear mixing ratio of H_2O–NH_3 under compression. It is likely that the most stable phases lie further below the separately linearly interpolated volume.

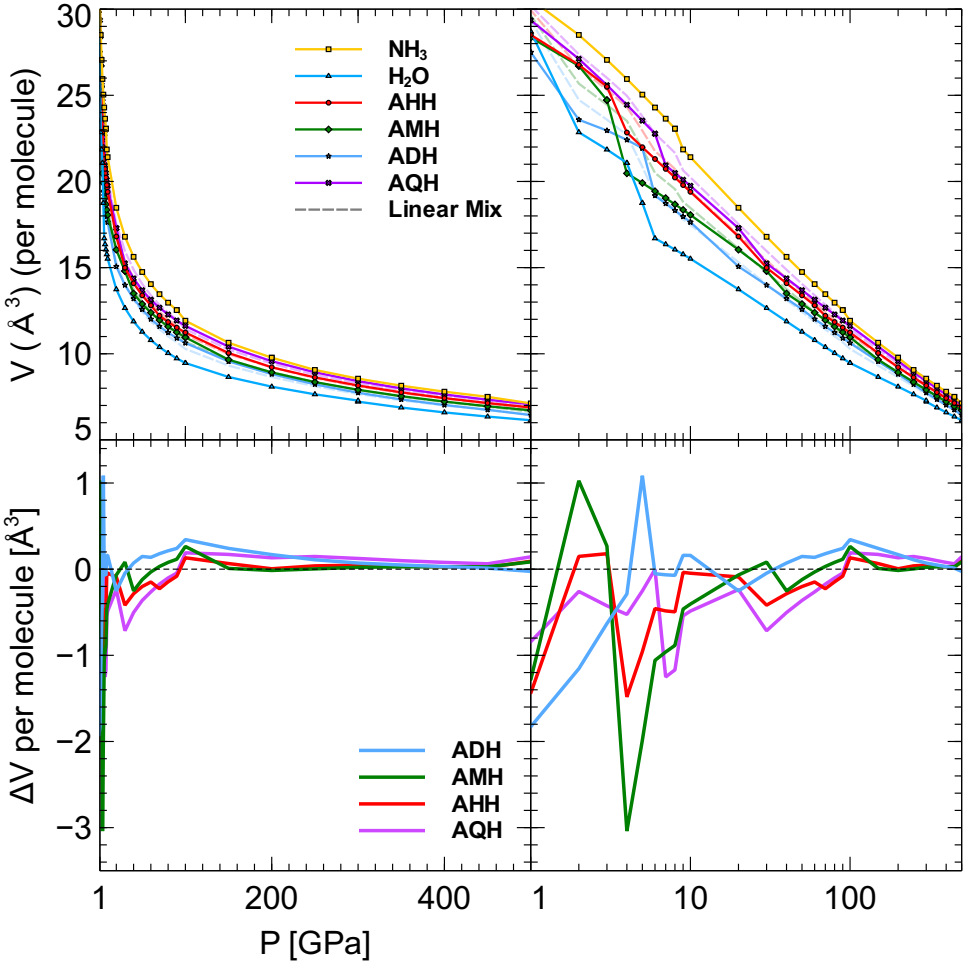

Figure 5.8 *Equations of state for the ammonia - water ice system, including all mixtures discussed in this work. Top are the equations of state on a linear (top left) and logarithmic scale (top right), as well as the linear mixing ratio volume for each mixture. Below we show the deviations from the linear mixing ratio on linear (bottom left) and logarithmic (bottom right) scales.*

However, when plotting the differences from the linear mixing ratio in figure 5.8, it is seen that this is only true below 100 GPa. This is perhaps due to the formation of ice-X and NH_3 forming ionic crystals and so the competing constituent ices

are much denser from here on. This implies that the stability of the hydrates beyond 100 GPa is due to U, the internal energy. This is consistent with all phases benefiting from ionic bonding under pressure which we explore further in the next section. All mixtures deviate mildly from the linear mixing ratio over the pressure range. For a liquid, these lines would be smoother, as crystals restrict degrees of freedom and lead to sudden discontinuous volume changes on phases transitions. It is likely that the deviations from the linear mixing would be within 1 percent for the liquid system.

5.4 Ionic Motifs Under Pressure

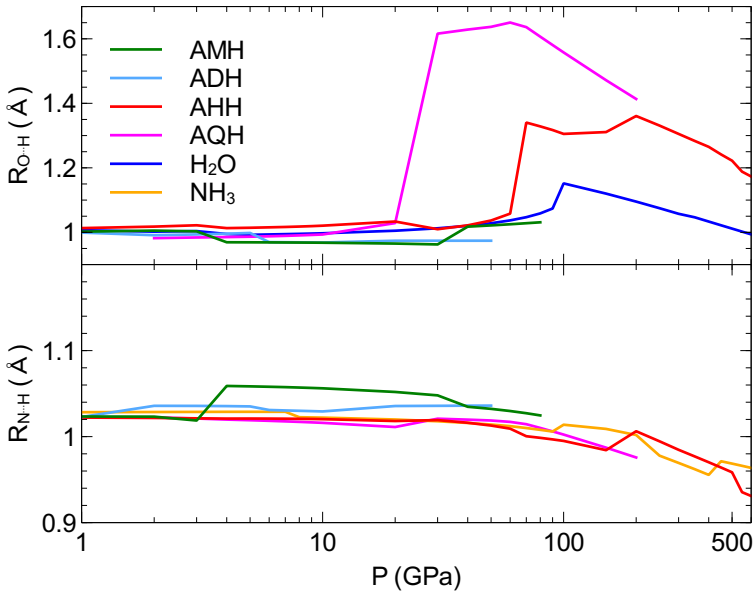

Figure 5.9 *Nearest-neighbor O–H (top) and N–H (bottom) separations across all ammonia hydrates and ices, in their respective most stable ground state phase as a function of pressure.*

Across all phases, ionization emerges as a clear pathway towards stability with increased pressure. All newly presented phases in the known hydrate stoichiometries, as well as the new ammonia quarterhydrate, benefit from proton transfer from water to ammonia. If the overall composition permits, water molecules tend to be fully deprotonated and the hydrates then comprise ionic motifs of the form $O^{2-}\cdot(NH_4^+)_2$ or $O^{2-}\cdot(N_2H_7^+)_2$ that are supported by copious hydrogen bonding. The cationic molecular units are very stable; none are predicted to undergo changes until the hydrates themselves decompose. In all cases, electrostatic contributions and more compact packing outweigh the energy cost of the ionization reactions. In Figure 5.9 we visualize the nearest-neighbor O–H and N–H separations across all relevant compounds as a function of pressure. The graphs are jagged because of internal phase transitions, but both trends and distinct changes in chemistry can be identified. The shortest O–H and N–H separations usually form covalent bonds that are quite incompressible and relatively independent of the particular structure. However, overall the N–H bonds tend to shorten with pressure, while the O–H bonds tend to remain constant or even lengthen; a sign of weakening of covalent O–H bonds under pressure. Very prominent rapid increases in $R_{\mathrm{O-H}}$ are visible at the onset of ice-

X in H_2O at 100 GPa; and the onset of fully ionic AHH and AQH phases around 30 and 70 GPa, respectively. All three events share the complete disintegration of the water molecule; in the hydrates, they signal the formation of hydronitrogen cations. At higher pressures, overall compression will shorten R_{O-H} again. The most prominent jump in R_{N-H} (much smaller in magnitude) is the appearance of the ionic $P4/nmm$ phase in AMH at 4 GPa, and signals that the covalent bonds in NH_4^+ are longer than in NH_3.

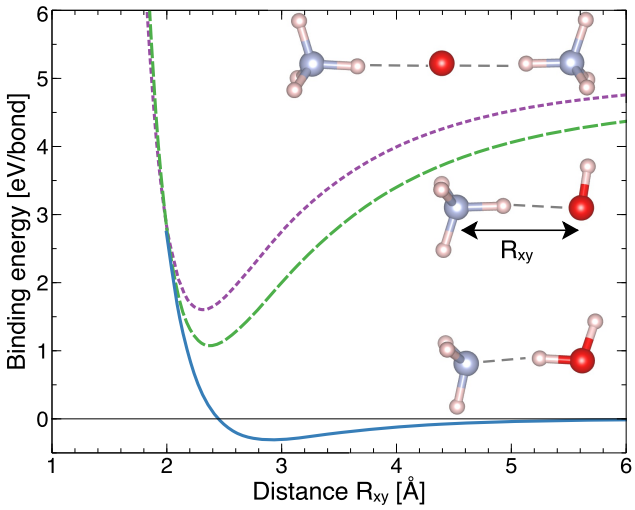

Figure 5.10 *Binding energies of water-ammonia dimers and trimers from PBE calculations, relative to neutral gas phase molecules, and normalized per hydrogen bond. Blue solid line: $HOH\cdots NH_3$; green dashed line: $H_3NH\cdots OH$; purple dotted line: $H_3NH\cdots O\cdots HNH_3$. Geometries are shown as insets.*

To further rationalize the successive deprotonation of water molecules in these hydrates under pressure we performed molecular calculations on selected water-ammonia dimers and trimers, using the Gaussian09 software package and aug-cc-pVTZ basis sets [266, 267]. In the gas phase (at large distances), the proton transfer reaction $H_2O + NH_3 \rightarrow OH^- + NH_4^+$ is endothermic by about 8 eV, and the second proton transfer, resulting in $O^{2-} + 2NH_4^+$, costs another 16 eV. However, electrostatic attraction largely makes up for this cost. As can be seen in Figure 5.10, the minima of the potential energies of $H_3NH\cdots OH$ and $H_3NH\cdots O\cdots HNH_3$ are only 1.4 and 1.9 eV per hydrogen bond above the minimum of the neutral hydrogen-bonded $HOH\cdots NH_3$ dimer. These metastable minima occur at smaller R_{N-O} separations than the most stable minimum but, crucially, these ionised structures have lower energies than the neutral dimer at small separations. Ultimately, at the smallest separation and along the repulsive part of the potential energy surface, fully de-protonated water is the most stable

configuration. While these simple models can not fully explain the behaviour of extended phases, where mutual coordination and other energy contributions are significant, they corroborate the behaviour seen in the compressed ammonia hydrates.

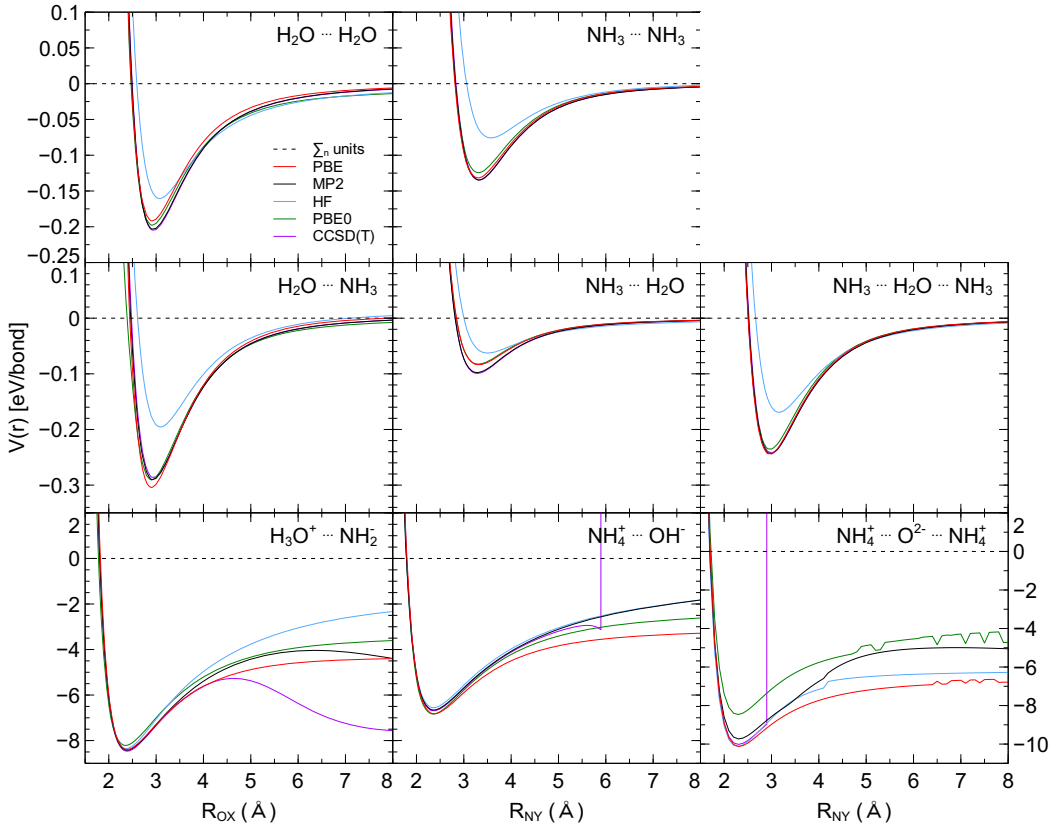

Figure 5.11 *Interaction potential energy surfaces for dimer and trimer setups taken from ammonia water crystals or the lowest energy representation calculated at different levels of theory.*

Other dimer setups found in ammonia-water crystals were also calculated and the potential energy surfaces are shown in figure 5.11. There are 4 different molecular dimers, and then 4 corresponding ionic dimers, however only combinations of ammonia and water were chosen for ionic dimers. Trimers of $NH_3 \cdots H_2O \cdots NH_3$ and $NH_4^+ \cdots O^{2-} \cdots NH_4^+$ were calculated due their occurrence at high pressure where ammonia-rich hydrates are stabilized by O^{2-} anions. Problems were encountered for ionic calculations combined with MP2 and CCSD(T). Here the minima were calculated correctly, but at greater, separation the calculated potential has maxima and turns over, seen in figure 5.11.

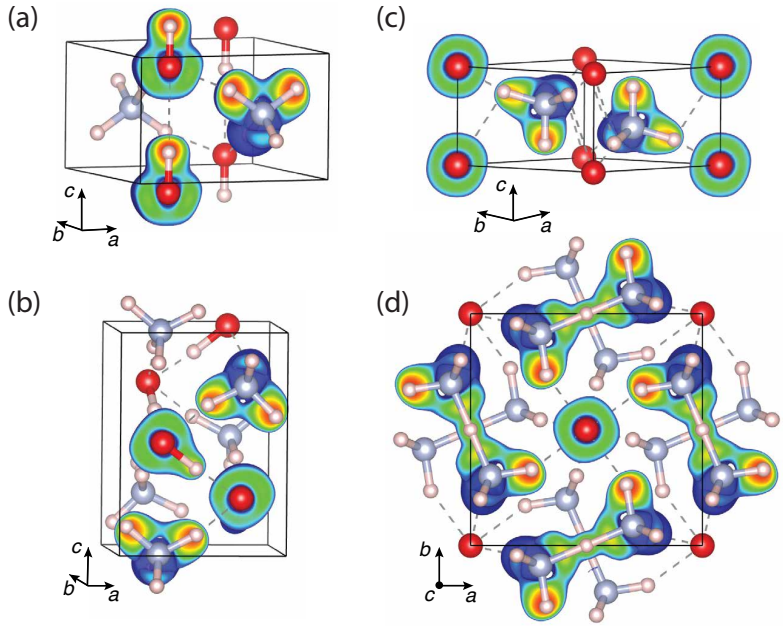

Figure 5.12 *Isosurfaces of the electron localisation function (ELF=0.7) in ammonia hydrates, together with cross sections from ELF=0.7 (blue) to ELF=1.0 (red). (a) AMH-P4/nmm at 10 GPa, (b) AMH-$P4_3$ at 100 GPa, (c) AHH-$P\bar{3}m1$ at 200 GPa, (d) AQH-I4/m at 100 GPa. All structures drawn to the same scale. Hydrogen bonds are indicated by dashed lines.*

The chemical interpretations, based so far on geometrical arguments and suggestive drawing of bonds, are corroborated by topological real-space analyses of the electronic charge density and the electron localization function (ELF) [140, 268, 269]. These real-space scalar fields are obtained with the VASP code in conjunction with hard projector-augmented wave (PAW) frozen core data sets [270, 271]. In Figure 5.12 we show ELF isosurfaces and cross sections for some of the most relevant structures across the different hydrates. These support the interpretation of the various atomic and ionic molecular units discussed so far: AMH structures feature localised OH^- and NH_4^+ groups; AHH and AQH feature near-spherical isolated oxygen anions and counterions NH_4^+ and $N_2H_7^+$, respectively.

Structure		n_{basin}	b.i.p	ELF	Partial charges	
AMH-$P4/nmm$	V(N,H_{8i})	2.066	N-$H_{8i}\cdot\bullet\cdot$O	0.244	q(NH_4)	+0.736
(10 GPa)	V(O,H_{2c})	1.643	d_H=0.539	d_O=1.136	q(OH)	-0.736
	V(O)	6.093				
			O-$H_{2c}\cdot\bullet\cdot$O	0.053		
			d_H=0.766	d_O=1.312		
AMH-$P4_3$	V(N,H_1)	2.092	N-$H_1\cdot\bullet\cdot$O	0.315	q(NH_4)	+0.683
(100 GPa)	V(N,H_2)	2.091	d_H=0.456	d_O= 1.011	q(OH)	-0.683
	V(N,H_4)	2.072	N-$H_2\cdot\bullet\cdot$O	0.353		
	V(N,H_5)	2.062	d_H=0.438	d_O= 0.994		
	V(O,H_3)	1.593	N-$H_4\cdot\bullet\cdot$O	0.351		
	V(O)	6.090	d_H=0.437	d_O=0.994		
			N-$H_5\cdot\bullet\cdot$O	0.278		
			d_H=0.462	d_O=0.997		
			O-$H_3\cdot\bullet\cdot$O	0.507		
			d_H=0.371	d_O=0.955		
AHH-$P\bar{3}m1$	V(N,H_{2d})	1.987	N-$H_{6i}\cdot\bullet\cdot$O	0.487	q(NH_4)	+0.650
(200 GPa)	V(N,H_{6i})	2.121	d_H=0.365	d_O= 0.912	q(O)	-1.299
	V(O)	7.299				
			N-$H_{2d}\cdot\bullet\cdot$N	0.314		
			d_H=0.454	d_N=0.954		
AQH-$I4/m$	V(N,H_{4c})	2.032	N$-\bullet-H_{4c}$	0.848	q(N_2H_7)	+0.655
(100 GPa)	V(N,H_{16i})	1.999	d_N=0.906	d_H=0.305	q(O)	-1.309
	V(N,H_{8h})	1.899	N-$H_{16i}\cdot\bullet\cdot$O	0.267		
	V(H_{4c})	0.422	d_H=0.506	d_O=1.053		
	V(O)	1.309	N-$H_{8h}\cdot\bullet\cdot$O	0.221		
			d_H=0.548	d_H=1.089		

Table 5.2 *Valence charge density analysis of ammonia hydrates based on the ELF partitioning of space.* n_{basin} *is total valence charge in each ELF basin; b.i.p.'s as sketched are characterised by their distances d to nearest atoms, and their ELF value; and partial charges q are summed up for the subunits discussed in the text.*

A quantitative analysis of the same data is summarised in Table 5.2, this analysis was performed by Dr. Miriam Marqués at the University of Edinburgh using the Critic code [141]. The topological analysis first identifies the critical points of the charge density and ELF scalar fields, i.e., points where their gradients vanish [269]. These are then classified as maxima, first- or second-order saddle points, or minima. The unit cell is unambiguously partitioned into topological atoms, defined by the union of the electron density maxima with their attraction basins and delimited by zero-flux surfaces. The density maxima are usually located at the nuclei, while the first-order saddle points (denoted bond critical points,

b.c.p.) usually correspond to chemical bonds, within the quantum theory of atoms in molecules [234, 272]. The electron density and its Laplacian at the b.c.p.'s can be used to characterize the bond strengths and their character. An equivalent partition of space based on the ELF also yields non-overlapping, space-filling basins with well-defined chemical interpretations: atomic shells, covalent bonds, and lone pairs. By definition, ELF is a relative measure of the electron localization with respect to the homogeneous electron gas (HEG) and its values are bound between 0 and 1.0, with 0.5 the value of the HEG. ELF commonly exhibits maxima and, in general, approaches 1.0 in the regions of space where electron pairing occurs.

We studied here not only the distribution of ELF maxima but also its first-order saddle points (called bond interaction points, b.i.p.), which can be used to establish connectivity between ELF basins and to characterize the chemical bonding. We also integrate the valence electron charge density over the distinct ELF basins of the hydrates' unit cells. This gives an effective charge associated with each ELF maximum, and thus partial charges associated with the different molecular subunits. Bonding between these units is analysed in terms of the b.i.p.'s: their locations and ELF values allow clear distinctions between covalent and hydrogen bonds present in these systems.

From Table 5.2 we first see that the covalent N–H and O–H bonds (where present) hold roughly 2.0 and 1.6 electrons each; the respective interpretations as NH_4 and OH units are justified. The partial charges on NH_4 ($+0.65 \cdots 0.74$ electrons) and N_2H_7 (+0.655) are consistent with a +1 formal charge (in NaCl the same analysis yields ± 0.85 electrons per ion). Likewise, partial charges on OH ($-0.68 \cdots 0.74$ electrons) and O (-1.3 electrons) are consistent with formal charges -1 and -2, respectively. The dashed lines shown e.g. in Figure 5.12 all have b.i.p.'s along the respective (O/N)-H$\cdots$(O/N) connections but these have very low ELF values, between 0.05 and 0.5; this is consistent with their interpretation as hydrogen bonds.

The strength of the hydrogen bonds is, in fact, determined by these ELF values, or, more precisely, by the difference between the ELF value at the b.i.p. separating core and valence of the proton donor AH (typically lower than 0.2) and the ELF value at the hydrogen bond interaction point defined as the b.i.p. linking the proton donor V(A,H) and proton acceptor V(B). A positive value for this difference, also called the core-valence bifurcation index, corresponds to weak hydrogen bonds, whereas negative values for this difference characterize medium

and strong hydrogen bonds [273, 274]. An extreme case appears on the N_2H_7 subunit, where the central H atom has its own detached monosynaptic basin with a population of 0.42 e^- and is strongly connected to the N atoms either side (ELF=0.848 at the b.i.p.). Therefore, this symmetrical very strong hydrogen bond can be considered as a true chemical bond. A similar bonding image has been found in ice X along the O-H-O line [245]. A Bader analysis, based purely on the topology of the electron density, gives the same results shown in table 5.3: partial charges on the different subunits are consistent with their formal charges stated throughout; strong covalent bonds exist within the subunits (with high densities, strongly negative Laplacians at the bond points), and they are connected by multiple hydrogen bonds (with low densities, weakly positive Laplacians at the bond points).

		n_{basin}	b.c.p.	ρ	$\nabla^2\rho$	Partial charges	
AMH-$P4/nmm$	H_{8i}	0.5169	H_{8i}-N	0.3138	-2.0817	$q(NH_4)$	+0.6985
	V(N)	6.2341	d_H=0.2593 d_N=0.7969			q(OH)	-0.6985
	V(O)	7.6985	H_{8i}-O	0.055	0.1159		
			d_H=0.5485 d_O=1.1211				
			H_{2c}-O	0.0182	0.0701		
			d_H=0.7686 d_O=1.3094				
AMH-$P4_3$	H_1	0.4709	H_1-N	0.34666	-2.3302	$q(NH_4)$	+0.6765
	H_2	0.4855	d_H=0.2280 d_N=0.79427			q(OH)	-0.6765
	H_4	0.4756	H_1-O	0.0930	0.2206		
	H_5	0.5115	d_H=0.4627 d_O=0.9996				
	V(N)	6.3800	H_2-O	0.1025	0.2291		
	V(O)	7.3479	d_H=0.0.4429 d_O=0.9810				
			H_4-O	0.0994	0.2324		
			d_H=0.4432 d_O=0.9811				
			H_5-O	0.0877	0.2494		
			d_H=0.4648 d_O=0.9897				
			H_3-O	0.1328	0.0197		
			d_H=0.3825 d_O=0.9424				
AHH-$P\bar{3}m1$	H_{6i}	0.4850	H_{6i}-O	0.1513	0.2245	$q(NH_4)$	0.6337
	V(O)	7.2674	d_H=0.3727 d_O=0.6766			q(O)	-1.2674
	V(N)	6.9114	H_{2d}-N	0.1044	0.3113		
			d_H=0.4570 d_O=0.9506				
AQH-$I4/m$	H_{4c}	0.5015	H_{4c}-N	0.2028	-0.5230	$q(N_2H_7)$	+0.6498
	H_{16i}	0.5666	d_H=0.3288 d_N=0.8823			q(O)	-1.2997
	H_{8h}	0.5788	H_{16i}-O	0.0761	0.1986		
	V(N)	6.2124	d_H=0.5093 d_O=1.0486				
	V(O)	7.2996	H_{8h}-O	0.0655	0.1720		
			d_H=0.5502 d_O=1.0816				

Table 5.3 *Bader QTAIM analysis for ammonia hydrates.* n_{basin} *denotes valence charge density integrated in each basin. Bond critical points (b.c.p.'s) are sketched out and characterised by their charge density* ρ*, Laplacian* $\nabla^2\rho$*, and separation from nearest atoms. Partial charges* q *for the different subunits come from sums of* n_{basin} *as appropriate.*

5.5 Conclusions

In summary, we have presented here a comprehensive computational study across the binary composition range of ammonia-water mixtures, as a function of compression. Chapter 4 highlighted a series of new phases stable in ammonia monohydrate, AMH, that were not considered before; presented a similar series of phases in ammonia hemihydrate, AHH, that are fully ionic solids; and suggest a sequence of new high-pressure phases for ammonia dihydrate, ADH. By sampling arbitrary binary ammonia-water mixtures we predict a new ammonia-rich compound, ammonia quarterhydrate or AQH, to become stable in an experimentally accessible pressure range. AQH features the unusual $N_2H_7^+$ cation above 60 GPa.

Compounds, where proton transfer from water to ammonia is limited by the number of acceptor ammonia molecules (ADH and AMH), are found to be stable only up to moderate pressures, about 1 Mbar, whereas compounds that allow full deprotonation of water (AHH and AQH) are stable to much higher pressures. The latter compounds feature cationic hydronitrogens, NH_4^+ and $N_2H_7^+$, that persist until the respective hydrates are predicted to decompose completely. Mixtures of ammonia and water thus choose a unique chemical response to compression: they combine water's propensity to give up its protons with ammonia's tendency to form ionized hydrogen-bonded structures.

We have shown that it is insufficient to study the phase transformations of individual hydrates, as their respective stability is mostly limited by decomposition into combinations of other hydrates, and not the constituent ices. By considering all these decomposition reactions, and finite temperature effects at the harmonic level, we were able to construct the full phase diagram of all ammonia hydrates at specific pressure and temperature conditions. Those findings are qualitatively unaffected by our choice of exchange-correlation functional.This phase diagram shows reasonable agreement with experiment regarding stabilities, phase transitions, and decomposition reactions amongst molecular hydrate phases at low pressures, even though the roles of DMA phases and unresolved hydrate structures such as AMH-IV and ADH-IV should be explored further.

At high pressures, the formation of fully ionic solids will have consequences for the finite temperature behavior of these phases. If strongly bound molecular cation motifs persist up to high pressures, partial melting of the mixtures (e.g.

the formation of superionic phases) might be shifted to higher temperatures, or even replaced by the formation of ionic liquids upon melting. This, in turn, will influence thermal and electric conductivities of any such mixture along icy planet isentropes. Testing these assumptions is the focus of the next chapter.

The trend that emerges here with pressure, towards the formation of ammonia-*rich* hydrates, is intriguing, as it runs counter to the cosmic abundance ratio of ammonia and water. It could suggest that all ammonia-water mixtures separate into water ice and ammonia-rich hydrates under sufficient compression. The latter would always be less gravimetrically dense than pure water ice and could therefore contribute to more complex inner structures in the mantles of icy planets than hitherto considered. Now we have considered the T = 0 K phase diagram for the ammonia water mixtures we can proceed from their stability to their finite temperature properties. In the next chapter, we will build from these stable phases and perform ab initio molecular dynamics simulations to assess the finite-temperature phase diagram of the mixtures and emergent properties.

Chapter 6

Ab Initio Molecular Dynamics

So far we have investigated the Ammonia-Water system in the ground state. Approximations were used, such as harmonic approximation, to predict free energies at finite temperature, but the dynamics at finite temperature remains to be investigated. Previously we have seen that ionization is the major stabilizing driving-force for mixtures under pressure, but will this remain true at temperature? Importantly what phase do these mixtures form for the Pressure, Temperature conditions found in icy planets such as Uranus and Neptune - is the mantle a superionic solid or liquid?

All mixtures are expected to transition into a superionic regime and eventually melt when heated sufficiently. This is true for NH_3 and H_2O separately [21], discussed in chapter 3, and previously calculated for AMH and ADH, [207, 229]. Plastic phases previously discussed also exist for the separate ices and should be kept in mind. Here we investigate the four mixtures we found to be stable: (ADH, AMH, AHH, AQH) with ab initio molecular dynamics (AIMD). Properties to investigate include melting, characteristics of the liquid, superionic transitions, molecularity vs ionicity, which chemical species exist, anisotropies between N and O, OH and NH bond life-times. General analysis tools include radial distribution functions, mean squared displacements, and diffusion coefficients. In total 1.528 nanoseconds of AIMD was trajectories were accumulated. Discussion of results starts by looking at the phase diagrams for individual mixtures. Experimentally these mixtures enter an alloy phase of DMA or DIMA [46, 49] at relatively low pressures and temperatures and we do not attempt to model the substitutional disorder in this work. This could be approached using Monte Carlo methods

for swapping molecular units in combination with total energy evaluations using classical potentials as the statistics require great sampling. Setting up AIMD initial conditions from BCC crystals with randomly assigned O or N based units can also be considered as investigated in [49], which may affect superionic transition and melting temperatures.

6.1 Previous Work

Previous AIMD studies on high temperature ammonia water mixtures include [207, 229] and a lower temperature study on AMH [49]. These works provide comparison as well as useful technical details and have different initial conditions. Studies of ammonia and water separately have been discussed in chapter 3 and can also be compared with results obtained in this work. A simple picture might expect results for mixtures to lie somewhere linearly in-between results for the separate ices. This seems to roughly hold for the EOS of molecular mixtures [241].

In the study of Bethkenhagen et al. [229] superionic behavior and melting were investigated for the 1:1 mixture AMH. As previously discussed in chapter 4, three high pressure phases (Ima2, Pma2, and Pm) were predicted using an evolutionary structure searching approach with XtalOpt [127] as a starting point for AIMD in planetary conditions. Shown in figure 6.1 is the resultant phase diagram which also compares with ammonia and water superionic data from earlier work. Here the diffusion coefficients for the mixture were compared to ammonia and water and found to be similar in the superionic regime.

The water-rich 1:2 mixture ADH was investigated by Jiang et al. [207] up to 40 GPa using a classical structure searching approach to predict new crystal phases with a Monte Carlo packing algorithm from POLYMORPH [276]. A new phase of $I4_1cd$ was found stable over 15 GPa as previously discussed in chapter 4. This phase was heated to explore the likely superionic transition. This phase has a very large unit cell, the discovery aided by using classical searching methods, and so requires very large simulation cells (192 molecules in the conventional cell, and a 2x1 supercell of 384 molecules was used in MD) for molecular dynamics runs. This study also notes that the kinetic contribution to the stress tensor has not been considered when reporting PT conditions for the AIMD results. From proton mean squared displacement (MSD) analysis a superionic transition line

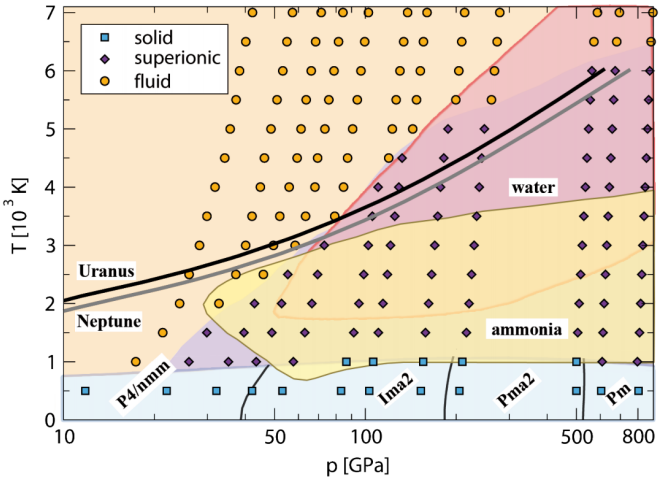

Figure 6.1 *Phase diagram for AMH calculated from AIMD, taken from [229]. Yellow and red shaded regions refer to the superionic phase space for ammonia and water respectively [198, 275]. Symbols are along isochores in T-P space including the thermal pressure. Different symbols indicate solid (blue squares), superionic (purple diamonds), and fluid (orange circles) states. Solid-Solid (black lines) phase boundaries are based on phonon free energy calculations. Adiabats for Uranus and Neptune indicate the T-P path expected inside these icy planets.*

was found between 4 and 40 GPa shown in figure 6.2. Remarkably they report the transition in which protons become 'obviously mobile' to occur at 2.45 GPa and 480 K which is a much lower temperature than the 1:1 mixture and the separate ices. Interestingly the first point for the superionic transition lies above the experimental melting line by about 240 K at 2.5 GPa (melting at 240 K experimentally). The MSD for N,O ions at 4 GPa is not provided in this study so it is not possible to tell if this in a liquid state or a super-heated solid.

In the work of Liu et. al [49] on AMH simulations were used in combination with experiments. The solid DMA phase was of most interest to this study and so simulations focused on studying this, and at temperatures below superionicity and melting. AIMD simulations, continued from classical potentials or randomly generated BCC initial conditions, were used to generate vibrational density of states which could be compared with experimental IR and Raman data. Simulation boxes contained 128-432 molecules with a lattice constant of $a = 3.320$ Å. Both showed evidence of neutral molecular H_2O and NH_3 units as well as ionic OH^- and NH_4^+ units.

Simulations of mixtures of H_2O, NH_3, and CH_4 were performed in previous studies, investigating the bonding properties in [277] and the linear mixing

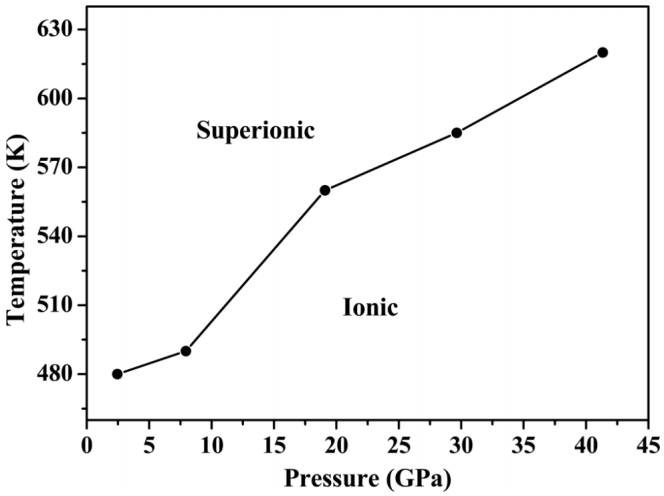

Figure 6.2 *Superionic transition phase diagram for ADH calculated from AIMD, taken from [207]. The ionic region refers to the solid $I4_1cd$ ADH phase.*

approximation in [241]. These simulations were performed at high temperatures and pressures, hot enough (20,000 K) to be within the molten state and so address liquid properties. This does not require knowledge of the solid phase diagram which is mostly unknown. Binary mixtures such as H_2O:CH_4 were used as well as ternary mixtures. Individual molten ice simulations could be compared with these mixtures to evaluate the linear mixing approximation find a deviation from the ideal linear mixing ratio of amounting to only -1% to 4%.

In chapter 4 an improved ground state stability is shown for AMH and ADH, and in chapter 5 the energetics of different mixtures reveal the stability of mixtures with pressure. This further motivates AIMD to be performed with the new structures and to compare results to these previous studies. In AMH and ADH more stable solid structures may subdue superionic transition and full melting temperatures.

6.2 Phase Diagrams

The PT phase spaces for AIMD were chosen for mixtures based on their enthalpic stability found in chapter 5 resulting in the phase diagrams shown in figure 6.3. For example, the most stable high pressure mixture of AHH was considered up to 600 GPa. The isentropes for Neptune and Uranus are included and data from previous studies are shown for AMH and ADH. Solid-solid phase boundaries from free energy calculations in chapter 3 were used. Further simulation details are listed in the appendix. For all mixtures, we find regions of solid phases, rotating or plastic solids, superionic, and finally liquid phases with temperature evolution. These states were classified by inspecting the MSD as in figure 6.4. Phases found between the solid and superionic regime are referred to as excited phases and described in more detail in section 6.3.

For ADH, simulations were chosen to have the same number of molecules (up to 432) as in [207] for consistent comparison and to accommodate the unit cell of the large $I4_1cd$ phase. As the superionic transition was reported at lower temperatures and pressures where a fine grid of PT points from 100–1000 K was chosen. On heating units were observed to rotate and at higher temperatures form superionic phases as expected. In comparison with the previous work, we find the solid–liquid melting transition between the first two points (500 K, 2 and 8 GPa) of the reported superionic transition showing the previously claimed superionic region is likely to be in a fluid state. In the $I4_1cd$ phase we find a transition starting between 500–600 K and 14 GPa in agreement with Jiang et al. however the transition is too excited phases and not the superionic regime.

Care must be taken when simulations are run for less than 2 ps which can lead to misleading MSD extrapolations. For the $I4_1cd$ phase we find the superionic transition higher in temperature, between 700–800 K. Higher in pressure the $Ama2$ phase is found more stable than $I4_1cd$, which has higher transition temperatures into the excited and superionic regions. For phase $P2_1/m$ no excited phases were found but could occur between 1000 or 1500 K. Results partly agree with Jiang et. al with differences in details of the transition conditions, the nature of the thermally excited phase, and show more stable phases can subdue these temperature-induced phase transitions.

Simulations of AMH were performed covering a smaller pressure range than the work of Bethkenhagen et al. [229] in temperature increments of 500 K.

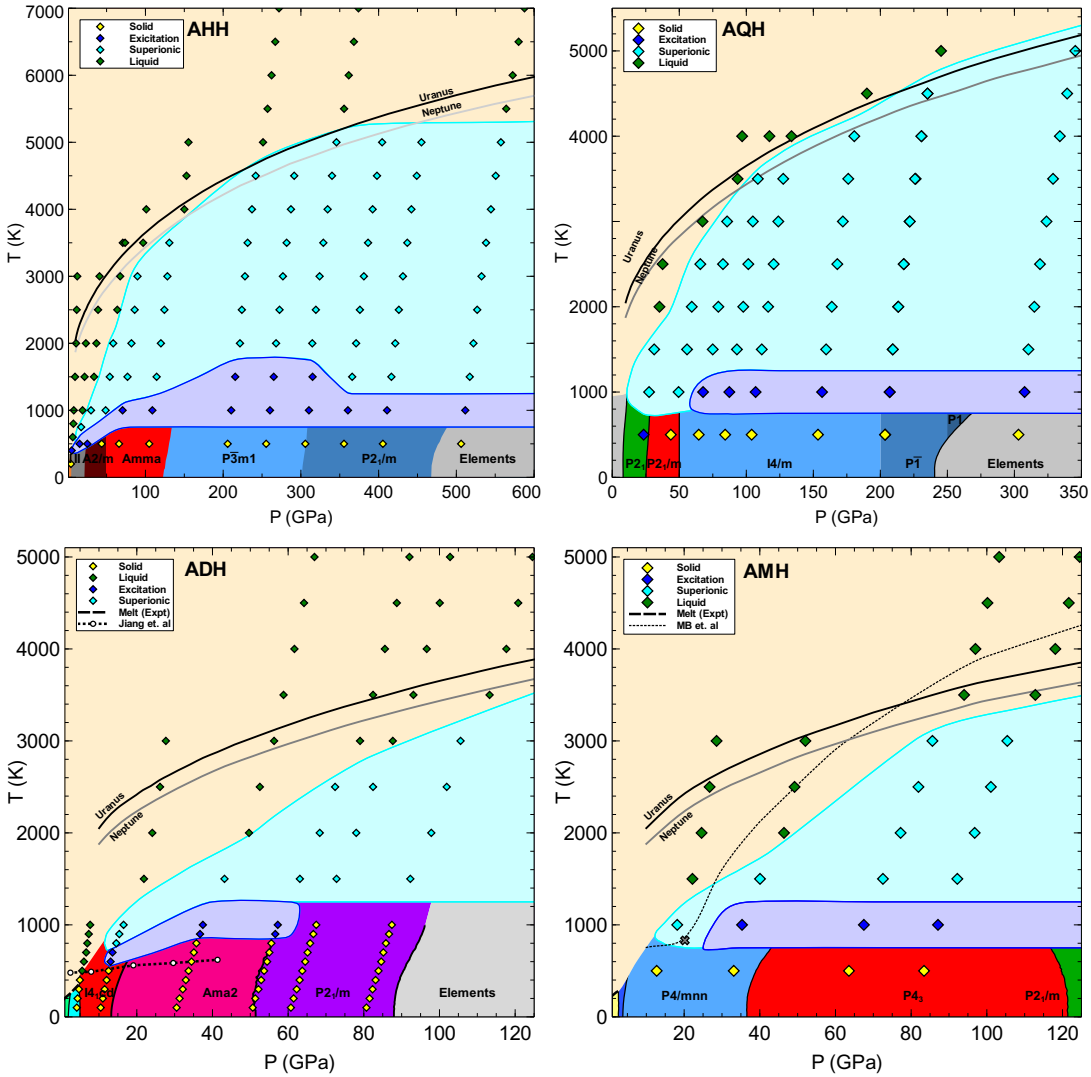

Figure 6.3 *Phase diagrams for the four mixtures in their region of stability. Dark blue and cyan shaded regions refer to excited (rotations and or ionised) systems and the superionic phase respectively. Orange shaded region is the liquid while solid phases are labeled and colored individually. Grey shaded region is the calculated decomposition the constituent ices of NH and OH. Experimental melt lines for ADH and AMH are from [48]. For AMH the grey cross notes the AMH triple point from [241] and the dash line represents the melt line from the same study. For ADH the dashed line with white diamonds represents the superionic transition line found in [207].*

While Bethkenhagen et al. used 32 molecules per cell, our simulations used 144-288 molecules per cell in each run. The differences between the simulations are the run-time, AIMD parameters, initial starting phase beyond $P4/nmm$ and the number of molecules. Results show different melting lines, superionic temperatures and in our case the emergence of excited phases. For the $P4/nmm$ phase starting from 10 GPa and heating this work does not show melting to occur

until 1500 K compared to 1000 K in Bethkenhagen et al. suggesting this PT point may be super-heated and wants to melt. This discrepancy is interesting as more molecules were used in this study, which normally leads to more accurate melting temperatures, though the total run-times afforded by using fewer molecules may lead to reaching the equilibrium state of the liquid.

At 30 GPa and above we find that at 1000 K AMH enters excited rotating phases (see figure 6.4) and is not yet superionic in contrast with the assignment by Bethkenhagen et al. In fact the superionic transition is not observed until 1500 K above 30 GPa. Above 30 GPa the melting line is found to be lower in temperature than reported by Bethkenhagen et al. This difference is interesting as more stable phases were used such as $P4_3$ which might be harder to melt and a greater number of molecules were used in our simulations making it easier to melt, suggesting this difference is likely due to the phases being super-heated. It seems unlikely that the less enthalpically stable phases found in previous work would lead to a higher temperature melt line. For all mixtures, the discovery of more stable phases, via predictive methods and experiments, could further stabilize high pressure phases around the isentropes of Neptune and Uranus and perhaps subdue the melting temperature further.

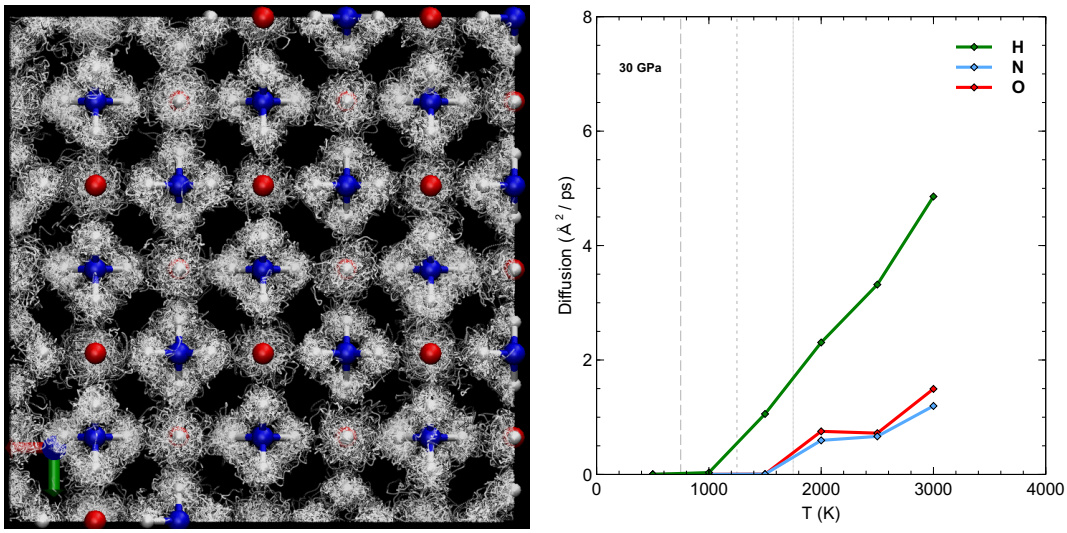

Figure 6.4 *AIMD data for AMH-P4/nmm at 30 GPa, left: proton trajectories for 10 ps run at 1000 K. Right: Diffusion constants for different atomic species as a function of temperature. Long dash / short dashed / dotted lines denote onsets of excited / superionic / fluid regimes.*

The solid phases of AHH were heated up to 500 GPa as this covers the pressure region where AHH is relevant among the water-ammonia mixtures. Supercell

details are included in the appendix. For AHH every phase entered an excited regime upon heating before either melting or becoming superionic and then eventually melting. Between 200 and 300 GPa the excited phases extend up to 1500 K, higher than other mixtures. The melting line appears to flatten out above 300 GPa causing the superionic phases to not include the isentropes of Uranus and Neptune above this pressure.

In AQH the phase diagram includes heated solid phases up to 300 GPa. Again most phases enter an excited regime at 1000 K above 60 GPa and then enter the superionic regime before eventual melting. Interestingly the $P2_1$ phase exhibits excited behavior at a modest temperature of 500 K and 20 GPa. This phase is in the low pressure regime where AQH is less stable and perhaps this allows for less tightly bound units with weaker interactions or greater free volume within the unit cell, allowing for rotations and temporary charge transfers. Above 100 GPa and 300 K the superionic region appears to be just stable along the isentropes of Uranus and Neptune.

6.2.1 Superionic Regions

Superionicity is an interesting region of phase space for ices as celestial icy bodies are likely to exhibit this behavior.

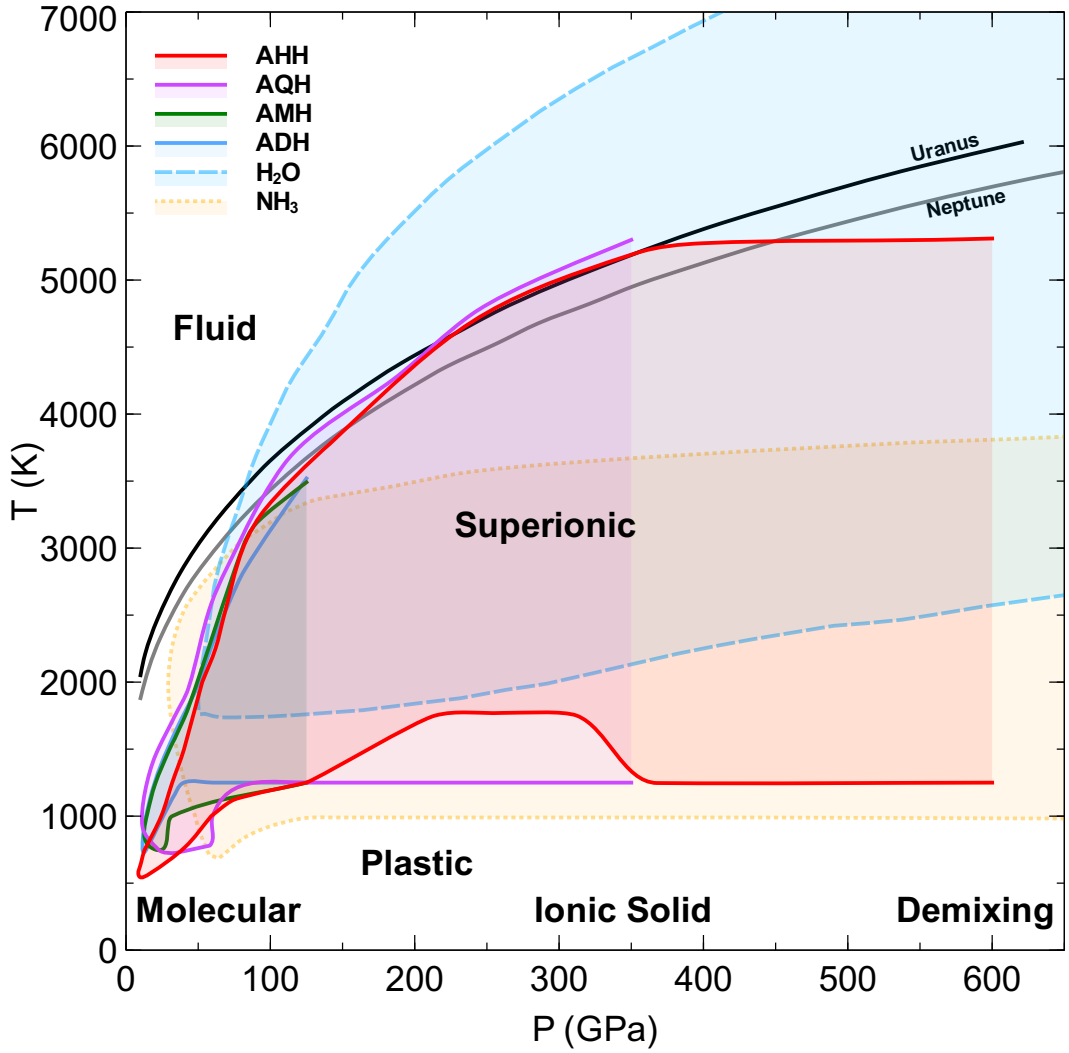

Figure 6.5 *Superionic regions for all four mixtures, and data for the individual ices is taken from [198, 275]. The highest shown pressure for each mixture corresponds to the AIMD PT grid used and roughly corresponds to their limit of stability.*

Water by itself remains the most stable ice compared with ammonia and their mixtures at high temperatures and high pressures (decomposing over 5 TPa) in figure 6.5 and appears to require the highest temperature to enter the superionic regime. The story is somewhat different in the recent work of Hernandez et. al [192] who identify the H_2O solid-superionic-liquid triple point at 16 GPa and 810 K. Differences exist due to the criterion used to designate superionicity and

the grid of P T values chosen for simulations.

Ammonia has a solid-superionic-liquid triple point at roughly 25 GPa and 1500 K from the work of [239] which does not report on any plastic phases in their AIMD simulations. Cavazzoni et. al [21] show quite a different phase diagram with a solid-plastic-liquid triple point around 10 GPa and 400 K reporting a more stable plastic regime. These two triple points are consistent along the melting line but disagree on whether the solid is in a superionic or plastic regime below 1500 K at 25 GPa.

For the mixtures, the solid-superionic-liquid triple points all occur below 30 GPa and 1000 K. For AHH the triple point appears around 10 GPa and 600 K however this is a plastic-superionic-liquid triple point unlike the other 3. Further simulations on a finer grid around these triple points would help identify exactly what type and where the triple points are for these mixtures similar to that of water [192]. The AQH triple point is around 10 GPa and 900 K though this temperature is likely lower than 900 K as no actual melting AIMD simulations were performed below 10 GPa and so the melting line is extrapolated below this pressure. For ADH the triple point occurs around 12 GPa and 800 K though data suggests this could also be a plastic-superionic-liquid triple point. For AMH the triple point occurs around 12 GPa and 850 K.

For ADH a fine grid was used up to 1000 K though with less simulation time due to a large number of atoms and so there is less sampling of equilibrium states yet the triple point is found to be similar to the other mixtures. In figure 6.5 we see AHH has the superionic transition shifted to a higher temperature between 150 and 350 GPa likely due to the strong ionic bonding these phases offer. The mixtures are all found to enter a plastic or excited regime which shifts up the superionic transition temperature with this intermediate state. In general, the mixtures have a superionic region that occupies mostly the same PT space. At lower pressures and temperatures the mixing of ammonia and water can lead to enhanced proton transfer and is likely the cause for lower PT requirements to enter the superionic regime than for water and ammonia separately. A quantitative analysis of the superionic regions is presented later in this chapter.

6.2.2 Melting Lines

Inspecting figures 6.5 and 6.6 the melting lines for mixtures appear to closely follow those of ammonia and water separately up to 100 GPa as expected from previous work. Above 100 GPa ammonia melts at much lower temperatures than water for example at 300 GPa ammonia melts around 3500 K and water at 6500 K in figure 6.5. In this higher pressure region, the mixtures appear to melt directly in between these for example at 5000 K at 300 GPa. Notably, the triple points of the mixtures appear at lower P T conditions in agreement with previous studies likely due to the favorable proton dynamics the mixed system offers. The calculated melt line also finds the mixed ice to be solid in the region of the Neptune and Uranus isentropes above 70 GPa.

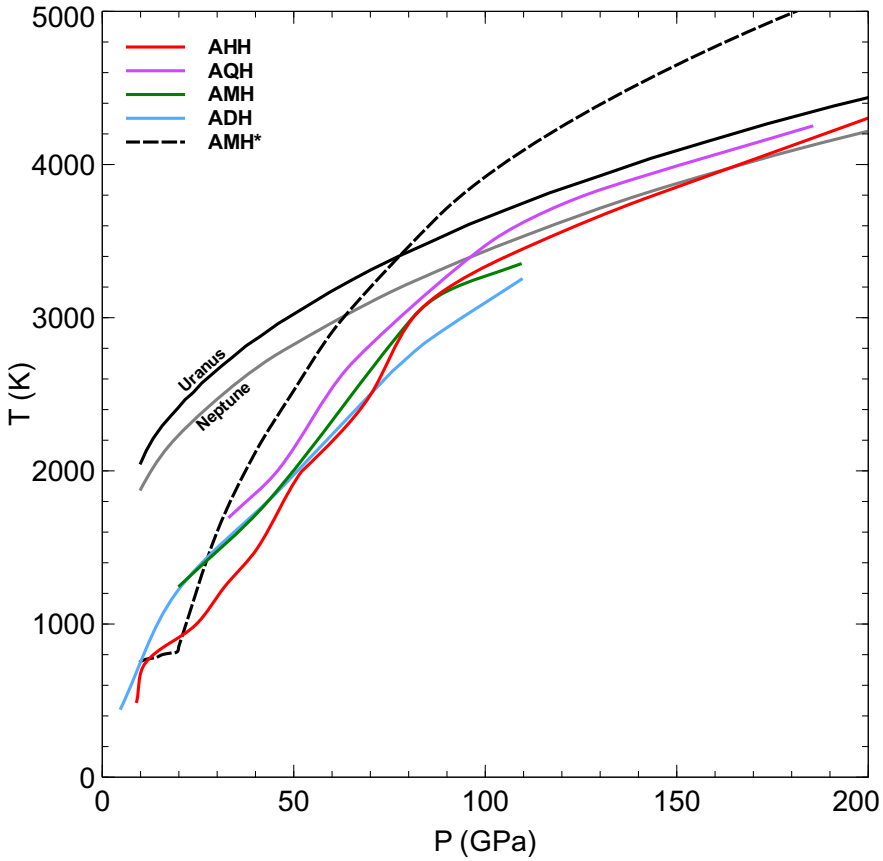

Figure 6.6 *Combined melt lines for all four mixtures and the melting line for AMH* from [229].*

In figure 6.6 the melting lines for the different hydrates are compared with previous data on AMH and one another. On the resolution of the PT grid chosen with steps of 500 K above 1000 K the melting lines are very similar above 50 GPa, rarely differing by more than 600 K. In the regions where a mixture is more stable,

the melting line appears to be higher. For example, ADH and AMH have higher melting lines below 50 GPa where they are more dominant on the binary convex hull. At higher pressures, AHH and AQH are more stable and have higher melting lines although ADH and AMH melt lines were not calculated above 100 GPa. In comparison with data by Bethkenhagen et. al [229] (labeled AMH* in figure 6.6), all melt lines in this work above 30 GPa are lower and likely indicate a systematic difference in how these were calculated such as finite-size effects and determination of melting by the MSD. The melt lines are close to the isentropes of Neptune and Uranus and so more precisely determining the melt line above 50 GPa could be of further interest. Investigating other melting methods such as the Z-method, annealing, thermodynamic integration, and phase-coexistence could aid this determination.

Both AHH and AQH have melting lines close to the isentropes of Neptune and Uranus (see figure 6.3). Melting lines were calculated using a "heat until it melts" method which has the shortcomings of super-heating and so is likely to over-estimate the melting temperature. This implies that along the Neptune and Uranus isentropes mixtures are likely in a liquid state. However, if these structures are still able to form an alloy at high PT conditions then this entropic gain may increase the stability of the superionic phase and push up the melt line. Furthermore, an ammonia-rich alloyed phase may take a different ammonia mixing ratio than 2:1 or 4:1 which can enhance the solid and superionic stability further.

6.3 Excited Region: Plastic and Warm Phases

Low pressure phases for AMH, ADH, and AHH have configurationally disordered phases, typically NH_3 molecules where the hydrogen bonding is the weakest and are the least tightly bound. Simulations starting from ordered approximants of these phases (for example AHH-I) may expect to find an order-disorder transition as observed in experiment at sufficiently high temperatures. When systems exhibit solid diffusion (where the system remains solid but slow diffusion of atoms of molecules may take place) of O and N sites, such as AHH-II, this can mean the crystal is close to melting or wants to undergo a phase transition. As the DMA/DIMA phase has been observed experimentally with substitutional disorder this is something to consider during analysis. The solid diffusion could be substitutionally disordering the BCC (or otherwise) crystal itself which is consistent with experiment, or entering a high temperature phase with a different symmetry or even trying to melt. These can be sensitive to the simulation time that was afforded, which can lead to superheating and a lack of sampling equilibrium states with AIMD. Simulations for ADH between T = 100–1000 K used a large number of atoms and were run for under 2 ps which may not be enough to see what kind of diffusion is occurring. For the mixtures of ices, the situation is more complicated as there are many different structural setups and sources of proton attraction.

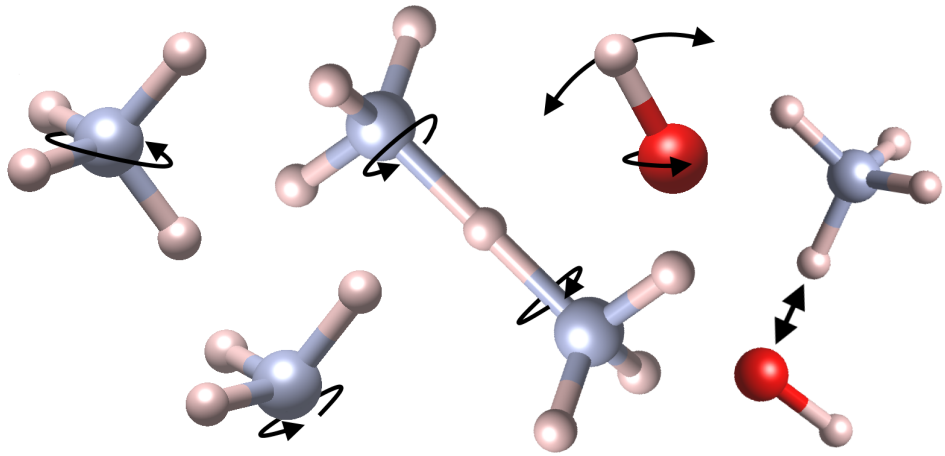

Figure 6.7 *Example movements of the excited phases at temperatures lower than the superionic regime. Left shows rotational modes for various unit types; Right shows temporary proton transfer.*

Visualizing low temperature simulations, being temperatures lower than the superionic regime but hot enough to sample excitations, reveals molecular and

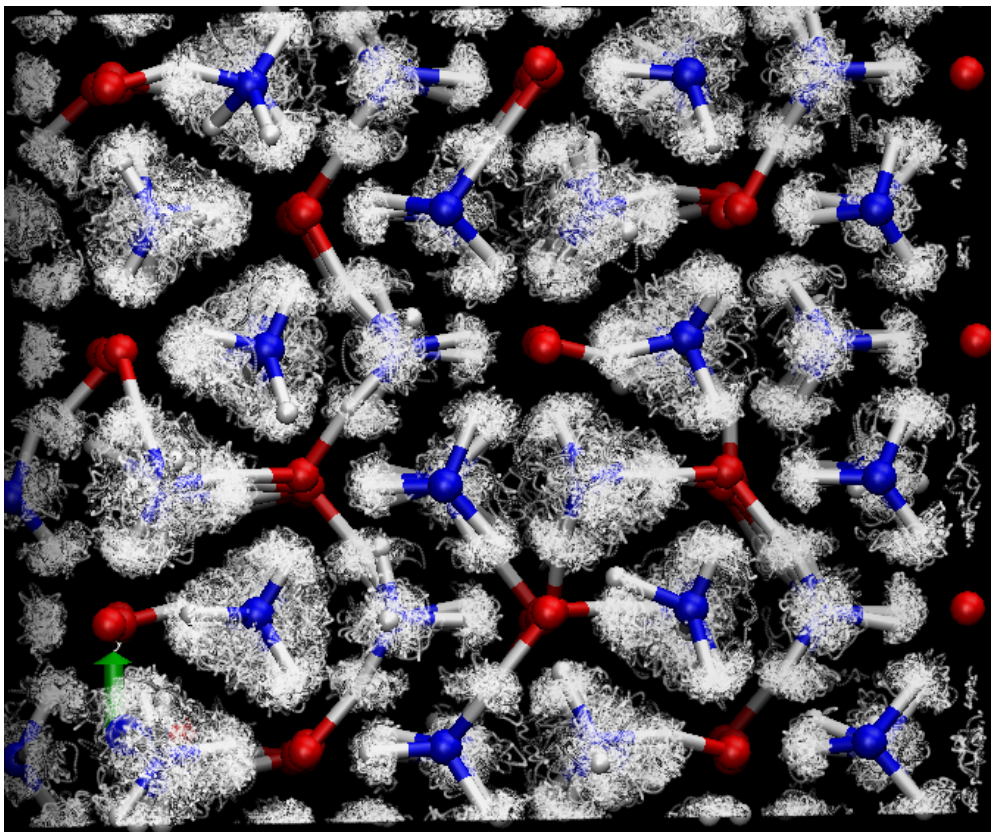

Figure 6.8 *Snapshot of AHH at 500 GPa and 1000 K with the proton trajectory for 5 ps shown as points. During the simulation some NH_4^+ units undergo rotations as well as temporarily donating a proton. Bonds are drawn between N,O and protons with a cutoff distance of 1.1 Å for the final trajectory step.*

ionic rotation, temporary charge transfer, and solid N-O diffusion shown in figure 6.7, before entering a clear superionic phase. These 3 events lead to increased proton mean squared displacement but with lower diffusion coefficients than with superionic protons. For a system of rotating molecules, the MSD should increase initially and oscillate around a converged value where protons are halfway from their maximum displacement. Rotations may be as quasi-free rotors, as in the plastic phase, or jumps/translations leading to configurational disorder. Proton transfer may occur either temporarily for example in the dynamic equilibrium with units of $NH_3 + H_2O \rightleftharpoons NH_4^+OH^-$ and returning to a molecular state and vice versa. Alternatively a different proton than the newly acquired proton transfers to another neighbour. This hopping mechanism, aided by quantum tunneling, exists in low temperature ices already [278], but with a very low diffusion rate.

Quantitative counting of translation and rotation rates could be performed

P (GPa)	T (K)	Phase	Description
3	200	I	NH_3 rotations
3	400	I	NH_3 and H_2O rotations
10	500	II	Rotation and ionization
10	750	II	Rotation and ionization
10	1000	II	Liquid
20	500	II	Rotation and ionization Substitution between O,N sites
20	1000	II	Superionic Substitution between O,N sites
20	1500	II	Liquid
40	1000	$A2/m$	Superionic along BCC diagonals
60	1000	$Amma$	Rotation and $NH_3 + H_2O \rightleftharpoons NH_4^+ + OH^-$
100	1000	$Amma$	Rotation and $NH_3 + H_2O \rightleftharpoons NH_4^+ + OH^-$
350	1000	$P\bar{3}m1$	Rotation and $NH_3 + H_2O \rightleftharpoons NH_4^+ + OH^-$
400	1000	$P\bar{3}m1$	Rotation and $NH_3 + H_2O \rightleftharpoons NH_4^+ + OH^-$
500	1000	$P\bar{3}m1$	Rotation and $NH_3 + H_2O \rightleftharpoons NH_4^+ + OH^-$
500	1500	$P\bar{3}m1$	Superionic

Table 6.1 *Summary of visual analysis of the dominant events in AHH-AIMD at temperatures below and across the superionic regime.*

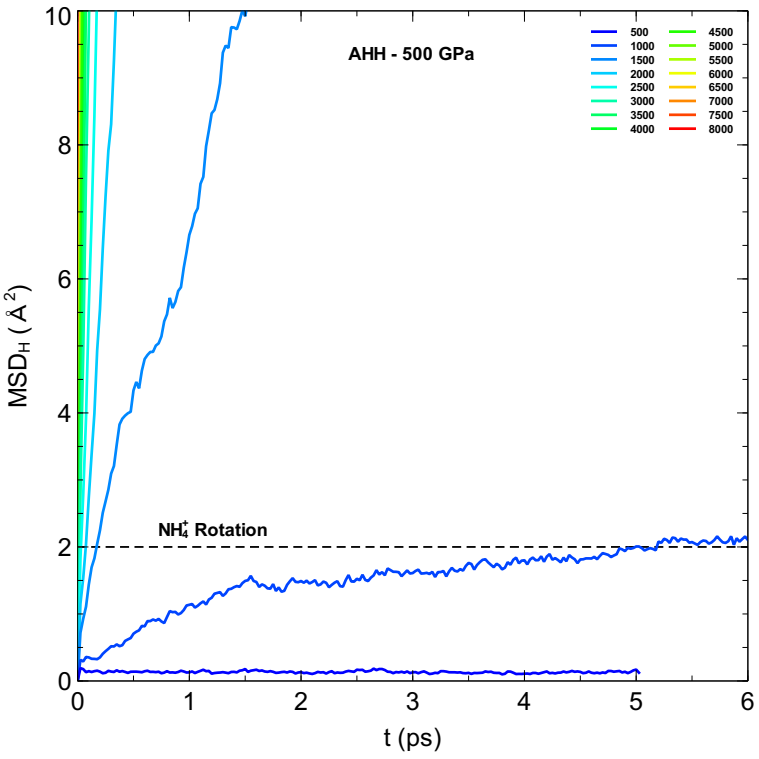

Figure 6.9 *Proton mean squared displacement for rotating units in warm AHH at 500 GPa.*

though is complicated by proton transfer and changes of a molecular unit type such as H_2O to H_3O^+. A qualitative description of what is observed in visualizing these phases is listed in table 6.1. Similar observations hold for all mixtures.

A high pressure example of molecular/ionic rotations is shown in figure 6.8 for AHH where NH_4^+ units rotates via occasionally flipping between hydrogen bond locations. The MSD for this simulation is shown in figure 6.9 which appears to continually rise for 1.5 ps but then begins to converge to a value around 1.75-2.0 Å^2. The distance between proton sites on the NH_4^+ unit in phase $P\bar{3}m1$ at 500 GPa is $d = 1.625$ Å, assuming the structure maintains the same symmetry before and after rotations the MSD should be expected to converge to $d^2 = 2.64 \times (3/4)$ Å^2 with (1/4) of the protons remaining in their initial position. This means there are certain finite values of MSD to look out for when simulating molecular compounds at extreme conditions, and in the work of Jiang. et al [207] plasticity may have been mistaken for superionicity.

6.4 Radial and Pair Distribution Functions

The radial distribution function alone reveals information about the system over the entire simulation. Whether the system is solid or liquid can be learned from inspecting the radial distribution function (RDF) for simple systems, however for a ternary ice complexity arises. A partial melt, as in the superionic phase, biases the RDF to that of a typical liquid by losing much of the peak structure yet retaining the peaks of the N,O sub-lattice. This is shown in figure 6.10 for AHH at 100 GPa in the P$\bar{3}$m1 phase. The full RDF shows the overall structure and examining individual pair distribution functions (PDF), where NH, OH, NO, HH, NN, and OO are possible, reveals what the full RDF is built from.

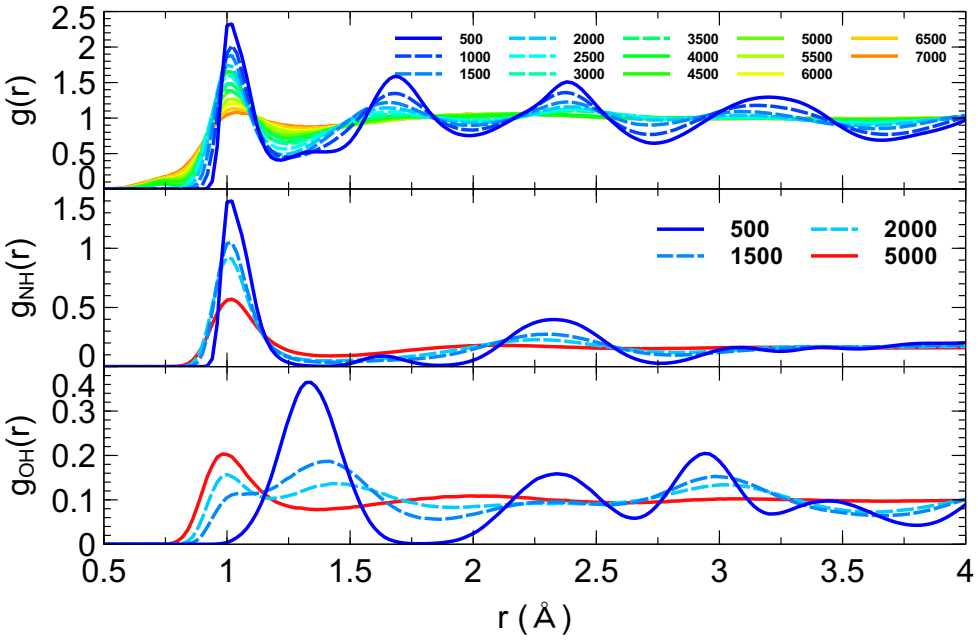

Figure 6.10 *RDF's and PDF's for AHH at 100 GPA where dashed lines indicate the superionic phase.*

As phase P$\bar{3}$m1 is ammonia-rich and consists of NH_4^+ and O^{2-} units $g_{NH}(r)$ will have a strong peak at lower r values than $g_{OH}(r)$ with no covalent bond in the solid phase. In figure 6.10 the effect of heating into the superionic phase shows the gradual build-up of OH covalent bonds as a peak grows in $g_{OH}(r)$ at 1 Å. The peak at 1.3 Å in $g_{OH}(r)$ decays but only disappears in the molten phase shown at 5000 K. On the other hand for $g_{NH}(r)$ the main peak at 1 Å only broadens with temperature, showing the perseverance of the NH bond. At long separation, the g(r) tends to a constant, unlike in a solid, which is similar to that of a liquid showing the analogy of the hydrogen sub-lattice melting in the superionic phase

transition.

In the molten state individual PDF's in figure 6.11 reveal high pressure temperature chemistry. Firstly in $g_{HH}(r)$ a peak around 0.7 Å begins to grow at 4000 K which is consistent with the typical H_2 bond length at 100 GPa, although isolated hydrogen is atomic at this temperature and pressure. The bond life-time is likely to be short-lived as a result of this though the other chemical bodies could encourage the molecular bond to form. This high temperature molecule formation can explain the growing shoulder and the lowest values of r in the full g(r). The molecule appears only to form when in the molten phase and the superionic phase does not accommodate H_2 molecules. Furthermore, $g_{NN}(r)$ in figure 6.11 shows the formation of N-N bonds peaked around 1.3 Å. These N-N bonds could range from N_2 molecules (1.1 Å) to more complex polymers (single N-N bond is 1.6 Å) with additional protons, though the bonds are likely to be short-lived.

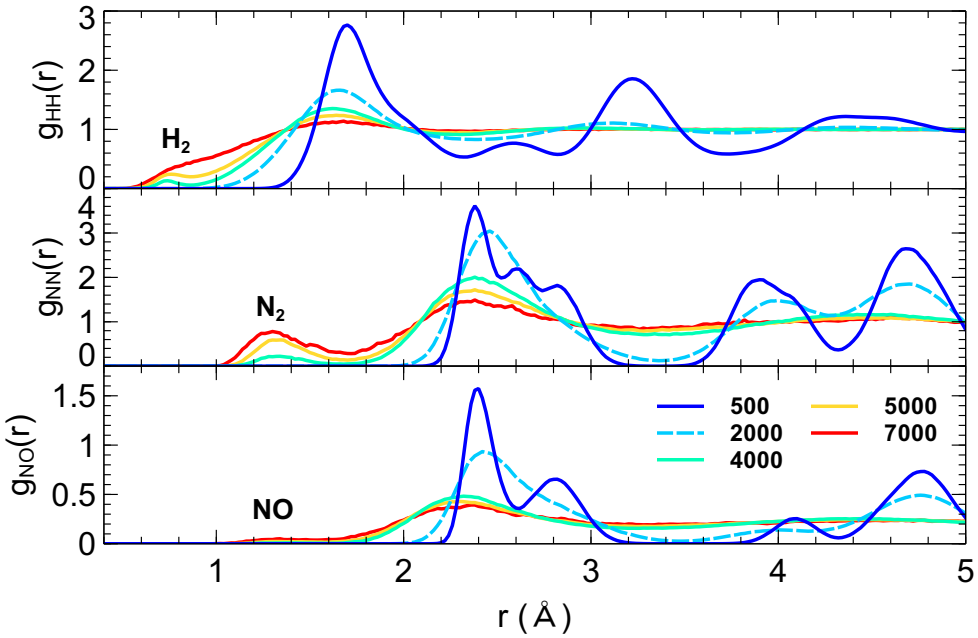

Figure 6.11 *PDF's for AHH at 100 GPa where dashed lines indicate the superionic phase. Labels indicate the likely chemistry where and a peak is observed around a typical covalent bond length at 100 GPa.*

The full data set of RDF's and PDF's at all densities and temperatures simulated is given in the appendix. For the case of AHH at 100 GPa the formation of O-O bonds appears much more difficult, though we can see the appearance, while marginal, of N-O bonds in $g(r)_{NO}$ as a small peak grows at 1.3 Å in the molten state. The fact these molecules appear to form at the same time in the molten

state may be connected: The molten system allows for N,O ions to be free and become close enough to form covalent bonds. This means there are less covalent NH and OH bonds allowing the hydrogens both space and the chemical freedom to form H_2 molecules. At higher temperatures still, the full dissociation of bonds is likely to occur on the way to a plasma. This can be seen for H_2 at 7000 K in figure 6.11 as the PDF begins to form a smooth distribution.

6.5 Neutral vs Charged Species

The ammonia-rich hydrates in particular benefit from proton transfer and the resultant formation of partially charged species to form ionic solids. To study the partition into neutral (molecular) and charged (ionic) species of these solids at finite temperature and what is happening in the superionic phase the trajectories were analyzed to identify molecular unit types such as H_2O and OH^-. The local environment for each heavy atom (N,O) was screened up to a typical bond length chosen as $r_c = 1.15$ Å to look for H atoms where a covalent bond could be assumed. Counting the number of covalent bonds per (N,O) indicates whether the unit is NH_2^- or NH_4^+ for example and thus we can count the number of molecular and ionic species in the simulation. This may be sensitive to equilibration and run-time but simulations appear to find a stable ratio quickly. In this analysis units NH_4^+ and OH^- were deemed "ionic" whereas NH_3 and H_2O are molecular. Data for ADH are shown in figure 6.12 and data for all simulations are given in the appendix.

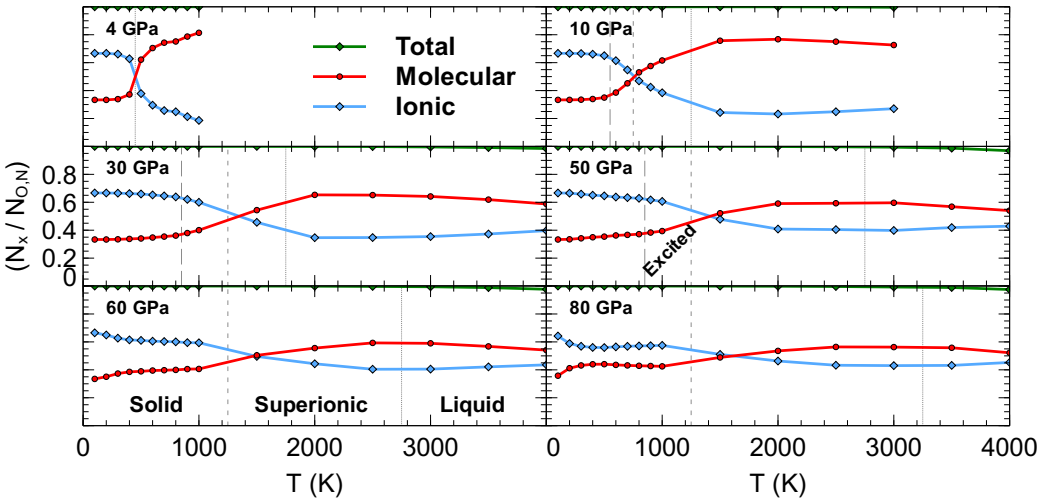

Figure 6.12 *Analysis of the units making up ADH as a function of P and T. Note that the starting configuration in the ground state always contained 2/3 ionic species. Dashed lines indicate the temperature at which a superionic phase was observed and dotted indicate the melting temperature.*

Below 200 GPa there is a crossover from ionic dominance to molecular dominance on heating into the superionic phase. Above 200 GPa (AHH and AQH only) the molecular and ionic units find a balance in the superionic phase, possibly due to the increased number of protons in the ammonia-rich mixtures and pressure

favoring ionic structures. Heating into the liquid state can find the total number of molecular and ionic units fall below 1.0 due to the formation of other species such as N_2 or rare examples such as NH_6^{3+}. In section 6.8 an analysis of the [N,O]–H bonding and radial distribution functions delves further into this. In general, high temperature finds a mixture of ionic and molecular units across the pressure range with pressure controlling how this deviates from a 50:50 split.

By interpolating data on the fraction of molecular units over a PT grid, molecular content phase diagrams can be produced shown in figure 6.13. Across all mixtures, low temperatures favor ionic phases as most phases started in ionic structures.

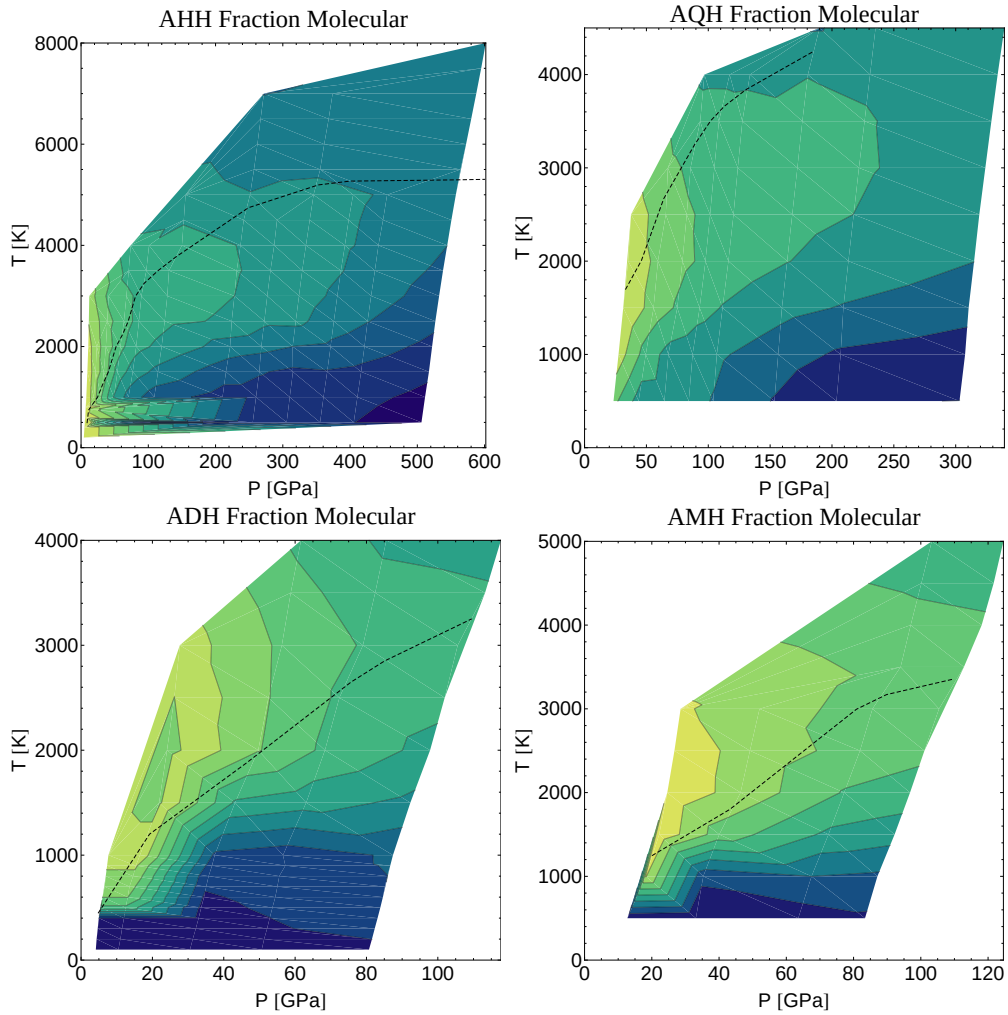

Figure 6.13 *Fraction of molecular units found in mixtures, black dashed lines are the respective melt lines. Dark blue (ionic) is a fraction of 0.0 and yellow (molecular) is 1.0.*

Further simulations which anneal the superionic state may find again the same ionic phases or may result in a glassy phase such as the topologically frustrated state suggested in previous AMH work [49]. On heating, the molecular

fraction rises as mixtures enter the superionic regime. In the liquid state, the molecular fraction appears to be temperature independent at very high temperature and instead depends on pressure, though very hot liquids would experience full decomposition of bonds eventually. Overall at low pressures and high temperatures the molecular fraction is high, whereas at high pressure and low temperature the ionic fraction is dominant.

6.6 Chemical Composition

Various chemical species can be found in the mixtures, from the expected H_2O to the rarer NH_5^{2+} with the same $r_c = 1.15$ Å, though abundance depends on the global stoichiometry. For example, AHH and AQH are likely to find O^{2-} units while ADH is likely to find far fewer. In figure 6.14 the fraction of each species tracked in ADH and normalized to a total of all heavy atoms (N+O) are plotted. In general, the chemical species follow the same trends as a function of P and T as the molecular fraction varies - though here this behavior is broken down unit by unit. Rare units increase in likelihood once the superionic phase has been entered. For the case of ADH, which has a fine temperature grid below 1000 K, the rise in NH_3 molecules mirrors the decrease in OH^- and NH_4^+ ionic species. This transition starts to begin before full superionicity sets in, showing some proton transfer in the excited and plastic regions.

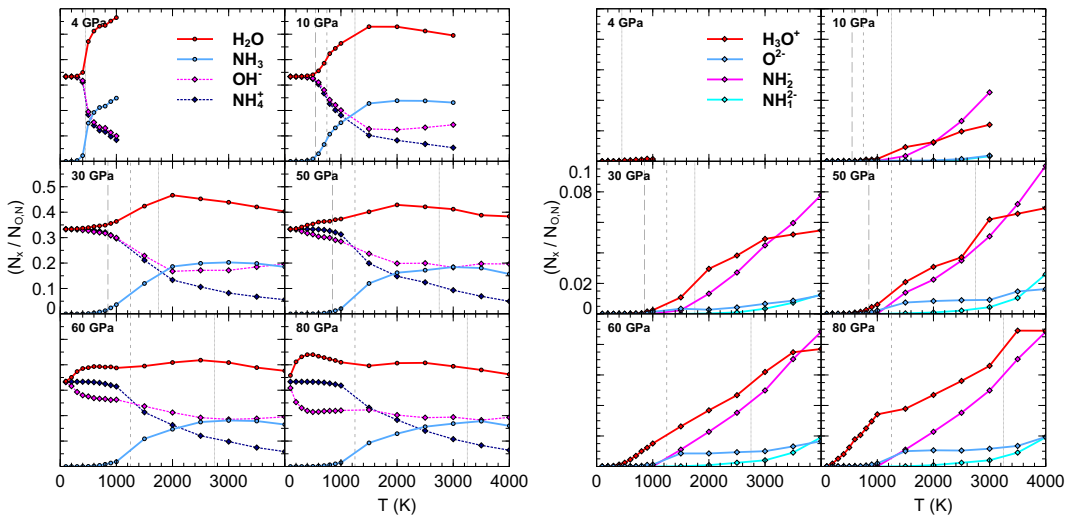

Figure 6.14 *Relative abundance of most relevant species in ADH simulations.*

Phases with OH chains complicate this counting as they may symmetrize protons with increased temperature and appear as O^{2-} or as H_2O instead. Overall the

unit fractions are dominated by the expected $NH_4^+ + NH_3 + H_2O + OH^- + O^{2-}$ units found in the ground state structures. Other mixtures exhibit similar behavior but depend also on the initial conditions. For example high pressure ammonia-rich hydrates with deprotonated oxygen O^{2-} start with low OH bearing species at low temperature but this increases with temperature as different regimes are entered, see figure 6.15.

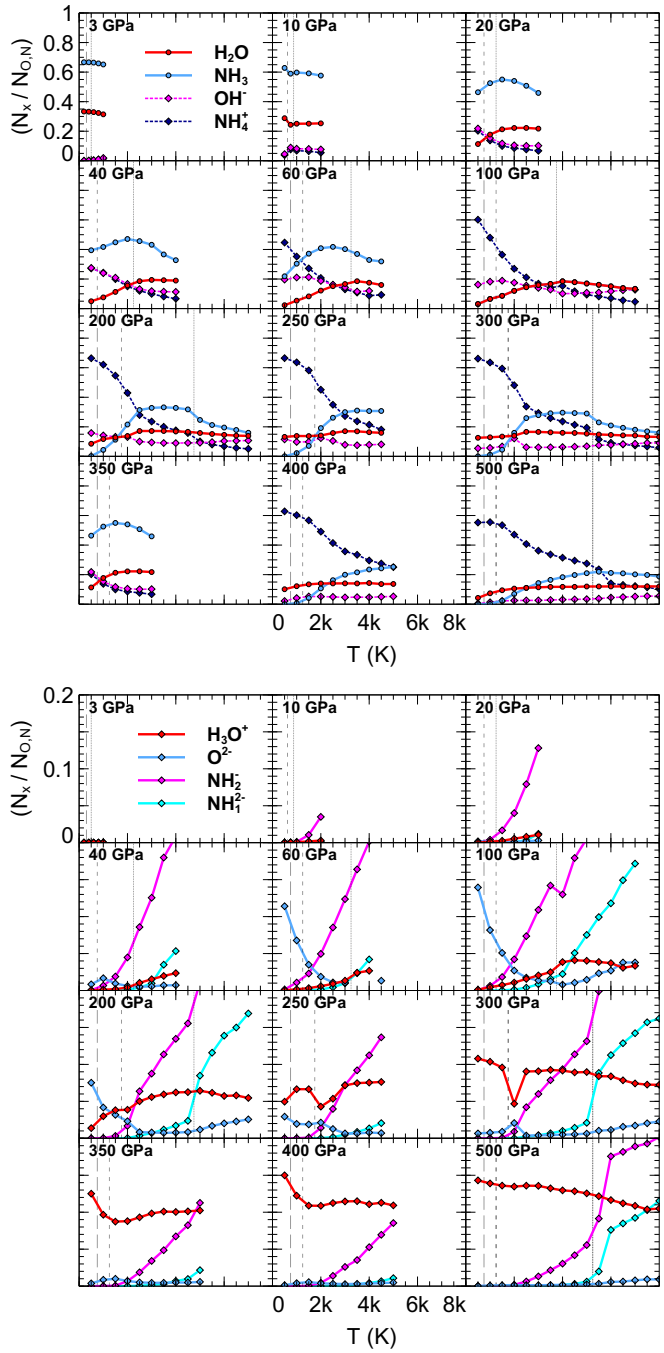

Figure 6.15 *Relative abundance of most relevant species in AHH simulations.*

6.7 Covalently Bonded Protons

The previous sections studied the bonding configurations of the heavy atoms in the mixtures. In contrast, we can also study the bonding of the hydrogens: how many covalent bonds do they form on average at various PT conditions? This could be relevant in the superionic region, where protons are diffusive but not necessarily unbound. Here we count the number of hydrogen covalent bonds again using $r_c = 1.15$ Å. Whether the bond is NH or OH is also recorded and summarized in figure 6.16 and normalized by the number of N,O–H covalent bonds in the ground state i.e. assuming an icy molecular structure.

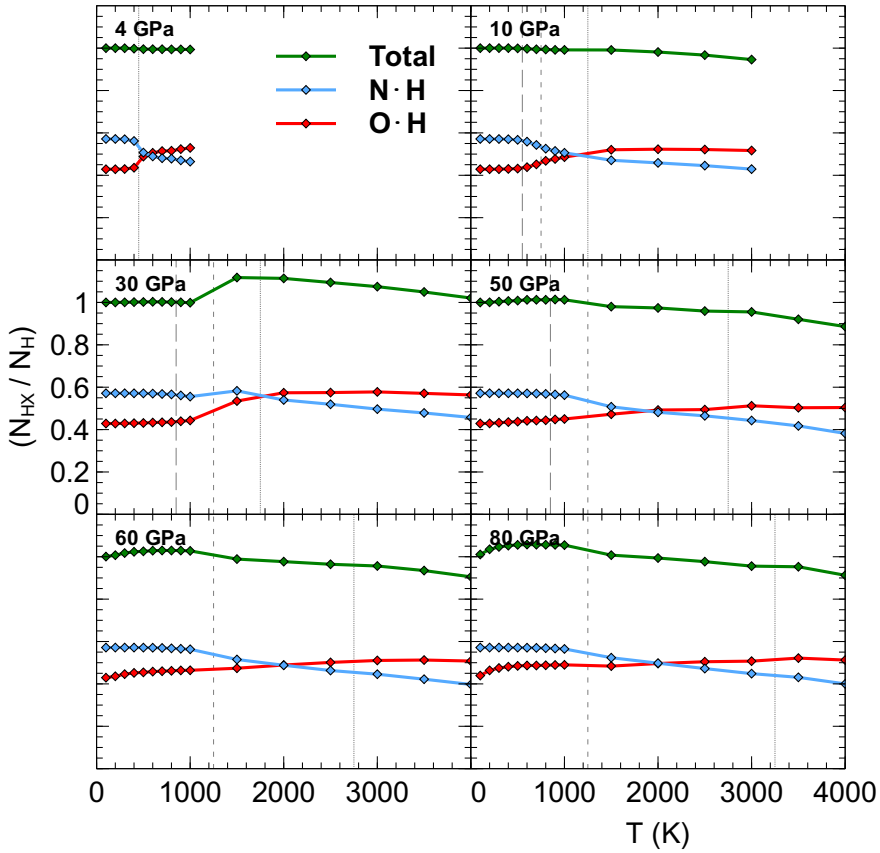

Figure 6.16 *Number of X-H (X = N,O) bonds and their type in ADH as a function of temperature for various pressures.*

For ADH the expected number bond fractions are 4/7 and 3/7 (NH, OH) in the solid ground state which is observed at the lowest temperatures. This then changes as different units are formed at higher temperatures. The number of bonds found increases above the number of hydrogen atoms, and so above 1.0 in figure 6.16, in high pressure phases and can be attributed to the system wanting

to form symmetric OH chains as in ice X. In the dynamic case with OH chains, a simple range-based definition of the OH covalent bond falls short. For all ADH phases chosen there is a transition from majority NH bonds to majority OH bonds. This also implies that the bond life-times will be anisotropic between OH and NH both species and differ again at low or high temperature.

For all mixtures there is in an increase of OH bonds at high temperature, entering the superionic regime can trigger onset. A likely cause for this is the more electronegative oxygen ion attracting more free protons even though nitrogen is able to form a greater number of bonds. Virtually all protons appear bonded to a heavy atom in the superionic region. On the opposite end of the mixing ratio, the covalently bonded protons are shown in figure 6.17. N-H bonds dominate the total numbers due to the chemistry but also due to the deprotonated O^{2-} units above 60 GPa. Heating the deprotonated AQH phases into the superionic regime shows the growth of O-H bonds returning.

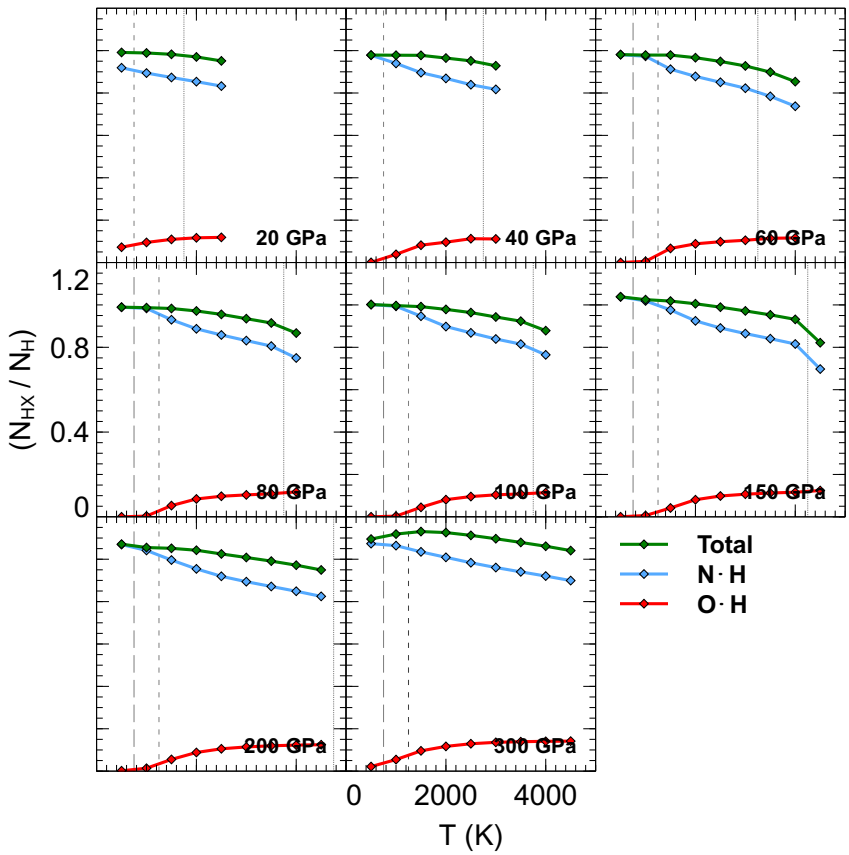

Figure 6.17 *Number of X-H (X = N,O) bonds and their type in AQH as a function of temperature for various pressures.*

6.8 Bond Life-times

To quantify the longevity of covalent bonds we calculated estimates of the bond life-times as shown in figure 6.18 following the methodology outlined in section 2.4.4. At low temperatures, NH bonds break less often and so last longer, though at higher temperatures there is a transition as OH bonds appear to have greater stability. This is perhaps because the mobile hydrogen ions are positively charged and the oxygen atoms are more likely to have a negative local environment acting as transient proton attractors. In general increasing pressure at lower temperatures stabilizes NH bonds and weakens OH bonds. However, at high temperatures (over 1500 K) the NH bonds can become weaker relative to the OH bonds. This relative bond strength turnover holds in other mixtures also where the temperatures are hot enough.

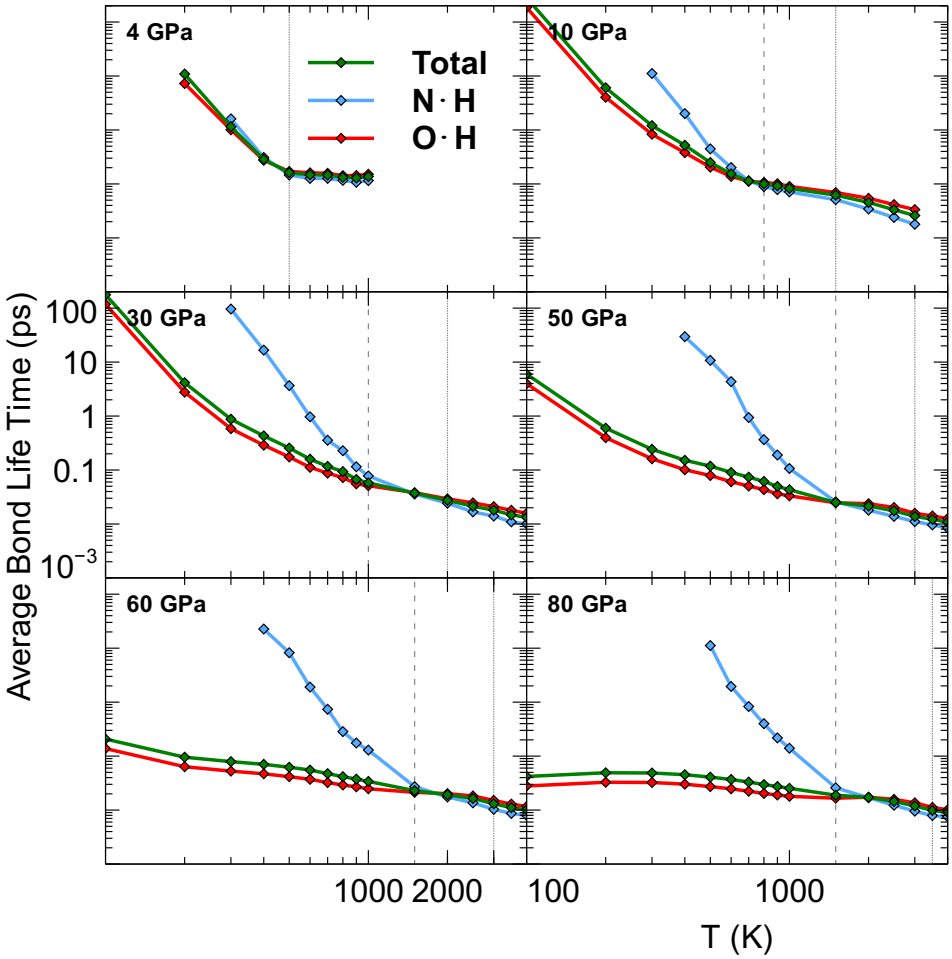

Figure 6.18 *Bond life-times of X-H bonds in ADH.*

There are problems with such a simple method of counting the life-time of a bond.

This approach requires all X-H bonds to be similar in length distribution, which is not the case in the AQH N_2H_7 units for example. A second assumption is that all bonds will break during the simulation at some point, which is not always the case. An alternative method is therefore used here to analyze the bonding in the form of a correlation function $B(t)$. This bond auto-correlation function (BAC) measures the probability that an initial bond at a time t is found at a time $t + \delta t$ later normalized to the number of covalent bonds assigned at the time t. A covalent bond is defined here in two ways: by the nearest heavy atom (N,O) to a proton and also within a radius of 2.0 Å. This means the number of covalent X-H bonds should be the same as the number of protons in the solid and superionic phase, and also uses information from persistent bonds that do not easily break.

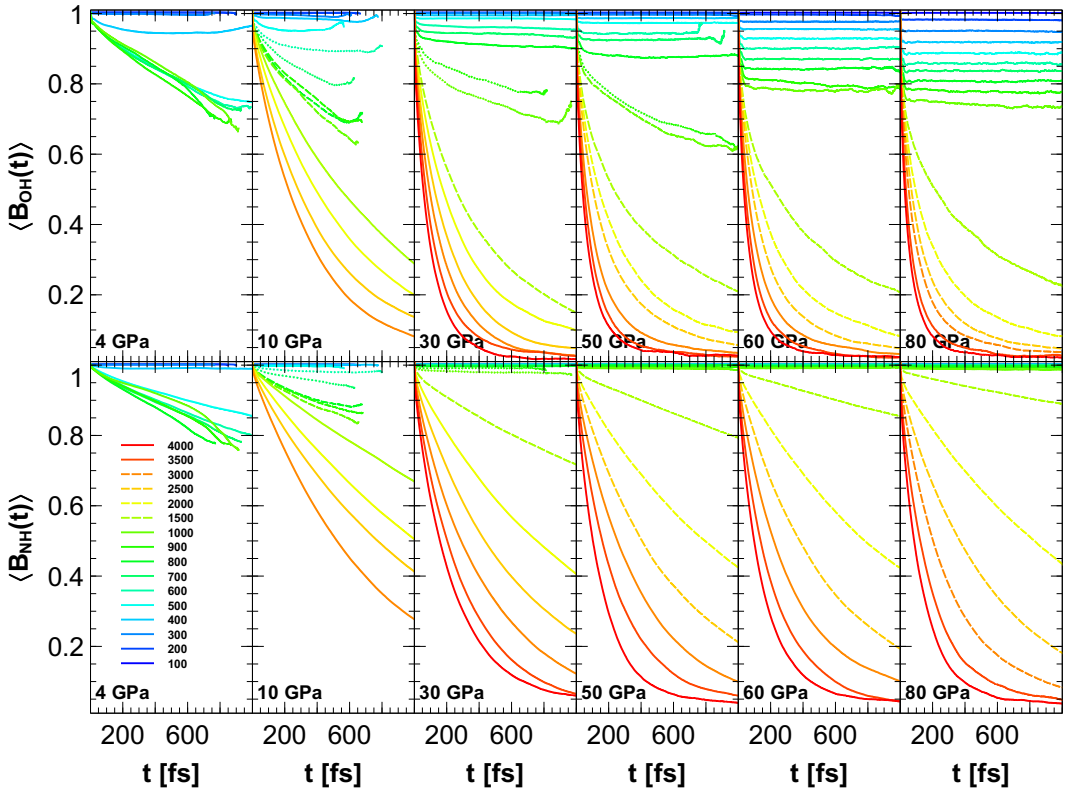

Figure 6.19 *Bond auto correlation functions for NH and OH bonds in ADH. Dash lines refer to the superionic phase and dotted lines refer to the excited states.*

The results of this analysis for ADH are shown in figure 6.19 and given for all mixtures in the appendix. The correlation function starts at 1.0 and decays as a function of time as a bond is less likely to be found at a time $t + \delta t$ later. At low temperatures bonds are found to be persistent and likely to survive into the future. Upon heating into the superionic regime and liquid state this changes as the protons become more mobile. It can be seen that OH bonds are more

likely to break than the persistent NH bonds meaning that more of the superionic diffusion is mediated by the oxygen ions. As this method measures the probability of maintaining the close nearest neighbour heavy atom, it captures information in systems with symmetric hydrogen bonds (AQH) or OH chains (AMH,ADH). This can be seen in figure 6.19 at 80 GPa for the OH correlations. These appear to decrease in a step-wise manner with increasing temperature yet remain fairly stable as they are not decaying exponentially. This is because at that pressure 1/3 of the protons form OH bonds and are in a double-well potential along the OH chains formed in the $P2_1/m$ ADH structure. With increasing temperature more of these protons are visiting the double or single potential well formed between oxygen atoms meaning the nearest neighbor is rapidly switching. On further heating to 1500 K the OH protons become much more mobile than the NH protons indicated by the relatively different gradients in the $B(t)_{OH}$ and $B(t)_{NH}$ functions which are more rapidly heading to zero.

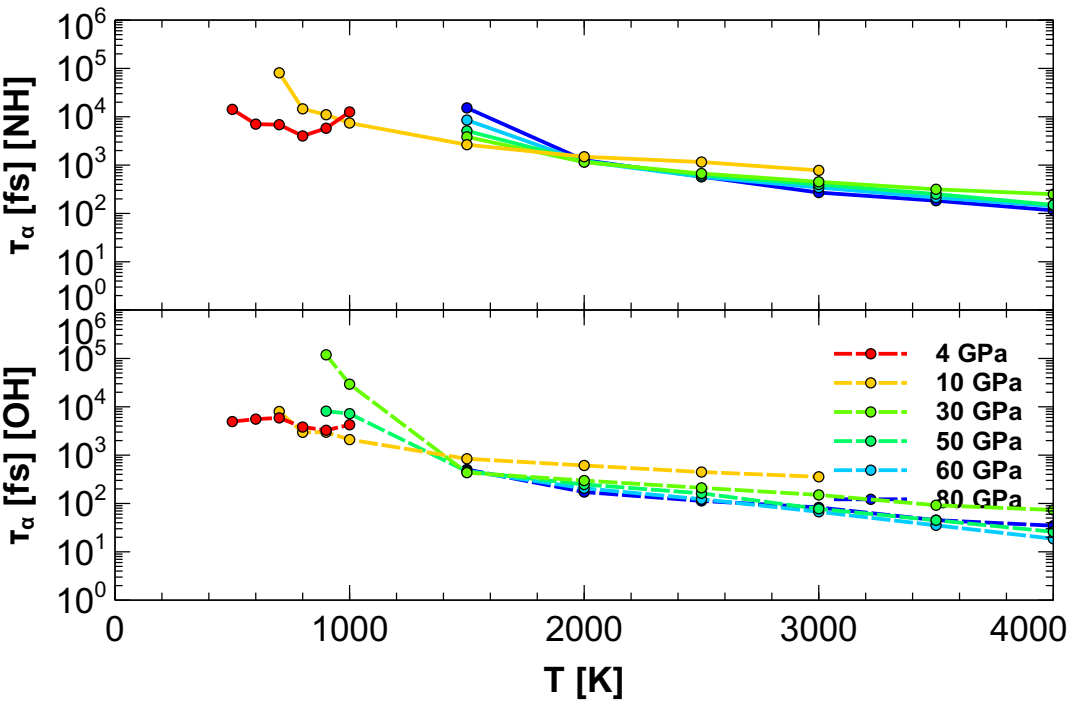

Figure 6.20 *Estimated bond life-times τ_α from the BAC in ADH.*

The exponentially decaying regime of the BAC has an associated time τ_α, which is shown in figure 6.20 for ADH. NH bonds are shown to be more persistent than OH bonds across the range of pressures and temperatures. The calculation of τ_α requires the BAC to be in the decaying regime in order to fit an exponential function and so limits the points at which data can be acquired. Once in the superionic and molten regimes bonds are readily breaking and the data collection

becomes more accurate.

6.9 Diffusion Regimes

Diffusion constants reveal the dynamics of the system and are expected to change for dynamical phase transitions. In the solid-state the Diffusion constant for H, N and O should be close to vanishing, though small solid-solid diffusion is possible especially at lower pressures with more open space. Transitioning into the superionic regime shows a sharp increase in D_H while maintaining a solid D_{NO} of zero. Finally, in the molten state, all three ions are thermally activated and diffusing through the simulation.

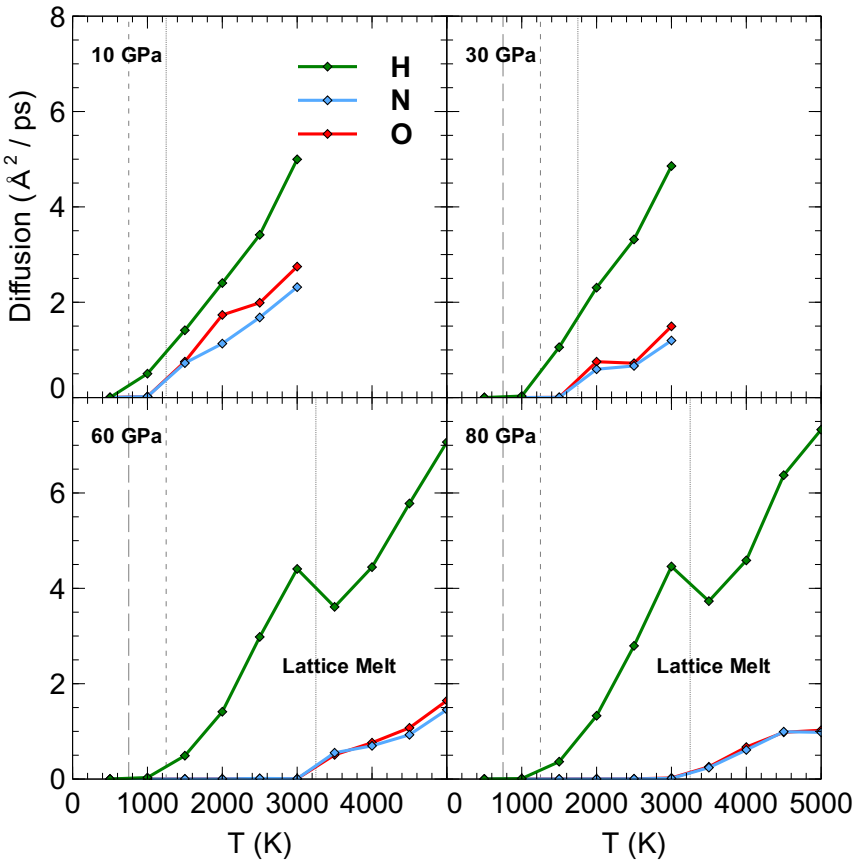

Figure 6.21 *Diffusion constants as a function of pressure in AMH.*

For pressures of 60 and 80 GPa an unexpected kink occurs in the hydrogen diffusion rate when the lattice melts, see figure 6.21. This kink does not occur at all pressures and not in all mixtures. This implies that the hydrogens no longer have a stable N,O (BCC or otherwise) lattice to flow through and have

mobile N,O atoms diffusing around making it easier to be obstructed and or form covalent bonds. Once in the molten state, the proton diffusion appears to regain the same scaling with increased temperature. Similar diffusion is seen for all mixtures however not all exhibit kinks on melting.

6.10 Concluding Remarks

Solid phases derived from the static ground state binary phase diagram of ammonia water mixtures were simulated at finite temperature. This heating led to similar phase transitions as those found in the individual ices of ammonia and water. Heating solid phases in the low pressure region directly enter the liquid regime. At moderate pressures above 10 GPa an excited plastic regime which can be combined with slow charge transfer can be found in all four mixtures before further heating into the superionic phase with fast diffusing protons. This phase sequence is similar to that of ice and ammonia separately although simulations with a finer resolution would be required to accurately compare the triple points for the solid-plastic-superionic phases. All mixtures enter the superionic phase and exhibit stronger, longer-lived, N-H bonding compared to the relatively weaker O-H bonding. This reflects the chemistry found in the ground state static calculations and suggests the high temperature convex hull of the ammonia-water system may still favour high ammonia content at high pressure.

The melting lines were calculated by simple direct heating providing analysis of the liquid that forms. The melting lines were shown to be very close to the isentropes of Uranus and Neptune and directly between those of ammonia and water separately. Interestingly the four mixture melting lines are very close in P T space rather than fanning out depending on composition as suggested from a linear mixing approximation. Simulations of ADH and AMH produce similar results to previous studies, though more stable phases were used and the excited plastic regime was identified in this work. Mixtures were simulated at PT conditions based on the stability found by the static ground state convex hull which does not account for the entropy gain of alloyed phases found in the mixtures experimentally. Sampling the entropy of mixing in the alloy could be possible by switching units around lattice sites along with MD, though very expensive for ab-initio methods, could extend the thermodynamic stability of the mixed system. No demixing was found in simulations though it may be expected at higher pressures where mixtures are found to be much more unstable.

Chapter 7

Conclusion

The ammonia water system has been investigated at extreme temperatures and pressures with a variety of theoretical methods. Crystal structures provided a powerful method for starting this investigation into an unknown crystal and chemical space. New structures and even a new hydrate, AQH, were predicted at pressures starting from roughly 14 GPa. At low pressures and temperatures ammonia and water mix first as molecular crystals, followed by a sequence of ionic transitions which, if possible, lead to fully ionic structures. Fully ionic structures can be formed by AMH, AHH, and AQH and so require a ratio of ammonia:water greater than or equal to 1:1. This appears to simply come out of the chemistry and water donates protons to ammonia in all these cases to form ionic structures. Ammonia to ammonia donation was not seen in this work but is possible for even richer ammonia content. In ADH water molecules are always retained, though at higher pressures which are beyond their stability on the ground state convex hull, the water molecules can become symmetric which could be considered a fully ionic structure as well.

For water to donate two protons to ammonia molecules the required ratio is 2:1 or greater, evident in the structures found for AHH and AQH. High pressure stabilizes the mixture of ammonia and water through ionic bonding and the complete deprotonation of the water molecule is the strongest observed form of that. For this reason the ground state convex hull over 100 GPa is dominated by ammonia-rich mixtures, contrary to the icy giants which are expected to be water-rich. The dehydration of ammonia hydrates has been observed experimentally under 10 GPa but the high pressure dominance of ammonia-rich hydrates has

not yet been explored. Experiments confirming the complete deprotonation of the water molecules, such as in AHH, would help support this conclusion. This implies a partitioning of the ices within the planet, perhaps into pure water and an ammonia-rich hydrate.

The experimentally observed DMA phase may provide a competing alternative explanation to partitioning, especially as this would be further stabilized by temperature effects. The DMA could be present throughout the low pressure regions, where the solid ices are stable. This could take the form of a structure similar to ice VII crystal but doped with ammonia randomly throughout, and possibly methane. In chapter 6 molecular dynamics simulations showed ground state crystal phases exhibit rotational and symmetry breaking changes such as proton transfer upon heating. Mixtures of ammonia and water could enable an earlier onset of these entropy favored states, followed later by superionicity at again lower temperatures than in pure water. In the future, eventually free energy calculations may be performed for mixtures of planetary ices which exhibit dynamical behavior (plasticity, superionicity) and could create an accurate convex hull at finite temperature.

Superionicity was observed for all of the mixtures, starting from temperatures higher than those of pure ammonia and less than those of pure water, in most cases. At lower pressures and temperatures (under 20 GPa and 1000 K) the mixtures, such as AHH, enter the superionic regime at even lower temperatures and pressures than the pure ammonia and pure water ices. This is likely mediated by greater variation of hydrogen bonding within the crystals, enabling rotational disorder, and the attractive potential of water donating protons to ammonia molecules aiding the initialization of the proton dynamics. Eventually, ammonia water mixtures melt at temperatures and pressures close to the Uranus and Neptune isentropes over 100 GPa. The melting lines of the mixtures fall between the melting lines of pure ammonia and pure water in this region of temperature and pressure space.

Above roughly 500 GPa all the mixtures of ammonia and water appear unstable to decomposition into their constituent ices. Temperature and alloying (providing an entropy of mixing) may offer some further stabilization but results in this work suggest mixtures become highly energetically unfavorable at these very high pressures. Considering the ternary systems of HNO and HCO, followed later by the quaternary system of HCNO, may further stabilize mixtures of planetary ices in a less conventional way. Here the binary system of NH_3 and H_2O was considered

and has provided a rich insight into how these planetary ices arrange themselves as a function of pressure. The future of structure searching benefits from improved methodology, in setup and self-learning, and scales with the improvements of high performance computing. Investigating more combinatorially difficult systems will become possible. By crystal structure searching and ab initio molecular dynamics simulations the extreme conditions phase diagram of the ammonia water system has been computationally explored. New crystal structures were predicted and their properties were computed. A surprising complete deprotonation of water molecules was observed first in AHH and then later in AQH. All mixtures have phase diagrams in pressure and temperature that relate to pure H_2O with added complexity due to the nature of the mixture and more diverse crystal structures and bonding.

Bibliography

[1] Victor Naden Robinson, Yanchao Wang, Yanming Ma, and Andreas Hermann. Stabilization of Ammonia-rich hydrate inside icy planets. *Proceedings of the National Academy of Sciences*, 114(34):9003–9008, aug 2017.

[2] Victor Naden Robinson, Miriam Marqués, Yanchao Wang, Yanming Ma, and Andreas Hermann. Novel phases in Ammonia-Water mixtures under pressure. *The Journal of Chemical Physics*, 149(23):234501, 2018.

[3] Victor Naden Robinson and Andreas Hermann. Plastic and superionic phases in ammonia-water mixtures at high pressures and temperatures. *Journal of Physics: Condensed Matter*, 2020.

[4] Gavin Woolman, Victor Naden Robinson, Miriam Marqués, Ingo Loa, Graeme J Ackland, and Andreas Hermann. Structural and electronic properties of the alkali metal incommensurate phases. *Physical Review Materials*, 2(5):053604, 2018.

[5] Victor Naden Robinson, Hongxiang Zong, Graeme J Ackland, Gavin Woolman, and Andreas Hermann. On the chain-melted phase of matter. *Proceedings of the National Academy of Sciences*, 116(21):10297–10302, 2019.

[6] W. B. Hubbard and J. J. MacFarlane. Structure and evolution of Uranus and Neptune. *Journal of Geophysical Research: Solid Earth*, 85(B1):225–234, jan 1980.

[7] Marvin Ross. The ice layer in Uranus and Neptune diamonds in the sky? *Nature*, 292:435–436, 1981.

[8] Leslie A. Young, S. Alan Stern, Harold A. Weaver, Fran Bagenal, Richard P. Binzel, Bonnie Buratti, Andrew F. Cheng, Dale Cruikshank, G. Randall Gladstone, William M. Grundy, David P. Hinson, Mihaly Horanyi, Donald E. Jennings, Ivan R. Linscott, David J. McComas, William B. McKinnon, Ralph McNutt, Jeffery M. Moore, Scott Murchie, Catherine B. Olkin, Carolyn C. Porco, Harold Reitsema, Dennis C. Reuter, John R. Spencer, David C. Slater, Darrell Strobel, Michael E. Summers,

and G. Leonard Tyler. New Horizons: Anticipated scientific investigations at the Pluto system. *Space Science Reviews*, 140(1-4):93–127, 2008.

[9] Yasuhito Sekine, Hidenori Genda, Seiji Sugita, Toshihiko Kadono, and Takafumi Matsui. Replacement and late formation of atmospheric N_2 on undifferentiated Titan by impacts. *Nature Geoscience*, 4(6):359–362, 2011.

[10] Ch Sotin, O Grasset, and A Mocquet. Mass–radius curve for extrasolar Earth-like planets and ocean planets. *Icarus*, 191(1):337–351, 2007.

[11] H. Rauer, C. Catala, C. Aerts, T. Appourchaux, W. Benz, A. Brandeker, J. Christensen-Dalsgaard, M. Deleuil, L. Gizon, M. J. Goupil, M. Güdel, E. Janot-Pacheco, M. Mas-Hesse, I. Pagano, G. Piotto, D. Pollacco, Santos, A. Smith, J. C. Suárez, R. Szabó, S. Udry, V. Adibekyan, Y. Alibert, J. M. Almenara, P. Amaro-Seoane, M. A V Eiff, M. Asplund, E. Antonello, S. Barnes, F. Baudin, K. Belkacem, M. Bergemann, G. Bihain, A. C. Birch, X. Bonfils, I. Boisse, A. S. Bonomo, F. Borsa, I. M. Brandão, E. Brocato, S. Brun, M. Burleigh, R. Burston, J. Cabrera, S. Cassisi, W. Chaplin, S. Charpinet, C. Chiappini, R. P. Church, Sz Csizmadia, M. Cunha, M. Damasso, M. B. Davies, H. J. Deeg, R. F. Díaz, S. Dreizler, C. Dreyer, P. Eggenberger, D. Ehrenreich, P. Eigmüller, A. Erikson, R. Farmer, S. Feltzing, F. de Oliveira Fialho, P. Figueira, T. Forveille, M. Fridlund, R. A. García, P. Giommi, G. Giuffrida, M. Godolt, J. Gomes da Silva, T. Granzer, J. L. Grenfell, A. Grotsch-Noels, E. Günther, C. A. Haswell, A. P. Hatzes, G. Hébrard, S. Hekker, R. Helled, K. Heng, J. M. Jenkins, A. Johansen, M. L. Khodachenko, K. G. Kislyakova, W. Kley, U. Kolb, N. Krivova, F. Kupka, H. Lammer, A. F. Lanza, Y. Lebreton, D. Magrin, P. Marcos-Arenal, P. M. Marrese, J. P. Marques, J. Martins, S. Mathis, S. Mathur, S. Messina, A. Miglio, J. Montalban, M. Montalto, M. J. P. F. G. Monteiro, H. Moradi, E. Moravveji, C. Mordasini, T. Morel, A. Mortier, V. Nascimbeni, R. P. Nelson, M. B. Nielsen, L. Noack, A. J. Norton, A. Ofir, M. Oshagh, R. M. Ouazzani, P. Pápics, V. C. Parro, P. Petit, B. Plez, E. Poretti, A. Quirrenbach, R. Ragazzoni, G. Raimondo, M. Rainer, D. R. Reese, R. Redmer, S. Reffert, B. Rojas-Ayala, I. W. Roxburgh, S. Salmon, A. Santerne, J. Schneider, J. Schou, S. Schuh, H. Schunker, A. Silva-Valio, R. Silvotti, I. Skillen, I. Snellen, F. Sohl, S. G. Sousa, A. Sozzetti, D. Stello, K. G. Strassmeier, M. Švanda, Gy M. Szabó, A. Tkachenko, D. Valencia, V. Van Grootel, S. D. Vauclair, P. Ventura, F. W. Wagner, N. A. Walton, J. Weingrill, S. C. Werner, P. J. Wheatley, and K. Zwintz. *The PLATO 2.0 mission*, volume 38. 2014.

[12] Lena Noack, Ignas Snellen, and Heike Rauer. Water in extrasolar planets and implications for habitability. *Space Science Reviews*, pages 877–898, 2017.

[13] M Podolak, A Weizman, and M Marley. Comparative models of Uranus and Neptune. *Planetary and Space Science*, 43(12):1517–1522, dec 1995.

[14] N. Nettelmann, K. Wang, J. J. Fortney, S. Hamel, S. Yellamilli, M. Bethkenhagen, and R. Redmer. Uranus evolution models with simple thermal boundary layers. *Icarus*, 275:107–116, 2016.

[15] Weiwei Zhang, Artem R. Oganov, Alexander F. Goncharov, Qiang Zhu, Salah Eddine Boulfelfel, Andriy O. Lyakhov, Elissaios Stavrou, Maddury Somayazulu, Vitali B. Prakapenka, and Zuzana Konôpková. Unexpected stable stoichiometries of Sodium Chlorides. *Science*, 342(6165):1502–5, dec 2013.

[16] Li Zhu, Hanyu Liu, Chris J. Pickard, Guangtian Zou, and Yanming Ma. Reactions of Xenon with Iron and Nickel are predicted in the Earth's inner core. *Nature Chemistry*, 6(7):644–8, jul 2014.

[17] Andreas Hermann and Peter Schwerdtfeger. Xenon suboxides stable under pressure. *The Journal of Physical Chemistry Letters*, 5:4336–4342, dec 2014.

[18] Sergey S Lobanov, Vitali B Prakapenka, Clemens Prescher, Zuzana Konôpkova, Hanns-Peter Liermann, Katherine Crispin, Chi Zhang, and Alexander F Goncharov. Pressure, stress, and strain distribution in the double-stage diamond anvil cell. *arXiv preprint arXiv:1504.00750*, 2015.

[19] Andreas Hermann. Chemical bonding at high pressure. In A. L. Parrill and K. B. Lipkowitz, editors, *Reviews in Computational Chemistry*, pages 1–41. John Wiley & Sons Inc., Hoboken, NJ, apr 2017.

[20] Laura Robin Benedetti, Jeffrey H. Nguyen, Wendell A. Caldwell, Hongjian Liu, Michael Kruger, and Raymond Jeanloz. Dissociation of CH_4 at high pressures and temperatures: Diamond formation in giant planet interiors? *Science*, 286(5437):100–102, oct 1999.

[21] C. Cavazzoni, G. L. Chiarotti, S. Scandolo, E. Tosatti, M. Bernasconi, and M. Parrinello. Superionic and metallic states of water and Ammonia at giant planet conditions. *Science*, 283(5398):44–46, jan 1999.

[22] Yanchao Wang, Hanyu Liu, Jian Lv, Li Zhu, Hui Wang, and Yanming Ma. High pressure partially ionic phase of water ice. *Nature Communications*, 2:563, nov 2011.

[23] Andreas Hermann, N. W. Ashcroft, and Roald Hoffmann. High pressure ices. *Proceedings of the National Academy of Sciences of the United States of America*, 109(3):745–750, dec 2012.

[24] Chris J. Pickard, Miguel Martinez-Canales, and Richard J. Needs. Decomposition and Terapascal phases of water ice. *Physics Review Letters*, 110(24):245701, jun 2013.

[25] Taras Palasyuk, Ivan Troyan, Mikhail Eremets, Vadym Drozd, Sergey Medvedev, Patryk Zaleski-Ejgierd, Ewelina Magos-Palasyuk, Hongbo Wang, Stanimir A. Bonev, Dmytro Dudenko, and Pavel Naumov. Ammonia

as a case study for the spontaneous ionization of a simple Hydrogen-bonded compound. *Nature Communications*, 5:3460, mar 2014.

[26] S. Ninet, F. Datchi, P. Dumas, M. Mezouar, G. Garbarino, a. Mafety, C. J. Pickard, R. J. Needs, and a. M. Saitta. Experimental and theoretical evidence for an ionic crystal of Ammonia at high pressure. *Physical Review B*, 89(17):174103, may 2014.

[27] Ciprian G. Pruteanu, Graeme J. Ackland, Wilson C. K. Poon, and John S. Loveday. When immiscible becomes misciblemethane in water at high pressures. *Science Advances*, 3(8):e1700240, 2017.

[28] MD Segall, Philip JD Lindan, MJ al Probert, CJ Pickard, PJ Hasnip, SJ Clark, and MC Payne. First-principles simulation: ideas, illustrations and the CASTEP code. *Journal of Physics: Condensed Matter*, 14(11):2717, 2002.

[29] Lijun Zhang, Yanchao Wang, Jian Lv, and Yanming Ma. Materials discovery at high pressures. *Nature Reviews Materials*, 2(4):17005, 2017.

[30] Artem R Oganov, Chris J Pickard, Qiang Zhu, and Richard J Needs. Structure prediction drives materials discovery. *Nature Reviews Materials*, page 1, 2019.

[31] Monica Pozzo, Chris Davies, David Gubbins, and Dario Alfe. Thermal and electrical conductivity of Iron at Earths core conditions. *Nature*, 485(7398):355, 2012.

[32] Gilles A de Wijs, Georg Kresse, Lidunka Vočadlo, David Dobson, Dario Alfe, Michael J Gillan, and Geoffrey D Price. The viscosity of liquid Iron at the physical conditions of the Earth's core. *Nature*, 392(6678):805, 1998.

[33] Yinwei Li, Jian Hao, Hanyu Liu, S Tse John, Yanchao Wang, and Yanming Ma. Pressure-stabilized superconductive Yttrium hydrides. *Scientific Reports*, 5:9948, 2015.

[34] Aiyasami Jayaraman. Diamond anvil cell and high pressure physical investigations. *Reviews of Modern Physics*, 55(1):65, 1983.

[35] William G Marshall and Duncan J Francis. Attainment of near-hydrostatic compression conditions using the Paris–Edinburgh cell. *Journal of Applied Crystallography*, 35(1):122–125, 2002.

[36] LB Fletcher, HJ Lee, T Döppner, E Galtier, B Nagler, P Heimann, C Fortmann, S LePape, T Ma, M Millot, et al. Ultrabright X-ray laser scattering for dynamic warm dense matter physics. *Nature Photonics*, 9(4):274, 2015.

[37] NK Bourne. A 50 mm bore gas gun for dynamic loading of materials and structures. *Measurement Science and Technology*, 14(3):273, 2003.

[38] J. S. Loveday and R. J. Nelmes. The Ammonia hydrates model mixed-Hydrogen-bonded systems. *High Pressure Research*, 24(1):45–55, jan 2004.

[39] A. Dominic Fortes and Mathieu Choukroun. Phase behaviour of ices and hydrates. *Space Science Reviews*, 153(1-4):185–218, 2010.

[40] Martin Asplund, Nicolas Grevesse, A. Jacques Sauval, and Pat Scott. The chemical composition of the sun. *Annual Review of Astronomy and Astrophysics*, 47:481–522, jul 2009.

[41] A. F. Goncharov, V. V. Struzhkin, M. S. Somayazulu, R. J. Hemley, and H. K. Mao. Compression of ice to 210 Gigapascals: Infrared evidence for a symmetric Hydrogen-bonded phase. *Science*, 273(5272):218–220, jul 1996.

[42] M. Benoit, M. Bernasconi, P. Focher, and M. Parrinello. New high-pressure phase of ice. 76(16):2934–2936, apr 1996.

[43] Chris J. Pickard and R. J. Needs. Highly compressed Ammonia forms an ionic crystal. *Nature Materials*, 7(10):775–9, oct 2008.

[44] Andrew D Fortes, Ian Geoffrey Wood, Maria Alfredsson, L Vočadlo, Kevin S Knight, WG Marshall, MG Tucker, and F Fernandez-Alonso. The high-pressure phase diagram of Ammonia dihydrate. *High Pressure Research*, 27(2):201–212, 2007.

[45] C. W. Wilson, C. L. Bull, G. Stinton, and J. S. Loveday. Pressure-induced dehydration and the structure of Ammonia hemihydrate-ii. *Journal of Chemical Physics*, 136(9):094506, mar 2012.

[46] JS Loveday and RJ Nelmes. Ammonia monohydrate VI: A Hydrogen-bonded molecular alloy. *Physical Review Letters*, 83(21):4329, 1999.

[47] J. S. Loveday, R. J. Nelmes, C. L. Bull, H. E. Maynard-Casely, and M. Guthrie. Observation of Ammonia dihydrate in the AMH-VI structure at room temperature possible implications for the outer solar system. *High Pressure Research*, 29(3):396–404, 2009.

[48] CW Wilson, CL Bull, GW Stinton, DM Amos, M-E Donnelly, and JS Loveday. On the stability of the disordered molecular alloy phase of Ammonia hemihydrate. *The Journal of Chemical Physics*, 142(9):094707, 2015.

[49] C. Liu, A. Mafety, J. A. Queyroux, C. W. Wilson, H. Zhang, K. Béneut, G. Le Marchand, B. Baptiste, P. Dumas, G. Garbarino, F. Finocchi, J. S. Loveday, F. Pietrucci, A. M. Saitta, F. Datchi, and S. Ninet. Topologically frustrated ionisation in a water-ammonia ice mixture. *Nat. Commun.*, 8:1065, 2017.

[50] Chunli Ma, Fangfei Li, Qiang Zhou, Fengxian Huang, Jingshu Wang, Mingzhe Zhang, Zhongwu Wang, and Qiliang Cui. Ammonia molecule

rotation of pressure-induced phase transition in Ammonia hemihydrates 2nh 3· h 2 o. *RSC Advances*, 2(11):4920–4924, 2012.

[51] Weitao Yang and Paul W Ayers. Density-functional theory. In *Computational Medicinal Chemistry for Drug Discovery*, pages 103–132. CRC Press, 2003.

[52] John C Slater. A simplification of the Hartree-Fock method. *Physical Review*, 81(3):385, 1951.

[53] Rodney J Bartlett. Many-body perturbation theory and coupled cluster theory for electron correlation in molecules. *Annual Review of Physical Chemistry*, 32(1):359–401, 1981.

[54] Chr Møller and Milton S Plesset. Note on an approximation treatment for many-electron systems. *Physical Review*, 46(7):618, 1934.

[55] Axel D Becke and Kenneth E Edgecombe. A simple measure of electron localization in atomic and molecular systems. *The Journal of Chemical Physics*, 92(9):5397–5403, 1990.

[56] Richard FW Bader. Atoms in molecules. *Accounts of Chemical Research*, 18(1):9–15, 1985.

[57] GJ Ackland, MC Warren, and SJ Clark. Practical methods in ab initio lattice dynamics. *Journal of Physics: Condensed Matter*, 9(37):7861, 1997.

[58] Scott M Woodley and Richard Catlow. Crystal structure prediction from first principles. *Nature Materials*, 7(12):937, 2008.

[59] Richard Car and Mark Parrinello. Unified approach for molecular dynamics and density-functional theory. *Physical Review Letters*, 55(22):2471, 1985.

[60] Max Born and Kun Huang. *Dynamical theory of crystal lattices*. Clarendon press, 1954.

[61] Douglas R Hartree. The wave mechanics of an atom with a non-coulomb central field. part I. theory and methods. In *Mathematical Proceedings of the Cambridge Philosophical Society*, volume 24, pages 89–110. Cambridge University Press, 1928.

[62] Carl-Olof Almbladh, Ulf von Barth, ZD Popovic, and Malcolm J Stott. Screening of a proton in an electron gas. *Physical Review B*, 14(6):2250, 1976.

[63] Vladimir Fock. Näherungsmethode zur lösung des quantenmechanischen mehrkörperproblems. *Zeitschrift für Physik*, 61(1-2):126–148, 1930.

[64] John C Slater. The theory of complex spectra. *Physical Review*, 34(10):1293, 1929.

[65] Pierre Hohenberg and Walter Kohn. Inhomogeneous electron gas. *Physical Review*, 136(3B):B864, 1964.

[66] Mel Levy. Universal variational functionals of electron densities, first-order density matrices, and natural spin-orbitals and solution of the v-representability problem. *Proceedings of the National Academy of Sciences*, 76(12):6062–6065, 1979.

[67] Mel Levy. Electron densities in search of Hamiltonians. *Physical Review A*, 26(3):1200, 1982.

[68] Mel Levy and John P Perdew. The constrained search formulation of density functional theory. In *Density Functional Methods In Physics*, pages 11–30. Springer, 1985.

[69] Haïm Brézis and Elliott Lieb. A relation between pointwise convergence of functions and convergence of functionals. *Proceedings of the American Mathematical Society*, 88(3):486–490, 1983.

[70] Walter Kohn and Lu Jeu Sham. Self-consistent equations including exchange and correlation effects. *Physical Review*, 140(4A):A1133, 1965.

[71] Yan Alexander Wang and Emily A Carter. Orbital-free kinetic-energy density functional theory. In *Theoretical Methods in Condensed Phase Chemistry*, pages 117–184. Springer, 2002.

[72] FG Scholtz, HB Geyer, and FJW Hahne. Quasi-Hermitian operators in quantum mechanics and the variational principle. *Annals of Physics*, 213(1):74–101, 1992.

[73] Arnold Sommerfeld. Zur elektronentheorie der metalle auf grund der fermischen statistik. *Zeitschrift für Physik*, 47(1-2):1–32, 1928.

[74] Paul AM Dirac. Note on exchange phenomena in the Thomas atom. In *Mathematical Proceedings of the Cambridge Philosophical Society*, volume 26, pages 376–385. Cambridge University Press, 1930.

[75] David M Ceperley and BJ Alder. Ground state of the electron gas by a stochastic method. *Physical Review Letters*, 45(7):566, 1980.

[76] John P Perdew and Alex Zunger. Self-interaction correction to density-functional approximations for many-electron systems. *Physical Review B*, 23(10):5048, 1981.

[77] MT Yin and Marvin L Cohen. Microscopic theory of the phase transformation and lattice dynamics of Si. *Physical Review Letters*, 45(12):1004, 1980.

[78] John P Perdew and Mel Levy. Physical content of the exact Kohn-Sham orbital energies: band gaps and derivative discontinuities. *Physical Review Letters*, 51(20):1884, 1983.

[79] John P Perdew, Kieron Burke, and Matthias Ernzerhof. Generalized gradient approximation made simple. *Physical Review Letters*, 77(18):3865, 1996.

[80] John P Perdew, Adrienn Ruzsinszky, Gábor I Csonka, Oleg A Vydrov, Gustavo E Scuseria, Lucian A Constantin, Xiaolan Zhou, and Kieron Burke. Restoring the density-gradient expansion for exchange in solids and surfaces. *Physical Review Letters*, 100(13):136406, 2008.

[81] Matthias Ernzerhof and Gustavo E Scuseria. Assessment of the Perdew–Burke–Ernzerhof exchange-correlation functional. *The Journal of Chemical Physics*, 110(11):5029–5036, 1999.

[82] Joel Ireta, Jörg Neugebauer, and Matthias Scheffler. On the accuracy of DFT for describing Hydrogen bonds: dependence on the bond directionality. *The Journal of Physical Chemistry A*, 108(26):5692–5698, 2004.

[83] WMC Foulkes, L Mitas, RJ Needs, and G Rajagopal. Quantum Monte Carlo simulations of solids. *Reviews of Modern Physics*, 73(1):33, 2001.

[84] John P Perdew, Matthias Ernzerhof, and Kieron Burke. Rationale for mixing exact exchange with density functional approximations. *The Journal of Chemical Physics*, 105(22):9982–9985, 1996.

[85] Jochen Heyd and Gustavo E Scuseria. Efficient hybrid density functional calculations in solids: Assessment of the Heyd–Scuseria–Ernzerhof screened Coulomb hybrid functional. *The Journal of Chemical Physics*, 121(3):1187–1192, 2004.

[86] Carlo Adamo and Vincenzo Barone. Toward reliable density functional methods without adjustable parameters: The PBE0 model. *The Journal of Chemical Physics*, 110(13):6158–6170, 1999.

[87] Stefan Grimme. Semiempirical GGA-type density functional constructed with a long-range dispersion correction. *Journal of Computational Chemistry*, 27(15):1787–99, nov 2006.

[88] Kyuho Lee, Éamonn D Murray, Lingzhu Kong, Bengt I Lundqvist, and David C Langreth. Higher-accuracy van der Waals density functional. *Physical Review B*, 82(8):081101, 2010.

[89] Alexandre Tkatchenko and Matthias Scheffler. Accurate molecular van der Waals interactions from ground-state electron density and free-atom reference data. *Physical Review Letters*, 102(7):073005, feb 2009.

[90] Alberto Ambrosetti, Anthony M Reilly, Robert A. DiStasio, and Alexandre Tkatchenko. Long-range correlation energy calculated from coupled atomic response functions. *Journal of Chemical Physics*, 140(18):18A508, may 2014.

[91] Ann E Mattsson. In pursuit of the "divine" functional. *Science*, 298(5594):759–760, 2002.

[92] Michael G Medvedev, Ivan S Bushmarinov, Jianwei Sun, John P Perdew, and Konstantin A Lyssenko. Density functional theory is straying from the path toward the exact functional. *Science*, 355(6320):49–52, 2017.

[93] Ferdi Aryasetiawan and Olle Gunnarsson. The GW method. *Reports on Progress in Physics*, 61(3):237, 1998.

[94] H Ehrenreich and Morrel H Cohen. Self-consistent field approach to the many-electron problem. *Physical Review*, 115(4):786, 1959.

[95] Jianmin Tao, John P Perdew, Viktor N Staroverov, and Gustavo E Scuseria. Climbing the density functional ladder: Nonempirical meta–generalized gradient approximation designed for molecules and solids. *Physical Review Letters*, 91(14):146401, 2003.

[96] Ingo Loa, RJ Nelmes, LF Lundegaard, and MI McMahon. Extraordinarily complex crystal structure with mesoscopic patterning in barium at high pressure. *Nature Materials*, 11(7):627, 2012.

[97] Jürgen Hafner. Ab-initio simulations of materials using VASP: Density-functional theory and beyond. *Journal of Computational Chemistry*, 29(13):2044–2078, 2008.

[98] Volker Blum, Ralf Gehrke, Felix Hanke, Paula Havu, Ville Havu, Xinguo Ren, Karsten Reuter, and Matthias Scheffler. Ab initio molecular simulations with numeric atom-centered orbitals. *Computer Physics Communications*, 180(11):2175–2196, 2009.

[99] Mike C Payne, Michael P Teter, Douglas C Allan, TA Arias, and JD Joannopoulos. Iterative minimization techniques for ab initio total-energy calculations: molecular dynamics and conjugate gradients. *Reviews of modern physics*, 64(4):1045, 1992.

[100] Artem R Oganov and Peter I Dorogokupets. All-electron and pseudopotential study of MgO: Equation of state, anharmonicity, and stability. *Physical Review B*, 67(22):224110, 2003.

[101] DR Hamann, M Schlüter, and C Chiang. Norm-conserving pseudopotentials. *Physical Review Letters*, 43(20):1494, 1979.

[102] David Vanderbilt. Soft self-consistent pseudopotentials in a generalized eigenvalue formalism. *Physical Review B*, 41(11):7892, 1990.

[103] Peter E Blöchl. Projector augmented-wave method. *Physical Review B*, 50(24):17953, 1994.

[104] Reinhold F Fink. Why does MP2 work? *The Journal of Chemical Physics*, 145(18):184101, 2016.

[105] Dieter Cremer. Møller–Plesset perturbation theory: from small molecule methods to methods for thousands of atoms. *Wiley Interdisciplinary Reviews: Computational Molecular Science*, 1(4):509–530, 2011.

[106] Matthew L Leininger, Wesley D Allen, Henry F Schaefer III, and C David Sherrill. Is Mo/ller–Plesset perturbation theory a convergent ab initio method? *The Journal of Chemical Physics*, 112(21):9213–9222, 2000.

[107] F Coester. Bound states of a many-particle system. *Nuclear Physics*, 7:421–424, 1958.

[108] Andriy O Lyakhov, Artem R Oganov, Harold T Stokes, and Qiang Zhu. New developments in evolutionary structure prediction algorithm USPEX. *Computer Physics Communications*, 184(4):1172–1182, 2013.

[109] Alec Belsky, Mariette Hellenbrandt, Vicky Lynn Karen, and Peter Luksch. New developments in the Inorganic Crystal Structure Database (ICSD): accessibility in support of materials research and design. *Acta Crystallographica Section B: Structural Science*, 58(3):364–369, 2002.

[110] MR Hoare and J McInnes. Statistical mechanics and morphology of very small atomic clusters. *Faraday Discussions of the Chemical Society*, 61:12–24, 1976.

[111] CJ Tsai and KD Jordan. Use of an eigenmode method to locate the stationary points on the potential energy surfaces of selected Argon and Water clusters. *The Journal of Physical Chemistry*, 97(43):11227–11237, 1993.

[112] David B Laks, LG Ferreira, Sverre Froyen, and Alex Zunger. Efficient cluster expansion for substitutional systems. *Physical Review B*, 46(19):12587, 1992.

[113] Christopher C Fischer, Kevin J Tibbetts, Dane Morgan, and Gerbrand Ceder. Predicting crystal structure by merging data mining with quantum mechanics. *Nature Materials*, 5(8):641, 2006.

[114] John Maddox. Waves caused by extreme dilution. *Nature*, 335:760–763, 1988.

[115] Gareth IG Griffiths, A Dominic Fortes, Chris J Pickard, and RJ Needs. Crystal structure of Ammonia dihydrate ii. *The Journal of Chemical Physics*, 136(17):174512, 2012.

[116] Zbigniew H Stachurski. On structure and properties of amorphous materials. *Materials*, 4(9):1564–1598, 2011.

[117] KJ Laws, DB Miracle, and M Ferry. A predictive structural model for bulk metallic glasses. *Nature Communications*, 6:8123, 2015.

[118] Bing Zhu, Dong Die, Ren-Cai Li, Hui Lan, Ben-Xia Zheng, and Zhi-Qin Li. Insights into the structural, electronic and magnetic properties of Ni-doped gold clusters: Comparison with pure gold clusters. *Journal of Alloys and Compounds*, 696:402–412, 2017.

[119] Chris J Pickard and RJ Needs. Ab initio random structure searching. *Journal of Physics: Condensed Matter*, 23(5):053201, 2011.

[120] Claire P Massen and Jonathan PK Doye. Power-law distributions for the areas of the basins of attraction on a potential energy landscape. *Physical Review E*, 75(3):037101, 2007.

[121] Shantanu Roy, Stefan Goedecker, and Vladimir Hellmann. Bell-Evans-Polanyi principle for molecular dynamics trajectories and its implications for global optimization. *Physical Review E*, 77(5):056707, 2008.

[122] Frank H Stillinger. Exponential multiplicity of inherent structures. *Physical Review E*, 59(1):48, 1999.

[123] Jonathan PK Doye and Claire P Massen. Characterizing the network topology of the energy landscapes of atomic clusters. *The Journal of Chemical Physics*, 122(8):084105, 2005.

[124] Linus Pauling. The principles determining the structure of complex ionic crystals. *Journal of the American Chemical Society*, 51(4):1010–1026, 1929.

[125] A Dominic Fortes, Emmanuelle Suard, Marie-Hélène Lemée-Cailleau, Christopher J Pickard, and Richard J Needs. Crystal structure of Ammonia monohydrate phase ii. *Journal of the American Chemical Society*, 131(37):13508–13515, 2009.

[126] Artem R Oganov and Colin W Glass. Crystal structure prediction using ab initio evolutionary techniques: Principles and applications. *The Journal of Chemical Physics*, 124(24):244704, 2006.

[127] David C Lonie and Eva Zurek. Xtalopt: An open-source evolutionary algorithm for crystal structure prediction. *Computer Physics Communications*, 182(2):372–387, 2011.

[128] Yanchao Wang, Jian Lv, Li Zhu, and Yanming Ma. Crystal structure prediction via particle-swarm optimization. *Physical Review B*, 82(9):094116, 2010.

[129] James Kennedy. Particle swarm optimization. In *Encyclopedia of Machine Learning*, pages 760–766. Springer, 2010.

[130] Russ C Eberhart and James Kennedy. A new optimizer using particle swarm theory. In *Proceedings of the sixth international symposium on micro machine and human science*, volume 1, pages 39–43. New York, NY, 1995.

[131] Yanchao Wang, Jian Lv, Li Zhu, and Yanming Ma. CALYPSO: A method for crystal structure prediction. *Computer Physics Communications*, 183(10):2063–2070, 2012.

[132] Yanchao Wang and Yanming Ma. Perspective: Crystal structure prediction at high pressures. *The Journal of Chemical Physics*, 140(4):040901, 2014.

[133] J Pannetier, J Bassas-Alsina, J Rodriguez-Carvajal, and V Caignaert. Prediction of crystal structures from crystal chemistry rules by simulated annealing. 1990.

[134] Maximilian Amsler and Stefan Goedecker. Crystal structure prediction using the minima hopping method. *The Journal of Chemical Physics*, 133(22):224104, 2010.

[135] David J Wales and Jonathan PK Doye. Global optimization by basin-hopping and the lowest energy structures of Lennard-Jones clusters containing up to 110 atoms. *The Journal of Physical Chemistry A*, 101(28):5111–5116, 1997.

[136] Roman Martoňák, Alessandro Laio, Marco Bernasconi, Chiara Ceriani, Paolo Raiteri, Federico Zipoli, and Michele Parrinello. Simulation of structural phase transitions by metadynamics. *Zeitschrift für Kristallographie*, 220(5/6/2005):489–498, 2005.

[137] Mel Levy and John P Perdew. Hellmann-feynman, virial, and scaling requisites for the exact universal density functionals. shape of the correlation potential and diamagnetic susceptibility for atoms. *Physical Review A*, 32(4):2010, 1985.

[138] A Loveridge-Smith, A Allen, J Belak, T Boehly, A Hauer, B Holian, D Kalantar, G Kyrala, RW Lee, P Lomdahl, et al. Anomalous elastic response of silicon to uniaxial shock compression on nanosecond time scales. *Physical Review Letters*, 86(11):2349, 2001.

[139] GP Francis and MC Payne. Finite basis set corrections to total energy pseudopotential calculations. *Journal of Physics: Condensed Matter*, 2(19):4395, 1990.

[140] Andreas Savin, Ove Jepsen, Jürgen Flad, Ole Krogh Andersen, Heinzwerner Preuss, and Hans Georg von Schnering. Electron localization in solid-state structures of the elements: the diamond structure. *Angewandte Chemie International Edition*, 31(2):187–188, 1992.

[141] Alberto Otero-de-la Roza, MA Blanco, A Martín Pendás, and Víctor Luaña. Critic: a new program for the topological analysis of solid-state electron densities. *Computer Physics Communications*, 180(1):157–166, 2009.

[142] Yunwei Zhang, Hui Wang, Yanchao Wang, Lijun Zhang, and Yanming Ma. Computer-assisted inverse design of inorganic electrides. *Physical Review X*, 7(1):011017, 2017.

[143] Daniel Sanchez-Portal, Emilio Artacho, and Jose M Soler. Projection of plane-wave calculations into atomic orbitals. *Solid State Communications*, 95(10):685–690, 1995.

[144] Robert S Mulliken. Electronic population analysis on LCAO–MO molecular wave functions. i. *The Journal of Chemical Physics*, 23(10):1833–1840, 1955.

[145] Graeme Henkelman, Andri Arnaldsson, and Hannes Jónsson. A fast and robust algorithm for Bader decomposition of charge density. *Computational Materials Science*, 36(3):354–360, 2006.

[146] Stefano Baroni, Stefano De Gironcoli, Andrea Dal Corso, and Paolo Giannozzi. Phonons and related crystal properties from density-functional perturbation theory. *Reviews of Modern Physics*, 73(2):515, 2001.

[147] Alexei A Maradudin, Elliott Waters Montroll, George Herbert Weiss, and IP Ipatova. *Theory of lattice dynamics in the harmonic approximation*, volume 3. Academic press New York, 1963.

[148] Bartomeu Monserrat, Neil D Drummond, Philip Dalladay-Simpson, Ross T Howie, Pablo López Ríos, Eugene Gregoryanz, Chris J Pickard, and Richard J Needs. Structure and metallicity of phase V of Hydrogen. *Physical Review Letters*, 120(25):255701, 2018.

[149] J Dana Honeycutt and Hans C Andersen. Molecular dynamics study of melting and freezing of small Lennard-Jones clusters. *Journal of Physical Chemistry*, 91(19):4950–4963, 1987.

[150] Denis J Evans and Brad Lee Holian. The Nose–Hoover thermostat. *The Journal of Chemical Physics*, 83(8):4069–4074, 1985.

[151] Dominik Marx and Michele Parrinello. Ab initio path integral molecular dynamics: Basic ideas. *The Journal of Chemical Physics*, 104(11):4077–4082, 1996.

[152] Sahin Buyukdagli, Alexander V Savin, and Bambi Hu. Computation of the temperature dependence of the heat capacity of complex molecular systems using random color noise. *Physical Review E*, 78(6):066702, 2008.

[153] Albert Einstein. On the motion of small particles suspended in liquids at rest required by the molecular-kinetic theory of heat. *Annalen der physik*, 17:549–560, 1905.

[154] C Cavazzoni, GL Chiarotti, S Scandolo, E Tosatti, M Bernasconi, and M Parrinello. Superionic and metallic states of Water and Ammonia at giant planet conditions. *Science*, 283(5398):44–46, 1999.

[155] Richard J Gowers and Paola Carbone. A multiscale approach to model Hydrogen bonding: The case of polyamide. *The Journal of Chemical Physics*, 142(22):224907, 2015.

[156] BHLB Hammer, Lars Bruno Hansen, and Jens Kehlet Nørskov. Improved adsorption energetics within density-functional theory using revised Perdew-Burke-Ernzerhof functionals. *Physical Review B*, 59(11):7413, 1999.

[157] Yanchao Wang, Jian Lv, Li Zhu, and Yanming Ma. Crystal structure prediction via particle-swarm optimization. *Physical Review B*, 82(9):094116, sep 2010.

[158] Thorsten Bartels-Rausch, Vance Bergeron, Julyan HE Cartwright, Rafael Escribano, John L Finney, Hinrich Grothe, Pedro J Gutiérrez, Jari Haapala, Werner F Kuhs, Jan BC Pettersson, et al. Ice structures, patterns, and processes: A view across the icefields. *Reviews of Modern Physics*, 84(2):885, 2012.

[159] John D Bernal and Ralph H Fowler. A theory of water and ionic solution, with particular reference to Hydrogen and Hydroxyl ions. *The Journal of Chemical Physics*, 1(8):515–548, 1933.

[160] Arthur P Ramirez, A Hayashi, RJ al Cava, R Siddharthan, and BS Shastry. Zero-point entropy in spin ice. *Nature*, 399(6734):333, 1999.

[161] Linus Pauling. The structure and entropy of ice and of other crystals with some randomness of atomic arrangement. *Journal of the American Chemical Society*, 57(12):2680–2684, 1935.

[162] Y Tajima, T Matsuo, and H Suga. Phase transition in KOH-doped hexagonal ice. *Nature*, 299(5886):810, 1982.

[163] Edgar A Engel, Andrea Anelli, Michele Ceriotti, Chris J Pickard, and Richard J Needs. Mapping uncharted territory in ice from zeolite networks to ice structures. *Nature Communications*, 9(1):2173, 2018.

[164] Yingying Huang, Chongqin Zhu, Lu Wang, Jijun Zhao, and Xiao Cheng Zeng. Prediction of a new ice clathrate with record low density: A potential candidate as ice xix in guest-free form. *Chemical Physics Letters*, 671:186–191, 2017.

[165] Marius Millot, Sebastien Hamel, J Ryan Rygg, Peter M Celliers, Gilbert W Collins, Federica Coppari, Dayne E Fratanduono, Raymond Jeanloz, Damian C Swift, and Jon H Eggert. Experimental evidence for superionic water ice using shock compression. *Nature Physics*, 14(3):297, 2018.

[166] Jiming Sun, Bryan K Clark, Salvatore Torquato, and Roberto Car. The phase diagram of high-pressure superionic ice. *Nature Communications*, 6:8156, 2015.

[167] Christoph G Salzmann, Paolo G Radaelli, Ben Slater, and John L Finney. The polymorphism of ice: five unresolved questions. *Physical Chemistry Chemical Physics*, 13(41):18468–18480, 2011.

[168] Yoshio Takii, Kenichiro Koga, and Hideki Tanaka. A plastic phase of water from computer simulation. *The Journal of Chemical Physics*, 128(20):204501, 2008.

[169] JL Aragones and C Vega. Plastic crystal phases of simple water models. *The Journal of Chemical Physics*, 130(24):244504, 2009.

[170] LE Bove, S Klotz, Th Strässle, M Koza, J Teixeira, and AM Saitta. Translational and rotational diffusion in water in the Gigapascal range. *Physical Review Letters*, 111(18):185901, 2013.

[171] Silvio Pipolo, Mathieu Salanne, Guillaume Ferlat, Stefan Klotz, A Marco Saitta, and Fabio Pietrucci. Navigating at will on the water phase diagram. *Physical Review Letters*, 119(24):245701, 2017.

[172] J Beau W Webber, John C Dore, John H Strange, Ross Anderson, and Bahman Tohidi. Plastic ice in confined geometry: the evidence from neutron diffraction and NMR relaxation. *Journal of Physics: Condensed Matter*, 19(41):415117, 2007.

[173] WB Durham, SH Kirby, HC Heard, LA Stern, and CO Boro. Water ice phases II, III, and V: Plastic deformation and phase relationships. *Journal of Geophysical Research: Solid Earth*, 93(B9):10191–10208, 1988.

[174] A Polian and M Grimsditch. New high-pressure phase of H_2O: Ice X. *Physical Review Letters*, 52(15):1312, 1984.

[175] Hugh F Wilson, Michael L Wong, and Burkhard Militzer. Superionic to superionic phase change in water: Consequences for the interiors of Uranus and Neptune. *Physical Review Letters*, 110(15):151102, 2013.

[176] Chris J Pickard, Miguel Martinez-Canales, and Richard J Needs. Decomposition and Terapascal phases of water ice. *Physical Review Letters*, 110(24):245701, 2013.

[177] IA Ryzhkin. Superionic transition in ice. *Solid state communications*, 56(1):57–60, 1985.

[178] Pierfranco Demontis, Richard LeSar, and Michael L Klein. New high-pressure phases of ice. *Physical Review Letters*, 60(22):2284, 1988.

[179] NC Holmes, WJ Nellis, WB Graham, and GE Walrafen. Spontaneous Raman scattering from shocked water. *Physical Review Letters*, 55(22):2433, 1985.

[180] Nir Goldman, Laurence E Fried, I-Feng W Kuo, and Christopher J Mundy. Bonding in the superionic phase of water. *Physical Review Letters*, 94(21):217801, 2005.

[181] Ronald Redmer, Thomas R Mattsson, Nadine Nettelmann, and Martin French. The phase diagram of water and the magnetic fields of Uranus and Neptune. *Icarus*, 211(1):798–803, 2011.

[182] Martin French, Michael P Desjarlais, and Ronald Redmer. Ab initio calculation of thermodynamic potentials and entropies for superionic water. *Physical Review E*, 93(2):022140, 2016.

[183] Martin French, Thomas R Mattsson, and Ronald Redmer. Diffusion and electrical conductivity in water at ultrahigh pressures. *Physical Review B*, 82(17):174108, 2010.

[184] Martin French, Sebastien Hamel, and Ronald Redmer. Dynamical screening and ionic conductivity in water from ab initio simulations. *Physical Review Letters*, 107(18):185901, 2011.

[185] JB Boyce, JC Mikkelsen Jr, and M O'keeffe. Ion dynamics and sublattice melting in the superionic conductor PbF_2. *Solid State Communications*, 21(10):955–958, 1977.

[186] Noriaki Kamaya, Kenji Homma, Yuichiro Yamakawa, Masaaki Hirayama, Ryoji Kanno, Masao Yonemura, Takashi Kamiyama, Yuki Kato, Shigenori Hama, Koji Kawamoto, et al. A lithium superionic conductor. *Nature Materials*, 10(9):682, 2011.

[187] James B Boyce and Bernardo A Huberman. Superionic conductors: transitions, structures, dynamics. *Physics Reports*, 51(4):189–265, 1979.

[188] Carlos Pinilla, Amir H Irani, Nicola Seriani, and Sandro Scandolo. Ab initio parameterization of an all-atom polarizable and dissociable force field for water. *The Journal of Chemical Physics*, 136(11):114511, 2012.

[189] Alexander F Goncharov, Nir Goldman, Laurence E Fried, Jonathan C Crowhurst, I-Feng W Kuo, Christopher J Mundy, and Joseph M Zaug. Dynamic ionization of water under extreme conditions. *Physical Review Letters*, 94(12):125508, 2005.

[190] Marius Millot, Federica Coppari, J Ryan Rygg, Antonio Correa Barrios, Sebastien Hamel, Damian C Swift, and Jon H Eggert. Nanosecond X-ray diffraction of shock-compressed superionic water ice. *Nature*, 569(7755):251, 2019.

[191] Jean-Alexis Hernandez and Razvan Caracas. Superionic-superionic phase transitions in body-centered cubic H_2O ice. *Physical Review Letters*, 117(13):135503, 2016.

[192] J-A Hernandez and R Caracas. Proton dynamics and the phase diagram of dense water ice. *The Journal of Chemical Physics*, 148(21):214501, 2018.

[193] Dongdong Kang, Jiayu Dai, Huayang Sun, Yong Hou, and Jianmin Yuan. Quantum simulation of thermally-driven phase transition and oxygen K-edge x-ray absorption of high-pressure ice. *Scientific reports*, 3:3272, 2013.

[194] Chris J Pickard and RJ Needs. Highly compressed Ammonia forms an ionic crystal. *Nature Materials*, 7(10):775–779, 2008.

[195] Guang-Rui Qian, Chao-Hao Hu, Artem R Oganov, Qingfeng Zeng, and Huai-Ying Zhou. Diverse chemistry of stable Hydronitrogens, and implications for planetary and materials sciences. *Scientific Reports*, 6:25947, 2016.

[196] Sandra Ninet and Frédéric Datchi. High pressure-high temperature phase diagram of Ammonia. *arXiv preprint arXiv:0801.0913*, 2008.

[197] S Ninet, F Datchi, and AM Saitta. Proton disorder and superionicity in hot dense Ammonia ice. *Physical Review Letters*, 108(16):165702, 2012.

[198] Mandy Bethkenhagen, Martin French, and Ronald Redmer. Equation of state and phase diagram of Ammonia at high pressures from ab initio simulations. *The Journal of Chemical Physics*, 138(23):234504, 2013.

[199] Gareth IG Griffiths, Alston J Misquitta, A Dominic Fortes, Chris J Pickard, and Richard J Needs. High pressure ionic and molecular crystals of Ammonia monohydrate within density functional theory. *The Journal of Chemical Physics*, 137(6):064506, 2012.

[200] David A Rodham, Sakae Suzuki, Richard D Suenram, Frank J Lovas, Siddharth Dasgupta, William A Goddard III, and Geoffrey A Blake. Hydrogen bonding in the Benzene–Ammonia dimer. *Nature*, 362(6422):735, 1993.

[201] George C Pimentel and Aubrey L McClellan. The Hydrogen bond. 1960.

[202] Stefan Grimme. Accurate description of van der Waals complexes by density functional theory including empirical corrections. *Journal of Computational Chemistry*, 25(12):1463–1473, 2004.

[203] M Gauthier, Ph Pruzan, JC Chervin, and JM Besson. Raman scattering study of ammonia up to 75 GPa: Evidence for bond symmetrization at 60 GPa. *Physical Review B*, 37(4):2102, 1988.

[204] Dafang Li, Cong Wang, Jun Yan, Zhen-Guo Fu, and Ping Zhang. Structural and transport properties of ammonia along the principal Hugoniot. *Scientific reports*, 7(1):12338, 2017.

[205] JS Loveday, RJ Nelmes, WG Marshall, JM Besson, S Klotz, and G Hamel. Structure of deuterated Ammonia IV. *Physical Review Letters*, 76(1):74, 1996.

[206] Mandy Bethkenhagen, Daniel Cebulla, Ronald Redmer, and Sebastien Hamel. Superionic phases of the 1:1 Water-Ammonia mixture. *Journal of Physical Chemistry A*, pages 10582–10588, 2015.

[207] Xue Jiang, Xue Wu, Zhaoyang Zheng, Yingying Huang, Jijun Zhao, and Supplementary Information. Ionic and superionic phases in Ammonia dihydrate NH_3 $2H_2O$ under high pressure. *Physical Review B*, 95(14):144104, apr 2017.

[208] Mal-Soon Lee and Sandro Scandolo. Mixtures of planetary ices at extreme conditions. *Nature Communications*, 2:185, 2011.

[209] Razvan Caracas. Dynamical instabilities of ice X. *Physical Review Letters*, 101(8):085502, 2008.

[210] M Benoit, M Bernasconi, P Focher, and M Parrinello. New high-pressure phase of ice. *Physical Review Letters*, 76(16):2934, 1996.

[211] Burkhard Militzer and Hugh F Wilson. New phases of water ice predicted at megabar pressures. *Physical Review Letters*, 105(19):195701, 2010.

[212] Jeffrey M McMahon. Ground-state structures of ice at high pressures from ab initio random structure searching. *Physical Review B*, 84(22):220104, 2011.

[213] Min Ji, Koichiro Umemoto, Cai-Zhuang Wang, Kai-Ming Ho, and Renata M Wentzcovitch. Ultrahigh-pressure phases of H_2O ice predicted using an adaptive genetic algorithm. *Physical Review B*, 84(22):220105, 2011.

[214] Yanchao Wang, Hanyu Liu, Jian Lv, Li Zhu, Hui Wang, and Yanming Ma. High pressure partially ionic phase of water ice. *Nature Communications*, 2:563, 2011.

[215] I Olovsson and DH Templeton. X-ray study of solid ammonia. *Acta Crystallographica*, 12(11):832–836, 1959.

[216] S Ninet, F Datchi, S Klotz, G Hamel, JS Loveday, and RJ Nelmes. Hydrogen bonding in ND_3 probed by neutron diffraction to 24 GPa. *Physical Review B*, 79(10):100101, 2009.

[217] S Ninet, F Datchi, P Dumas, M Mezouar, G Garbarino, A Mafety, CJ Pickard, RJ Needs, and AM Saitta. Ionic Ammonia ice. *arXiv preprint arXiv:1401.1419*, 2014.

[218] Biswajit Santra, Jiří Klimeš, Dario Alfè, Alexandre Tkatchenko, Ben Slater, Angelos Michaelides, Roberto Car, and Matthias Scheffler. Hydrogen bonds and van der Waals forces in ice at ambient and high pressures. *Physical Review Letters*, 107(18):185701, 2011.

[219] M Marques, GJ Ackland, and JS Loveday. Nature and stability of ice X. *High Pressure Research*, 29(2):208–211, 2009.

[220] JC Cheftel, J Levy, and E Dumay. Pressure-assisted freezing and thawing: principles and potential applications. *Food Reviews International*, 16(4):453–483, 2000.

[221] M Song, H Yamawaki, H Fujihisa, M Sakashita, and K Aoki. Infrared absorption study of fermi resonance and hydrogen-bond symmetrization of ice up to 141 gpa. *Physical Review B*, 60(18):12644, 1999.

[222] Viktor V Struzhkin, Alexander F Goncharov, Russell J Hemley, and Ho-kwang Mao. Cascading fermi resonances and the soft mode in dense ice. *Physical Review Letters*, 78(23):4446, 1997.

[223] Alexander F Goncharov, Viktor V Struzhkin, Ho-kwang Mao, and Russell J Hemley. Raman spectroscopy of dense h 2 o and the transition to symmetric hydrogen bonds. *Physical Review Letters*, 83(10):1998, 1999.

[224] Paul Loubeyre, René LeToullec, Elodie Wolanin, Michel Hanfland, and Daniel Hausermann. Modulated phases and proton centring in ice observed by X-ray diffraction up to 170 GPa. *Nature*, 397(6719):503–506, 1999.

[225] Michele Ceriotti, Wei Fang, Peter G. Kusalik, Ross H. McKenzie, Angelos Michaelides, Miguel A. Morales, and Thomas E. Markland. Nuclear quantum effects in water and aqueous systems: Experiment, theory, and current challenges. *Chemical Reviews*, 116(13):7529–7550, 2016.

[226] A Dominic Fortes, Emmanuelle Suard, Marie Hélène Lemée-Cailleau, Christopher J Pickard, and Richard J Needs. Crystal structure of Ammonia monohydrate phase ii. *Journal of the American Chemical Society*, 131(11):13508–13515, 2009.

[227] Gareth I. G. Griffiths, A. Dominic Fortes, Chris J. Pickard, and R. J. Needs. Crystal structure of Ammonia dihydrate ii. *Journal of Chemical Physics*, 136(17):174512, may 2012.

[228] A. D. Fortes, J. P. Brodholt, I. G. Wood, L. Vocadlo, and H. D. B. Jenkins. Ab initio simulation of Ammonia monohydrate (NH_3H_2O) and Ammonium hydroxide (NH_4 OH). *Journal of Chemical Physics*, 115(15):7006, 2001.

[229] Mandy Bethkenhagen, Daniel Cebulla, Ronald Redmer, and Sebastien Hamel. Superionic phases of the 1: 1 Water–Ammonia mixture. *The Journal of Physical Chemistry A*, 119(42):10582–10588, 2015.

[230] J. S. Loveday and R. J. Nelmes. Structural studies of Ammonia hydrates. In M. H. Manghnani, W. J. Nellis, and M. F. Nicol, editors, *Science and technology of high pressure : proceedings of the International Conference on High Pressure Sciene and Technology (AIRAPT-17)*, pages 133–136, Hyderabad, India, 2000. Universities Press.

[231] Shuai Zhang, Hugh F. Wilson, Kevin P. Driver, and Burkhard Militzer. H_4O and other Hydrogen-Oxygen compounds at giant-planet core pressures. *Physical Review B*, 87:024112, 2013.

[232] Ronald Redmer, Thomas R. Mattsson, Nadine Nettelmann, and Martin French. The phase diagram of water and the magnetic fields of Uranus and Neptune. *Icarus*, 211(1):798–803, jan 2011.

[233] Francis S. Galasso, N. Kurti, and R. Smoluchowski. *Structure and Properties of Inorganic Solids*. Pergamon Press, 1970.

[234] Richard F. W. Bader. *Atoms in Molecules: A Quantum Theory*. Oxford University Press, Oxford, UK, 1994.

[235] P. D. Mitev, G. Gajewski, and K. Hermansson. Anharmonic OH vibrations in brucite: Small pressure-induced redshift in the range 0-22 GPa. *Am. Mineral.*, 94(11-12):1687–1697, 2009.

[236] A Hermann, W G Schmidt, and P Schwerdtfeger. Resolving the optical spectrum of water: Coordination and electrostatic effects. *Physics Review Letters*, 100:207403, 2008.

[237] Andreas Hermann and Peter Schwerdtfeger. Blueshifting the onset of optical uv absorption for water under pressure. *Physics Review Letters*, 106(18):187403, may 2011.

[238] J. D. Dill, L. C. Allen, W. C. Topp, and J. A. Pople. A systematic study of the nine Hydrogen-bonded OH_2, and HF dimers involving NH_3, OH_2, and HF. *Journal of the American Chemical Society*, 97(25):7220–7226, 1975.

[239] Mandy Bethkenhagen, Martin French, and Ronald Redmer. Equation of state and phase diagram of Ammonia at high pressures from ab initio simulations. *Journal of Chemical Physics*, 138(23):234504, jun 2013.

[240] Gareth I.G. Griffiths, Alston J. Misquitta, A. Dominic Fortes, Chris J. Pickard, and Richard J. Needs. High pressure ionic and molecular crystals of Ammonia monohydrate within density functional theory. *Journal of Chemical Physics*, 137(6):064506, aug 2012.

[241] Mandy Bethkenhagen, Edmund R. Meyer, Sebastien Hamel, Nadine Nettelmann, Martin French, Ludwig Scheibe, Christopher Ticknor, Lee A. Collins, Joel D. Kress, Jonathan J. Fortney, and Ronald Redmer. Planetary ices and the linear mixing approximation. *The Astrophysical Journal*, 848(1):67, 2017.

[242] Andreas Hermann, N. W. Ashcroft, and Roald Hoffmann. Lithium Hydroxide, LiOH, at elevated densities. *Journal of Chemical Physics*, 141(2):024505, jul 2014.

[243] Andreas Hermann. High-pressure phase transitions in Rubidium and Caesium hydroxides. *Physical Chemistry Chemical Physics*, 18(24):16527–16534, 2016.

[244] Razvan Caracas. Dynamical instabilities of ice X. *Physics Review Letters*, 101(8):85502, aug 2008.

[245] M. Marqués, G. J. Ackland, and J. S. Loveday. Nature and stability of ice X. *High Pressure Research*, 29(2):208–211, jun 2009.

[246] K. Aoki, H. Yamawaki, M. Sakashita, and H. Fujihisa. Infrared absorption study of the Hydrogen-bond symmetrization in ice to 110 GPa. *Physical Review B. Condensed Matter*, 54(22):15673–15677, dec 1996.

[247] AD Fortes, IG Wood, L Vočadlo, KS Knight, WG Marshall, MG Tucker, and F Fernandez-Alonso. Phase behaviour and thermoelastic properties of perdeuterated Ammonia hydrate and ice polymorphs from 0 to 2 GPa. *Journal of Applied Crystallography*, 42(5):846–866, 2009.

[248] Andrew Fortes. *Computational and experimental studies of solids in the Ammonia-Water system.* PhD thesis, University of London, 2004.

[249] M. L. Troost. Sur de nouvelles combinaisons de l'acide bromhydrique et de l'acide iodhydrique avec l'ammoniaque. *Comptes rendus de l'Acadmie des Sciences*, 92:715–718, 1881.

[250] George W. Watt and William R. McBride. Ammoniates of the Ammonium Halides. *Journal of the American Chemical Society*, 77(5):1317–1320, 1955.

[251] Hans Joachim Berthold, Wolfgang Preibsch, and Elke Vonholdt. On the structure of the cation N_2H_7 with an N-H N Hydrogen bond in the monoammonia adduct of Ammonium Iodide. *Angewandte Chemie International Edition in English*, 27(11):1524–1525, 1988.

[252] Xianqi Song, Ketao Yin, Yanchao Wang, Andreas Hermann, Hanyu Liu, Jian Lv, Quan Li, Changfeng Chen, and Yanming Ma. Exotic hydrogen bonding in compressed Ammonia hydrides. *The Journal of Physical Chemistry Letters*, 10:2761–2766, 2019.

[253] Yael Bronstein, Philippe Depondt, Fabio Finocchi, and Antonino Marco Saitta. Quantum-driven phase transition in ice described via an efficient Langevin approach. *Physical Review B*, 89(21):214101, 2014.

[254] Yael Bronstein, Philippe Depondt, and Fabio Finocchi. Thermal and nuclear quantum effects in the Hydrogen bond dynamical symmetrization phase transition of δ-AlOOH. *European Journal of Mineralogy*, 29(3):385–395, jun 2017.

[255] S Boone and MF Nicol. Ammonia-water mixtures at high pressures-melting curves of Ammonia dihydrate and Ammonia monohydrate and a revised high-pressure phase diagram for the water-rich region. In *Lunar and Planetary Science Conference Proceedings*, volume 21, pages 603–610, 1991.

[256] Kersti Hermansson, Grzegorz Gajewski, and Pavlin D Mitev. Origin of the OH vibrational blue shift in the LiOH crystal. *The Journal of Physical Chemistry A*, 112(51):13487–13494, 2008.

[257] Bartomeu Monserrat, ND Drummond, and RJ Needs. Anharmonic vibrational properties in periodic systems: energy, electron-phonon coupling, and stress. *Physical Review B*, 87(14):144302, 2013.

[258] Biswajit Santra, Jiří Klimeš, Alexandre Tkatchenko, Dario Alfè, Ben Slater, Angelos Michaelides, Roberto Car, and Matthias Scheffler. On the accuracy of van der Waals inclusive density-functional theory exchange-correlation functionals for ice at ambient and high pressures. *The Journal of Chemical Physics*, 139(15):154702, 2013.

[259] Michael J Gillan, Dario Alfè, and Angelos Michaelides. Perspective: How good is DFT for water? *The Journal of Chemical Physics*, 144(13):130901, 2016.

[260] Jianwei Sun, Richard C Remsing, Yubo Zhang, Zhaoru Sun, Adrienn Ruzsinszky, Haowei Peng, Zenghui Yang, Arpita Paul, Umesh Waghmare, Xifan Wu, et al. Accurate first-principles structures and energies of diversely bonded systems from an efficient density functional. *Nature Chemistry*, 8(9):831, 2016.

[261] Pattanasak Teeratchanan. First-principles studies of gas hydrates and clathrates under pressure. 2018.

[262] Jan Kosata, Padryk Merkl, Pattanasak Teeratchanan, and Andreas Hermann. Stability of Hydrogen hydrates from second-order Møller–Plesset perturbation theory. *The Journal of Physical Chemistry Letters*, 9(18):5624–5629, 2018.

[263] Pattanasak Teeratchanan and Andreas Hermann. Computational phase diagrams of noble gas hydrates under pressure. *The Journal of Chemical Physics*, 143(15):154507, 2015.

[264] Miguel Martinez-Canales, Chris J Pickard, and Richard J Needs. Thermodynamically stable phases of Carbon at multiterapascal pressures. *Physical Review Letters*, 108(4):045704, 2012.

[265] Andreas Hermann, Neil W Ashcroft, and Roald Hoffmann. Isotopic differentiation and sublattice melting in dense dynamic ice. *Physical Review B*, 88(21):214113, 2013.

[266] M J Frisch, G W Trucks, H B Schlegel, G E Scuseria, M A Robb, J R Cheeseman, G Scalmani, V Barone, B Mennucci, G A Petersson, H Nakatsuji, M Caricato, X Li, H P Hratchian, A F Izmaylov, J Bloino, G Zheng, J L Sonnenberg, M Hada, M Ehara, K Toyota, R Fukuda, J Hasegawa, M Ishida, T Nakajima, Y Honda, O Kitao, H Nakai, T Vreven, J A Montgomery Jr., J E Peralta, F Ogliaro, M Bearpark, J J Heyd, E Brothers, K N Kudin, V N Staroverov, R Kobayashi, J Normand, K Raghavachari, A Rendell, J C Burant, S S Iyengar, J Tomasi, M Cossi, N Rega, J M Millam, M Klene, J E Knox, J B Cross, V Bakken, C Adamo,

J Jaramillo, R Gomperts, R E Stratmann, O Yazyev, A J Austin, R Cammi, C Pomelli, J W Ochterski, R L Martin, K Morokuma, V G Zakrzewski, G A Voth, P Salvador, J J Dannenberg, S Dapprich, A D Daniels, Ö Farkas, J B Foresman, J V Ortiz, J Cioslowski, and D J Fox. Gaussian 09 revision A.02.

[267] Thom H Dunning, Jr. Gaussian basis sets for use in correlated molecular calculations. i. the atoms Boron through Neon and Hydrogen. *Journal of Chemical Physics*, 90(2):1007–1023, 1989.

[268] A. D. Becke and K. E. Edgecombe. A simple measure of electron localization in atomic and molecular systems. *Journal of Chemical Physics*, 92(9):5397–5403, 1990.

[269] A. Otero-de-la Roza, Erin R. Johnson, and Víctor Luaña. Critic2: A program for real-space analysis of quantum chemical interactions in solids. *Computer Physics Communications*, 185(3):1007–1018, mar 2014.

[270] G. Kresse and J. Furthmüller. Efficient iterative schemes for Ab initio total-energy calculations using a plane-wave basis set. *Physical Review B*, 54(16):11169–11186, oct 1996.

[271] G. Kresse and D. Joubert. From ultrasoft pseudopotentials to the projector augmented-wave method. *Physical Review B*, 59:1758–1775, 1999.

[272] W. Tang, E. Sanville, and G. Henkelman. A grid-based Bader analysis algorithm without lattice bias. *Journal of Physics: Condensed Matter*, 21(8):084204, feb 2009.

[273] Franck Fuster and Bernard Silvi. Does the topological approach characterize the Hydrogen bond? *Theoretical Chemistry Accounts*, 104(1):13–21, 2000.

[274] Bernard Silvi and Henryk Ratajczak. Hydrogen bonding and delocalization in the ELF analysis approach. *Physical Chemistry Chemical Physics*, 18(39):27442–27449, 2016.

[275] Martin French, Thomas R Mattsson, Nadine Nettelmann, and Ronald Redmer. Equation of state and phase diagram of water at ultrahigh pressures as in planetary interiors. *Physical Review B*, 79(5):054107, 2009.

[276] Reinier LC Akkermans, Neil A Spenley, and Struan H Robertson. Monte Carlo methods in materials studio. *Molecular Simulation*, 39(14-15):1153–1164, 2013.

[277] Edmund R. Meyer, Christopher Ticknor, Mandy Bethkenhagen, Sebastien Hamel, Ronald Redmer, Joel D. Kress, and Lee A. Collins. Bonding and structure in dense multi-component molecular mixtures. *Journal of Chemical Physics*, 143(16), 2015.

[278] Dominik Marx, Mark E Tuckerman, Jürg Hutter, and Michele Parrinello. The nature of the Hydrated excess proton in water. *Nature*, 397(6720):601, 1999.

The First Appendix - Crystallographic Information

AHH - Crystallographic information

In the following tables, we give the crystal structures of the AHH phases discussed in this work, each at a relevant pressure point.

A2/m at 40 GPa			
Lattice Parameters	(Å)	(°)	
	a=5.01170	α=90.35538	
	b=5.01170	β=90.35538	
	c=4.42760	γ=49.49192	
Atom	x	y	z
H1	-1.401262	0.001637	1.261673
H2	-0.789822	-0.227092	0.756344
H3	-0.853953	0.146047	1.077493
H4	-0.633092	0.366908	1.038542
H5	-1.134164	-0.134164	0.559657
H6	-1.336092	-0.336092	1.426181
N1	-0.735693	0.264307	0.754234
N2	-0.927824	0.072176	1.248501
O1	-1.416524	-0.416524	0.753799

Table 1 *Crystallographic information $AHHA2/m$*

P-1 at 40 GPa			
Lattice Parameters	(Å)	(°)	P (GPa)
	a=4.18483	α=93.53268	40
Space Group	b=4.89899	β=114.50651	
P-1	c=5.05895	γ=111.34557	
Atom	x	y	z
H1	-0.031562	0.555233	0.277870
H2	0.571216	-0.055934	0.275155
H3	0.477958	0.729867	0.606652
H4	-0.090408	0.735246	0.524810
H5	0.086474	-0.080546	0.304915
H6	0.153359	0.777879	-0.036526
H7	0.569473	0.767817	-0.025791
H8	0.358976	0.556349	0.170563
N1	0.083386	0.755452	0.422716
N2	0.410853	0.760689	0.092884
O1	0.733732	0.737477	0.758691

Table 2 *Crystallographic information $AHHP-1$*

Cm at 40 GPa			
Lattice Parameters	(Å)	(°)	
	a=5.01170	α=90.35538	
	b=5.01170	β=90.35538	
	c=4.42760	γ=49.49192	
Atom	x	y	z
H1	1.826421	0.236235	0.950516
H2	0.654700	0.262343	0.498742
H3	1.361322	0.975228	0.899360
H4	-0.059241	0.349228	0.417302
H9	0.135036	0.135036	0.135697
H10	0.656185	0.656185	0.763917
H11	-0.091769	-0.091769	0.119227
H12	0.667353	0.667353	0.538020
H13	1.186632	1.186632	0.796638
H14	-0.405337	0.594663	0.258806
H15	0.271351	1.271351	0.616189
H16	-0.237799	0.762201	0.231508
N1	0.427344	0.427344	0.432090
N2	0.965679	0.965679	0.951005
N3	1.287807	1.287807	0.941160
N4	0.089876	1.089876	0.426344
O1	0.764723	-0.235277	0.436290
O2	1.603323	0.603323	0.933290

Table 3 *Crystallographic information $AHHCm$*

Amma at 100 GPa			
Lattice Parameters	(Å)	(°)	
	a=4.10159	α=90.0000	
	b=3.93591	β=90.0000	
	c=8.34930	γ=90.0000	
Atom	x	y	z
H1	1.249907	0.470293	0.947169
H2	1.750156	0.518141	0.254183
H3	2.054955	0.250000	0.606497
H4	1.961905	0.250000	0.404644
H5	1.537959	0.250000	0.404637
H6	1.444750	0.250000	0.606550
N1	1.749879	0.250000	0.483109
N2	1.250191	0.750000	1.177484
O1	1.750188	0.750000	0.661922

Table 4 *Crystallographic information AHHAmma*

P-3m1 at 100 GPa			
Lattice Parameters	(Å)	(°)	
	a=3.87096	α=90.00000	
	b=3.87096	β=90.00000	
	c=2.58199	γ=120.0000	
Atom	x	y	z
H1	0.666667	0.333333	0.742039
H2	0.360936	0.180468	0.238696
N1	0.666667	0.333333	0.357703
O1	0.000000	0.000000	0.000000

Table 5 *Crystallographic information AHHP*$\bar{3}m1$

Pnna at 300 GPa			
Lattice Parameters	(Å)	(°)	
	a=3.91915	α=90.00000	
	b=3.72074	β=90.00000	
	c=6.71249	γ=90.00000	
Atom	x	y	z
H1	-0.022939	0.956920	1.147448
H2	-0.462344	0.451029	1.136614
H3	-0.176545	0.762465	0.656199
H4	-0.347914	0.739631	0.443158
N1	-0.398162	0.748495	0.587527
O1	-0.115451	0.250000	0.250000

Table 6 *Crystallographic information AHHPnna*

Pnma at 600 GPa			
Lattice Parameters	(Å)	(°)	
	a=3.96707	α=90.00000	
	b=3.22762	β=90.00000	
	c=5.98678	γ=90.00000	
Atom	x	y	z
H1	1.156792	0.495967	0.851905
H2	1.677432	0.509783	0.320586
H3	1.984307	0.250000	0.679619
H4	1.862624	0.250000	0.443980
H5	1.496334	0.250000	0.459493
H6	1.154936	0.250000	0.457907
N1	1.681498	0.250000	0.557029
N2	1.300080	0.750000	1.118227
O1	1.968856	0.750000	0.723700

Table 7 *Crystallographic information AHHPnma*

$P2_1/m$ at 400 GPa			
Lattice Parameters	(Å)	(°)	
	a=5.70349	α=90.00000	
	b=3.52038	β=97.90412	
	c=2.24096	γ=90.00000	
Atom	x	y	z
H1	0.319669	-0.511019	0.302069
H2	0.848876	-0.006609	0.181909
H9	0.410249	-0.750000	0.897519
H10	0.557144	-0.750000	0.339177
H13	0.924471	-0.250000	0.716142
H14	1.111486	-0.250000	0.278069
N1	0.392262	-0.750000	0.472131
N3	0.941276	-0.250000	0.286887
O1	0.279157	-0.250000	-0.079104

Table 8 *Crystallographic information AHHP*$2_1/m$

$P2_1/c$ at 600 GPa			
Lattice Parameters	(Å)	(°)	
	a=10.83316	α=90.00000	
	b=3.37127	β=99.57314	
	c=2.15195	γ=90.00000	
Atom	x	y	z
H1	0.153288	0.476515	0.311418
H2	0.425244	0.015799	0.174453
H3	0.339784	1.008925	0.701268
H4	0.074128	0.482431	0.825957
H9	0.202084	0.218927	0.923936
H10	0.276246	0.274393	0.359065
H13	0.462693	0.770254	0.709074
H14	0.561760	0.763523	0.302229
N1	0.192773	0.239126	0.489587
N3	0.473403	0.766567	0.266675
O1	0.143322	0.734427	0.909052

Table 9 *Crystallographic information* $AHHP2_1/c$

AHH-I at 1 GPa			
Lattice Parameters	(Å)	(°)	
	a=5.36458	α=90.000000	
	b=7.89413	β=92.571178	
	c=8.08543	γ=90.000000	
Atom	x	y	z
H1	0.386473	0.533238	0.826563
H2	0.924102	0.463913	0.171713
H3	0.923993	0.833118	-0.048053
H4	0.622616	0.859833	-0.085704
H5	0.724078	0.725106	0.056162
H6	0.245945	0.587084	0.997357
H7	0.260117	0.803133	0.794102
H8	0.264519	1.004506	0.841259
N1	0.235628	0.596894	0.870305
N2	0.243294	0.158007	0.992918
O1	0.285347	0.920860	0.747851

Table 10 *Crystallographic information AHHI*

AHH-II at 10 GPa			
Lattice Parameters	(Å)	(°)	
	a=3.16423	α=90.00000	
	b=8.84224	β=93.33907	
	c=8.33336	γ=90.00000	
Atom	x	y	z
H1	0.761617	0.027000	0.367719
H2	0.775042	0.126474	0.537683
H3	0.383072	0.145450	0.401705
H4	0.733247	0.875884	0.024040
H5	0.722634	0.777506	0.855109
H6	0.338617	0.894919	0.889162
H7	0.147588	0.781785	0.182418
H8	0.168637	0.966279	0.187997
N1	0.703285	0.131017	0.415613
N2	0.658850	0.881119	0.902831
O1	0.037847	0.874446	0.240317

Table 11 *Crystallographic information AHHII*

Molecular $P\bar{1}$ at 5 GPa			
Lattice Parameters	(Å)	(°)	
	a=4.6192	α=88.102	
	b=4.9412	β=115.88	
	c=5.6751	γ=89.655	
Atom	x	y	z
H1	0.52813	0.52813	0.52813
H2	0.89506	0.89506	0.89506
H3	-0.3142	-0.3142	-0.3142
H4	-0.8456	-0.8456	-0.8456
H5	0.39908	0.39908	0.39908
H6	0.13203	0.13203	0.13203
H7	0.60200	0.60200	0.60200
H8	0.82916	0.82916	0.82916
N1	0.23133	0.23133	0.23133
N2	0.46127	0.46127	0.46127
O1	-0.0871	-0.0871	-0.0871

Table 12 *Crystallographic information $AHHmolecularP1$*

AMH - Crystallographic information

Here lists the crystallographic information for AMH phases used in this work.

AMH - I ($P2_12_12_1$) at 1 GPa			
Lattice Parameters	**(Å)**		**(°)**
a	4.3741	α	90
b	5.4402	β	90
c	9.5271	γ	90
Atom	**x**	**y**	**z**
H1	0.45325	0.21244	0.00427
H5	0.23071	0.02792	0.44826
H9	0.42153	0.37079	0.35954
H13	0.04724	0.37014	0.35249
H17	0.24476	0.21632	0.23297
N1	0.23598	0.26220	0.33728
O1	0.26829	0.10892	0.02318

AMH - II ($P2_12_12_1$) at 3 GPa			
Lattice Parameters	**(Å)**		**(°)**
a	18.143	α	90
b	6.6162	β	90
c	6.5939	γ	90
Atom	**x**	**y**	**z**
H1	0.03096	0.66663	0.97043
H2	0.04653	0.84084	0.14141
H3	0.98023	0.66862	0.17859
H4	0.12796	0.32161	0.24711
H5	0.09478	0.54970	0.23080
H6	0.19656	0.57976	0.05479
H7	0.26088	0.60316	0.87593
H8	0.19488	0.77570	0.89761
H9	0.12110	0.43235	0.54302
H10	0.15088	0.49719	0.77004
N1	0.03251	0.69150	0.12284
N2	0.20627	0.62479	0.90837
O1	0.13612	0.46444	0.29622
O2	0.11163	0.41301	0.69162

$P4/nmm$ at 10 GPa			
Lattice Parameters	**(Å)**		**(°)**
a	4.8697	α	90
b	4.8697	β	90
c	3.0459	γ	90
Atom	**x**	**y**	**z**
H1	0.68000	0.50000	0.30657
H9	0.50000	1.00000	0.20796
N1	0.50000	0.50000	0.50000
O1	0.50000	1.00000	0.89020

$P4_3$ at 50 GPa			
Lattice Parameters	**(Å)**		**(°)**
a	4.8697	α	90
b	4.8697	β	90
c	3.0459	γ	90
Atom	**x**	**y**	**z**
H1	0.68000	0.50000	0.30657
H9	0.50000	1.00000	0.20796
N1	0.50000	0.50000	0.50000
O1	0.50000	1.00000	0.89020

$P2_1/m$ at 200 GPa			
Lattice Parameters	**(Å)**		**(°)**
a	3.6885	α	89.885
b	4.1386	β	90
c	9.3466	γ	90
Atom	**x**	**y**	**z**
H1	0.24998	0.24997	-0.00003
H2	0.27190	0.44168	0.34378
H3	0.76826	0.57240	0.09119
H4	-0.00003	0.41347	0.20464
H5	0.49997	0.36395	0.20031
H6	0.25359	0.75375	0.24054
H9	0.49997	0.59215	0.48727
H10	-0.00003	0.62598	0.94726
H12	0.73436	0.83662	0.38758
H13	0.23283	0.09060	0.15746
H14	0.99997	0.90772	0.05480
H15	0.49997	0.96946	0.52585
H19	0.49997	0.10419	0.32743
H20	0.99997	0.12042	0.30507
H21	0.24997	0.24998	0.49997
N1	-0.00003	0.17358	0.19698
N2	0.49997	0.82238	0.44239
N3	0.99997	0.66822	0.05577
N4	0.49997	0.33852	0.30930
O1	0.99997	0.17806	0.94345
O2	0.49997	0.82694	0.19127
O3	-0.00003	0.68268	0.30472
O5	0.99997	0.17320	0.44365

ADH - Crystallographic information

Here lists the crystallographic information for ADH phases used in this work.

ADH - I at 1 GPa ($P2_12_12_1$)			
Lattice Parameters	**(Å)**		**(°)**
a	6.964	α	90
b	6.8162	β	90
c	6.9508	γ	90
Atom	**x**	**y**	**z**
H1	0.25732	0.76030	0.73190
H2	0.79469	0.66740	0.48772
H3	0.93488	0.24138	0.18111
H4	0.67605	0.57261	0.76744
H5	0.15020	0.48148	0.84768
H6	0.51764	0.34674	0.34412
H7	0.84951	0.15804	0.48792
N1	0.62482	0.87228	0.13029
O1	0.65460	0.34741	0.85401
O2	0.69709	0.70770	0.71263

ADH - I* at 1 GPa ($P2_12_12_1$)			
Lattice Parameters	**(Å)**		**(°)**
a	6.542	α	90
b	6.4833	β	90
c	6.4937	γ	90
Atom	**x**	**y**	**z**
H1	0.22027	0.72384	0.75262
H2	0.81194	0.65277	0.54207
H3	0.90715	0.21885	0.19702
H4	0.66853	0.52244	0.85362
H5	0.17242	0.47292	0.81431
H6	0.51974	0.34468	0.32253
H7	0.82972	0.16537	0.49496
N1	0.63359	0.87305	0.14976
O1	0.63418	0.37538	0.89862
O2	0.72481	0.73953	0.76024

ADH - II at 3 GPa ($P2_1/c$)			
Lattice Parameters	**(Å)**		**(°)**
a	5.7961	α	90
b	6.4522	β	102.525
c	7.4272	γ	90
Atom	**x**	**y**	**z**
H1	0.73896	0.02045	0.41595
H2	0.68137	0.83853	0.26437
H3	1.01994	0.22685	0.50916
H4	0.67169	0.05555	0.71768
H5	0.55345	0.47420	0.71507
H6	0.65708	0.65386	0.59518
H7	0.79044	0.35950	0.53918
N1	0.80106	0.01977	0.83081
O1	0.29732	0.13119	0.60018
O2	0.14778	0.74076	0.55076

ADH - II* at 10 GPa ($P2_1/c$)			
Lattice Parameters	**(Å)**		**(°)**
a	5.251	α	90
b	5.9752	β	99.816
c	7.079	γ	90
Atom	**x**	**y**	**z**
H1	0.73006	0.03565	0.42079
H2	0.67121	0.84264	0.25635
H3	1.03125	0.23601	0.51246
H4	0.68055	0.06793	0.70647
H5	0.52032	0.47175	0.73186
H6	0.62731	0.67251	0.60325
H7	0.77121	0.38670	0.55771
N1	0.82280	0.02919	0.81970
O1	0.31697	0.12829	0.60021
O2	0.14981	0.72575	0.54811

$I4_1cd$ at 10 GPa			
Lattice Parameters	**(Å)**		**(°)**
a	6.508	α	90
b	6.508	β	90
c	19.992	γ	90
Atom	**x**	**y**	**z**
H1	0.33828	0.59712	0.04355
H2	0.57789	0.74536	0.97454
H3	0.83516	0.91252	0.93753
H4	0.66974	0.09735	0.94194
H5	0.40933	0.65454	0.79536
H6	0.58726	0.66616	0.85955
H7	0.40748	0.85141	0.85133
N1	0.50046	0.75136	0.82537
O1	0.43506	0.74945	0.98807
O2	0.75529	0.01295	0.90876

***Ama2* at 40 GPa**			
Lattice Parameters	**(Å)**		**(°)**
a	5.035	$\boldsymbol{\alpha}$	90
b	5.035	$\boldsymbol{\beta}$	90
c	4.0285	$\boldsymbol{\gamma}$	50.843
Atom	**x**	**y**	**z**
H1	0.82441	-0.77019	0.54379
H2	0.06280	0.58518	1.03709
H9	0.51109	0.42916	0.25000
H11	0.25248	0.13822	0.75000
H12	0.63846	-0.25811	0.75000
N1	0.00175	0.51489	0.25000
O1	0.33493	-0.15414	0.25000
O3	0.18118	0.69093	0.75000

$\boldsymbol{P2_1/m}$ **at 80 GPa**			
Lattice Parameters	**(Å)**		**(°)**
a	3.8791	$\boldsymbol{\alpha}$	66.858
b	4.0058	$\boldsymbol{\beta}$	90
c	4.7144	$\boldsymbol{\gamma}$	90
Atom	**x**	**y**	**z**
H1	0.85933	0.95468	0.45962
H2	0.07176	0.49476	0.73641
H3	0.30097	0.73797	0.86179
H6	0.57177	0.85855	0.15221
H9	0.57179	0.29943	0.12478
N1	0.07177	0.99449	0.32304
O1	0.57174	0.80529	0.68989
O2	0.57175	0.47950	0.33879

AQH - Crystallographic information

Here lists the crystallographic information for AQH phases used in this work.

$P2_1$-molecular at 5 GPa			
Lattice Parameters	**(Å)**		**(°)**
a	6.5216	α	90
b	6.9451	β	90
c	5.2011	γ	87.505
Atom	**x**	**y**	**z**
H1	0.45362	0.05247	0.49839
H2	0.04126	0.53310	0.49905
H3	0.10672	0.24443	0.15625
H4	0.92440	0.76583	0.15846
H5	0.24964	0.90643	0.15861
H6	0.79223	0.07417	0.15699
H7	0.24737	0.90771	0.84311
H8	0.79468	0.07549	0.84305
H9	0.92226	0.76933	0.84328
H10	0.11082	0.24494	0.84114
H11	0.13373	0.07067	0.50126
H12	0.74268	0.86057	0.50010
H13	0.07389	0.84626	0.50058
H14	0.82290	0.24610	0.49999
N1	0.90503	0.68295	-0.00058
N2	0.14373	0.32411	-0.00029
N3	0.70411	0.10776	-0.00085
N4	0.33644	0.87518	-0.00031
O1	0.00884	-0.01466	0.50176

$P2_1$-ionic at 20 GPa			
Lattice Parameters	**(Å)**		**(°)**
a	6.6416	$\boldsymbol{\alpha}$	90
b	4.5334	$\boldsymbol{\beta}$	86.134
c	5.7555	$\boldsymbol{\gamma}$	90
Atom	**x**	**y**	**z**
H1	0.98772	0.93038	0.82728
H2	0.54063	0.92895	0.67598
H3	0.68781	0.93452	0.95400
H4	0.81416	0.93119	0.54442
H9	0.01143	0.06818	0.17095
H10	0.45937	0.07085	0.32409
H11	0.31217	0.06542	0.04602
H12	0.18568	0.06879	0.45525
H17	0.79521	0.25005	0.22372
H18	0.25778	0.24986	0.78809
H19	0.82899	0.25015	0.89140
H20	0.60174	0.24997	0.50038
H21	0.49730	0.24992	0.89116
H22	0.99498	0.25001	0.58747
N1	0.45004	0.74991	0.66274
N2	0.06591	0.75008	0.87212
N3	0.85123	0.74988	0.44375
N4	0.65650	0.74995	0.05492
O1	0.73416	0.24978	0.75726

$P2_1/m$ at 40 GPa			
Lattice Parameters	**(Å)**		**(°)**
a	5.9219	α	90
b	5.9281	β	90
c	4.0941	γ	89.925
Atom	**x**	**y**	**z**
H1	0.49645	0.03186	0.50000
H2	0.02782	0.50525	0.50000
H3	0.05111	0.20108	0.20230
H4	0.94355	0.79240	0.19872
H5	0.20329	0.94523	0.20279
H6	0.79183	0.05212	0.19853
H11	0.24172	0.15557	0.50000
H12	0.75659	0.84389	0.50000
H13	0.15367	0.75934	0.50000
H14	0.84074	0.24224	0.50000
N1	0.91184	0.69331	0.00000
N2	0.08876	0.29847	0.00000
N3	0.69454	0.08891	0.00000
N4	0.30157	0.90994	0.00000
O1	0.01378	0.00216	0.50000

$I4/m$ at 60 GPa			
Lattice Parameters	**(Å)**		**(°)**
a	5.7662	α	90
b	5.7662	β	90
c	3.947	γ	90
Atom	**x**	**y**	**z**
H1	0.00000	0.50000	0.00000
H2	0.54890	0.70296	0.20645
H3	0.24038	0.16105	0.00000
N1	0.41339	0.19728	0.00000
O1	0.00000	0.00000	0.00000

$P2_1$ at 250 GPa			
Lattice Parameters	**(Å)**		**(°)**
a	4.0057	$\boldsymbol{\alpha}$	107.945
b	4.0139	$\boldsymbol{\beta}$	72.072
c	6.1407	$\boldsymbol{\gamma}$	100.089
Atom	**x**	**y**	**z**
H1	0.03402	0.00784	0.26136
H2	-0.40121	1.48071	-0.23097
H3	0.70330	1.24245	-0.05726
H4	0.20478	0.72680	0.48662
H5	0.95865	0.69207	0.33562
H6	-0.66657	1.00766	-0.63087
H7	-1.37768	1.84402	0.13734
H8	0.13124	1.40694	1.10311
H9	-0.25176	0.26094	0.26777
H10	0.13514	0.30804	0.41303
H11	0.61379	0.83367	-0.11745
H12	0.65727	0.86448	0.38848
H13	-0.22358	0.55226	0.11826
H27	0.50000	0.50000	0.50000
H28	0.00000	0.00000	0.00000
N1	-0.19293	2.01531	0.89980
N2	0.30925	0.50522	0.39724
N3	-1.40816	1.99365	0.30003
N4	-0.09487	1.48717	1.20744
O1	0.00000	0.00000	0.50000
O2	0.50000	0.50000	0.00000

***P*1 at 300 GPa**			
Lattice Parameters	**(Å)**		**(°)**
a	3.9289	$\boldsymbol{\alpha}$	108.21
b	3.9399	$\boldsymbol{\beta}$	71.88
c	6.0194	$\boldsymbol{\gamma}$	100.09
Atom	**x**	**y**	**z**
H1	0.01091	0.01247	0.25242
H2	0.60326	0.47962	0.76730
H3	0.68907	0.24318	0.93905
H4	0.21713	0.73194	0.49419
H5	0.97109	0.70041	0.33008
H6	0.33364	0.01519	0.37786
H7	0.61182	0.82953	0.14097
H8	0.12948	0.39126	0.09746
H9	0.74957	0.26635	0.26811
H10	0.12850	0.30651	0.41171
H11	0.61806	0.82520	0.88495
H12	0.65067	0.85643	0.39612
H13	0.77322	0.54748	0.11379
H14	0.97626	0.98999	0.73695
H15	0.39269	0.52201	0.22567
H16	0.28792	0.75270	0.05915
H17	0.79516	0.27368	0.50650
H18	0.03439	0.30765	0.66336
H19	0.67499	1.00988	0.63989
H20	0.34148	0.10368	0.87582
H21	0.87215	0.60310	0.90060
H22	0.25554	0.72912	0.72416
H23	0.86835	0.70042	0.57877
H24	0.39951	0.15900	0.14163
H25	0.35343	0.16679	0.62331
H26	0.23123	0.44354	0.87866
H27	0.50181	0.49702	0.49453
H28	-0.01870	0.00823	0.00128
N1	0.80775	0.01780	0.89990
N2	0.30744	0.50283	0.39323
N3	0.59671	0.99016	0.30283
N4	0.90621	0.48851	0.20470
N5	0.20252	0.99075	0.09995
N6	0.69416	0.50029	0.59966
N7	0.41136	0.00980	0.69837
N8	0.09701	0.51517	0.79218
O1	0.00578	0.00237	0.49914
O2	0.50153	0.49876	-0.00478

The Second Appendix - Phonon Dispersions

AHH - Phonon dispersions -v2

Below, we show the phonon dispersion relations for all phases discussed in the main manuscript at pressure points relevant to their respective stability range. For the monoclinic phases points have the following coordinates:
Z = (0,0,1/2) Γ = (0,0,0) Y = (0,1/2,0) A = (-1/2,1/2,0) B = (-1/2,0,0) D = (-1/2,0,1/2) E = (-1/2,1/2,1/2) C = (0,1/2,1/2)

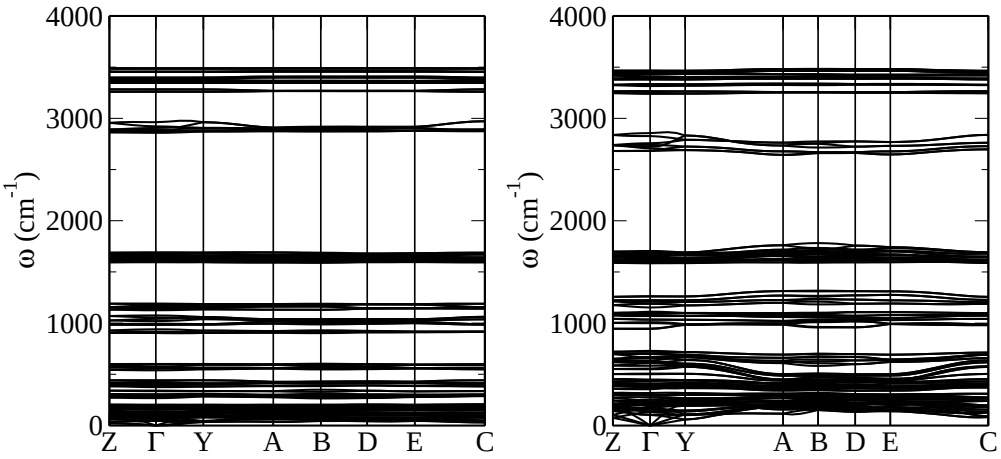

Figure 1 *Left: AHH-I at 1 GPa; right: AHH-II at 10 GPa.*

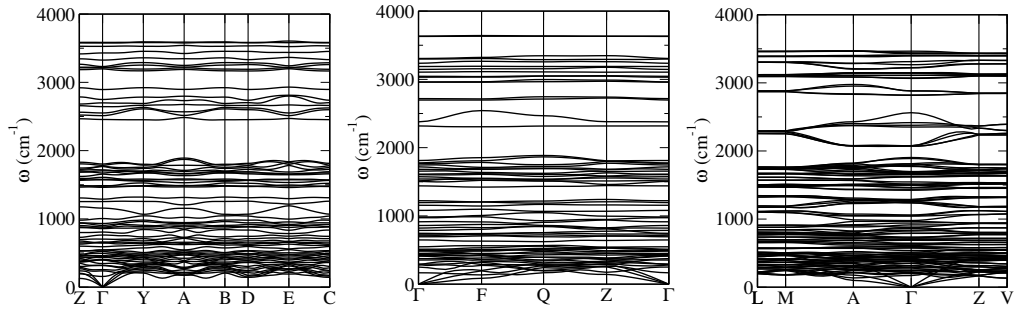

Figure 2 *From left: Cm, $P\bar{1}$, and $A2/m$ phases, all at 30 GPa.*

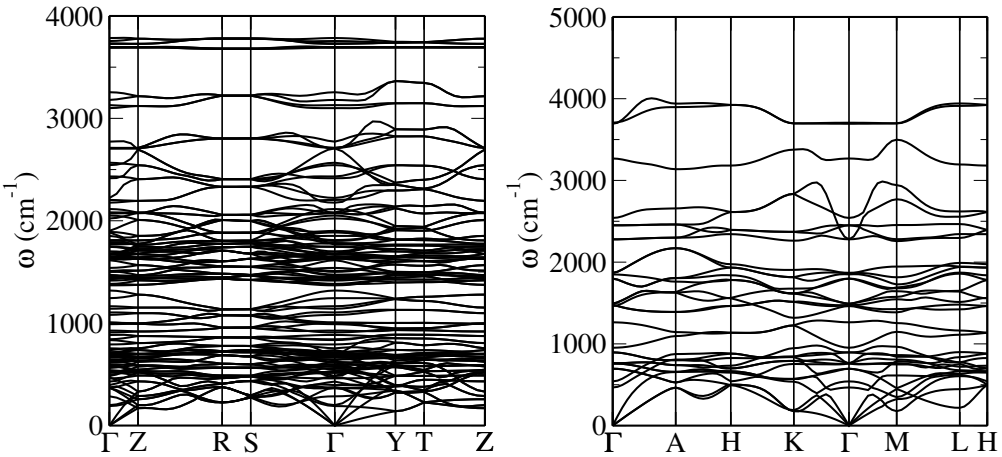

Figure 3 *Left: Amma at 100 GPa; right: $P\bar{3}m1$ at 150 GPa.*

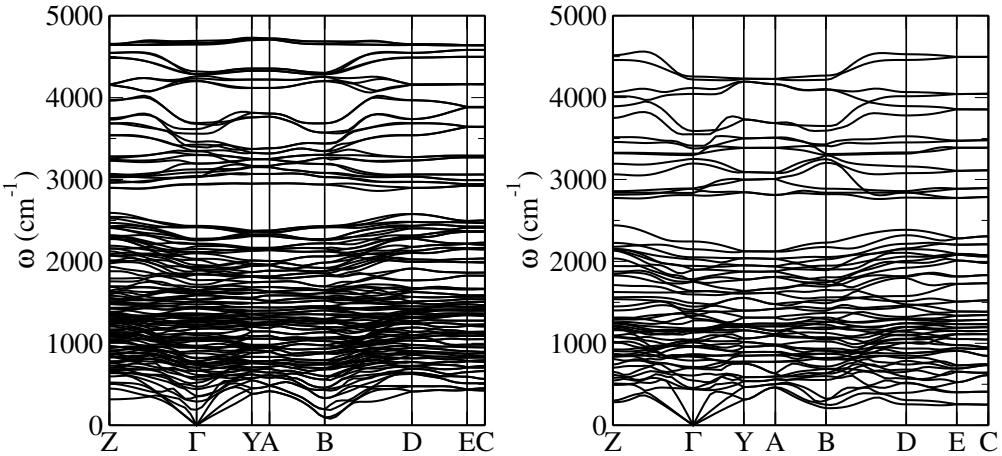

Figure 4 *Left: $P2_1/m$ at 400 GPa; right: $P2_1/c$ at 650 GPa.*

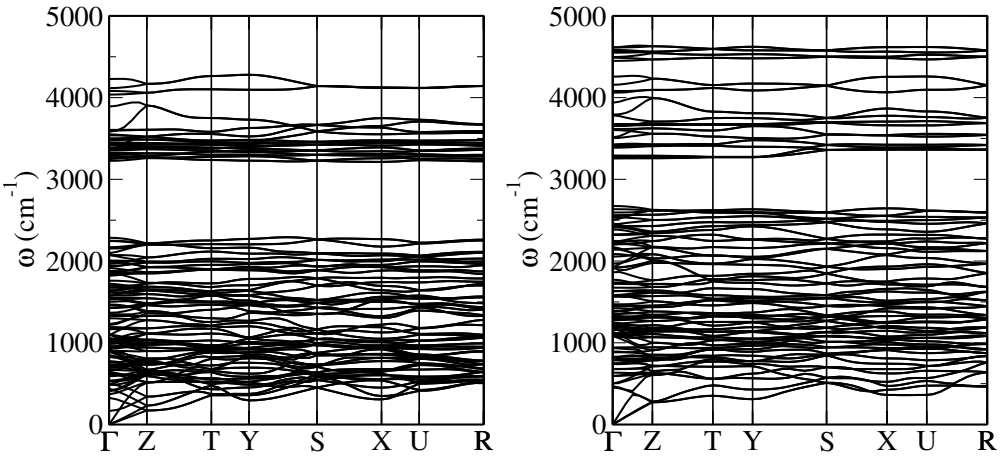

Figure 5 *Left: Pnna at 300 GPa; right: Pnma at 700 GPa.*

AMH - Phonon dispersions

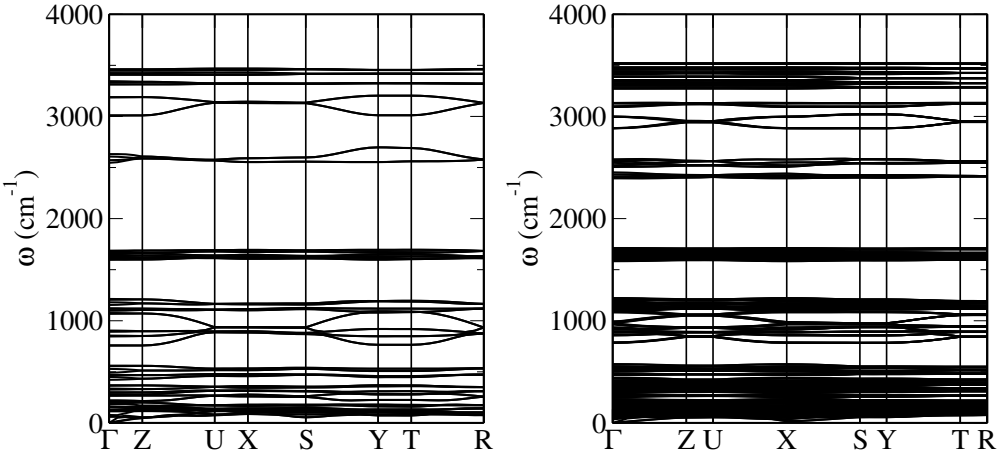

Figure 6 *Left: AMH-I at 1 GPa; right: AMH-II at 3 GPa.*

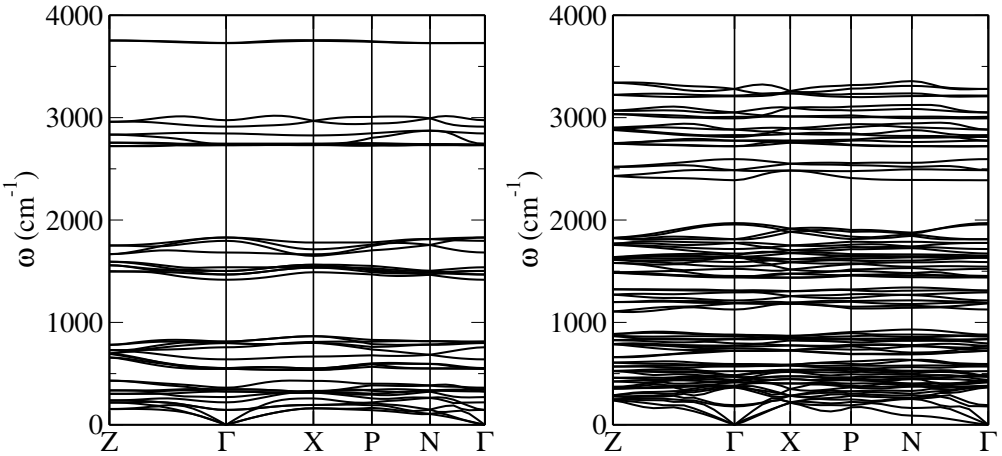

Figure 7 *Left: P4/nmm at 10 GPa; right: $P4_3$ at 50 GPa.*

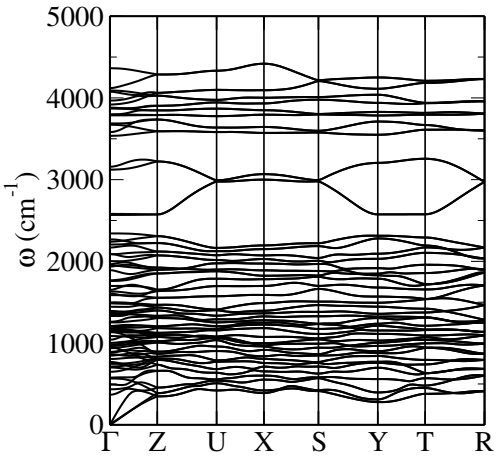

Figure 8 *AMH-I at 500 GPa.*

ADH - Phonon dispersions

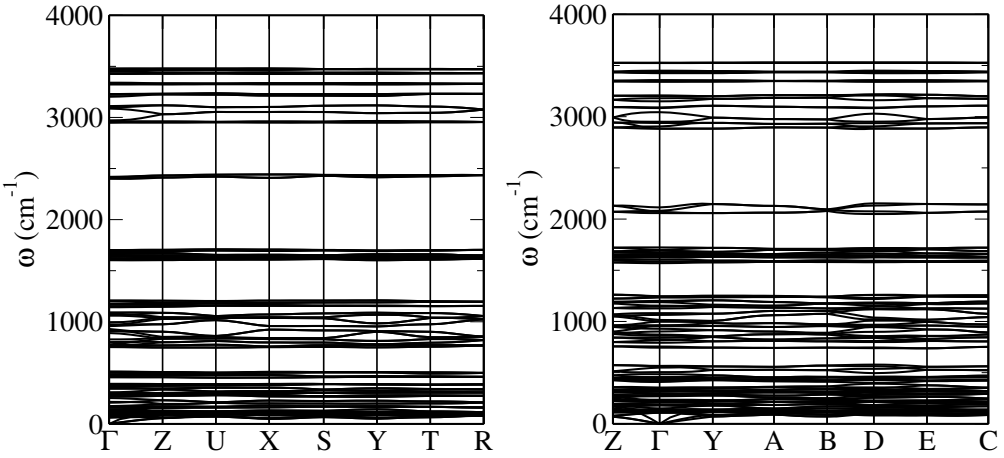

Figure 9 *Left: ADH-I at 1 GPa; right: ADH-II at 5 GPa.*

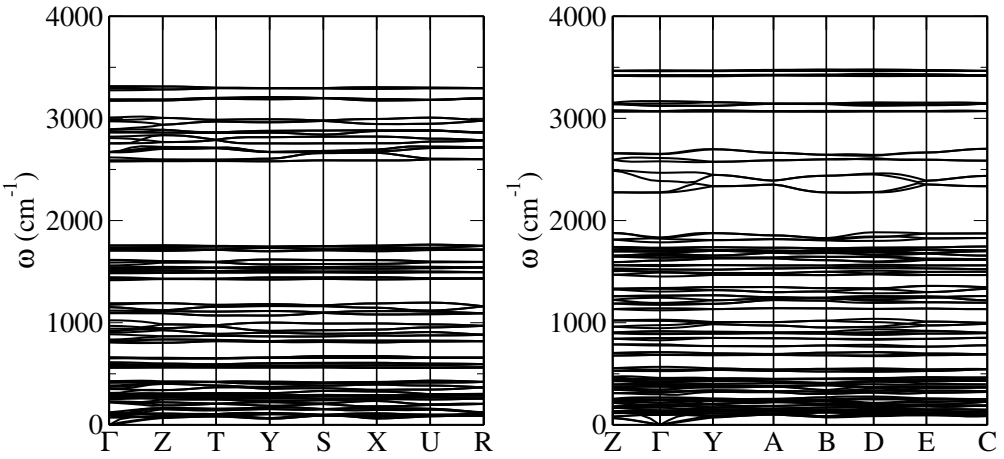

Figure 10 *Left: ADH-I* at 4 GPa; right: ADH-II** at 5 GPa.*

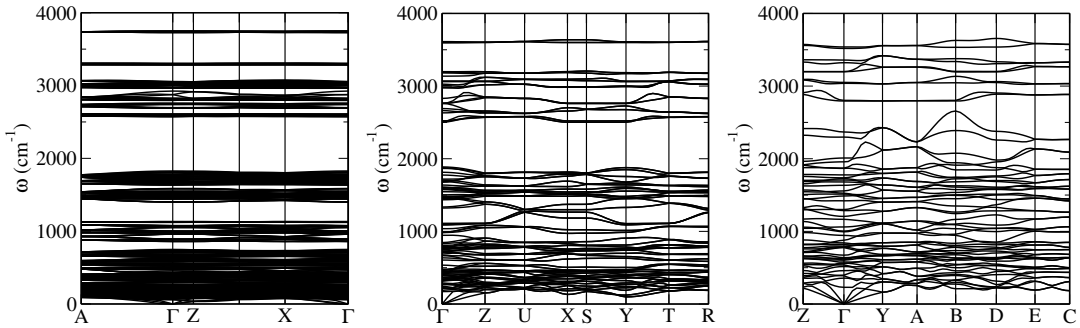

Figure 11 *From Left: $I4_1cd$ at 8 GPa, $Ama2$ at 30 GPa, and $P2_1/m$ at 80 GPa.*

AQH - Phonon dispersions

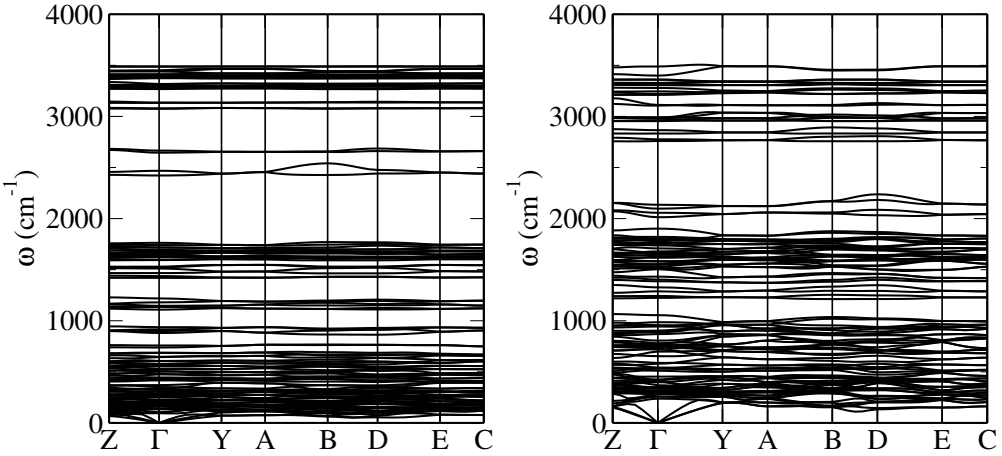

Figure 12 *Left: $P2_1$ at 5 GPa; right: $P2_1/m$ at 30 GPa.*

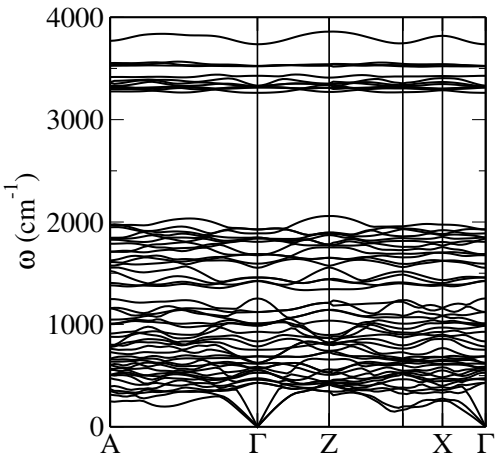

Figure 13 *$I4/m$ at 100 GPa.*

The Third Appendix - Molecular Dynamics

Here lists the details and analysis data of AIMD simulations.

Simulation Details

Details for ADH simulations:

Table 13 *ADH simulation time (ps) summary and details for low T.*

	P (Gpa)					
T (K)	**4**	**10**	**30**	**50**	**60**	**80**
100	0.85	0.62	1.38	1.06	1.09	1.31
200	0.91	0.66	1.16	1.31	1.07	1.38
300	0.77	0.59	1.50	1.13	1.35	1.45
400	1.16	0.76	1.30	1.39	1.41	1.47
500	1.39	0.57	1.55	1.18	1.42	1.22
600	0.99	0.81	1.54	0.78	1.16	1.25
700	0.94	0.58	1.19	0.92	1.37	1.41
800	0.78	0.69	1.24	1.07	1.10	1.56
900	0.88	0.69	0.78	1.03	1.28	1.32
1000	0.88	0.66	0.97	1.04	1.02	1.29
Molecules	432	384	324	384	384	384
Atoms	1440	1280	1080	1280	1280	1280
Phase	$P2_12_12_1$	$I4_1cd$	$Ama2$		$P2_1/m$	
ρ (g/cm^3)	1.31	1.66	2.10	2.33	2.44	2.62

Table 14 *ADH simulation time (ps) summary and details for high T.*

	P (GPa)					
T (K)	**4**	**10**	**30**	**50**	**60**	**80**
1500		3.42	3.86	6.59	4.75	3.22
2000		3.33	3.27	4.15	3.81	3.74
2500		3.94	3.96	4.95	5.76	5.80
3000		3.75	3.14	5.30	5.78	5.88
3500			3.02	4.77	5.90	3.25
4000			2.66	3.52	4.75	4.59
4500			2.50	4.81	4.00	1.65
5000			2.02	3.71	4.69	1.63
Molecules		96	108	72	72	72
Atoms		320	360	240	240	240

Table 15 *ADH finite temperature pressure (GPa)*

	P (GPa)					
T (K)	**4**	**10**	**30**	**50**	**60**	**80**
100	4.97	10.46	30.53	50.65	60.73	80.70
200	4.71	11.02	31.31	51.31	61.45	81.54
300	4.36	11.49	32.16	52.15	62.26	82.31
400	4.14	12.03	32.96	52.87	63.04	83.11
500	5.56	12.53	33.68	53.64	63.73	83.88
600	6.02	13.07	34.46	54.44	64.50	84.60
700	6.62	13.57	35.08	55.02	65.14	85.16
800	6.92	14.58	35.75	55.56	65.81	85.84
900	7.30	15.37	36.71	57.26	66.66	86.66
1000	7.67	16.51	37.46	56.60	67.43	87.42

T (K)	**4**	**10**	**30**	**50**	**60**	**80**
1500		21.88	43.17	63.10	72.80	92.30
2000		24.10	49.66	68.36	78.00	97.83
2500		26.14	52.52	72.41	82.44	101.92
3000		27.68	56.28	79.01	87.66	105.57
3500		58.78	82.44	93.11	113.24	
4000		61.66	85.57	96.63	117.68	
4500		64.19	88.72	100.08	120.81	
5000		66.96	92.07	102.80	124.57	

Details for AMH simulations:

Table 16 *AMH simulation times (ps)*

	P (GPa)								
T (K)	**10**	**30**	**60**	**80**	**100**	**200**	**300**	**400**	**500**
500	8.71	9.02	7.34	10.15	0.62	0.75	0.69	0.50	0.88
1000	6.36	10.21	8.29	10.16	0.56	0.74	0.65	0.58	0.87
1500	5.72	8.77	7.43	9.73	0.58	0.80	1.19	0.56	0.87
2000	5.83	6.60	7.50	8.28	0.44	0.71	0.68	0.54	0.85
2500	6.01	8.70	5.81	6.98	0.48	0.50	0.62	0.53	0.80
3000	5.36	2.36	7.64	8.33	0.39	0.57	1.10	0.50	0.77
3500			3.34	3.14	0.19	0.67	1.08	0.45	0.72
4000			3.30	2.84	0.12	0.46	1.03	0.46	0.65
4500			3.10	3.05	0.03	0.43	0.49	0.43	0.67
5000			2.33	3.86		0.03	0.31	0.23	0.36
Molecules	144	144	144	144	288	288	288	288	288
Atoms	504	504	504	504	1008	1008	1008	1008	1008
Phase	$P\bar{4}/nmm$		$P4_3$		$P2_1/m$				
rho (g/cm3)	1.61	1.97	2.35	2.51	2.71	3.26	3.68	4.03	4.33

Table 17 *AMH Finite temperature pressure (GPa)*

	P (GPa)								
T (K)	**10**	**30**	**60**	**80**	**100**	**200**	**300**	**400**	**500**
500	12.74	33.11	63.55	83.40	106.62	205.65	305.43	405.13	504.78
1000	18.17	35.30	67.50	87.09	111.44	210.83	310.72	410.32	510.25
1500	22.19	40.05	72.54	92.20	117.62	216.10	316.08	415.61	514.31
2000	24.61	46.39	77.21	96.79	124.93	222.92	321.55	419.52	517.28
2500	26.73	49.18	81.92	101.07	129.94	228.54	326.71	424.19	522.39
3000	28.57	52.04	85.62	105.41	134.26	233.69	331.67	429.88	527.92
3500			93.99	112.82	140.26	238.29	336.98	435.47	534.30
4000			96.99	118.10	144.85	243.89	342.51	441.94	540.54
4500			100.17	121.66	145.68	249.00	348.64	448.17	547.52
5000			103.26	124.56		255.57	356.35	454.43	554.36

Details for AHH simulations: Note for simulations marked with a * the number of molecules is one half of that described, seen for 60 GPa.

Table 18 *AHH simulation times (ps)*

	P (GPa)		
T (K)	**3**	**T (K)**	**10**
200	4.12	500	15.28
400	5.09	750	17.26
600	6.42	1000	19.08
800	7.29	1500	21.66
1000	7.80	2000	23.38
1500	9.40		
2000	10.75		
2500	11.57		
3000	12.25		
Molecules	96		96
Atoms	352		352
Phase	*I*		*II*
ρ **(g/cm^3)**	1.13		1.49

	P (GPa)									
T (K)	**20**	**40**	**60**	**100**	**200**	**250**	**300**	**350**	**400**	**500**
500	1.10	1.51	5.04	5.45	13.21	2.32	10.82	2.01	2.73	5.04
1000	0.90	1.89	4.53	4.78	11.50	2.07	10.83	2.00	2.04	7.56
1500	0.87	1.24	5.01	4.56	11.22	2.20	10.65	1.75	1.91	7.38
2000	0.46	1.79	3.94	4.23	10.78	1.98	10.09	1.86	2.64	5.67
2500	0.82	1.22	3.93	4.18	10.36	1.84	10.72	1.78	2.16	4.84
3000	0.82	1.54	3.81	4.27	10.41	1.94	10.34	1.42	1.71	5.29
3500		0.16	5.13*	4.68	10.38	1.89	10.86	0.73	0.64	6.51
4000		73.80	4.67*	2.41	11.32	1.37	10.51	0.59	0.71	5.23
4500			2.66	2.35	7.74	1.30	11.52	0.53	0.55	5.27
5000				2.36	2.21		10.90	0.42	0.43	3.45
5500				0.47	1.77		9.97			3.51
6000				0.47	1.00		9.94			3.25
6500				0.47	1.28		2.89			3.09
7000				0.46	1.57		2.82			2.95
7500							1.72			2.96
8000							1.31			2.95
Molecules	96	108	216	216	135	288	135	288	288	180
Atoms	352	396	792	792	495	1056	495	1056	1056	660
Phase	*II*	*A2m*	*Amma*		$P\bar{3}m1$					
ρ **(g/cm^3)**	1.72	2.05	2.28	2.57	3.11	3.32	3.51	3.71	3.88	4.19

Table 19 *AHH finite temperature stress (GPa)*

	P (GPa)									
T (K)	**3**	**T (K)**	**10**							
200	4.12	**500**	15.28							
400	5.09	**750**	17.26							
600	6.42	**1000**	19.08							
800	7.29	**1500**	21.66							
1000	7.80	**2000**	23.38							
1500	9.40									
2000	10.75									
2500	11.57									
3000	12.25									
T (K)	**20**	**40**	**60**	**100**	**200**	**250**	**300**	**350**	**400**	**500**
500	25.25	43.65	66.01	104.83	205.80	255.31	305.68	355.45	405.50	506.15
1000	29.94	48.78	70.58	108.90	210.34	260.20	310.35	360.50	410.88	511.50
1500	33.85	54.13	76.92	114.40	215.49	265.04	315.03	365.98	416.43	517.27
2000	36.90	58.51	81.98	119.88	221.62	268.06	314.64	371.04	421.41	521.99
2500	39.02	63.80	86.11	124.35	224.04	272.51	319.26	375.92	426.04	526.83
3000	40.94	67.49	89.76	128.23	228.04	276.86	324.08	381.03	431.28	532.42
3500	70.89	97.04	130.75	231.46	281.66	328.86	386.40	436.91	538.19	
4000	73.80	101.09	150.02	237.06	287.20	334.42	392.31	442.18	544.49	
4500	152.80	241.85	291.39	340.03	397.89	449.06	550.66			
5000	155.36	251.27	345.75	404.53	455.09	557.29				
5500	257.15	355.56	564.19							
6000	262.27	361.56	572.49							
6500	267.02	368.19	580.14							
7000	271.83	374.07	587.66							
7500	594.96									
8000	601.87									

Details for AQH simulations:

Table 20 *AQH simulation times (ps) and details*

	P (GPa)							
T (K)	**20**	**40**	**60**	**80**	**100**	**150**	**200**	**300**
500	11.09	10.07	11.04	10.10	11.81	13.38	3.07	3.18
1000	9.98	10.69	10.27	10.60	10.00	11.44	2.88	3.30
1500	8.61	10.15	10.14	10.34	10.78	11.20	2.76	3.30
2000	9.04	10.22	10.45	11.39	10.43	10.31	2.72	3.02
2500	8.91	10.25	10.59	10.41	10.40	10.12	2.57	2.96
3000		10.24	10.66	10.51	11.69	10.20	2.55	2.86
3500			2.25	5.49	4.91	10.68	2.62	2.90
4000			2.12	2.34	4.09	9.89	2.35	2.58
4500						2.93	1.17	2.48
Molecules	120	120	120	120	120	120	160	160
Atoms	456	456	456	456	456	456	608	608
Phase	*P21*	*P21m*	*I4/m*				*P-1*	
ρ **(g/cm^3)**	1.65	1.99	2.18	2.33	2.46	2.75	2.99	3.41

Table 21 *AQH finite temperature stress (GPa)*

	P (GPa)							
T (K)	**20**	**40**	**60**	**80**	**100**	**150**	**200**	**300**
500	23.41	43.68	64.52	84.23	104.00	153.48	203.62	303.05
1000	27.47	49.47	67.74	87.33	106.94	156.52	206.99	307.60
1500	31.27	55.79	74.95	93.00	111.54	159.55	209.20	310.46
2000	35.21	59.31	79.14	97.73	116.29	163.77	213.27	314.88
2500	37.56	65.69	82.59	101.49	120.41	167.89	217.55	319.09
3000		67.34	85.68	104.88	123.88	172.02	221.79	323.95
3500			93.49	108.61	127.55	176.05	226.33	328.84
4000			96.89	117.25	133.71	180.55	230.77	333.91
4500						189.95	235.23	339.37

The Fourth Appendix - ADH AIMD Analysis

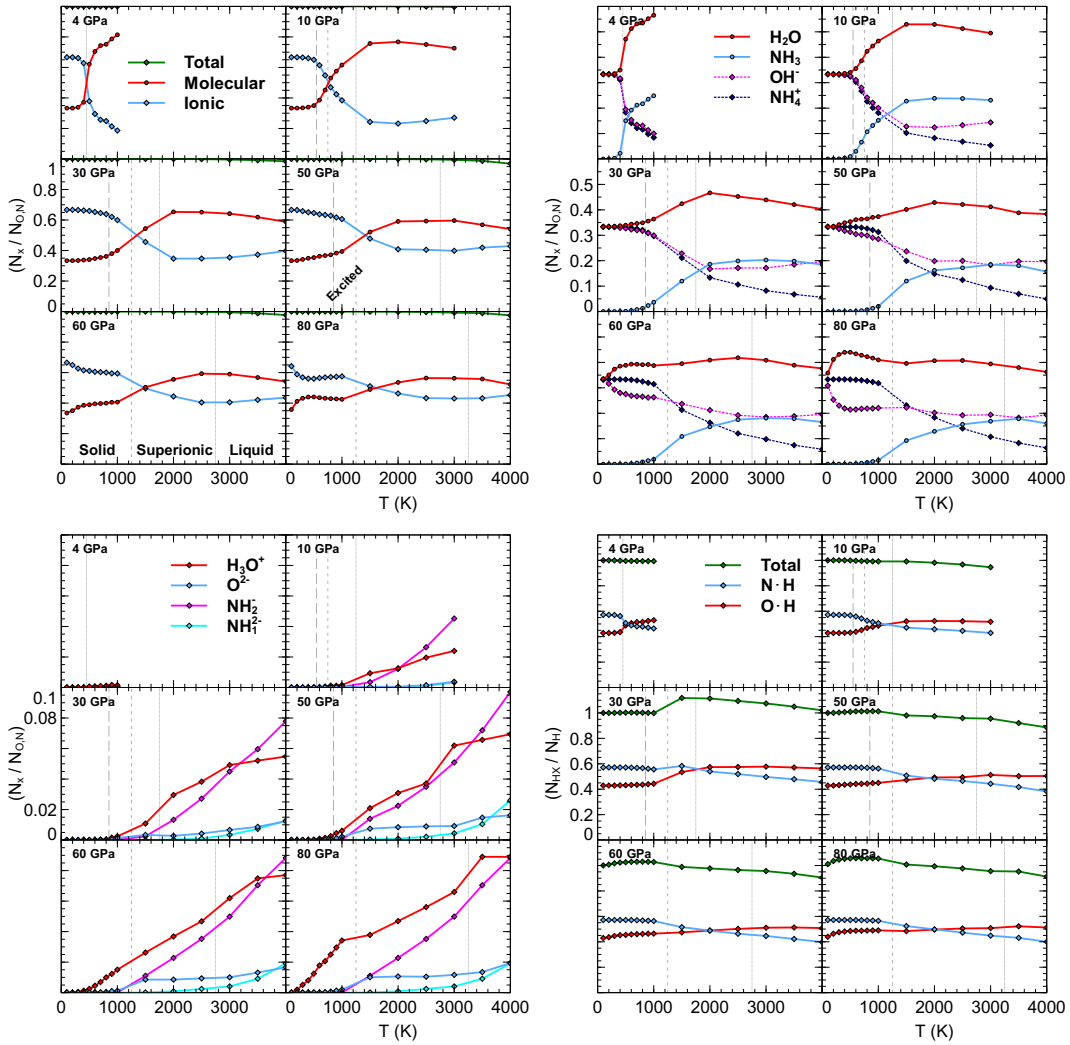

Figure 14 *ADH analysis of ionicity (top left), unit types (top right, bottom left), and covalent hydrogen bonds (bottom right).*

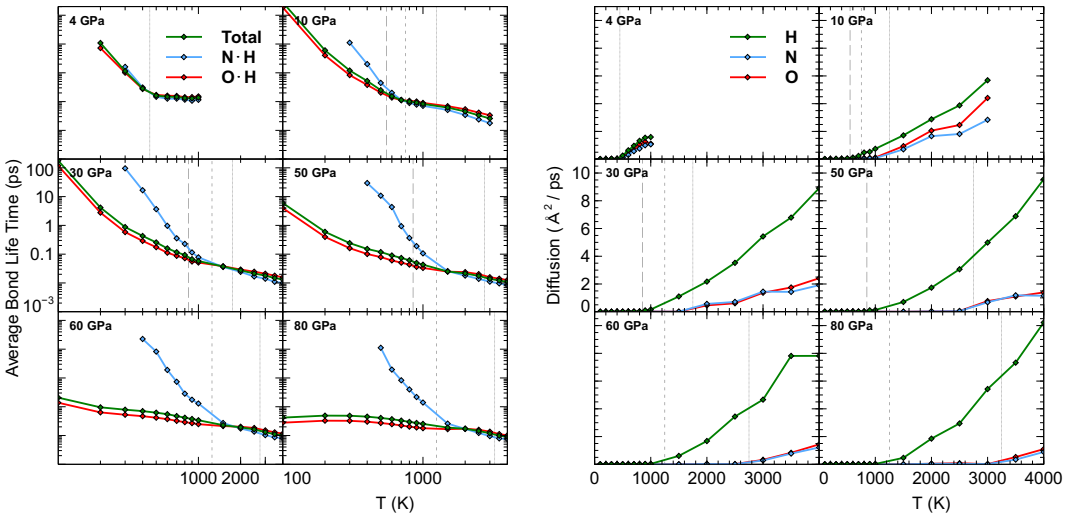

Figure 15 *ADH analysis of estimated bond life times (top left), ion diffusion (top right).*

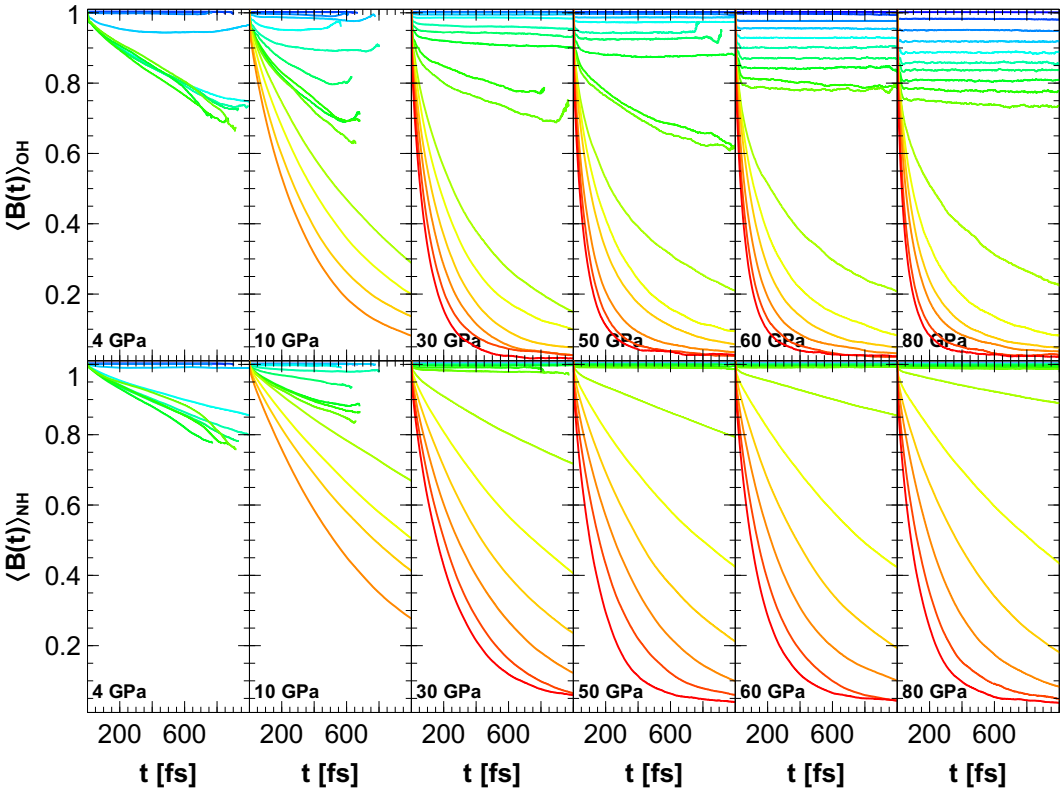

Figure 16 *ADH analysis of bond auto correlation function.*

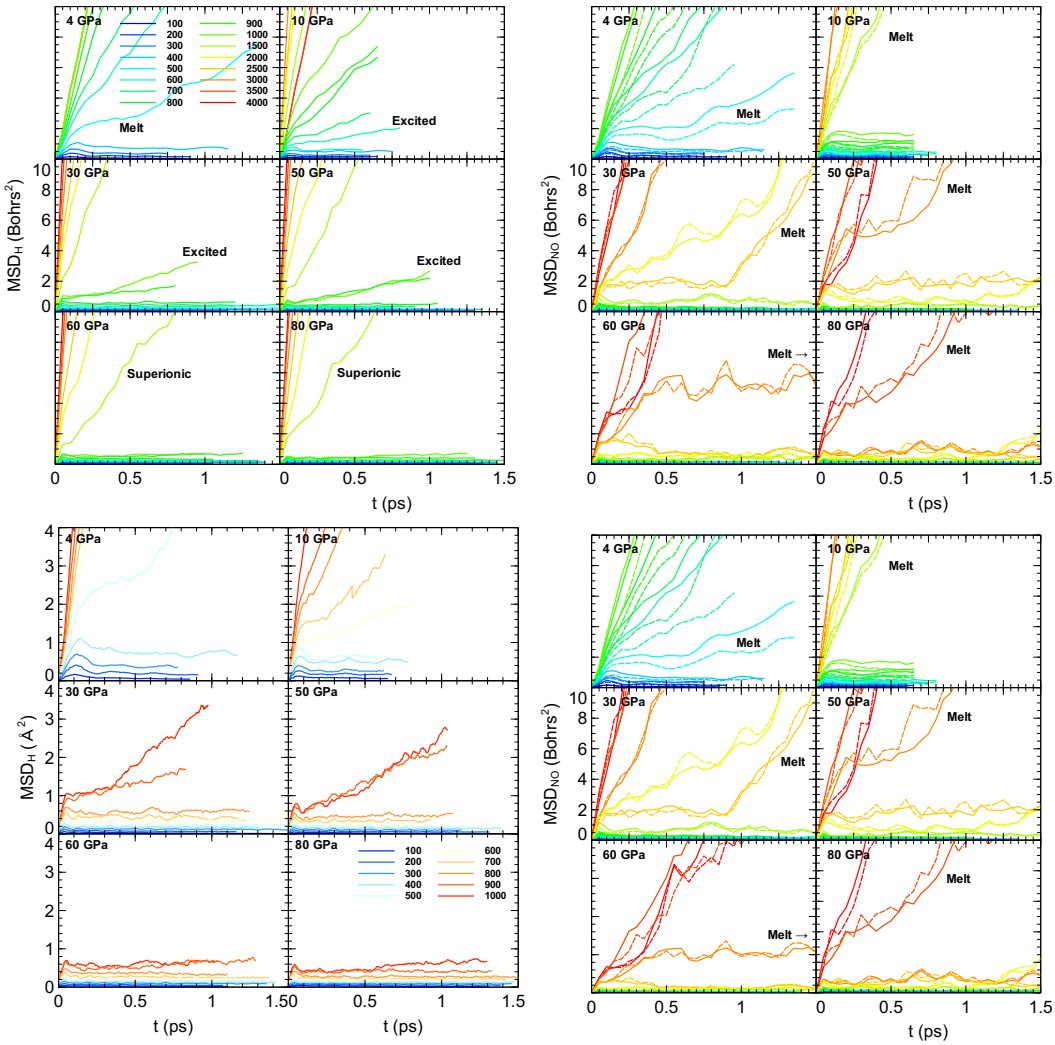

Figure 17 *ADH analysis of MSD.*

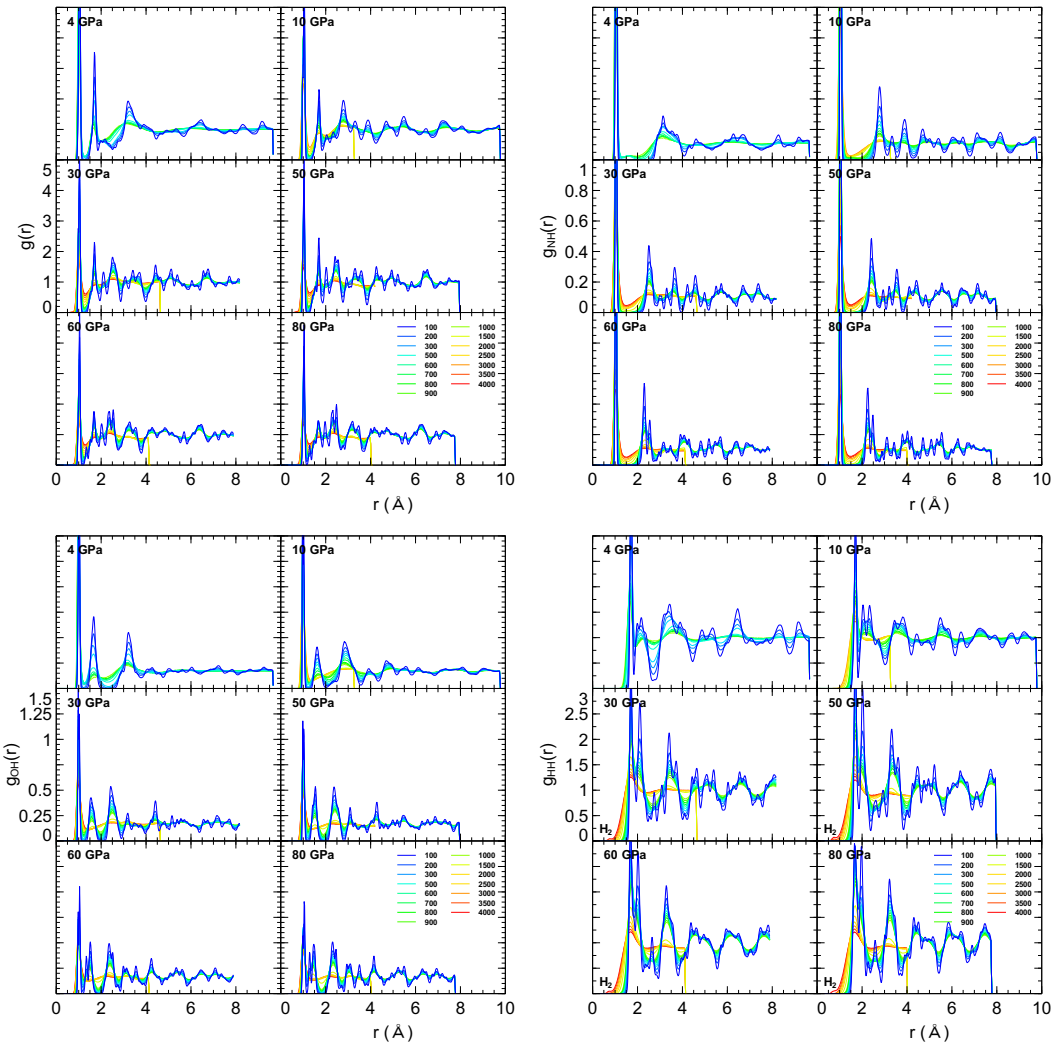

Figure 18 *ADH analysis of RDF and PDF (NH,OH,HH).*

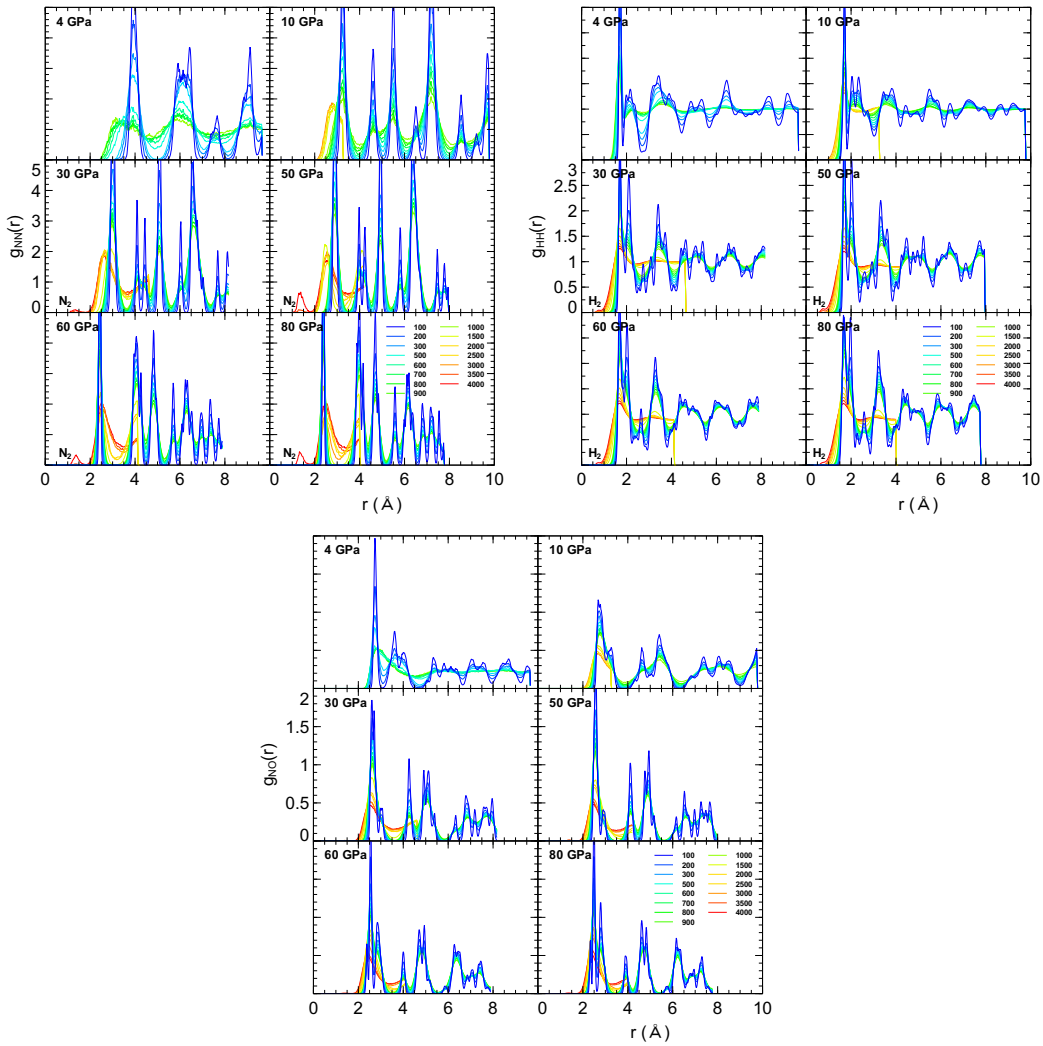

Figure 19 *ADH analysis of PDF (NN,OO,NO).*

The Fifth Appendix - AMH AIMD Analysis

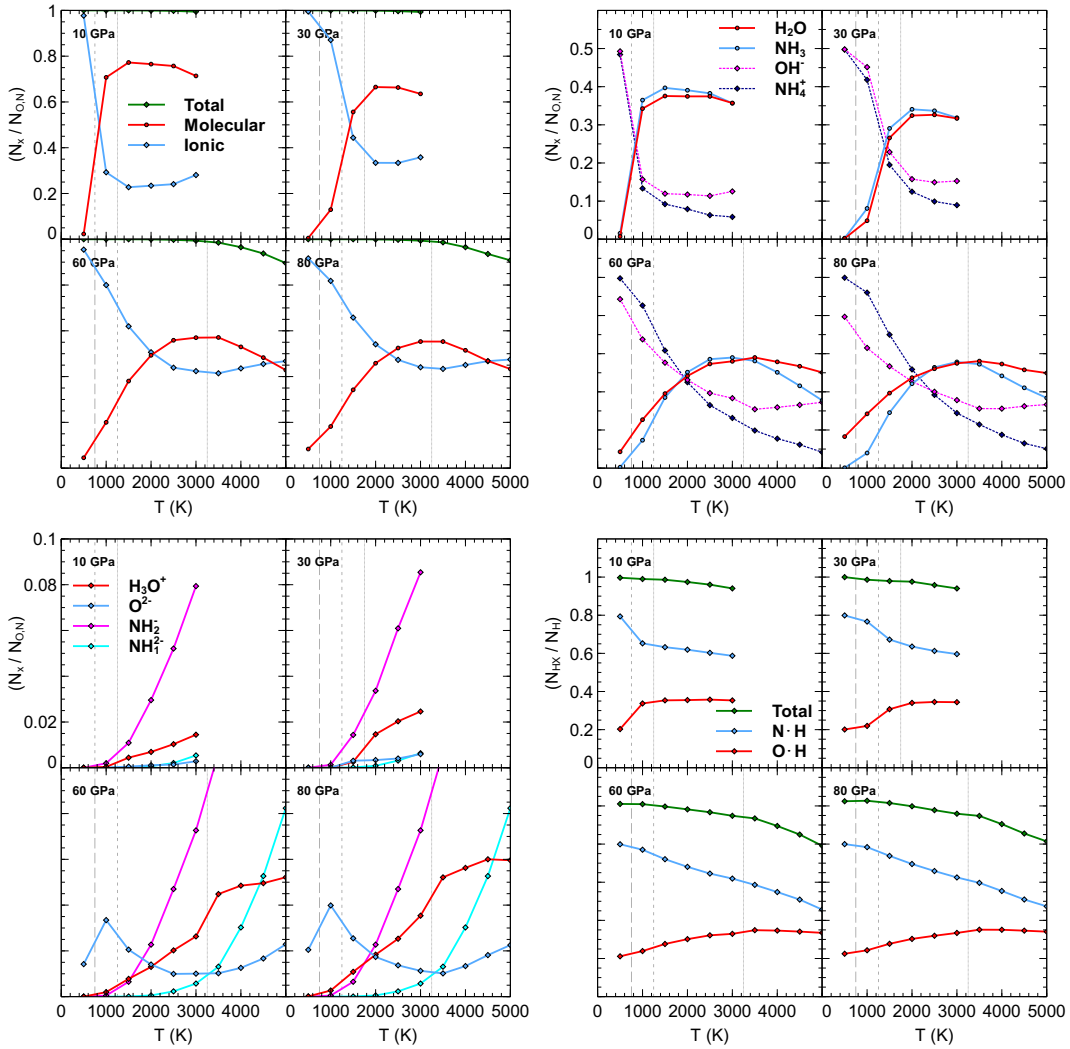

Figure 20 *AMH analysis of ionicity (top left), unit types (top right, bottom left), and covalent hydrogen bonds (bottom right).*

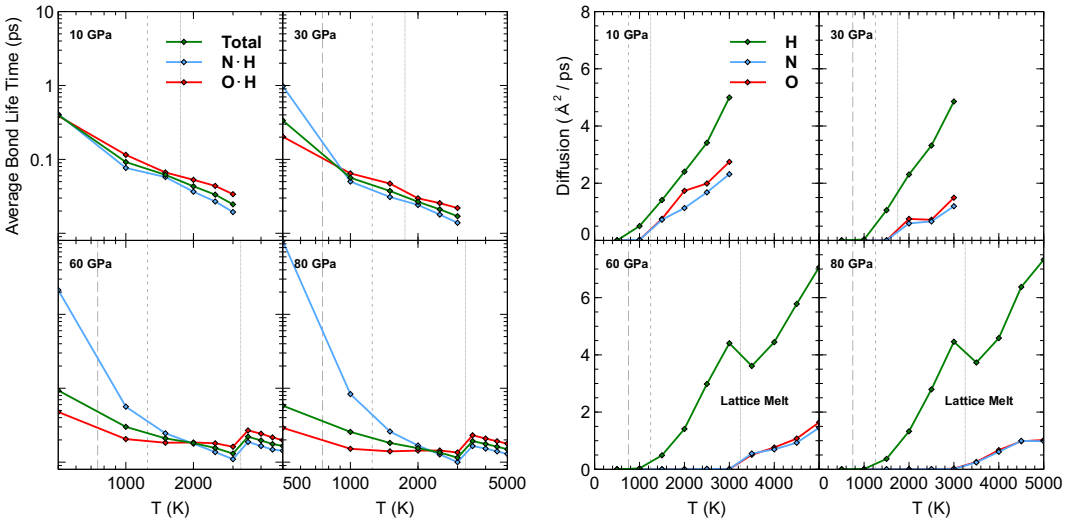

Figure 21 *AMH analysis of estimated bond life times (top left), ion diffusion (top right).*

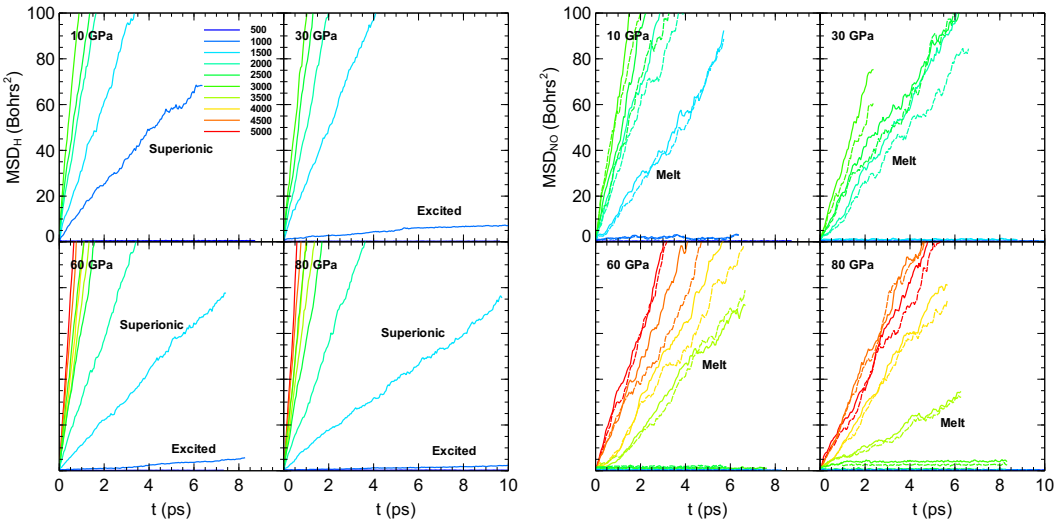

Figure 22 *AMH analysis of MSD.*

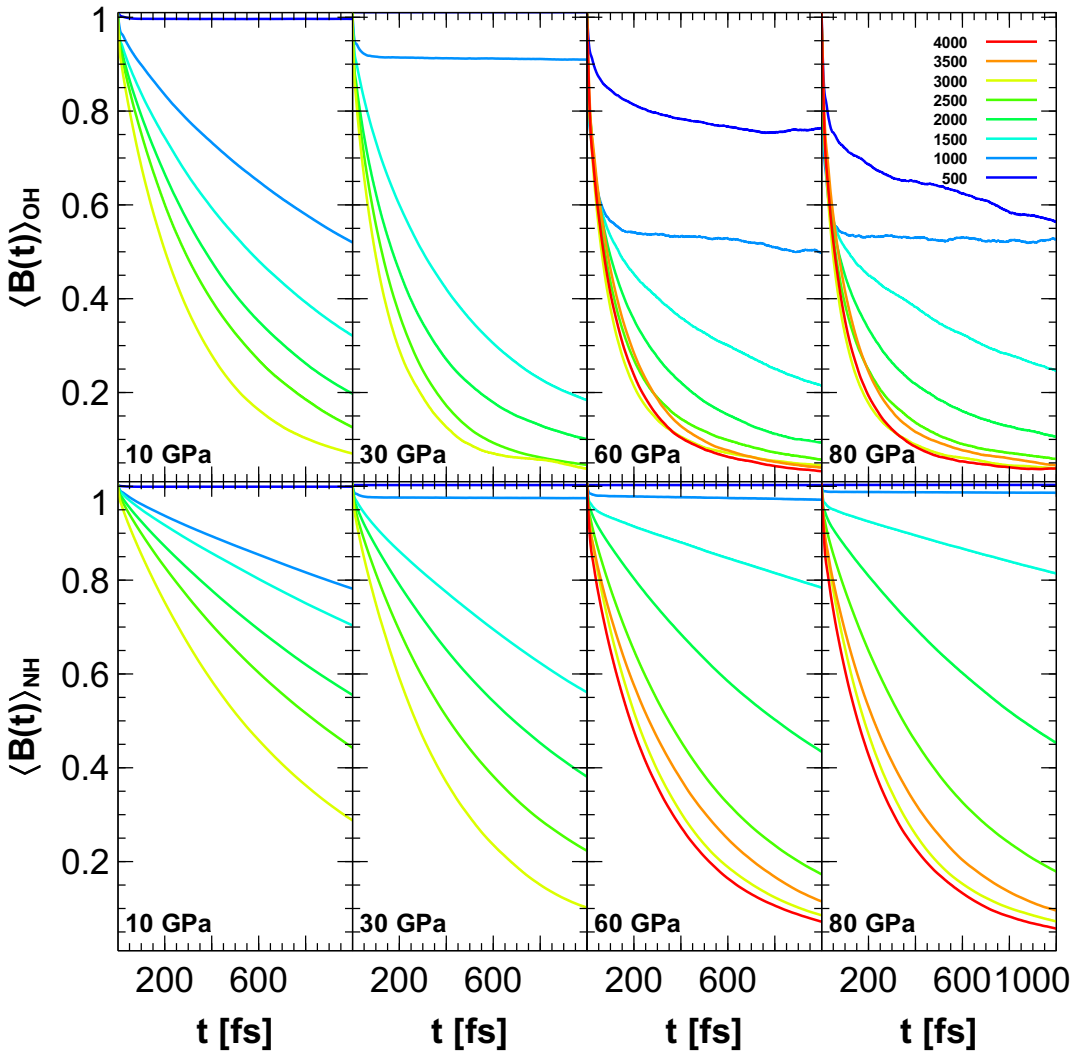

Figure 23 *AMH analysis of bond auto correlation function.*

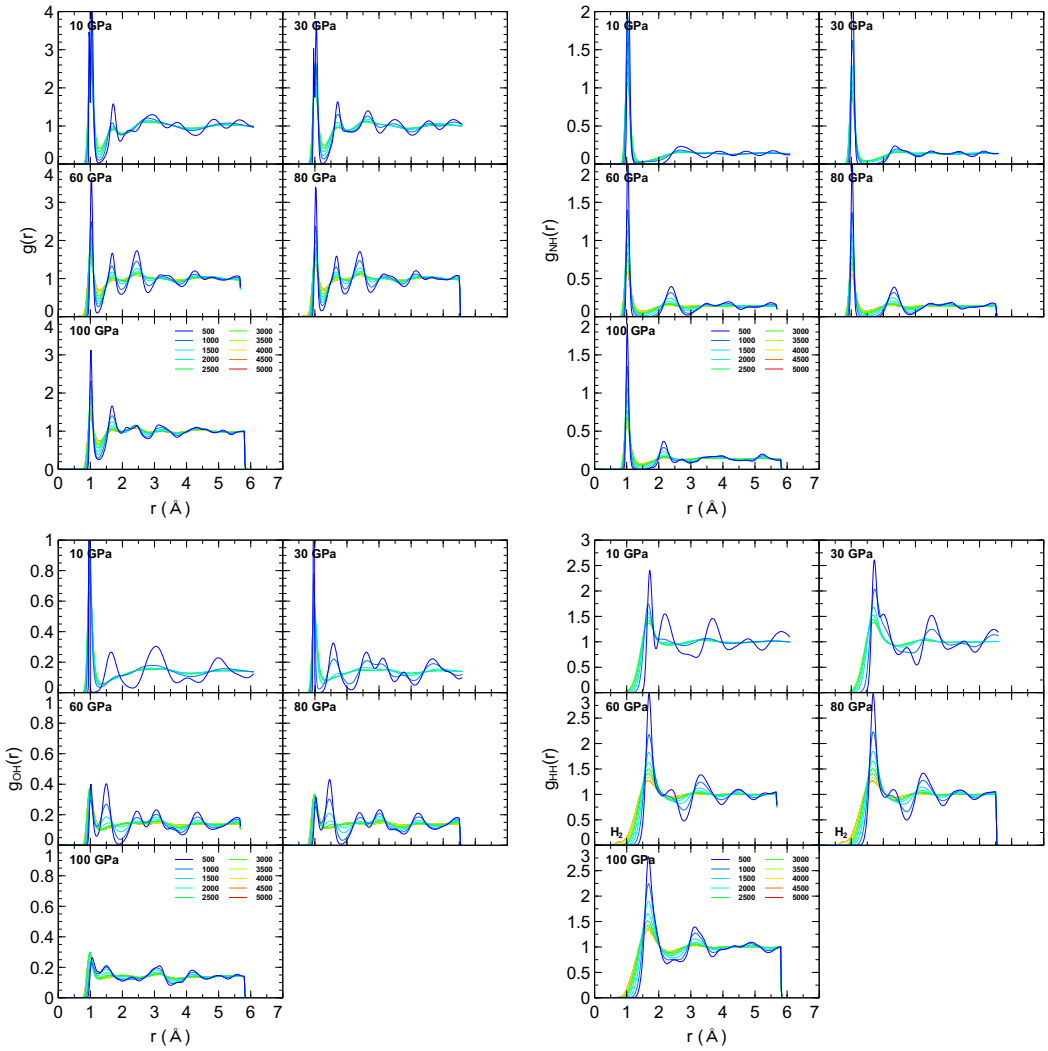

Figure 24 *AMH analysis of RDF and PDF (NH,OH,HH).*

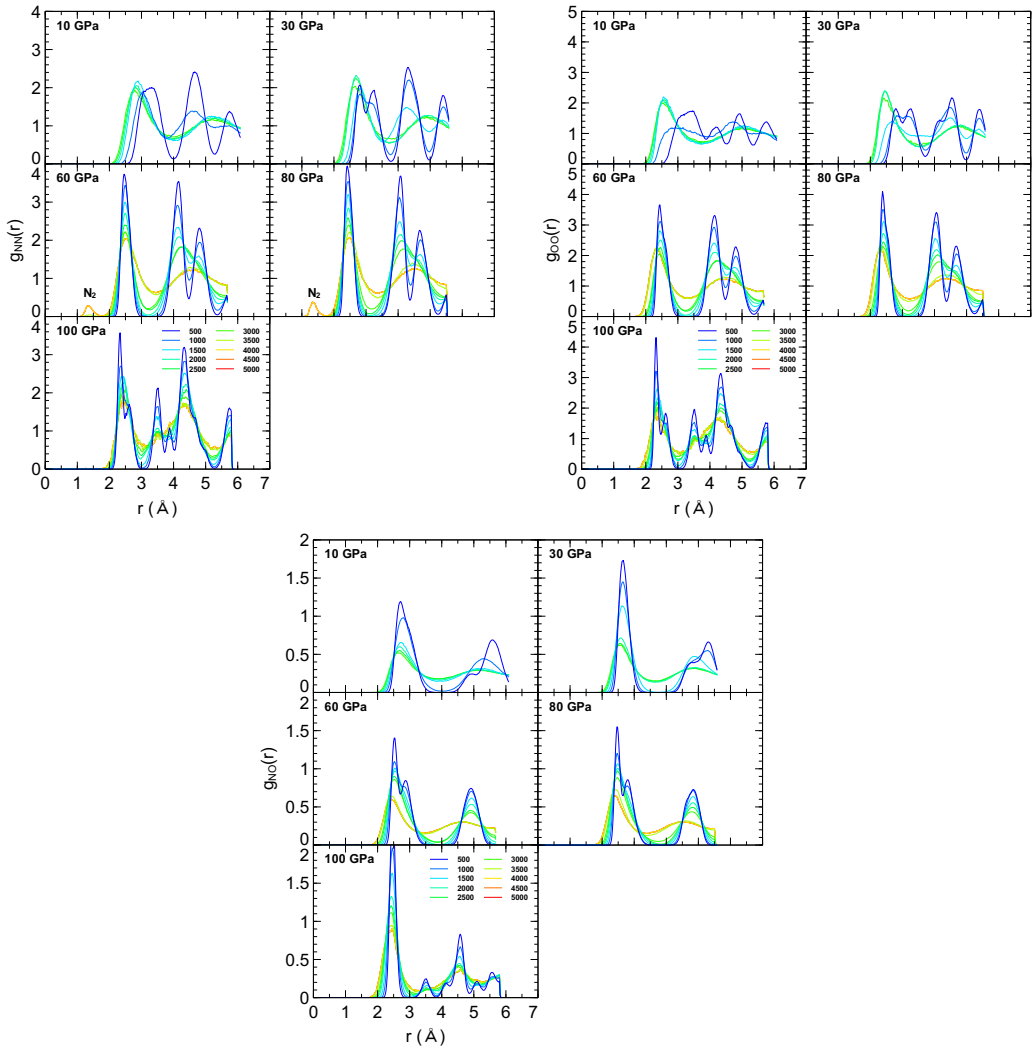

Figure 25 *AMH analysis of PDF (NN,OO,NO).*

The Sixth Appendix - AQH AIMD Analysis

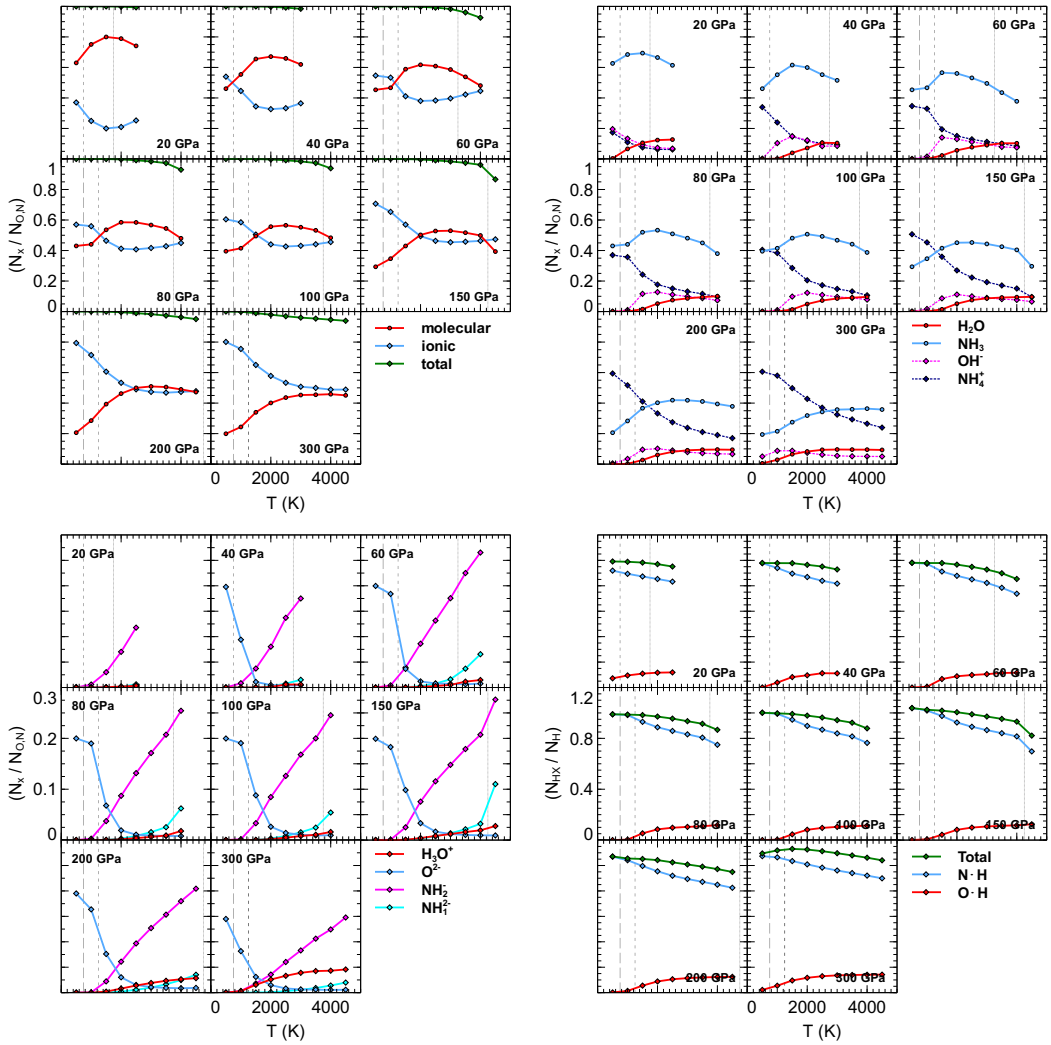

Figure 26 *AQH analysis of ionicity (top left), unit types (top right, bottom left), and covalent hydrogen bonds (bottom right).*

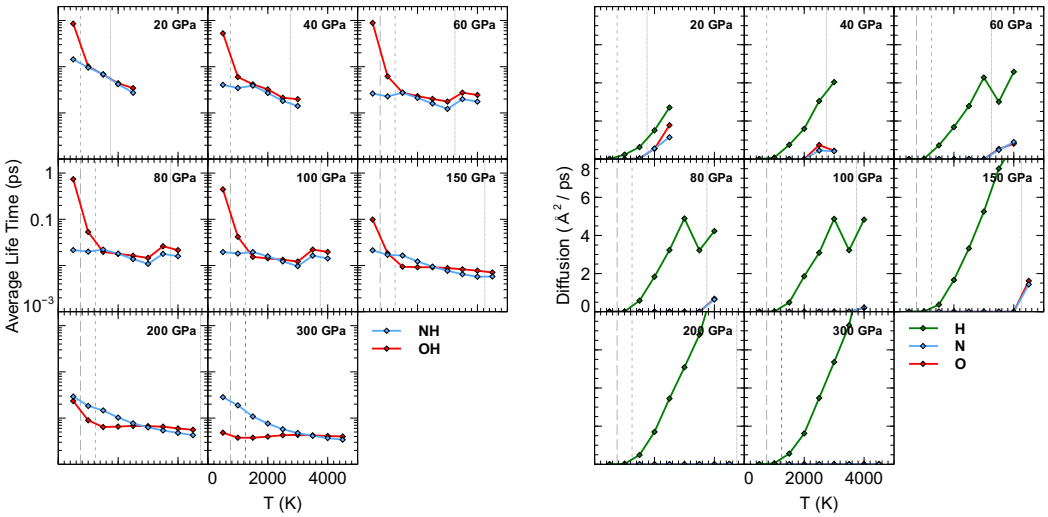

Figure 27 *AQH analysis of estimated bond life times (top left), ion diffusion (top right).*

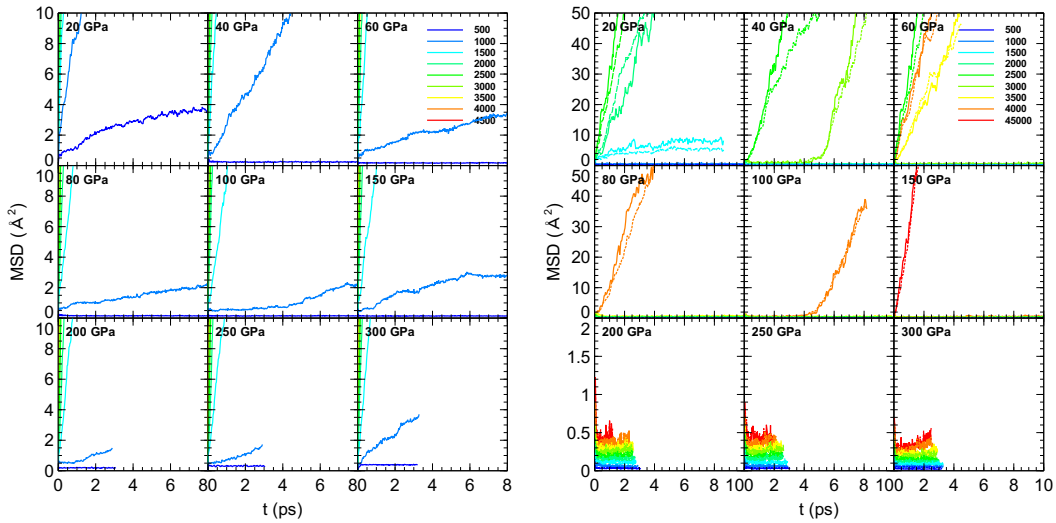

Figure 28 *AQH analysis of MSD.*

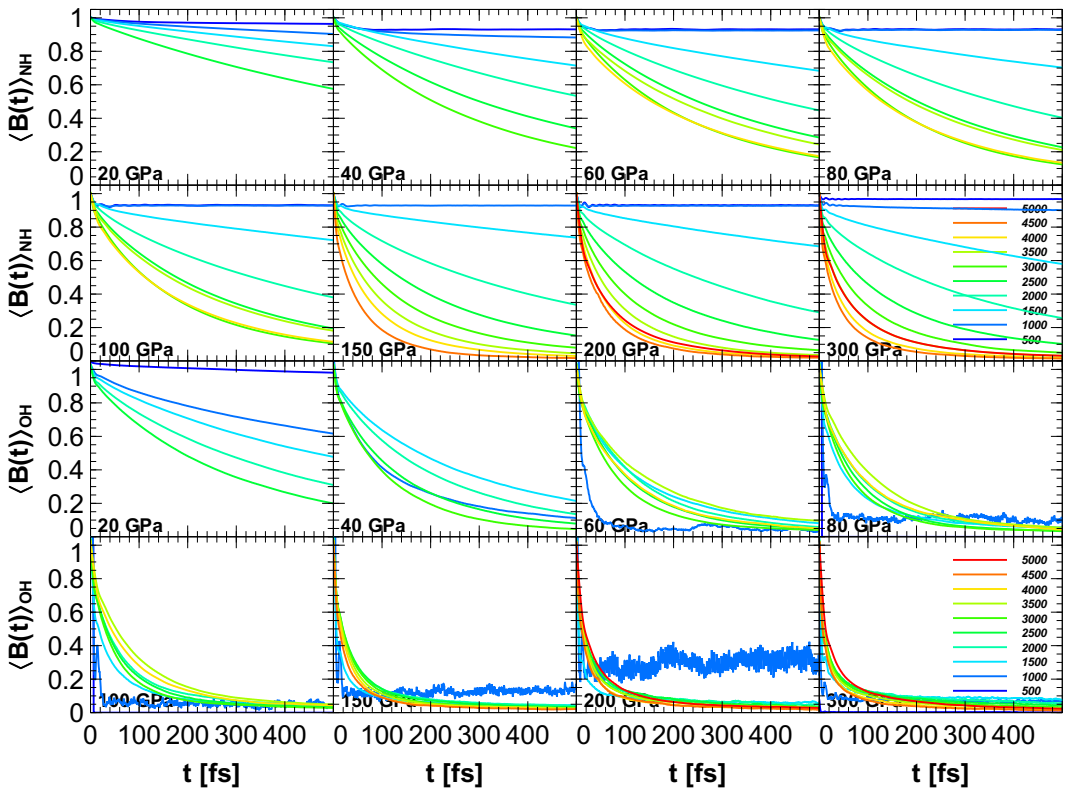

Figure 29 *AQH analysis of bond auto correlation function.*

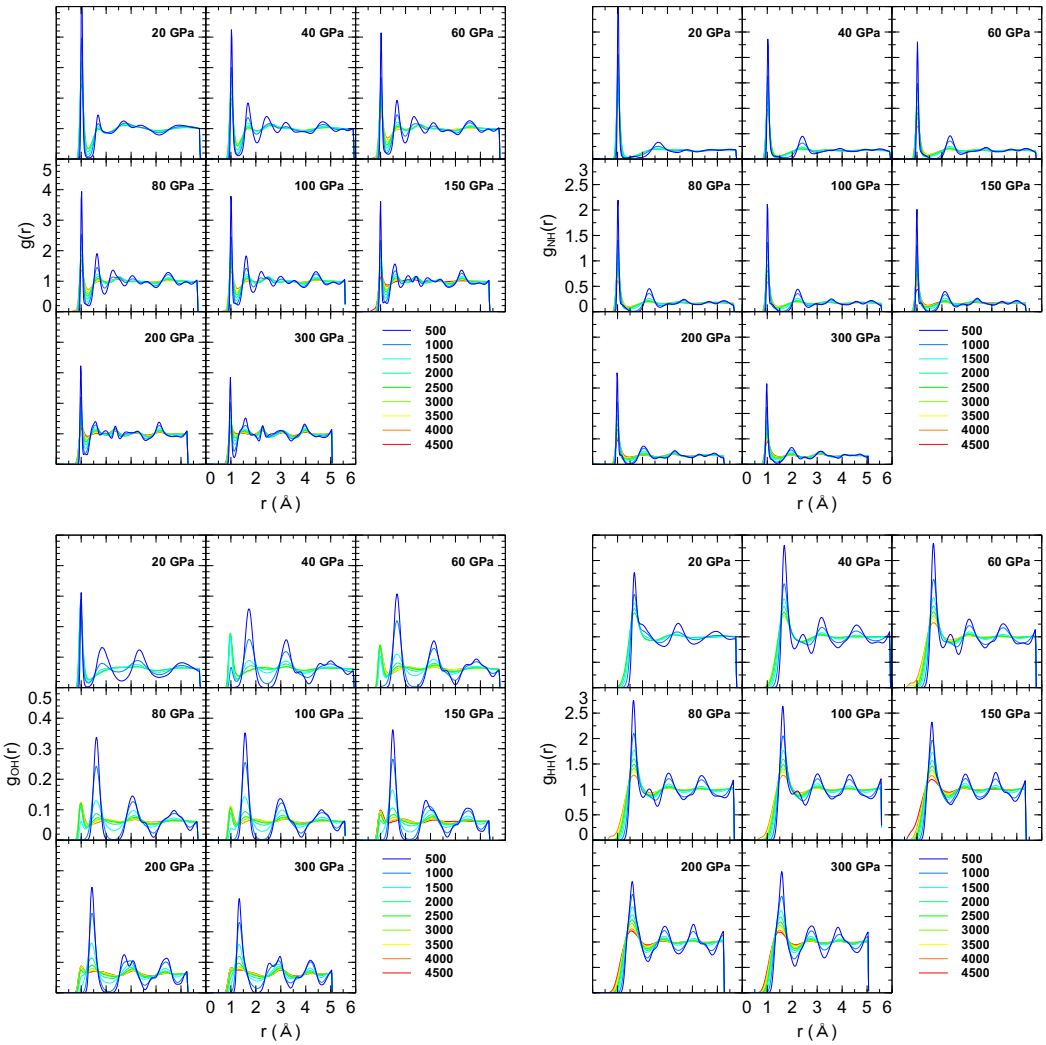

Figure 30 *AQH analysis of RDF and PDF (NH,OH,HH).*

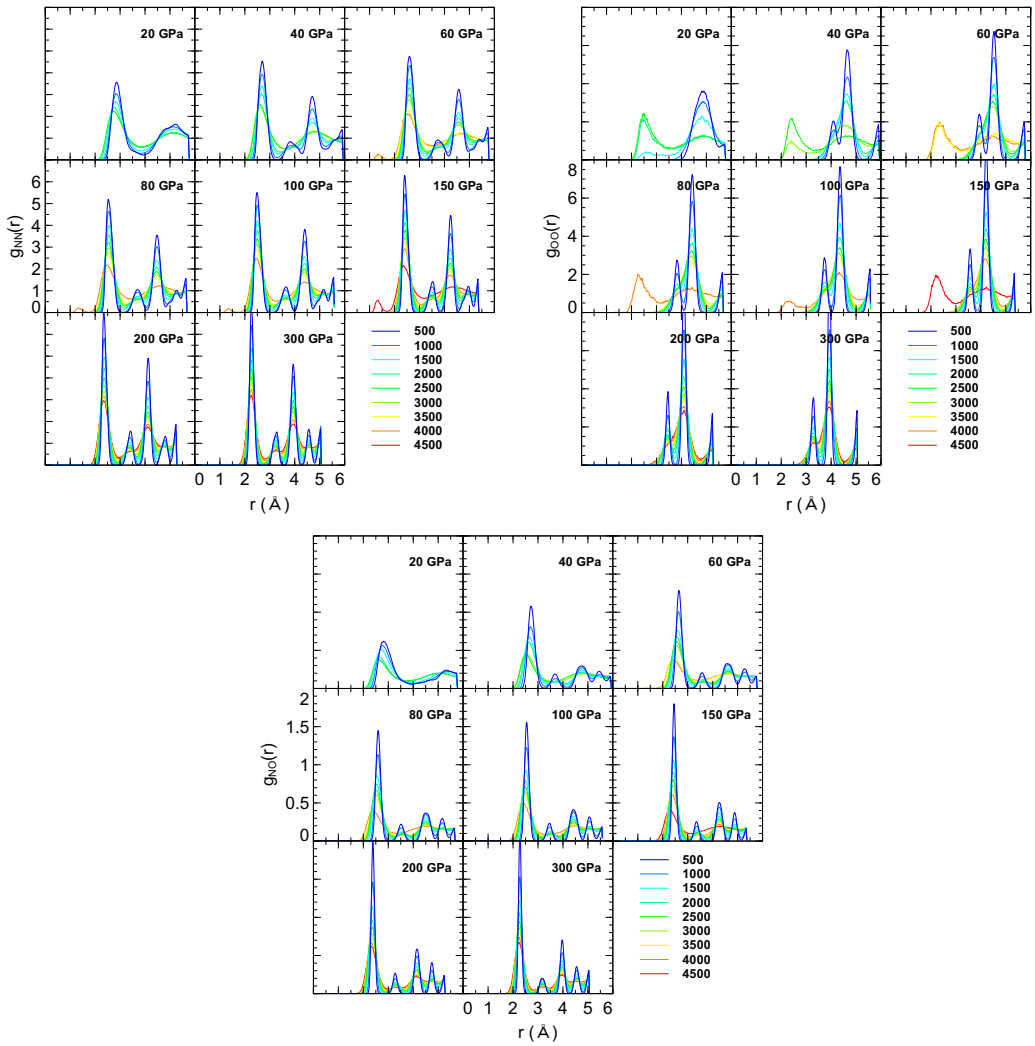

Figure 31 *AQH analysis of PDF (NN,OO,NO).*

The Seventh Appendix - AHH AIMD Analysis

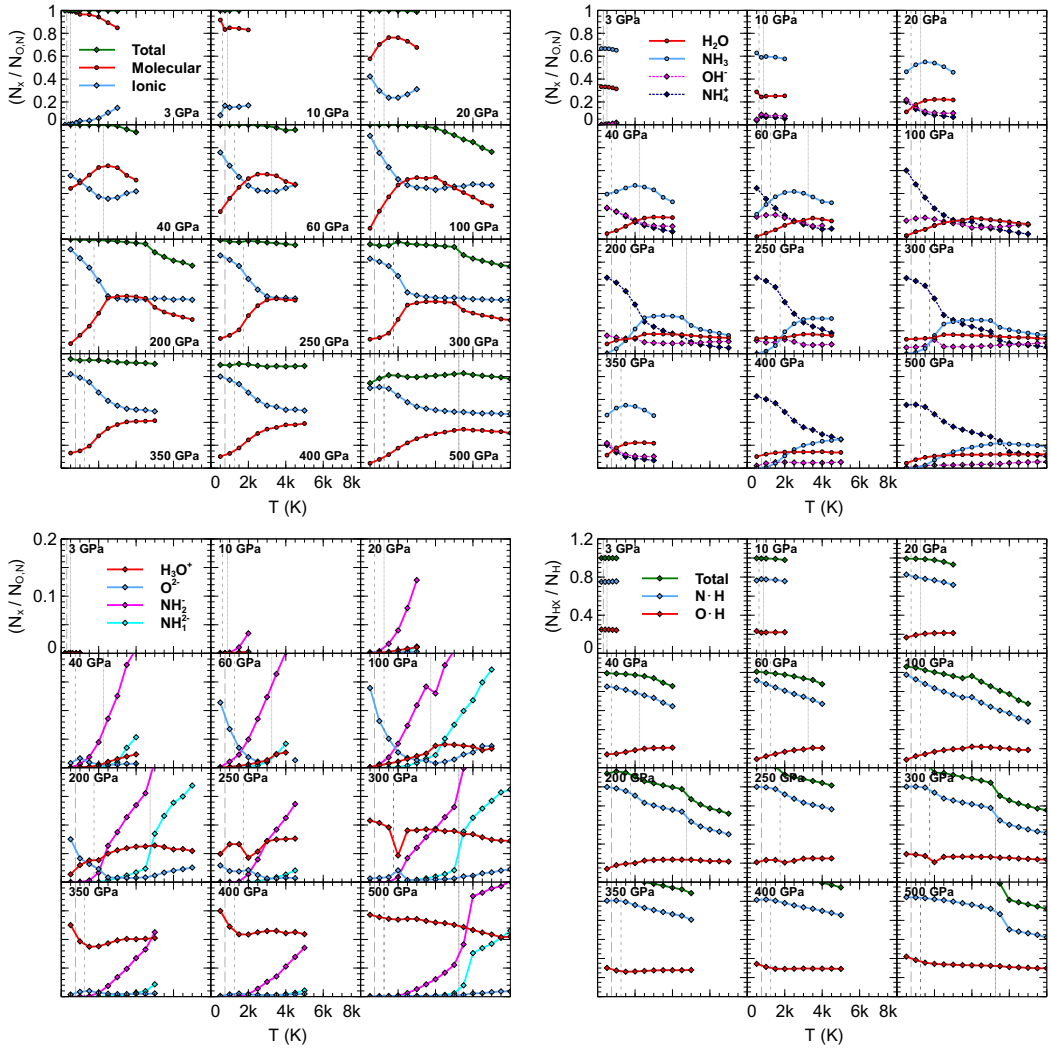

Figure 32 *AHH analysis of ionicity (top left), unit types (top right, bottom left), and covalent hydrogen bonds (bottom right).*

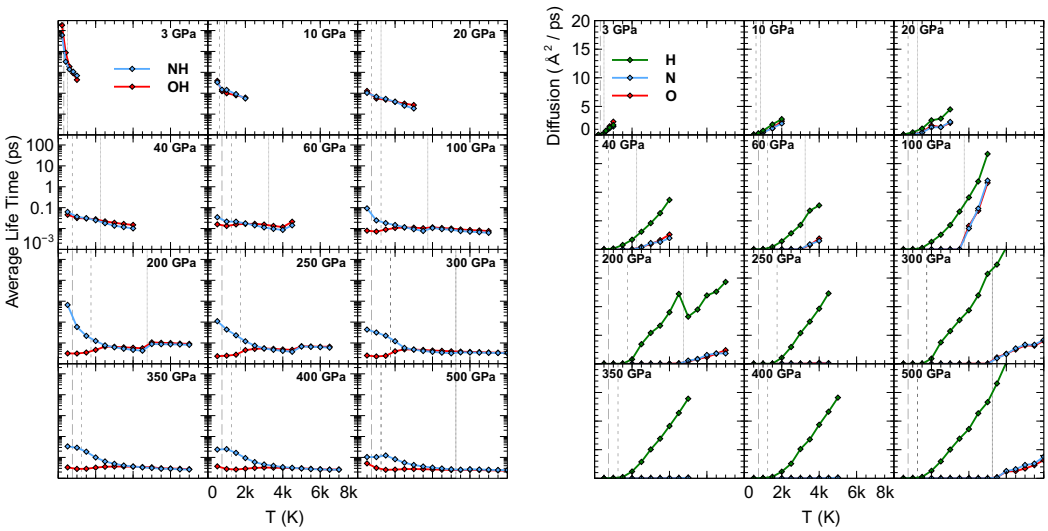

Figure 33 *AHH analysis of estimated bond life times (top left), ion diffusion (top right).*

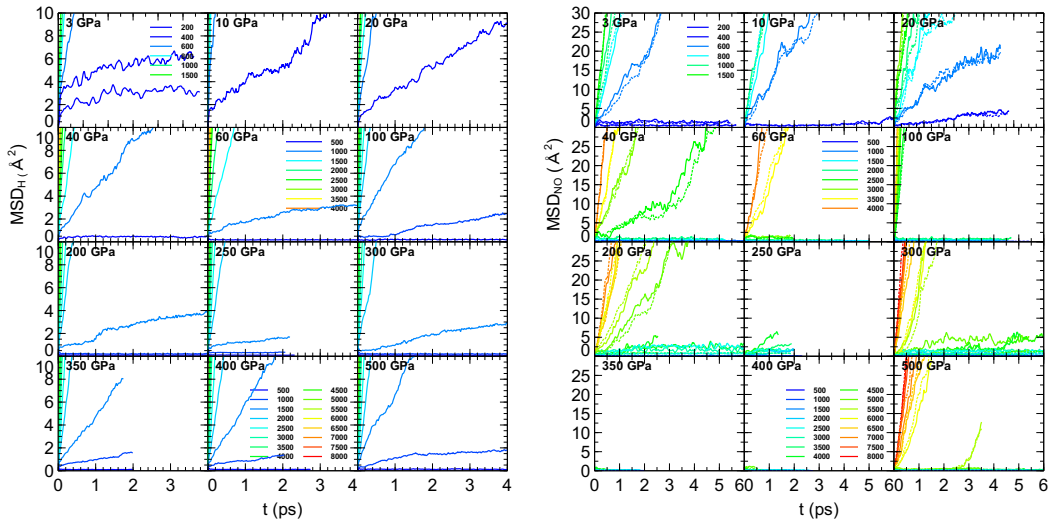

Figure 34 *AHH analysis of MSD.*

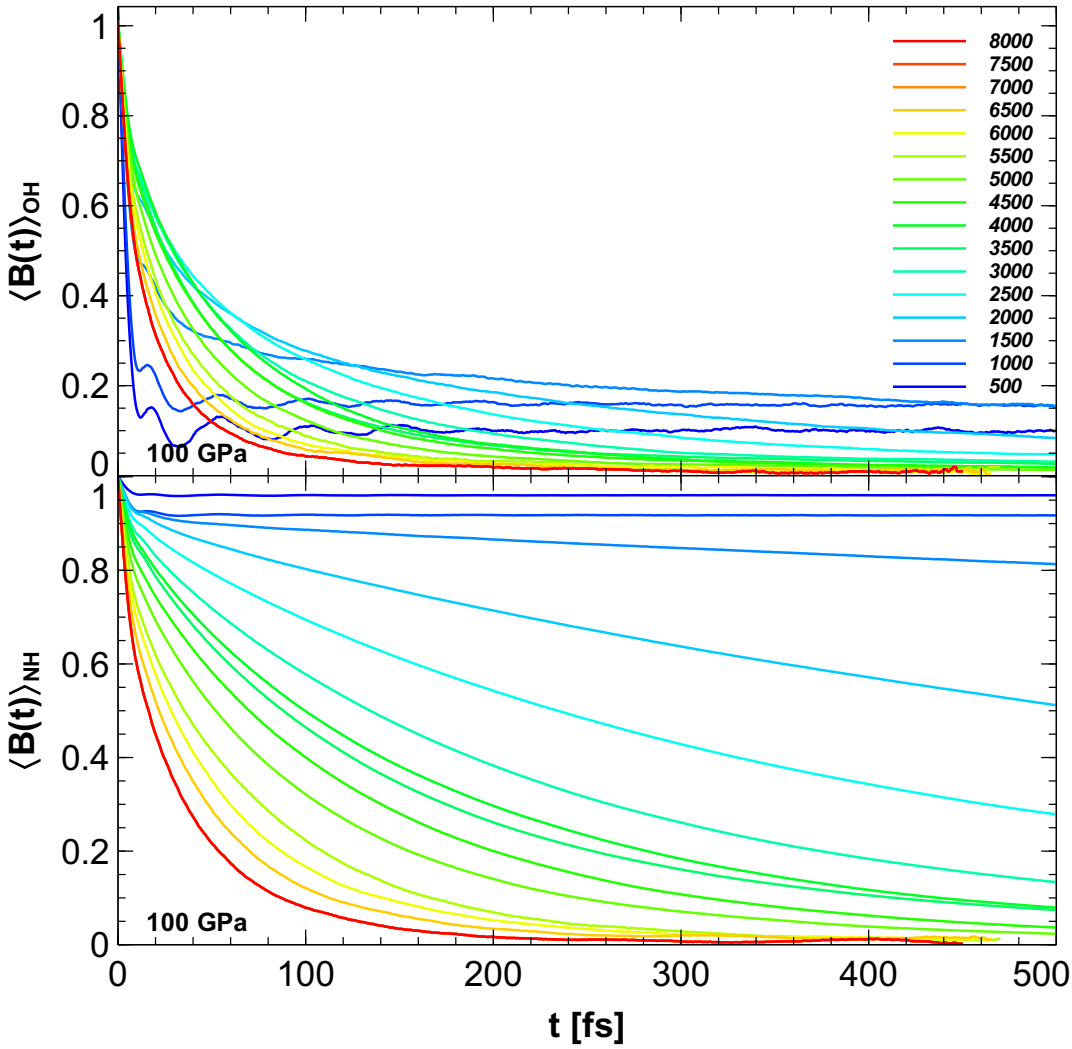

Figure 35 *AHH analysis of bond auto correlation function.*

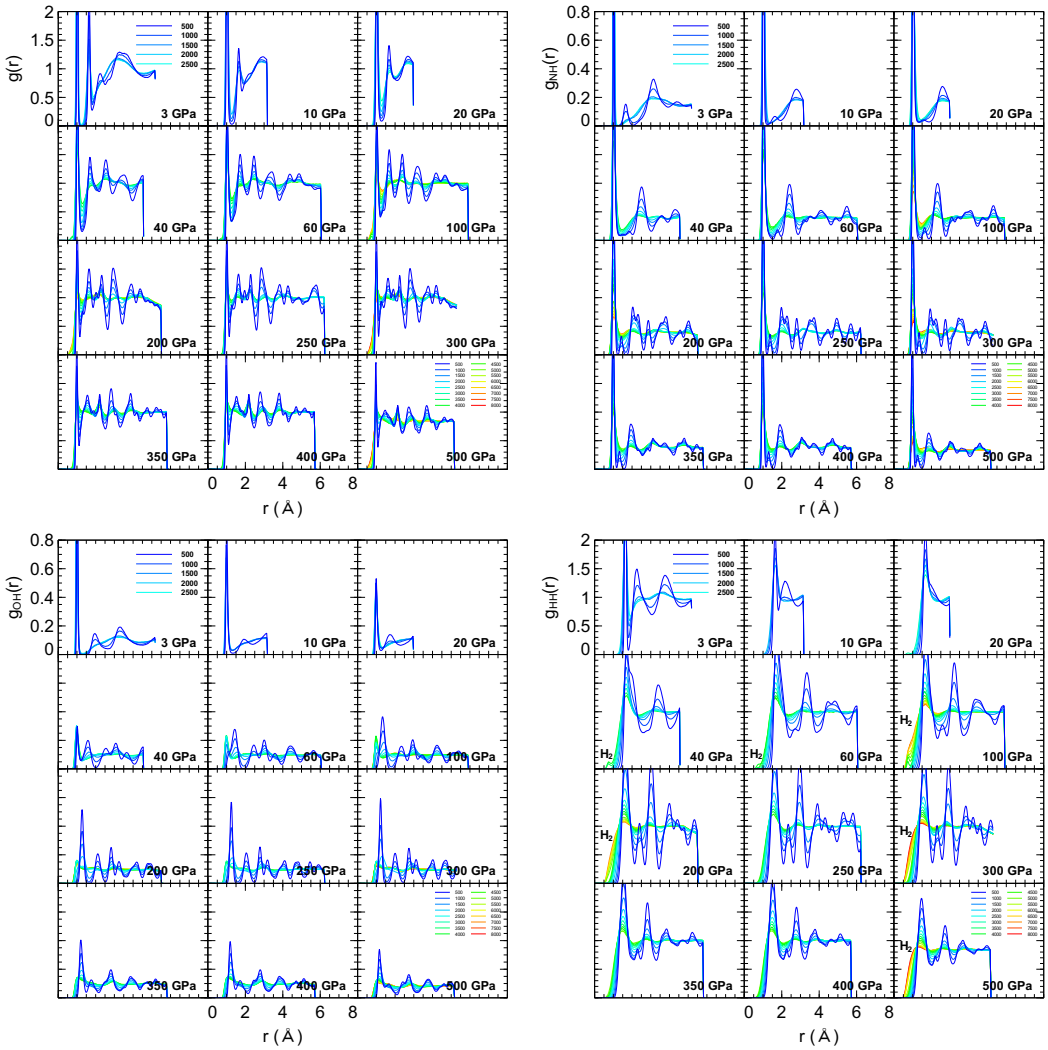

Figure 36 *AHH analysis of RDF and PDF (NH,OH,HH).*

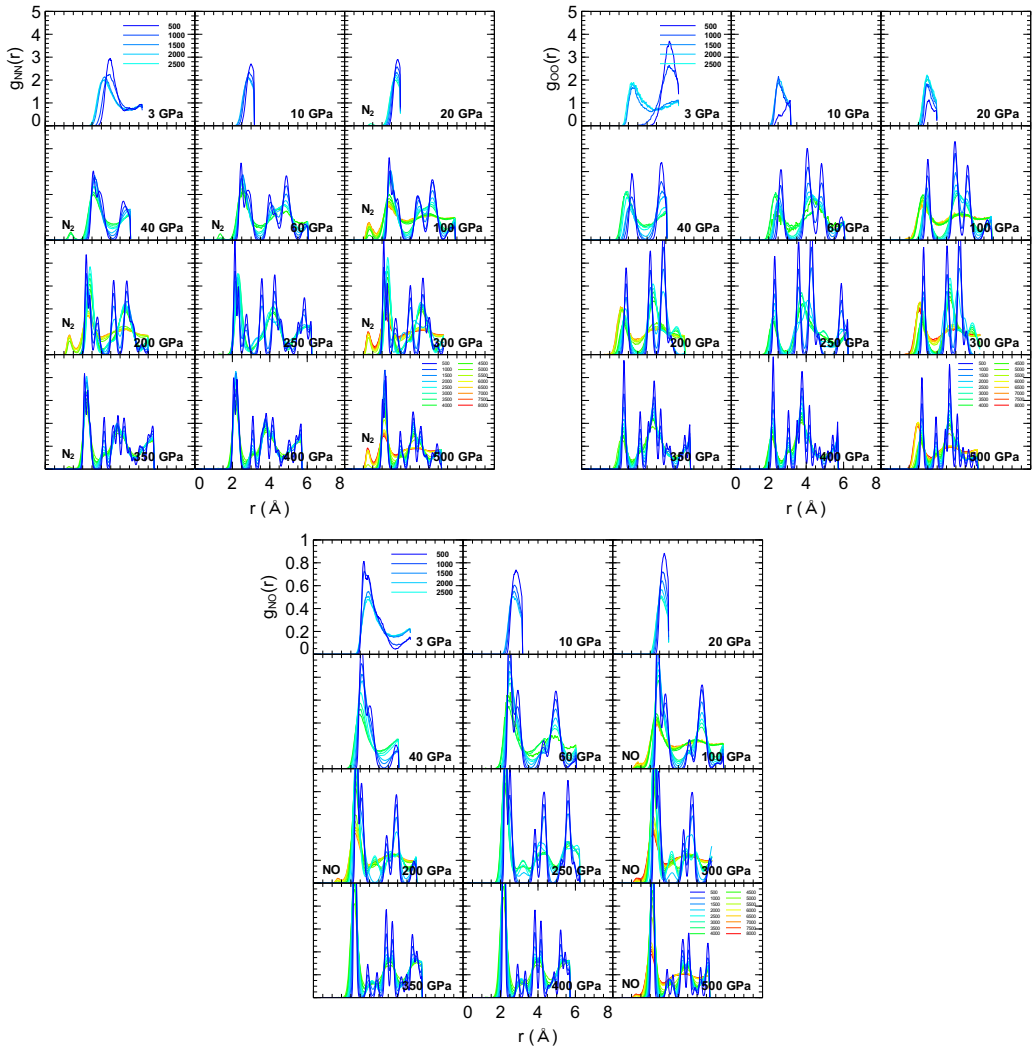

Figure 37 *AHH analysis of PDF (NN,OO,NO).*